Role of infragravity waves on port agitation during storm events

Florian Bellafont

▶ **To cite this version:**

Florian Bellafont. Role of infragravity waves on port agitation during storm events. Civil Engineering. Université de Pau et des Pays de l'Adour, 2019. English. NNT : 2019PAUU3047 . tel-02881282

HAL Id: tel-02881282
https://theses.hal.science/tel-02881282

Submitted on 25 Jun 2020

HAL is a multi-disciplinary open access archive for the deposit and dissemination of scientific research documents, whether they are published or not. The documents may come from teaching and research institutions in France or abroad, or from public or private research centers.

L'archive ouverte pluridisciplinaire **HAL**, est destinée au dépôt et à la diffusion de documents scientifiques de niveau recherche, publiés ou non, émanant des établissements d'enseignement et de recherche français ou étrangers, des laboratoires publics ou privés.

N ° d'ordre: — Année 2019

Rôle des ondes infragravitaires sur l'agitation portuaire en période de tempête

Thèse

présentée à

l'Université de Pau et des Pays de l'Adour

École doctorale :

Sciences Exactes & leurs applications (ED211)

par

Florian BELLAFONT

pour l'obtention du grade de

DOCTEUR

Spécialité :

Génie Civil

Soutenance programmée le 12/12/2019 devant la Commission d'examen formée de :

Jury MM.

Gaël ANDRÉ	Docteur - Encadrant de thèse	SHOM
Philippe BONNETON	Directeur de Recherche - Rapporteur	UMR EPOC
France FLOC'H	Maître de Conférences - Examinatrice	UBO
Denis MORICHON	Maître de Conférences (HDR) - Directeur de thèse	UPPA
Ad RENIERS	Professeur - Rapporteur	TU DELFT
Volker ROEBER	Chercheur - Co-directeur de thèse	UPPA
Philippe SERGENT	Directeur de Recherche - Examinateur	CEREMA

Abstract

Infragravity (IG) waves are surface long waves whose periods are ranging between 30 s and 5 to 10 min. IG waves are associated with incident wind-induced short waves (5-30 s) and generated by nonlinear phenomena. These long waves are difficult to dampen by port protective structures, such as dikes or breakwaters, due to their large wavelength. Once they enter a harbor, they can be amplified and excite semi-closed port basins and/or cargo-type moored vessels. Such phenomenon affects port operations.

This PhD thesis is part of a research project involving port of Bayonne on behalf of the Nouvelle Aquitaine Region council and the SHOM. This study aims to improve the knowledge about the dynamic of infragravity waves in river seaports during storm events. Port of Bayonne (France), located at the Adour river mouth, constitutes the main study site. Situated at the bottom of Bay of Biscay (Atlantic ocean), it is exposed to very energetic winter swells, favorable to the generation of significant IG waves. Port of Bayonne is also representative of operating river seaports whose shipping channel depth is maintained by regular dredging operations. A marina, composed of two connected basins, is located on the left riverbank.

An intensive measurement campaign was conducted over 3 consecutive winters (2016-2019) in order to characterize the port behavior and identify the generation mechanisms of external forcing. The offshore agitation data, continuously recorded by a directional wave buoy, were supplemented by the deployment of five pressure sensors in the port. This unique dataset covers a large range of external forcing scenarios: calm and energetic offshore incident waves, different water level and tide phases. The results show that the IG waves control port agitation and propagate freely in the river, which acts as a wave guide. IG waves lose little energy during their propagation in the river, and a cargo-type moored vessel can remain exposed to resonance phenomenon even at several kilometers from the river mouth.

Based on offshore incident short waves bulk parameters (height, period and direction of waves), a predictive model of the IG wave height at the river mouth was developed and validated. This model constitutes the first step in the development of an IG hazard prediction system, whose purpose is to improve port operations management.

A one-year return period storm event was simulated with a Boussinesq-type wave model, which allows to describe both non-linear interactions and dispersive effects at wave scale. It is intended to assess the impact of port activities (dredging operations and river mouth configuration) on the IG waves dynamic in the nearshore area and in the river. The results suggest that the position of a dredging disposal can be critical as it can favor the concentration of incident wave energy on port entrance. A new spatial configuration of the river mouth, consisting of the creation of an outer harbor basin, was simulated. The results show that an appropriate spatial configuration of a river mouth could reduce the incoming IG wave amplitude in the river.

Résumé

Les ondes infragravitaires (IG) sont des vagues de surface dont la période est comprise entre 30 s et 5-10 min. Elles sont principalement générées par des phénomènes non-linéaires associés aux vagues courtes incidentes (5-30 s). Du fait de leur grande longueur d'onde, les vagues IG sont difficilement amorties par les structures de protection portuaires, telles que les digues et les brise-lames, et pénètrent facilement dans les ports. Une fois dans le port, elles peuvent entraîner la mise en résonance du bassin et/ou des navires de commerce amarrés à quai et impacter l'exploitation portuaire.

Cette étude, réalisée dans le cadre d'un projet de recherche en collaboration avec le Port de Bayonne et le SHOM , se concentre sur la transformation des ondes IG dans un milieu estuarien en présence d'un port maritime en se focalisant sur les événements de tempête. Le port de Bayonne (France), situé à l'embouchure de l'Adour, constitue le site d'étude. Localisé au fond du Golfe de Gascogne, il est exposé à des houles hivernales très énergétiques, propices à la génération d'ondes IG. En outre, le port de Bayonne est représentatif des ports fluviaux aménagés dont la profondeur du chenal de navigation est maintenue par des opérations régulières de dragage. Il présente également un port de plaisance composé de deux bassins connectés sur la rive gauche du fleuve.

Une campagne de mesure intensive a été reconduite pendant trois hivers consécutifs (2016-2019) afin de caractériser l'oscillation portuaire et le comportement du port sous différentes conditions, et d'étudier les mécanismes de génération du forçage extérieur. La mesure en continue de l'état de mer au large par une bouée de houle directionnelle a été complétée par le déploiement temporaire de cinq capteurs de pression dans le port. L'étude montre que l'agitation portuaire est majoritairement contrôlée par les ondes IG qui se propagent librement dans le fleuve qui fait alors office de guide d'ondes. Les ondes IG se dissipent peu dans le fleuve si bien qu'à plusieurs kilomètres de l'embouchure, un bateau amarré peut être exposé au phénomène de résonance.

Basé sur les paramètres globaux d'agitation au large (hauteur, période et direction des vagues), un modèle prédictif de l'amplitude des ondes IG à l'embouchure du port a été développé et validé. Ce modèle constitue la première étape dans la mise en place d'un système d'alerte opérationnel.

Un événement de tempête de période de retour annuelle a été simulé par un modèle de vagues à phase résolue, basé sur les équations de Boussinesq, afin de compléter les données expérimentales et d'étudier l'impact des activités portuaires (dragage et configuration de l'embouchure du fleuve) sur la dynamique des ondes IG en proche côtier et dans le fleuve. L'étude montre que les activités de dragage peuvent avoir un impact défavorable sur l'agitation portuaire. Une nouvelle configuration de l'embouchure du fleuve, consistant en la création d'un avant-port, a été simulée. Les résultats des simulations numériques montrent que cet aménagement limite l'agitation portuaire dans la bande infragravitaire, pour l'événement simulé.

Remerciements

Ce projet a été financé par le port de Bayonne par l'intermédiaire d'une bourse de la région Nouvelle-Aquitaine, et par le SHOM. Je tiens à remercier Simon Fages et Stéphane Gubert du port de Bayonne pour leur confiance et leur soutien tout au long de ce projet, ainsi que l'équipe technique du port pour leur support et expertise lors des campagnes des mesures.

Je tiens à adresser mes remerciements les plus sincères à Denis Morichon, directeur de cette thèse, pour la confiance qu'il m'a témoignée, pour son appui et sa disponibilité aux moments les plus cruciaux de cette thèse, notamment la rédaction de ce manuscrit, et pour les nombreuses discussions scientifiques stimulantes. J'adresse un grand merci à Volker Roeber, co-directeur de cette thèse, pour ses conseils et son expertise sur la modélisation numérique, ainsi que son soutien et sa disponibilité. Je tiens à remercier chaleureusement Gaël André, référant au SHOM pour ce projet et encadrant de cette thèse, pour sa confiance, son soutien et sa disponibilité, malgré la distance nous séparant. Je remercie les membres du jury, et particulièrement les rapporteurs Philippe Bonneton et Ad Reniers, pour la qualité de leurs rapports et leurs remarques constructives.

J'adresse mes sincères remerciements, ainsi qu'une pensée chaleureuse à l'ensemble de l'équipe de l'ISA BTP qui m'a d'abord formé en tant qu'ingénieur en bâtiment et travaux public, et ensuite accueilli en tant que collègue pendant cette thèse. Je remercie l'école doctorale de l'université de Pau pour son soutien et son accompagnement sincères témoignés envers les thésards.

J'adresse un immense merci à mes collègues thésards et postdocs pour leur soutien, les bons moments partagés, ainsi que les discussions stimulantes : Sophie, Iñaki, Manu, Lucie, Benoît, Thomas, Olivier, PA, Youssef, Fariza, Delphine, Amaia, Ximun, Paul, Jonas, Fatima, Ana, Ali, Rafik, Ange, Omar, Hui.

À titre personnel, j'adresse un remerciement plein d'amour à ma famille, mes parents et beaux-parents, et mon frère, qui m'ont toujours soutenu dans mes projets et qui sont une grande source d'inspiration pour moi. Enfin, j'adresse un grand merci à Lucie qui partage ma vie.

Contents

Introduction

General context

Historically, ports were settled in areas relatively sheltered from direct exposure to incident waves in order to limit harmful oscillations in harbor. For instance, port of Rotterdam, in Netherlands, was originally established upstream of an estuary, 40 km from the North Sea coast, before beginning its donwstream development at the early 20th century. Other ports, like Liverpool (United Kingdon) or Bordeaux (France) lie along river banks more or less far from a river mouth. Ports have also been established in the shelter of islands such as ports of Lorient in France or Vigo in northwestern Spain. Port of Brest, in France, located in a roadstead, is also a good example of naturally protected port just like the one of Capbreton that benefits from the protection of an underwater trench (the Gouf of Capbreton) at its entrance.

Ports have a central role in our current liberal and globalized economy. About 80% of global trade by volume (70% by value) were carried on board ships (on Trade and Development, 2017) in 2016. Total seaborne volume reached 10.7 billion tons in 2017 (on Trade and Development, 2018) with 17.1% for containerized trade, 29.9% for major dry bulks (iron ore, grain and coal) and 29.4% for oil and gas. Asia leads the world maritime trade in 2017 and represents 42% and 61% of exports and imports of world commodities compared to 17% and 20% for Europe, and 21% and 13% for Americas. World seaborne volume trade is projected to expand at a annual growth rate of 3.8% between 2018 and 2023 (with the fastest growth for containerized and dry bulk commodities trades). Confronted with a high competition (especially in the container market segment), the ports enhance their terminal performance by modernizing existing facilities and/or by building new infrastructures. Consequently in the last century, river seaports move, expand or create new facilities downstream near the coast in order to have a greater water-depth to handle larger vessels and reduce navigation time to reach docks. For example, port of Bordeaux built a container terminal at the Gironde Estuary in 1976. Port of Rotterdam expanded by gaining land on the North Sea during the two Maasvlakte extensions in 1960 and 2013. Port of Ferrol (Spain) created a new area at the mouth of Ferrol river for bulk carriers

and container vessels by building a 1070 m breakwater in 2005 (López et al., 2012). A container terminal extension Liverpool2, located close to the River Mersey mouth, opened on 2016. In addition, complex and dynamic morphology features, in particular at river mouth, can often disrupt or even prevent the access to and the exploitation of a port. Regular dredging operations are thus necessary to maintain a sufficient depth for shipping channels and in front of wharves.

Generally, the construction of new basin or new port is accompanied by the construction of protective structures such as breakwaters or seawalls to dampen ocean sea and swell waves (more generally short waves (SW) of periods 5-25s). Their purpose is to limit harbor oscillation in this frequency band, considering that the recommended maximum value of Hs_{SW} is around 0.40 m for fishing boats and 0.70 m for general cargo (Thoresen, 2003). Harbor infrastructures aim to facilitate ship navigation and berthing, limit the motion of moored vessels at dock and allow efficient commodities transfers. These structures work well in most cases, but many harbors experience agitation problems caused by long waves with periods longer than 30 s.

Long waves are difficult to dampen by port protective structures due to their large wavelength. Once they enter a harbor, they can be amplified and force the generation of seiches or the resonance of a mooring-ship system (Van Der Molen et al., 2006). Such phenomenon results in excessive surge movements of cargo-type moored vessels, affecting port operations, and sometimes lead to a sudden breaking of mooring lines. Seiche corresponds to a standing wave that can be generated either in a closed (lake) or semi-enclosed (port, bay, inlet) basin after the excitation of the basin natural resonance mode by an external forcing (Rabinovich, 2009). If the period of the incident long waves is close to an eigen period of the basin, resonance phenomenon occurs (Wilson, 1972). The eigen periods of harbor, only determined by its geometry, cover a large range of periods. Consequently, a wide variety of forcing mechanisms can cause seiche such as tsunamis (Rabinovich et al., 2006), atmospheric processes (Hibiya and Kajiura, 1982; De Jong et al., 2003; Monserrat et al., 2006; Marcos et al., 2009; Tappin et al., 2013) and infragravity (IG) waves (Bertin et al., 2018b) associated with incident wind-induced short waves and generated by nonlinear phenomena. This study focuses on the latter forcing.

IG waves are surface long waves whose periods are ranging between 30 s and 300 to 600 s. They are expected to excite semi-closed port basins of small to intermediate size (Okihiro and Guza, 1996; Bellotti and Franco, 2011; López et al., 2012; Thotagamuwage and Pattiaratchi, 2014b) and cargo-type moored vessels whose typical natural periods are in the order of one minute for a traditional mooring system (Thoresen, 2003; Van Der Molen et al., 2006). The role of IG waves have been largely studied in coastal environments as they contribute to nearshore hydrodynamics (Guza and Thornton, 1982;

Elgar et al., 1992) and are involved in many coastal processes such as sediment transport (De Bakker et al., 2016a), sandy beach erosion (Roelvink et al., 2009), run-up and overwashing (Bricker and Roeber, 2015; Stockdon et al., 2006). Most of studies about IG waves focus on their transformation in intermediate to shallow waters, namely their dissipation through bottom friction, nonlinear energy transfers and breaking (Battjes et al., 2004; De Bakker et al., 2015, 2016b), as well as their reflection at the coastline (Van Dongeren et al., 2007). However, few studies have looked at the transformation of IG waves once they enter and propagate inside an estuary in presence of a seaport.

Objectives of the thesis

This PhD thesis is part of a research project involving the SIAME laboratory (Université de Pau et des Pays de l'Adour), port of Bayonne on behalf of the Nouvelle Aquitaine Region council and the SHOM. Port of Bayonne constitutes the main study site. It is located in the south west of France. It was selected for this study as it is representative of a seaport located nearby a river mouth in a very energetic environment favorable to the generation of significant IG waves during storm events. With an annual cargo throughput of several million tonnes, port of Bayonne is the third port of the regional council of Nouvelle Aquitaine and plays a relevant role in local economy. It has recently developed its containerized trade activity by the construction of a 200 m long terminal in 2014 (Castel terminal) with an expansion project planned in a few years. It is located at the Adour river mouth in a mesotidal environment. It includes a deep-water commercial river seaport and a small marina (semi-closed basin). Situated on the Atlantic coast at the southern part of the Bay of Biscay, port of Bayonne is directly exposed to strong winter swells and faces problems in keeping boats docked during storm conditions. Furthermore, long-period oscillations have led to resonance of the marina several times a year. The Adour river mouth is characterized by a strong anthropogenic impact. The entrance of the river is protected by breakwaters, the longest of which is 1 km long. The river is channeled from it mouth up to 9 km upstream. In the port zone, frequent dredging operations are necessary to limit the silting of the river bed and allow permanent access to the navigation channel. An underwater sediment deposit, originated from river multiple dredging operations, is located between 2.5 and 3.5 km off the coast and peaks at -17 m.

The objective of the study is twofold. First, it aims to understand the functioning of the different sections of port of Bayonne and the role of incident infragravity waves. The study is based on an extensive dataset covering various climatic conditions. Secondly, the data are complemented by numerical simulations carried out with a phase resolving model to investigate the processes of transformation of IG waves including the effect of

harbor coastal defense and dredging operations. This study constitutes a contribution for harbor management and design in providing new knowledge that can influence, in the future, the planning of harbor modifications to minimize disturbance caused by IG waves.

Outline of the thesis

This dissertation is divided into six chapters. The introduction is followed by Chapter 1 which presents a state of the art of studies on coastal seiche. In this chapter, particular attention is paid to studies dealing with IG waves, including their mechanisms of generation and transformation, and their impact on port operations. Chapter 2 presents the characteristics of the study site from its historical evolution to its current functioning. Chapter 3 deals with the methodology used in this study. It includes a section on the development of a measurement device specific for this study and the data analysis methods used. The other section focuses on the numerical approach used to complement the dataset. In the chapter 4, the water elevation data acquired during a series of field campaigns are analyzed and discussed in order to understand the port functioning. The findings are then compared with results obtained at other French ports located along the Atlantic coast in chapter 5. Finally, an alert system to predict the amplitude of harbor oscillations based on forecasted bulk wave parameters is proposed and tested. Chapter 6 is dedicated to the numerical study of the port functioning. The model is first validated with data measured during a storm to verify its ability to simulate the measured harbor oscillations. Then different scenarios are simulated to study the influence of dredging activities and breakwaters configuration on the IG waves penetrating in the seaport. An overall discussion and conclusions are presented in Chapter 7.

Chapter 1

State of the art

1.1 Introduction

Ports are artificial structures located on the coast or in rivers, intended for economic and commercial activities (exchange of goods and transport of people, ...) and have a central role in our liberal and globalized economy. Seaports are located on the coast, connected to the ocean or the sea by one or more openings, and generally protected by defense structures (seawall, breakwater, jetty, ...). Located at the port entrance, their function is to dampen incident sea and swell waves (periods between 5 s and 25/30s), in order to minimize harbor oscillations and allow efficient port operations: navigation, berthing and ship docking. These structures work well in most cases.

A breakwater is classically a rubble mound with a superficial protective revetment slope (armor units made of concrete or natural hard rock with a rectangular shape or an other shape like tetrapod or accropode). The wave energy is therefore dissipated by depth-induced breaking and friction in the porous media (Hunt, 1959). Another technique used is the immersion of caissons offshore (vertical breakwater) in order to create an artificial port basin. These caissons are generally prefabricated (hollow) in concrete, brought to their final position and immersed by ballasting (filled with sand for example). In their emerged part, a (Jarlan-type) dissipation zone can be built to limit wave reflection. In cross-section, it is composed of an openwork wall with vertical perforations (open-sea side), a dissipation zone (buffer zone) and a vertical and waterproof wall (harbor side). This technique has recently been used to form the port of Tanger-Med II basin and is being applied (in July 2019) in Monaco for its extension project on the sea.

Despite the presence of protective structures at port entrances, agitation problems caused by long waves with periods longer than 30 s are often observed. These long waves are difficult to dampen due to their large wavelength, therefore they can easily enter port basins. Their small amplitude outside the port can be amplified once they penetrate

inside a semi-enclosed basin and force the generation of coastal seiche. They can also interact directly with a mooring-ship system and induce its resonance. These different amplification mechanisms are particularly evident during stormy periods.

In this chapter, the phenomenon of coastal seiche as well as the different approaches to estimate natural resonance mode of a basin are first presented. The external forcing of coastal seiche, namely incident long waves, is described. The study focuses on infragravity (IG) waves. IG waves behavior is then presented from the generation and shoreward propagation and their transformation and dissipation at the coastline. Finally, IG wave dynamics and their impact on port operations are presented.

1.2 Coastal seiche

Any closed (lake) or semi-closed (port, bay, fjord, inlet, ...) water body is an oscillating system with Natural Resonance Modes (NRM) in the same way as a guitar string in acoustic or a building subjected to an earthquake in civil engineering. After an initial displacement due to a disturbing force, an oscillating system will perform free oscillations for re-establishing its equilibrium position. The resulting oscillations are characteristic of the system only. A seiche is defined as free oscillations of closed or semi-closed water body and its period depends on the basin geometry (Rabinovich, 2009). The amplitude of the free oscillations dampens exponentially due to friction until the basin returns to its equilibrium state, namely a still water surface. The restoring force is provided by the action of gravity. If the external forcing is continuous and periodic, forced oscillations occur.

A NRM of a partially enclosed basin is characterized by an eigen period, a spatial distribution of the free surface, a radiation damping through the basin opening and an amplification factor of the external forcing (Wilson, 1972). The external forcing of harbor basins are mainly long waves entering through their mouth from the open ocean. If its period is close to an eigen period, resonance phenomenon occurs. The basin geometry causes the amplification of the incident waves and a standing wave occurs (figure 1.1). In this case, the oscillations are forced and the definition of seiche presented above does not strictly apply. However, for the rest of the study, the definition is extended to include these forced oscillations (amplified by the resonance) and the free oscillations that will continue after the external forcing stops.

A standing wave is a stationary long wave characterized by the presence of node(s) and anti-node(s), water motions at an anti-node being entirely vertical (no horizontal current), while at a node they are entirely horizontal (no vertical oscillation). With energetic external forcing, the resonance can generate strong vertical oscillations and

currents which can seriously interfere with harbor operations (interruption of berthing, downtime, ...)(Rabinovich, 2009).

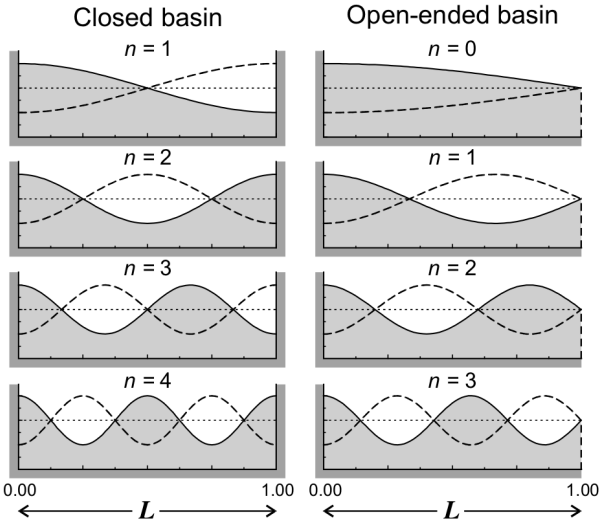

Figure 1.1 – Standing wave patterns for the first four NRM in closed and open-ended rectangular basins of uniform depth. Node and anti-node respectively correspond to maximal vertical amplitude and maximal horizontal current. Figure reproduced from Rabinovich (2009).

1.2.1 Determination of basin resonance modes

Estimation of harbor resonance periods in 1D

Harbors NRM are only determined by the geometry of the basin (water surface and depth) and the associated eigen period can be estimated applying the Merian formula (equation 1.1), valid only for simple geometry, namely long and narrow rectangular basin of uniform depth.

$$T_{CB,n} = \frac{2L}{n\sqrt{gh}} \ (n \geq 1) \ ; \ T_{OEB,m} = \frac{4L}{(2m+1)\sqrt{gh}} \ (m \geq 0) \tag{1.1}$$

where $T_{CB,n}$ and $T_{OEB,m}$ are the periods of the n and m modes in closed and open-ended basins respectively, L and h are respectively the basin length and depth, and g is the gravitational acceleration. For $n = 1$ and $m = 0$, the mode is qualified as fundamental. For closed basin, the condition of no-flow through the basin solid boundaries leads to the presence of two antiphase anti-nodes for the fundamental mode. For open-ended basin, a nodal line is located at the entrance.

The Merian formula is useful for a first estimation of basin eigen periods (Thotagamuwage and Pattiaratchi, 2014b). Wilson (1972) presented seiche analytic solutions for

other basin spatial configurations such as triangular or semiparabolic depth profile, and triangular or semielliptic plan form for open-ended configurations. It is worthy to note that the previous 1D approach is not suitable if the basin is not long and narrow. Indeed 2D effects can play an important role such as compound mode corresponding to the superposition of transversal and longitudinal modes in rectangular basin, or coupled modes occurring in harbors with complex geometry, notably with several linked basins (Thotagamuwage and Pattiaratchi, 2014b). Moreover, the Merian formula is determined with a nodal line located exactly at the basin entrance but this condition does not take into account radiation through the mouth, which involves the moving of nodal line offshore. This radiation effect depends on two parameters that will correct the effective length of the basin: the basin aspect ratio $q = l/L$ where l is the basin width, and the aperture ratio $v = b/l$ where b is the mouth width (Rabinovich, 2009). Radiation into the open sea is important when the semi-closed basin is broad and has a large entrance (q and v close to 1), and negligible when the basin is long and narrow (q small).

Estimation of harbor amplification factor

In addition to the period and the spatial pattern of the standing wave, a resonance mode is characterized by a damping factor which plays a double role. In the case of forced oscillations and resonance, it is a measure of the dynamic amplification of the external forcing by the harbor geometry, after the forcing stops it indicates the rate of time decay of free oscillations. The lower the damping factor, the stronger will be the amplification of the incoming waves and the slower will be the energy decay. In addition, the energy decay of seiches in closed basins is mostly due to friction dissipation, while in semi-closed basin as harbors is mainly due to radiation through the harbor entrance.

Figure 1.2 shows a (μ) dynamic amplitude diagram defined as the ratio over the wave frequency between the wave height inside the harbor and the offshore incident wave height. Resonance occurs when the (σ) external forcing period is close to the (ω) basin eigen period and is maximum when $\sigma/\omega \simeq 1$. In this case, μ is equal to the damping factor, also defined as the quality factor Q (Q-factor). Basins with a low aspect ratio or a low aperture ratio have a high Q-factor values and correspond to elongated and narrow inlets or to harbors with narrow entrances.

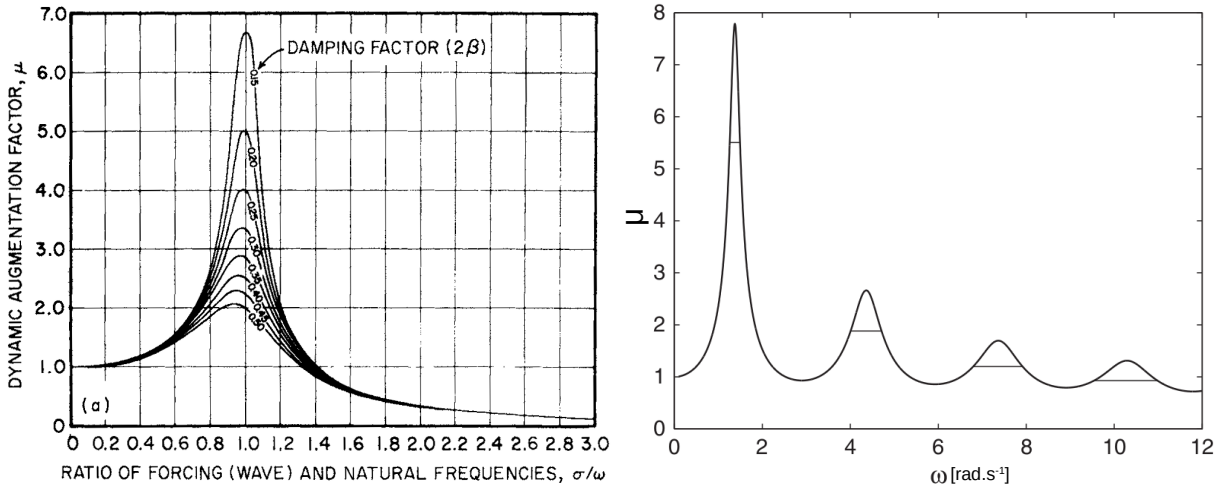

Figure 1.2 – (left panel) Dynamic amplification factor μ (linear damped vibration) as functions of frequency ratio σ/ω and damping factor 2β. (right panel) Dynamic amplification diagram (analytical solution) at the upstream solid boundary of a long and narrow open-ended basin of uniform depth ($l = 0.06\ m$, $L = 0.3\ m$ and $h = 0.01\ m$). Horizontal line indicates half power bandwidth $\Delta\omega$ for each modes such as $\mu \geq \mu_{max}/\sqrt{2}$. Figures reproduced from Wilson (1972) and Bellotti et al. (2012), respectively.

The damping factor can be estimated from a spectral analysis of observation data (Wilson, 1972). For a resonance mode, the half power bandwidth $\Delta\omega$, determined for $\mu \geq \mu_{max}/\sqrt{2}$, is equal to 2β (figure 1.2).

Field data

From free surface measurement, the inherent behavior or natural topographic response of a water basin can be determined when the incident waves (external forcing) energy is small and supposedly evenly distributed over all frequencies. Indeed, the basin spatial configuration, through amplification/attenuation of the incident waves, generates a frequency spectral signature of basin response called background spectrum (Marcos et al., 2009; Rabinovich, 2009). A background spectrum, determined at an observation point in the basin, is unique and may not contain all the NRM: if a gauge measuring the free surface vertical oscillations is located near a node of the standing wave, the dynamic amplification of this mode will be low at the measurement point, as well as if a current meter is situated near an anti-node. As shown in figure 1.1, an anti-node is generally located on the solid upstream boundary of a basin that is a recommended position for a gauge deployment (as pressure sensor) if its installation is technically possible.

Numerical simulations

As seen above, the analytical method of Merian is useful for estimating basin eigenmodes and gives an order of magnitude of the resonance periods, but it is only valid for basins with simple shapes, which is rarely the case for real ports. The background spectrum determined from a punctual field data is relevant but can provide incomplete information: unmeasured resonance mode and partial waveform of the stationary wave. To complete or extend the measurements of the water body behavior, numerical simulations are often used for existing harbors or in the framework of a construction or modification of harbors.

One numerical approach is to propagate different monochromatic waves (sinusoidal wave whose frequency, amplitude and direction are constant over time) from offshore into the basin in order to determine the dynamic amplification factor (figure 1.2) for each point of the mesh and each incident wave frequency: this is the so-called frequency scanning method. The peaks of the amplification diagram are assumed to represent NRM, and the corresponding standing wave pattern can be deduced. The numerical model equations can be linear (Bellotti, 2007; Pons et al., 2008) or non-linear (Losada et al., 2005; Shi et al., 2003; Thotagamuwage, 2014).

An other method allows to directly compute the eigenvalues (resonant period) and eigenvectors (spatial description of the standing wave) of the basin by an iteration method. The time-depending problem is converted into an eigen values one using the linear shallow water equations (Rao, 1966; Sobey, 2006; Bellotti et al., 2012). The computational domain is defined by the bathymetry (i.e. water level) of the basin and boundary conditions applied along the contour line. Two types of boundary conditions are usually defined: fully reflection condition along solid boundaries and nodal line (zero surface elevation) applied at the open sea boundary. Bellotti et al. (2012) applied an approximate radiation condition at the open sea boundary which allows waves to leave the numerical domain and thus to integrate the radiation damping phenomenon into the simulation.

These two numerical methods are used to determine the natural topographic response of a water basin but do not take into account the external forcing. Indeed, if the periods of incoming waves are far from the basin resonance periods or if the external forcing energy is weak, the resonance phenomenon will be weak.

1.2.2 Incident long waves

The eigen periods of harbor are only determined by the basin geometry and cover a large range of periods. A wide variety of forcing mechanism can cause seiche such as seismic activities, atmospheric processes and infragravity (IG) waves associated with incident wind-induced short waves and generated by nonlinear phenomena. Figure 1.3 presents the

periods and relative amplitudes of ocean surface waves and their generation mechanisms.

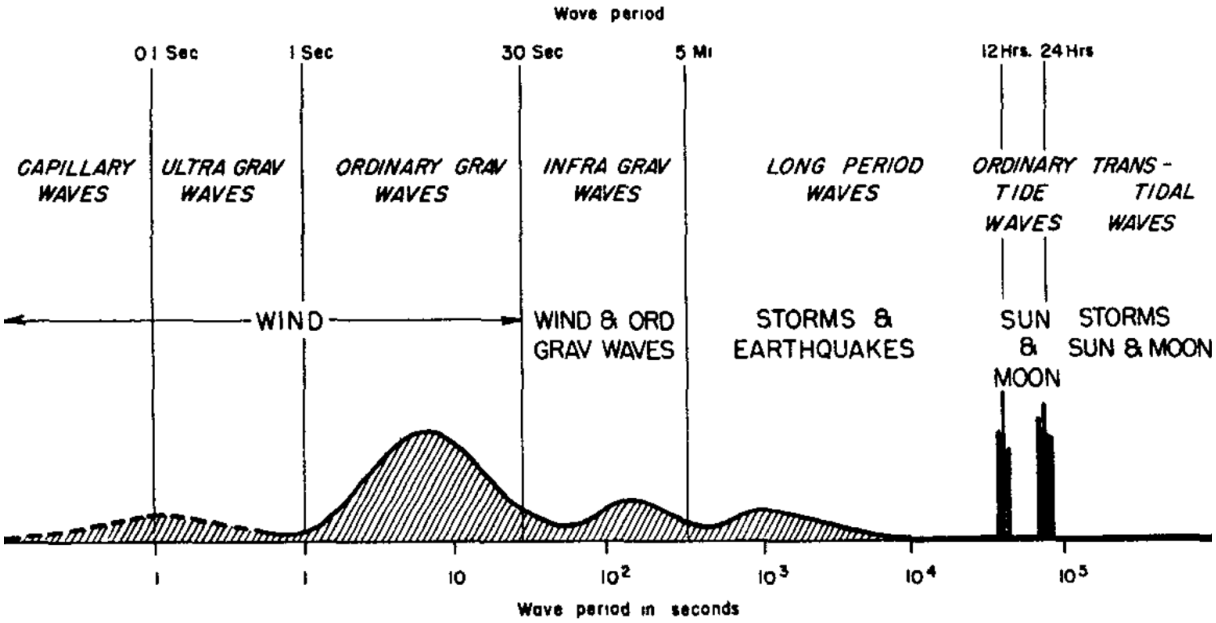

Figure 1.3 – Classification of the ocean surface waves according to wave period and forces responsible for wave generation. The y-axis represent an arbitrary amplitude scale. Figure reproduced from Munk (1951).

Tsunamis

Tsunamis are mainly generated by underwater earthquakes, submerged landslides or volcanic explosions (Rabinovich, 2009). These relatively rare events can produce significant damage when arriving at the coast. Tsunami can generate strong seiche oscillations in bays, inlets and harbors. The earthquake that occurred in the Indian Ocean offshore of Indonesian coast on 26 December 2004 (magnitude of 9.3) generated a catastrophic tsunami. Waves were recorded by tide gauges around the world such as near-source zones (Indian Ocean) and remote locations of the North Pacific and North Atlantic, and generated coastal seiche oscillations (Rabinovich et al., 2006). The offshore tsunami waves had a broad frequency spectrum with the most energy in the 40-50 min period band, but the waves recorded at the coast were influenced by the local topography and induced local resonance modes.

Meteo-tsunami

Meteo-tsunami are tsunami-like waves (same temporal and spatial scales) but are generated by atmospheric processes (Monserrat et al., 2006). Atmospheric pressure changes can generate small-scale sea level oscillations (with periods of a few minutes to a few

hours) through atmospheric gravity waves (Gossard and Munk, 1954; Monserrat et al., 1991) or isolated pressure jumps (Hibiya and Kajiura, 1982) for instance, but they reach only a few hPa (i.e. a few cm of free surface changes). These atmospheric perturbations can be generated by the passage of cold fronts, tornados, storms, squalls, etc. Several resonance phenomena occurring between the ocean and the atmospheric forcing can feed the initial disturbance with energy and increase the sea level oscillations: Proudman resonance (Proudman, 1929) occurs when the atmospheric disturbance speed (U) is close to the ocean long wave phase velocity c ($c = \sqrt{gh}$). Furthermore the Greenspan resonance (Greenspan, 1956) can occur if the atmospheric disturbance alongshore speed is close to an edge waves mode phase speed. In addition, the shelf can amplify the offshore incident waves through bathymetry resonance if the period and/or the wavelength are close to the resonant period and/or the wavelength of the shelf region (Bertin et al., 2012). These resonant phenomena may amplify incident atmospherically-generated waves approaching the coast but cannot generate waves with sufficient energy to extensively affect the open coast, unless the waves reach the entrance of a semi-closed basin (bay or harbor) and excite a basin eigenmode with a high Q-factor (mainly the fundamental mode) (figure 1.4).

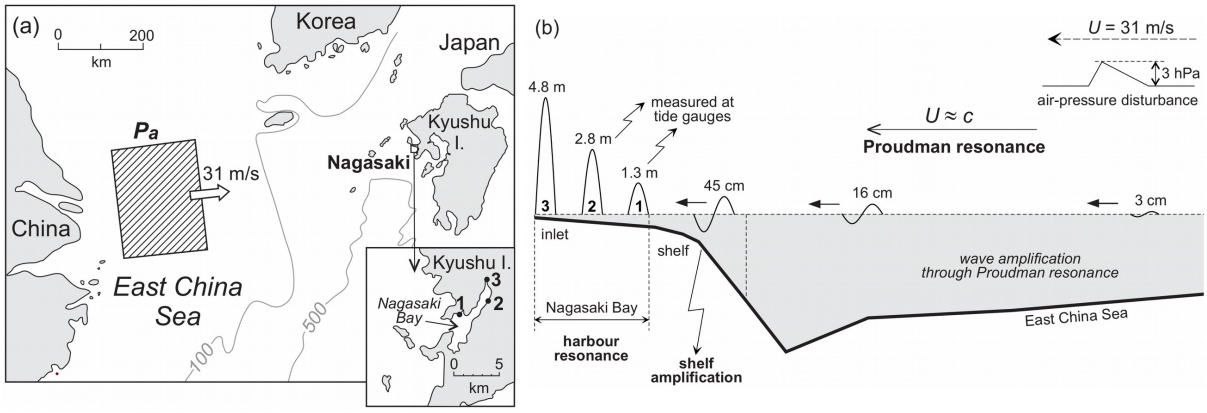

Figure 1.4 – (a) Map of Nagasaki Bay and the initial atmospheric pressure disturbance (shaded rectangular region). (b) A sketch illustrating the physical mechanism for formation of the meteotsunami at Nagasaki Bay (Japan) on 31 March 1979. The numbers 1, 2 and 3 shown in (a) and (b) are positions of tide gauges Nezumi, Nagasaki and the head of the bay. Reproduced from Monserrat et al. (2006).

Catastrophic meteotsunamis are the result of a double resonance: amplification of offshore small initial disturbances during their propagation to the coast through ocean-atmosphere energy transfers and eventually shelf resonance, and amplification of incident waves by coastal semi-closed basins (excitation of the fundamental mode) (Monserrat et al., 2006). These events are rare and restricted to specific locations (Monserrat et al., 2006; Rabinovich, 2009), for example: Nagasaki Bay (Japan) (Hibiya and Kajiura, 1982)

(figure 1.4); Balearic Islands, Ciutadella inlet (Spain) (Gomis et al., 1993; Vilibić et al., 2008; Marcos et al., 2009; André et al., 2013) (figure 1.5); Longkou Harbour (China) (Wang et al., 1987); Adriatic Sea (Vilibić et al., 2004; Vilibić, 2005); coasts of British Columbia (Canada) and Washington State (USA) (Thomson et al., 2009); Port of Rotterdam, North Sea (Netherlands) (De Jong et al., 2003; De Jong and Battjes, 2004). Figure 1.5 shows the effects of a meteotsunami that occurred in Ciutadella Harbour (Spain), this phenomenon is locally called rissaga.

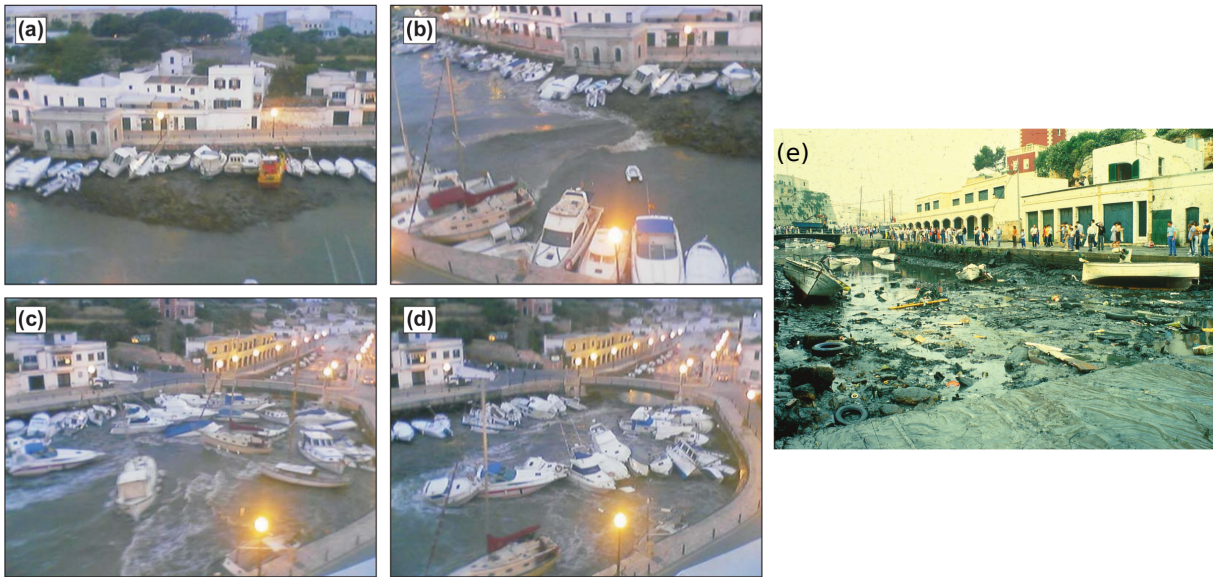

Figure 1.5 – (a,b,c,d) Photographs taken during the strong rissaga event of 15 June 2006 at Ciutadella Harbour (Spain). (a) After the first negative wave (-4 m), most of the boats broke free from their moorings and were left high and dry on the harbor bottom. (b) A few minutes later, the water re-entered the harbor and the boats were freely dragged by the current. (c) and (d) More than 40 boats were severely damaged. (e) Rissaga of 21 June 1984. Reproduced from Monserrat et al. (2006) (a,b,c,d) and Rabinovich (2009) (e).

Tappin et al. (2013), studying the origins of 'tsunami' and seiche oscillations in the Yealm Estuary (England), identified a meteotsunami event in the Bay of Biscay whose resulting waves were recorded by tide gauges located on the Spanish, British and French coasts.

Infragravity waves

IG waves are surface long waves whose periods are between 30 s and 300-600 s and are expected to excite semi-closed port basins of small to intermediate size (Okihiro and Guza, 1996; Bellotti and Franco, 2011; López et al., 2012; Thotagamuwage and Pattiaratchi, 2014b) and cargo-type moored vessels whose typical natural periods are 1 min or so for

a traditional mooring system (Thoresen, 2003; Van Der Molen et al., 2006). This study focuses exclusively on IG waves and the following section aims to describe the mechanisms of generation and transformation of these long waves.

1.3 Infragravity waves

Infragravity (IG) waves are surface ocean long waves whose periods are higher than the sea and swell waves (hereafter short waves) which are directly generated by the wind (figure 1.3). The short and IG waves can be separated at an arbitrary cut-off period (mainly 20, 25 or 30 s) or at a cut-off period determined from the short wave peak period T_p and equal to $2T_p$ (Hamm and Peronnard, 1997). For a wave spectrum, a clear separation is generally visible and appears as a local minimum of spectral energy. The upper limit period of IG waves varies according to the literature but is generally set between 200 and 300 s and can sometimes be extended to 600 s.

1.3.1 Generation mechanisms

The presence of short-wave groups is directly or indirectly responsible for the generation of IG waves by nonlinear phenomena. Bore merging is an other mechanism for IG wave generation, but it seems marginal compared to the two phenomena presented below (Tissier et al., 2017; Bertin et al., 2018b).

Bound IG wave

Biésel (1952) and Longuet-Higgins and Stewart (1962) firstly demonstrated that a second-order IG wave, called bound IG wave, is forced by non-linear interactions between short waves. Bound waves are phase-locked to the wave group and travel at the group velocity.

Considering a bichromatic short wave field propagating over a horizontal bed, the wave amplitudes are added where the wave trains are in phase and cancel out where they are out of phase. This pattern results in a wave groups structure whose frequency is equal to the difference between the frequency of the two considered short waves (figure 1.6). Waves with higher amplitudes transporting more radiation stress push the mean water level down and at the smaller waves location this results in a water level set-up. The modulation of the mean water level at the group wave scale is a wave itself that is out of phase with the short waves envelope, travels phase-lock to the wave group as a bound wave.

In the case of uniform depth, the resulting mean surface elevation $\bar{\zeta}$ is given by the

following equilibrium solution (Longuet-Higgins and Stewart, 1962, eq 5.3):

$$\bar{\zeta} = -\frac{S_x}{\rho(gh - c_g^2)} + \text{const.} \tag{1.2}$$

$$S_x = E\left(\frac{2c_g}{c} - \frac{1}{2}\right) \text{ with } E = \frac{1}{2}\rho g a^2 \tag{1.3}$$

where S_x is the wave radiation stress, h is the still water depth, ρ is the water density, g is the gravitational acceleration, c and c_g are the phase and the wave group velocities, a is the wave amplitude.

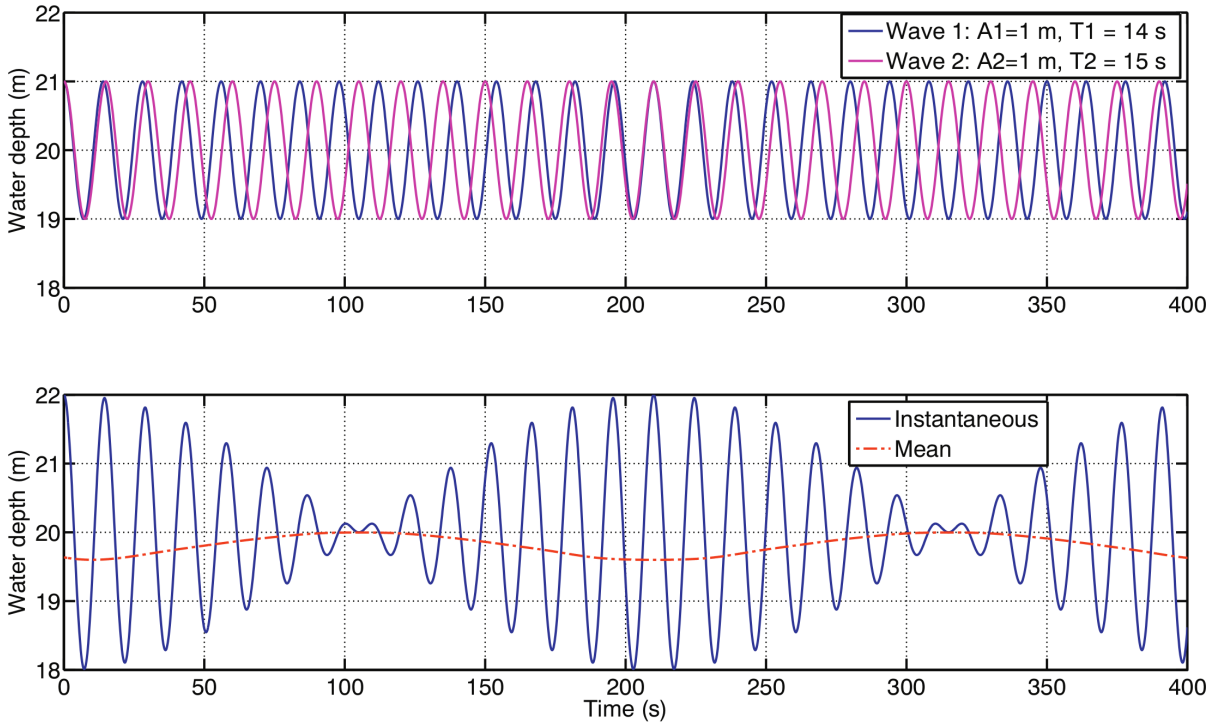

Figure 1.6 – (top) Time series of two sinusoidal waves traveling over a flat bottom by 20 m water depth. (bottom) Resulting free surface elevation (blue) and bound wave (red) as computed according to equation 1.3. Reproduced from Bertin et al. (2018b).

In nature, sea and swell waves field is composed of a multitude of random wave components (frequency, direction, amplitude and phase) and a bound sea surface spectrum can be determined according to the theory of Hasselmann (1962) which is a generalization of Longuet-Higgins and Stewart (1962) in two spatial dimensions. The bound wave components are determined considering each pair of primary short waves in the spectrum. The resulting bound wave amplitude, frequency and direction are calculated with a coupling coefficient (Sand, 1982; Okihiro et al., 1992). Herbers et al. (1994) confirmed that Hasselmann's theory accurately predicts locally forced IG waves.

The equilibrium solution of Longuet-Higgins and Stewart (1962) is only valid for a flat seabed and states that the bound IG wave is out of phase with the short waves envelope. However, when wave groups propagate shoreward on slopping bottom, a phase shift occurs between the wave envelope and the bound wave that lags behind the wave groups. This phase lag was observed in field (Masselink, 1995; Inch et al., 2017b) and in laboratory experiments (Battjes et al., 2004; de Bakker et al., 2013), and demonstrated theoretically (Janssen et al., 2003; Guérin et al., 2019). The phase lag allows energy transfer from short waves to bound IG waves through nonlinear triad interactions and the growth in amplitude of the IG waves during the shoaling phase. The growth rate is between $h^{-1/4}$ (conservation of the energy flux, Green's law) and $h^{-5/2}$, the shallow-water equilibrium solution of Longuet-Higgins and Stewart (1962). The bound wave shoaling mechanism is dominant in coastal environments with a gentle and relatively uniform slope where the shoaling zone is large enough to allow significant energy transfers. The normalized bed slope parameter β_b (equation 1.4) is an indicator of the beach slope regime (Battjes et al., 2004).

$$\beta_b = \frac{h_x T}{2\pi}\sqrt{\frac{g}{h_b}} \tag{1.4}$$

where h_x is the bed slope, T is the period of IG (or low-frequency) waves and h_b is the mean breaking depth. β_b is equivalent to the parameter χ of Symonds et al. (1982) and is related as $\chi = 1/\beta_b^2$.

Van Dongeren et al. (2007) found that for $\beta_b < 0.3$ the shoreline has a mild-slope regime for which the bound wave shoaling mechanism is dominant over the moving breakpoint mechanism (section 1.3.1). Figure 1.7 shows the growth in amplitude of the bound IG wave as a function of β_b.

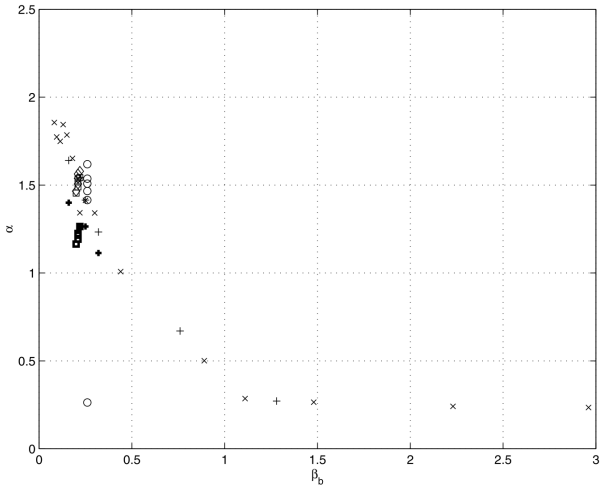

Figure 1.7 – Growth rate of the bound IG amplitude during the shoaling phase ($\bar{\zeta} \sim h^{-\alpha}$) as a function of β_b. Symbols represent different scenarios: variations of offshore depth; primary waves frequency, modulation and amplitude; bed slope. (bold symbols) Physical and (thin symbols) numerical experiments. Reproduced from Van Dongeren et al. (2007).

The β_b formula (equation 1.4) and the figure 1.7 suggest that the growth in amplitude (and the phase shift) is frequency dependent. More precisely, the smaller is the bound IG wave period, the greater is its growth in amplitude during the shoaling phase. The laboratory experiments of Battjes et al. (2004) and de Bakker et al. (2013) have shown that the phase shift phenomenon was frequency dependent but these two studies found contradictory results: the phase lag and the resulting growth of bound IG waves were larger either for the lowest (de Bakker et al., 2013) or the highest (Battjes et al., 2004) IG frequencies. A new semi-analytical solution of the phase lag proposed by Guérin et al. (2019), based on the theoretical work of Schäffer (1993), allows to study the influence of the bottom slope, the water depth, the incident short-wave peak period and the incident group period on this phenomenon. For all considered bed slope (1% to 5%), the phase lag increases with higher short-wave peak periods (especially for near-breaking short waves condition) and with lower water depths (Guérin et al., 2019, figure 9). However, the effects of the group period and the bottom slope are not univocal. For a 1-percent bed slope, the phase lag increases with higher wave group periods until near-breaking short wave condition where the phase lag is quite similar for the two considered group periods (Guérin et al., 2019, figure 8). For bed slopes of 4 and 5%, the phase lag decreases with higher wave group periods (most marked differences when shoaling starts) and with lower bed slopes. Guérin et al. (2019) concluded that the unequivocal influences of the bed slope and group period on the phase lag may explain the contradictory findings of Battjes et al. (2004) and de Bakker et al. (2013).

Masselink (1995) and Inch et al. (2017b), among others, observed that the depth-limited breaking of the short waves involves the disappearance of the wave group structure at the coastline. The bound IG waves are then no longer bound to the group and propagate as free waves with their own celerities, IG waves are released. However, List (1991) showed that some wave grouping can persist within the surf zone based on field data analysis. In addition, significant energy transfer from SW to IG waves can still occur in the surf zone (De Bakker et al., 2015, 2016b).

Moving breakpoint

An other mechanism for the generation of IG waves is the moving breakpoint caused by the presence of incident wave group. The higher short waves break further offshore than the lower ones, then the short wave break point moves onshore and offshore at the group period, generating free long waves. The gradient in radiation stress associated with initial breaking waves, caused by the periodic variation of the breakpoint, induces a time-variation of the wave set-up.

Symonds et al. (1982) first studied analytically the moving breakpoint mechanism using the depth-integrated, linearized shallow water equations for the flow averaged over the incident wave period, with the incident wave amplitude varying sinusoidally at the group frequency. Symonds et al. (1982) considered that the short-wave modulation was totally destroyed by the breaking, so that the wave height remains a fixed proportion of the water depth in the surf zone. Figure 1.8 shows the cross-shore variation of the wave height and the resulting set-up modulation. Symonds et al. (1982) did not considered the bound IG wave associated with the wave group and found that shoreward of the forcing region the solutions are in the form of a standing wave while an outgoing progressive wave exists seaward the forcing region (figure 1.8). Long waves are radiated away from the forcing region both seaward and shoreward. The outgoing free wave is then the sum of the shoreward wave reflected at the coast moving through the forcing region and the directly seaward radiated wave. Its amplitude depends on the relative phase between these two waves.

Later, Schäffer (1993) proposed an other approach including the incident bound IG waves in the depth-integrated, linearized shallow water equations. A hybrid model was proposed for the breaking and shoreward decay of incident waves in order to allow a partial transmission of grouping into the surf zone, which is consistent with the field data observations of List (1991). The solution shows a gradual change from a standing wave at the shoreline to a seaward progressive wave, which is in agreement with the results of Symonds et al. (1982).

The generation of free IG waves by the moving breakpoint mechanism has been partly

confirmed by laboratory experiment (Baldock and Huntley, 2002), and by field experiments conducted on a fringing reef (Pomeroy et al., 2012; Péquignet et al., 2014) and on a sandy barred beach (Contardo and Symonds, 2013). Generally the bed slope is a good indicator of the dominant mechanisms for the generation of IG waves: the bound wave shoaling mechanism should be dominant on milder slope ($\beta_b \leq 0.3$) as shown above, while the breakpoint forcing is expected to be dominant on steeper slope for $\beta_b \geq 1$ (figure 1.9, 1:20 sloping profile) (Battjes et al., 2004; Van Dongeren et al., 2007; De Bakker et al., 2016b).

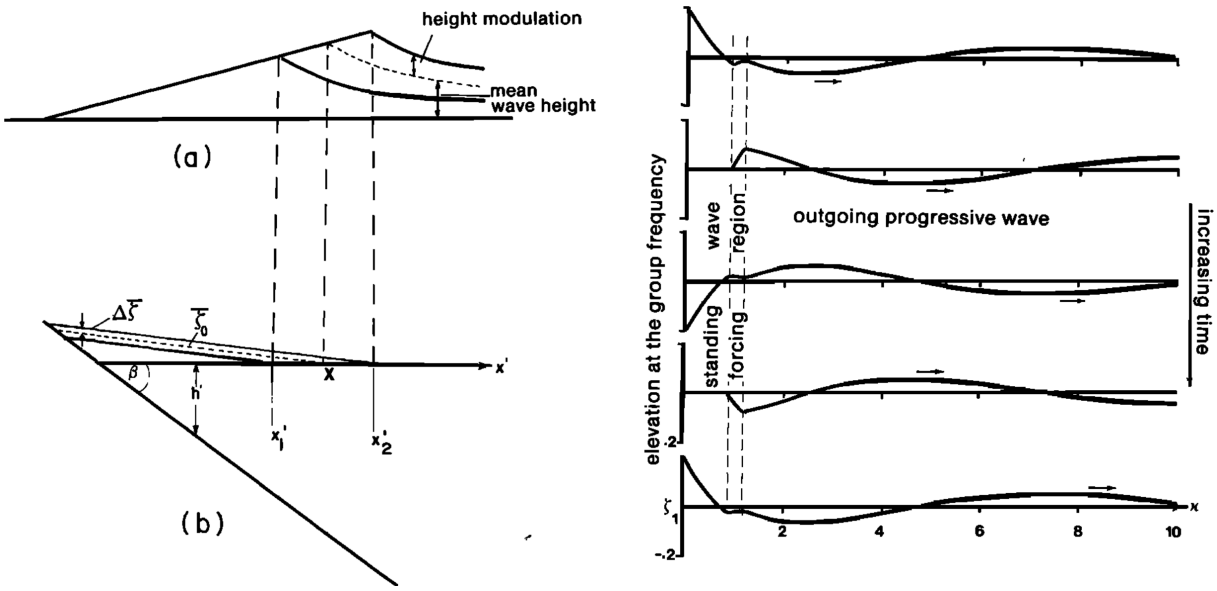

Figure 1.8 – (left figures) Schematic representation of (a) wave height and (b) set up through the surf zone. x'_1 and x'_2 denote the minimum and maximum positions of the breakpoint, respectively. (right figures) Typical solutions for elevation at different stages. Reproduced from Symonds et al. (1982).

1.3.2 Propagation and transformation processes

Nonlinear energy transfer

Nonlinear triad interactions occur between three phase-coupled frequencies during shoreward propagation of ocean waves and involve energy transfers in the wave spectrum. Generally, these interactions involve the dominant spectral peak f_p whose energy is spread over the spectrum. Sum interactions ($f_1 + f_2 = f_3$) transfer energy to higher wave frequencies and generate higher harmonics whose frequencies are multiples of f_p ($f_3 \approx 2f_p$ if $f_1 \approx f_2 \approx f_p$). The development of higher harmonics results in an asymmetrical and skewed wavefront during shoaling and a sawtooth-like shape during breaking (Elgar and Guza, 1985). At the same time, difference interactions ($f_1 - f_2 = f_3$) transfer energy

to lower wave frequencies which are bound IG waves. By this phenomenon, energy is transferred from short waves to bound IG waves resulting in their growth in amplitude during the shoaling phase.

Based on laboratory dataset obtained during the Gently Sloping Experiment (GLOBEX) project (Ruessink et al., 2013), De Bakker et al. (2015) studied non-linear IG interactions and completed the analysis with a numerical study (De Bakker et al., 2016b). Figure 1.9 presents the cross-shore evolution of significant wave heights of short wave (SW) and of incoming and outgoing IG waves (left panels), as well as the different non-linear interactions for high energy sea wave condition (case A2) and 1:80 sloping profile (right panels). At the beginning of the surf zone where H_{SW} starts to decrease (x=45.5 m), incoming IG waves continue to growth in amplitude until reaching a relatively horizontal level (between 59 and 78 m) and then rapidly decrease close to the shoreline.

In the surf zone, the incoming IG waves receive energy from short waves through non-linear energy interactions, which can be identified by bispectral analysis (figure 1.9, right panels). After the beginning of short wave breaking, IG waves receive energy from short waves mainly through $S_{nl,III}$ interactions involving one IG and two SW waves and to a smaller degree through $S_{nl,II}$ interactions involving two IG and one SW waves (difference of color scale on the figure). Within the IG period band ($S_{nl,I}$ interactions), energy transfers occur from high to low IG frequencies. During the relatively horizontal level of H_{IG}, an energy equilibrium is found between the energy gain from SW waves through $S_{nl,II}$ interactions and energy lost to SW through $S_{nl,III}$ interactions. From the maximum values of H_{IG} (x=67.1 m), energy transfers in the IG band ($S_{nl,I}$ interactions) are reversed and are from low to high IG frequency waves. From x=78 m, the fast decrease of H_{IG} is due to an energy transfer in cascade from low to high IG frequency ($S_{nl,I}$) and then to SW frequencies ($S_{nl,II}$) where the energy is dissipated (De Bakker et al., 2015). The IG interactions ($S_{nl,I}$) induce higher harmonics associated with the steepening and asymmetric shape of IG waves (sawtooth wave front) and the eventual breaking of IG waves (as shown by the biphases, figure 14 of De Bakker et al. (2016b)). This phenomenon was also observed in Van Dongeren et al. (2007) study.

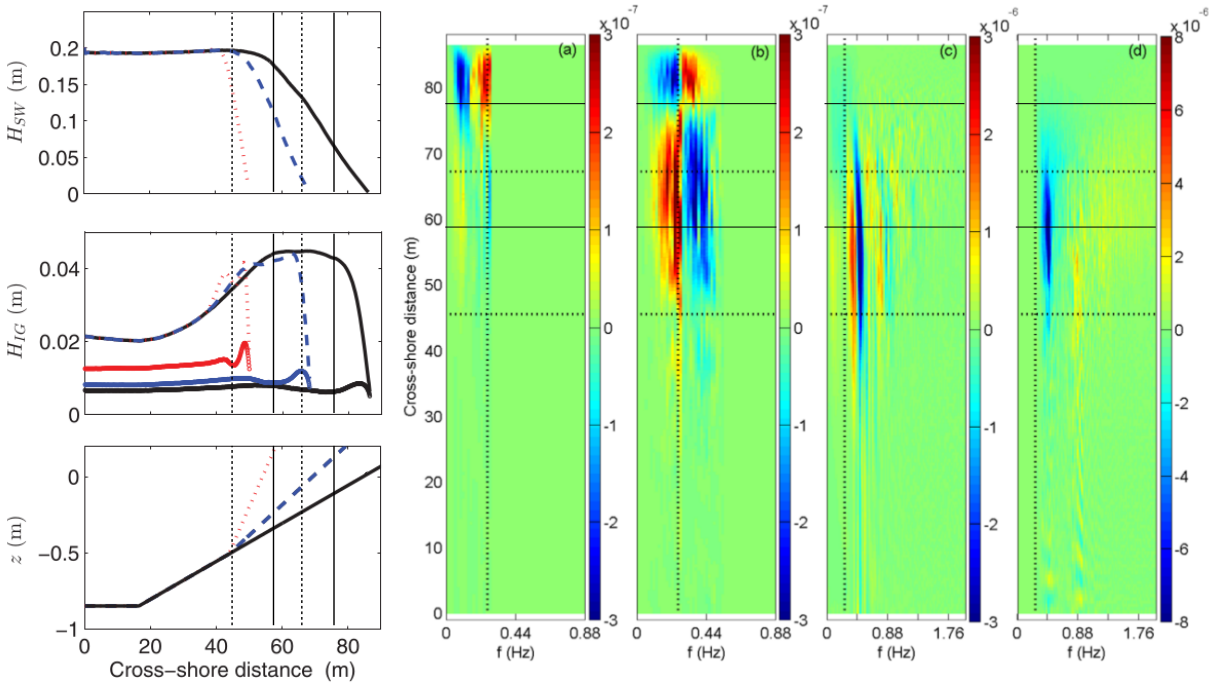

Figure 1.9 – (left vertical panels) Total sea-swell waves H_{SW}; (upper curves) incoming and (lower curves) outgoing IG waves H_{IG}; and bathymetry: (red, dotted) 1:20, (blue, dashed) 1:50 and (black, solid) 1:80 slopes. (right horizontal panels) Nonlinear source term S_{nl} estimated from the modeled incoming wave signal of case A2 on a 1:80 slope, versus frequency f and cross-shore position x. With (a) only IG waves ($S_{nl,I}$), (b) two IG and one SW waves ($S_{nl,II}$), (c) two SW and one IG waves ($S_{nl,III}$), and (d) only SW waves ($S_{nl,IV}$). The vertical line indicates the cutoff frequency between IG and SW waves. The horizontal dashed lines indicate the locations of the maximum IG (x=67.1 m) wave heights and the outer edge of surf zone (x=45.5 m). The horizontal solid lines indicate the position of a relatively constant H_{IG} (x=59 m and x=78 m, graphic interpretation). Modified from De Bakker et al. (2016b).

Dissipation

As shown in figure 1.9, IG wave energy can considerably decrease close to the shoreline and other studies have observed this phenomenon such as laboratory experiments (Battjes et al., 2004; Van Dongeren et al., 2007; De Bakker et al., 2015), numerical studies (Van Dongeren et al., 2007; Ruju et al., 2012; De Bakker et al., 2016b) and in the field (Ruessink, 1998; Sheremet et al., 2002; De Bakker et al., 2014; Inch et al., 2017b).

Two main mechanisms are proposed for IG waves dissipation at the shoreline: bottom friction and nonlinear energy transfer from IG band to higher frequencies. First studied by Henderson and Bowen (2002), bottom friction dissipation is dominant in environment with high friction coefficient such as coral reefs (Pomeroy et al., 2012; Van Dongeren et al., 2013; Péquignet et al., 2014), but is only a secondary mechanism for sandy beaches

whose friction coefficient is too low to induce significant dissipation (Henderson et al., 2006; Van Dongeren et al., 2007; De Bakker et al., 2014).

On sandy beaches, IG energy is not directly dissipated but it is transfered away from the IG band to higher frequencies. On gentle slopes (figure 1.9), nonlinear energy transfers occur in cascade from low IG to high IG frequencies and even to SW band. The development of higher IG harmonics induces changes in wave shape, which becomes skewed and asymmetric (sawtooth pattern), and the steepening of the wave front can lead to IG waves breaking (Battjes et al., 2004; Van Dongeren et al., 2007). On rather steep slopes (for instance 1:20 slopping profile, see figure 9 in De Bakker et al. (2016b)), IG energy is transfered back to SW band and at these frequencies the energy is then dissipated (De Bakker et al., 2015).

Reflection

Reflection can be characterized by a reflection coefficient R defined in equation 1.5. For $R = 1$, the incoming wave energy is totally reflected (classically against a vertical wall) and a standing wave occurs, whereas for $R < 1$ the partial reflection leads to a partially standing wave pattern. So, the identification of the cross-shore wave pattern can be a method to study the wave reflection, for example an empirical orthogonal function analysis was done by Henderson et al. (2001) to study the IG wave reflection in frequency-domain.

Reflection is linked to the dissipation rate of the incoming IG wave and Battjes et al. (2004) proposed that the IG wave reflection was controlled by a normalized bed slope parameter β_H defined in equation 1.6, which is slightly different from β_b.

$$R = \frac{H_{o,IG}}{H_{i,IG}} \tag{1.5}$$

$$\beta_H = \frac{h_x T}{2\pi}\sqrt{\frac{g}{H_{i,IG}}} \tag{1.6}$$

where $H_{o,IG}$ and $H_{i,IG}$ are respectively the wave heights of the outgoing and incoming IG waves near the shoreline, R is the reflection coefficient.

The reflection coefficient is a function of the bed slope and of the long waves frequency (figure 1.10). Steep slopes and/or low IG frequencies (to a lesser extent low $H_{i,IG}$) lead to large reflection, whereas lower reflection occurs with gentle slopes and/or high IG frequencies (Ruju et al., 2012). Thresholds of β_H can be used to identify the type of beach slope regime (mild or steep), but the location where the reflection coefficient is estimated influences the threshold values. During field campaigns, gauges are generally deployed in the inner surf zone rather than in the swash zone for technical issues, and the wave field is irregular in contrast to laboratory conditions (mainly bichromatic wave

forcing). That is why the transition between mild and steep slope regime was identified around β_H equal to 1 from laboratory data (figure 1.6) (Battjes et al., 2004; Van Dongeren et al., 2007), as opposed to a value of β_H around 3 from field experiments (de Bakker et al., 2013; Inch et al., 2017b).

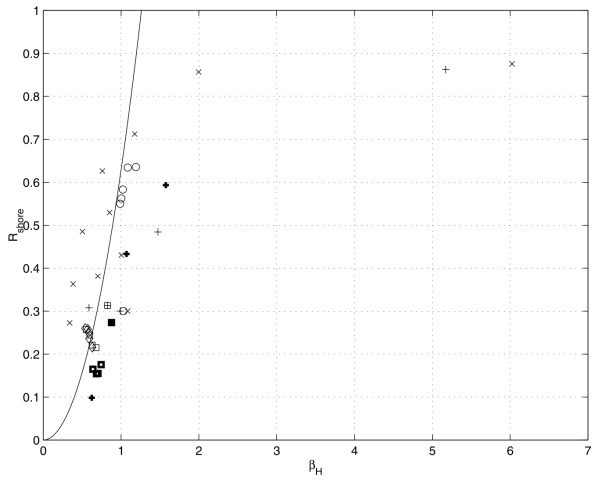

Figure 1.10 – Shoreline reflection coefficient R as a function of β_H. Equation $R = 0.2\pi\beta_H^2$ is plotted as the solid line. Reproduced from Van Dongeren et al. (2007).

The method used for separation of the incoming and outgoing wave signals can lead to error in the estimation of R, especially when using an array of wave gauges due to random noise in the data (Inch et al., 2017a).

Edge waves

The reflection of IG waves at the shoreline generates free waves that can either escape to deep water as leaky waves or be refractively trapped that leads to edge waves (figure 1.11). Edge waves are alongshore periodic free waves that are trapped between the coast by reflection phenomenon and the edge of the sea by refraction over a sloping bathymetry. Edge waves present a cross-shore standing pattern and usually have a progressive alongshore behavior (Ursell, 1952; Huntley et al., 1981; Herbers et al., 1995b,a; Van Dongeren et al., 2003).

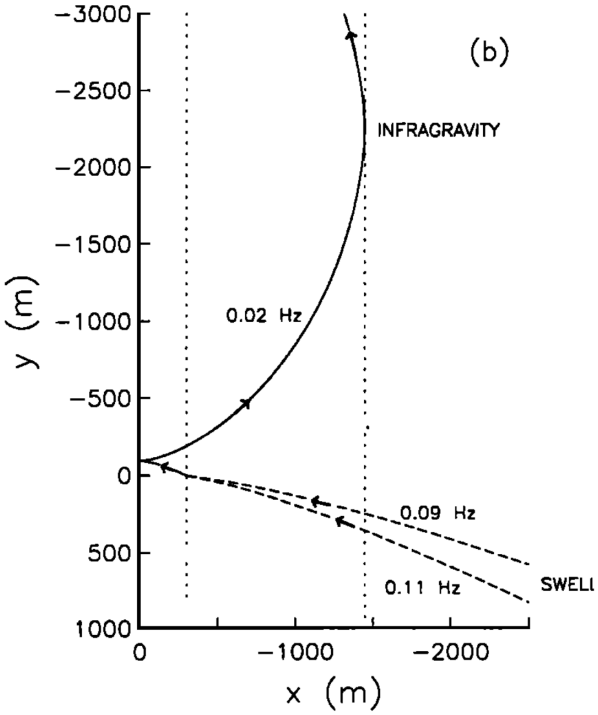

Figure 1.11 – Schematic of edge IG wave generation on a plane beach ($\beta = 0.01$) by nonlinear interaction of two swell components with frequencies and deep water incidence angles of (0.09 Hz,-25°) and (0.11 Hz,-30°). The forced, shoreward propagating bound IG wave with the difference frequency 0.02 Hz is nearly resonant in shallow water. After the dissipation of incident swell waves through depth-limited breaking, the forced IG wave is released as free wave, reflects from the beach, and radiates seaward. Well outside the surf zone, the outgoing free IG wave is refractively trapped and becomes an edge wave. Reproduced from Herbers et al. (1995a).

Edge wave motion is characterized by a dispersion relation relating the alongshore wavenumber k_e to the wave angular frequency σ_e. Eckart (1951) presented an analytical model based on shallow water theory for a plane beach with a linear slope $h(x, y) = \beta x$ and found a dispersion relation for small amplitude waves (equation 1.7). The amplitude of edge wave is maximum at the shoreline and its cross-shore evolution is given by the equation 1.8.

$$\sigma_e^2 = g k_e (2n + 1)\beta \tag{1.7}$$

$$\phi_n(x) = e^{-k_e x} L_n(2k_e x) \tag{1.8}$$

where x is the cross-shore spatial coordinate positive to seaward, n is the edge wave modal number, L_n is the Laguerre polynomial of order n.

Holman and Bowen (1979) used a numerical model to find the edge wave modes on a real beach with a concave profile. They found that simple formulation to estimate edge

wavelength, as for plane beach, can be wrong by around 100% at a fixed water level, and the time evolution of beach profile due to tide introduced further error as well as the presence of sandbars.

Edge waves can cause sedimentary alongshore patterns which are regular and periodic (Bowen and Inman, 1971) and potentially generate seiche in open-ended basin (Chen et al., 2004).

Uncles et al. (2014) investigated IG oscillations in a very small estuary. Coastal edge waves are the main source of IG waves in the area and are amplified by alongshore resonance between the headlands of the bay. Using Merian formula for an open-ended configuration (equation 1.1), along-estuary resonant seiching periods were estimated by defining an estuarine tidal length L_E (analogue to basin length L) which is the distance between the river mouth and the upstream point where IG wave currents are less than 0.001 $m.s^{-1}$. The standing wave pattern is similar to an open-ended configuration and implies that the river mouth is a node and the upstream point is an anti-node (maximum vertical oscillations). Based on this formula and hydrodynamic model results, Uncles et al. (2014) found that IG waves were amplified within the estuary due to the resonance mode 1 with a period range between 3.5 and 4.5 min. Periods of internal resonance of the salt wedge pycnocline can also be estimated using simple formula.

1.3.3 Coastal impacts

IG waves considerably contribute to nearshore hydrodynamics (Guza and Thornton, 1982; Elgar et al., 1992) and are involved in many coastal processes such as sediment transport (De Bakker et al., 2016a) and erosion (Roelvink et al., 2009); run-up, overwashing and inundation (Bricker and Roeber, 2015; Stockdon et al., 2006). Many studies concern IG waves transformation at the coast, namely their dissipation through nonlinear energy transfers and breaking (De Bakker et al., 2015, 2016b), as well as their reflection at the coastline (Van Dongeren et al., 2007). IG waves can have many impacts on port operations.

1.4 Studies on IG wave dynamics and their impact on port operations

1.4.1 Seiche generation

Thotagamuwage and Pattiaratchi (2014b) investigated IG period oscillations occurring in a small marina (Two Rocks Marina) located in south-west Australia and situated in an

area dominated by energetic winter swell waves. The marina is fronted by two shallow reefs located several kilometers from the shoreline. Measured water levels analysis showed that natural resonant periods of the basin are in the IG period band and the background spectrum presents a clear signature of amplification by harbor geometry. During storm conditions, the external forcing is more energetic, but the same peak periods are visible in the spectrum. The role of the reef system was studied with numerical simulations using a Boussinesq-type wave model (Thotagamuwage and Pattiaratchi, 2014a). The model results indicated that free IG waves were generated as the short waves propagated over the reef systems independent of the external forcing. During storm condition, the IG energy over the primary and secondary reefs increased by a factor about 10 and 8 respectively, compared to the IG energy at offshore. The IG wave spectrum near the marina entrance did not contain any major energy peaks, and had an almost constant energy distribution across the IG wave frequencies.

Okihiro and Guza (1996) used field observations to characterize seiches in three small harbors, Barbers Point and Kahului Harbors located in Hawaii and Oceanside Harbor in California. These three ports are subjected to the same swell wave forcing. The results show that amplification factors are largest at the fundamental mode period. At all three harbors, the average amplification of the fundamental band decreases (by at least a factor of two) with increasing seiche energy, which is consistent with nonlinear dissipation mechanisms. Based on correlation analysis, they showed that the ocean swells were the primary energy source for harbor seiches at frequencies above 0.002 Hz, namely the IG period band. While for frequencies lower than 0.002 Hz, seiches are excited by other phenomena including meteorological processes or tsunamis. A tidal modulation is observed in harbor spectra due to water level variation in the ports. Moreover, at a harbor located in mesotidal environment, IG waves energy increases at high tide by a factor of 5 to 10 compared to low tide. The concave shape of the neighboring beach induces strong variations of the bathymetry with water depth changes that affect mechanisms for generation of IG waves (Okihiro and Guza, 1995).

Bellotti and Franco (2011) experimentally studied oscillations in a small port, named Marina di Carrara, located in the North-West Mediterranean Sea, where the effective fetch is limited by the Corsica island. They found that IG energy was strongly correlated with the energy of the incoming short waves, and the spectra of the incoming long waves had a weak variation with the frequency.

Based on field measurements, López et al. (2012) characterized long period oscillations in port of Ferrol (northwest of Spain) located at the mouth of a ria, a drowned river valley, that is very narrow (or even closed) at its upstream end. A clear signature of amplification by harbor geometry is visible on power spectral density. As for the studies

presented above, IG period band exhibits a high correlation with the offshore swell energy, both outside and inside the harbor. The study showed that the generation of long waves outside the harbor was not affected by tidal modulation.

Figure 1.12 shows long wave Hs calculated from FUNWAVE numerical results for a port, named Port of Gerardton, located in a reef environment (Western Australia) (Van Dongeren et al., 2016). An approach channel was realized to allow ship navigation to harbor. IG waves, mainly generated at the reef slope and edge, are refracted by the channel and propagate on the shallow part located along the channel. By a refraction process, the channel acts as a wave guide and favors concentration of long wave energy at the harbor mouth, and IG waves can excite natural resonance mode of harbor basin and/or of a boat moored in the harbor.

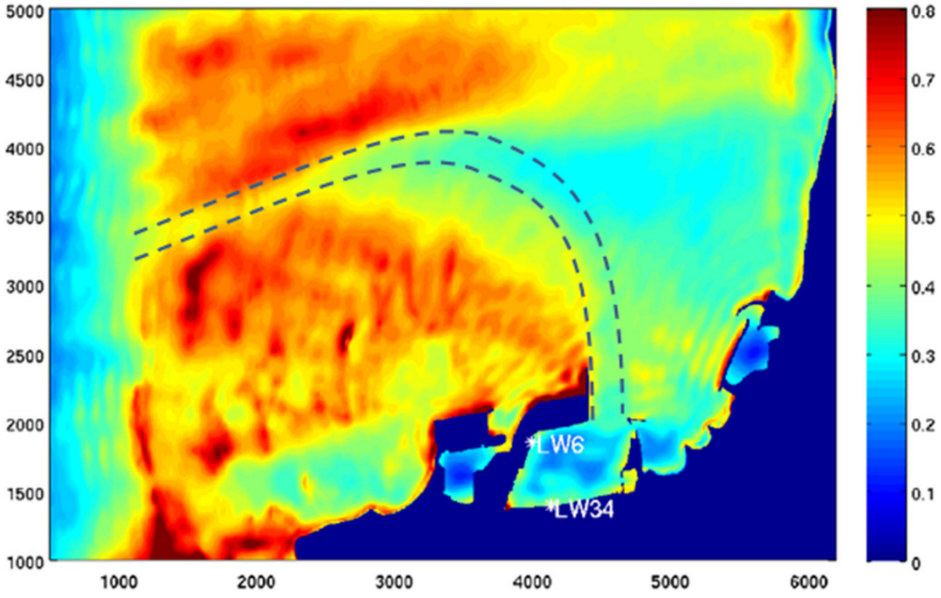

Figure 1.12 – Long period wave significant wave height for sea-swell waves input with Hs and Tp of 4.1 m and 17.3 s respectively. Units in m. (dashed lines) Approach channel. Figure reproduced from Van Dongeren et al. (2016).

1.4.2 Surge motion of moored boat

The dynamic behavior of a moored boat is analogue to a damped harmonic oscillator. The particularity of the system is the interactions between the boat and the water. Movements of moored ships can be caused by various external influences such as winds, currents, waves, seiches, tides, passing ships and cargo handling operations (Elzinga et al., 1993). The motion of a rigid body has six degrees of freedom, three translations and three rotations (figure 1.13).

Before moving, the mass of the system is composed of the boat weight and its load.

Moored boat is in contact with fenders through mooring lines. The resulting friction contributes to energy dissipation during movement and to oscillations damping. In port, fenders are generally placed against dock to absorb kinetic energy of a cargo-type vessel during berthing in order to limit stresses in the vessel hull as well as horizontal forces in the dock (low reaction force). Being typically manufactured out of rubber, elastomer or plastic, fenders have low coefficients of friction. Mooring lines, made of natural or artificial materials, hold a ship to a dock and are placed to the quay on bollards. Mooring lines only work in traction and their aim is to limit the displacement of the boat (figure 1.13): surge motions are mainly limited by aft bow and forward quarter springs, which respectively reduce forward and backward movements, and to a lesser extent by the head and stern lines. The latter limit the yawing movement. Forward breast and aft breast lines limit sway motion.
The waves by their periodic forcing contribute to initiate the movement of the dynamic system. The displacement of the boat in the fluid implies hydrodynamic reactions: added mass, viscous damping and hydrostatic restoring forces (Van Der Molen et al., 2006).

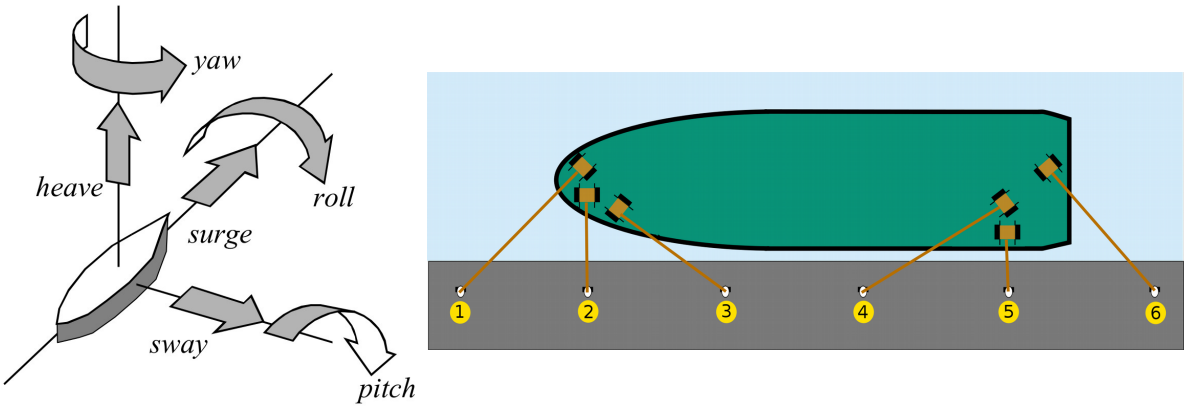

Figure 1.13 – (left figure) Six degrees of freedom of a rigid body. (right figure) Typical mooring scheme. (1) Head and (6) stern lines; (2) forward breast and (5) aft breast lines ; (3) aft bow and (4) forward quarter springs. Figures reproduced from Holthuijsen (2007) and historicair (2006).

Van Der Molen et al. (2006) numerically studied the surge motion of boat that occurred during moderate incident waves condition. The closeness of the resonance periods of the moored boat and harbor basin strongly amplified the external forcing that resulted in significant surge motion and led to breaking of mooring lines. A pretension solution is proposed to prevent this phenomenon and consists of the application of an initial force to the mooring lines via winches. The stiffness of the system increases, then the surge motion amplitude is reduced, the fundamental frequency of the moored vessel increases

and moves away from that of the harbor basin (figure 1.14). The pretension does not necessarily generate more effort in the mooring lines, since the additional forces due to the surge motion are reduced (Van Der Molen et al., 2006, table 5).

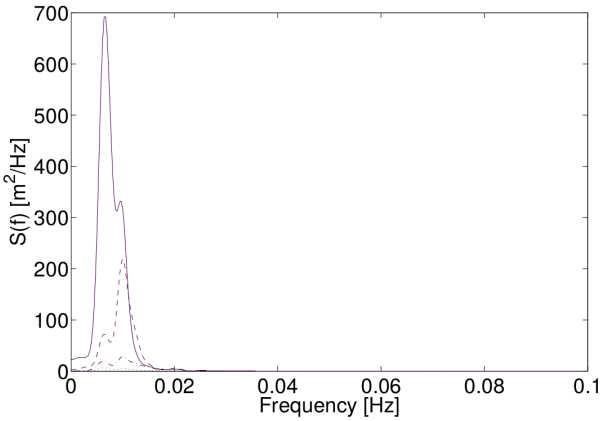

Figure 1.14 – Surge motion spectra of a moored boat for different pretensions in mooring lines. Simulation (solid line) without initial tension in springs and 2.5 ton in head and stern lines; (dashed line) 5 ton, (dash-dotted line) 10 ton and (dotted line) 20 ton pretension in all lines. Figure reproduced from Van Der Molen et al. (2006).

Without modifying the shape and hydrodynamic characteristics of the boat, it is possible to change the system properties in order to reduce ship motion. Boat loading has an influence on the submerged hull height and on boat-fluid interactions. This parameter is difficult to anticipate and modifying it can cause logistical problems for container ship management. Damping of the system can be enhanced by increasing the boat contact force against the docking fenders, by pushing the vessel with tugs for instance, in order to favor dissipation by friction. The low friction coefficient of fenders makes this solution potentially inefficient. As seen above, the increase in the stiffness leads to both a decrease in surge motion amplitude and a decrease in the resonance period of the system, for example winches can apply a pretension in the mooring lines. Conventional mooring lines can be replaced by a vacuum pad system which is attached to the ship hull and fixed to the wharf (de Bont et al., 2010). Reducing external forcing intensity is another solution to limit boat oscillations. The vessel may be moved away from the forcing if it is moved upstream in a river port for example, or if it is temporarily placed in a basin isolated from the waves by a lock. Port improvements such as basin geometric modification can finally be considered.

1.5 Conclusion

The geometry of a harbor can lead to the amplification of incident waves by resonance phenomena if the period of external wave forcing is close to one of the resonance periods of the semi-closed basin (coastal seiche). Eigen periods of basin are only determined by its geometry and cover a large range of periods. Therefore a wide variety of forcing mechanism can cause seiche, such as tsunamis, atmospheric processes and infragravity waves. The role of IG waves in port oscillations has been shown in many studies concerning semi-closed port basins. However, few studies focus on harbor oscillations in estuarine environments. This study aims to improve the knowledge about the dynamic of infragravity waves in river seaports, and particularly:

- their contribution to harbor oscillations,
- their interactions with port activities, such as dredging operations and port infrastructures,
- their transformation and dissipation in river environment.

Chapter 2

Study site: port of Bayonne

Our study site, port of Bayonne, is located on the southwest coast of France at the bottom of Bay of Biscay (Atlantic ocean) close to the Spanish border (figure 2.1). The Adour river mouth is characterized by a strong anthropogenic impact that began in the 1400's and continued until the last few decades. In this chapter, the most significant Adour river mouth development operations are first presented. In the next section, the infrastructures of the port together with the nature of the commercial activities are presented. The economic issues linked to potential problems of harbor maintenance operations during energetic conditions are pointing out. Finally, the offshore wave climate of the study is presented, as well as the hydrodynamic characteristics of the study zone.

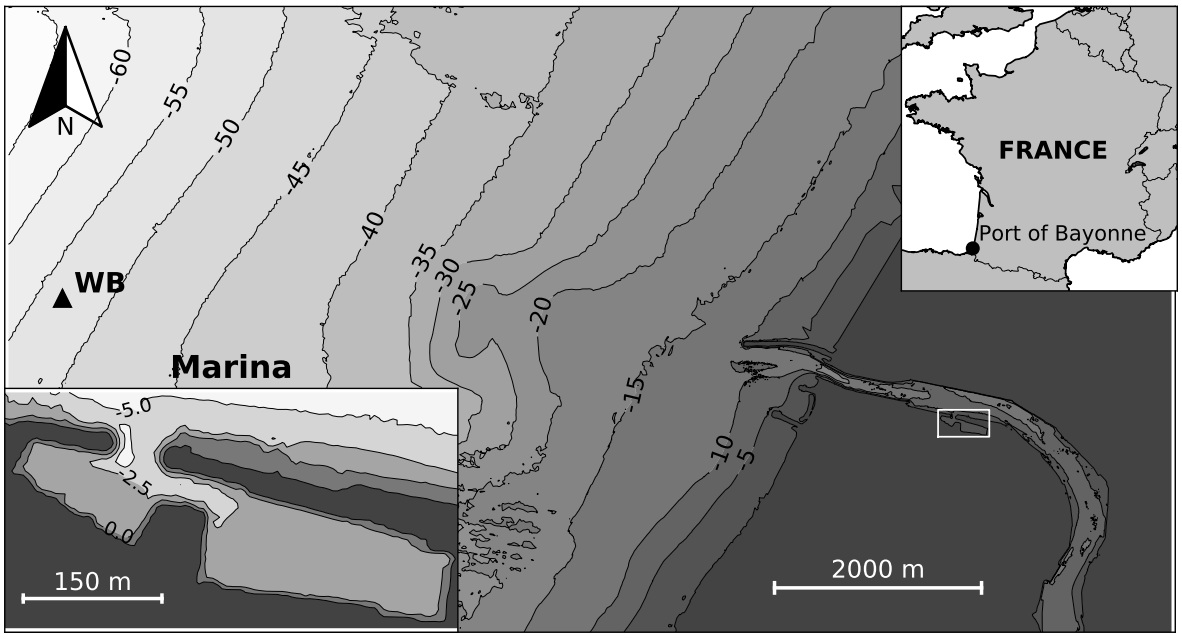

Figure 2.1 – Port of Bayonne. Zoom on the marina in the lower left corner (white rectangle on the map). (WB) Wave buoy position.

2.1 History of the Adour river mouth

2.1.1 Final position of Adour river in 1900s

The mouth of the Adour is totally artificial and has been channeled to its final position after many works that began in the 1600s following a major modification of the Adour riverbed. Indeed, until the 1400s, the Adour River flowed into the Atlantic Ocean at Cabreton and its bed, forming a right angle in front of the Bayonne coast, traveled 15 km northward to finally reach Capbreton (figure 2.2). At that time, Bayonne was a prosperous inner port and Capbreton was a port relatively protected from the swell by the presence of the underwater canyon in front of the city, which leads to a reduction of incident waves through refraction processes. However, under the combined effects of a strong storm causing the silting up of the mouth at Capbreton and a major river flood, the mouth of the Adour river moved 13 km northward close to the current city of Vieux-Boucau (figure 2.2). Boucau means mouth in gascon (local language). Despite a secondary river mouth at Capbreton, navigation to the city of Bayonne was complicated and the port commercial activities have declined since then. This decline was accentuated by the competing activity from the ports of Capbreton and the new Port of Albret created in Vieux-Boucau.

For political reasons, King Charles IX ordered in 1562 to create a new river mouth near the city of Bayonne. The engineer Louis de Foix was in charge of the works. They were based on the digging of a new channel for the Adour river that can directly flow into the ocean, and the condemnation of the downstream river part where it turned at right angle to the north. After difficult and costly works for the city of Bayonne, and not without tension with the inhabitants of the cities of Capbreton and Vieux-Boucau, the work succeeded in creating a new mouth at the right of the coast in 1578 (figure 2.2): it was the "diversion" of Adour river. Since the 1600s and after this major modification, many works have been carried out to definitely establish and channel the unstable river mouth location (figure 2.2). There was also the recurrent formation of a sandbank at the river mouth (the "barre" of the Adour) which was problematic for boat navigation. After successive embankment works, the final position of the mouth was established following the construction of two lateral jetties in 1900 (called locally convergent), which were designed to narrow the section of the river in order to increase the flow velocity and dispel sediment (figures 2.2 and 2.6).

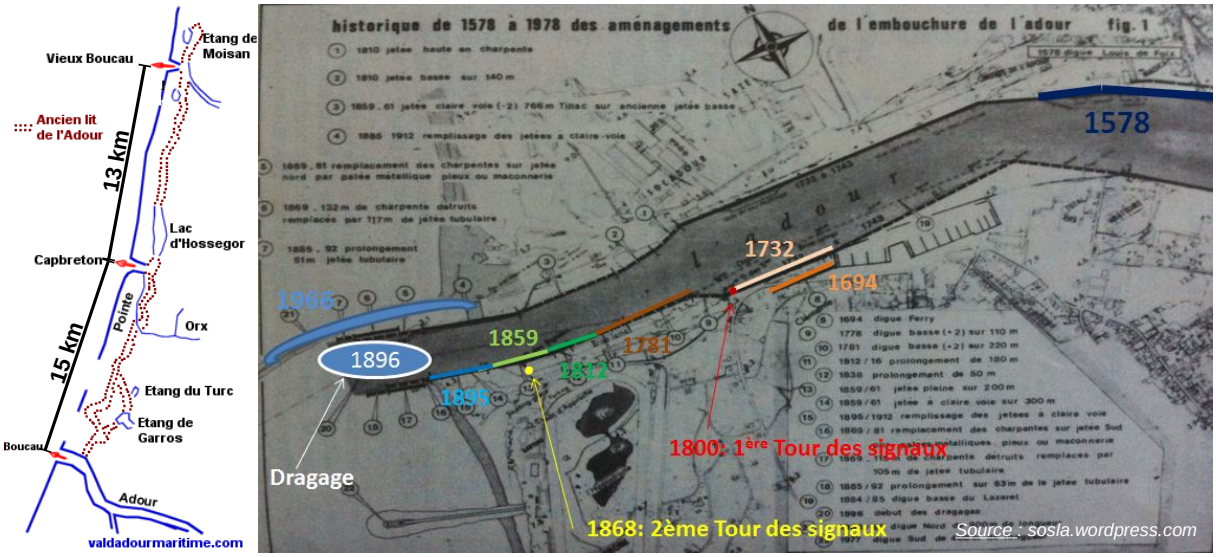

Figure 2.2 – (left panel) Former riverbed of the Adour before the deviation of its mouth in 1578. (right panel) Successive embankment works to stabilize the position of the Adour.

2.1.2 North breakwater construction

Despite the construction of the convergent, the port was still facing the problem of silting of the mouth by the formation of an underwater sandbar (littoral Angloy, 2015). Major dredging work has been undertaken to limit its formation or even remove it definitively (in vain). The sandy materials dredged from the 1900s to the 1970s were totally stored offshore and resulted in the formation of an underwater sediment deposit located between 2.5 and 3.5 km from the coast (visible in figure 2.1). Despite this major dredging effort, the sandbar remained and a breakwater of more than 1 km was built north of the river mouth from 1963 to 1965 in order to protect the harbor entrance from lateral currents and swell waves and limit the sandbar formation (figure 2.6). However, the wave-protected zone located behind the breakwater generated a wave energy differential as a consequence of a south-north oriented current from the surrounding beaches to the river mouth, and therefore the entrance silting (Abadie et al., 2008) (figure 2.4, left panel). Dredging operations at the mouth continued and intensified.

2.1.3 South breakwater construction

To deal with the new problems created following the construction of the North breakwater, a project for the construction of a south breakwater was studied. The aim was to protect the channel against excessive and rapid silting due to the new alongshore current and to contain the south-north sand drift in order to reduce maintenance dredging. The study

was carried out on a scale model in a laboratory by the Laboratoire Central d'Hydraulique de France (LCHF) and the general report was produced in 1975 (LCHF, 1975). Several projects have been proposed and one of them consisted of the construction of a 400 m long straight groyne, which would then be extended by a concave section to ensure a 350 m width harbor opening (figure 2.3).

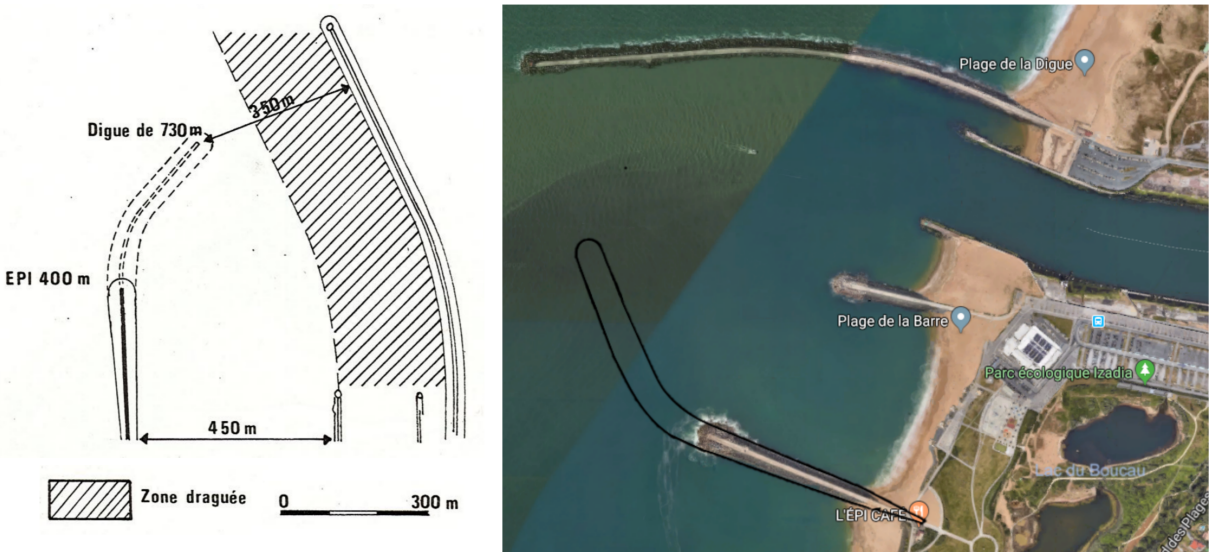

Figure 2.3 – (left panel) Project for the construction of the south breakwater in two phases: a 400 m straight groyne, then extended by a concave dike. (right panel) Concave extension in the present configuration of the river mouth. Figure reproduced from LCHF (1975) and image from `google.maps`.

The results of the LCHF's study showed that the 400 m straight groyne formed a screen for the South-North sediment transit by stopping almost all the sediments transported to the channel (figure 2.4). A small amount of sediment remains transported by the flood currents associated with wave currents. The sediment bypasses the end of the groyne and continues to feed the access channel. Swell currents deviated by the structure carry some of the suspended sediments that are deposited offshore. Significant scouring caused by the simultaneous action of storm and the eroding power of flood currents are also to be feared at the groyne head.

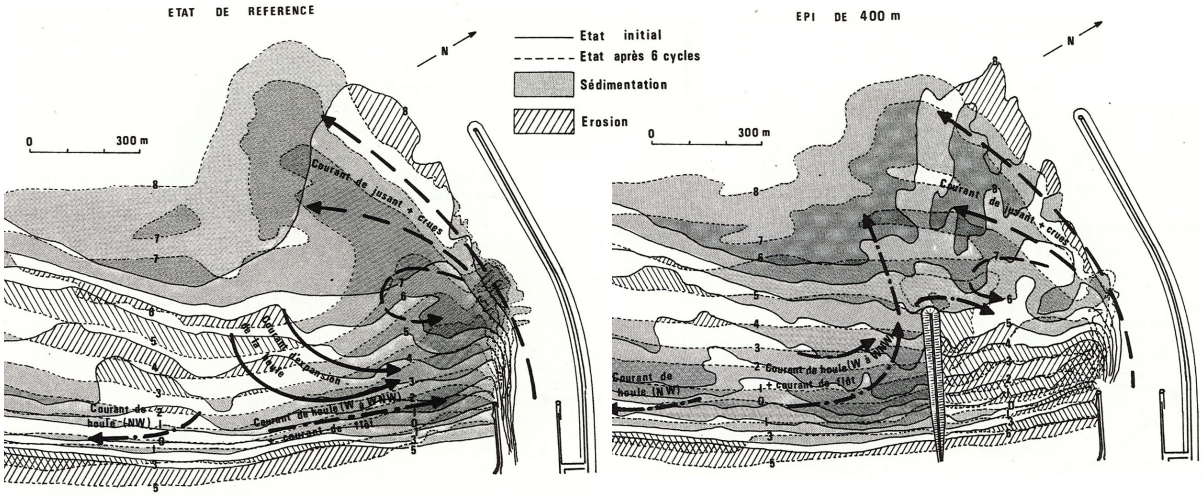

Figure 2.4 – (left panel) Reference state, only North breakwater. (right panel) Influence of the 400 m right groyne on seabed evolution after 6 annual cycles. Figures reproduced from LCHF (1975).

The objective of the concave extension was to transform the river mouth into a vast harbor basin protected not only against sedimentary inputs but also against incident swells. Sediments continue to accumulate south of the structure due to the concentration of storm energy (figure 2.5). However, there is a slight risk of sediment entrainment into the channel as a result of the acceleration of flood currents at the end of the structure. This current can dangerously scour the foot of the breakwater, which requires effective protection. A sedimentary equilibrium seems to be emerging in the basin due to the new distribution of diffracted swells within it. Limited dredging operation of the access channel would be located near the new port mouth. The study suggested that this project would make it possible to widen the river entrance, which is desirable for the expansion of port traffic.

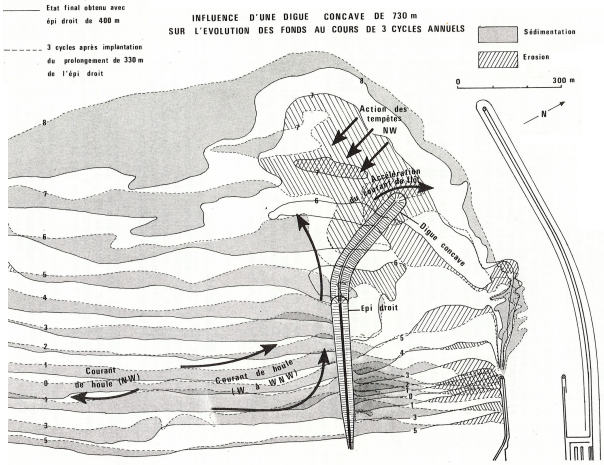

Figure 2.5 – Influence of the concave extension of groyne on seabed evolution after 3 annual cycles. Figures reproduced from LCHF (1975).

During the years 1973-1975, the 400 m right groyne was built without the concave extension (figure 2.6).

2.1.4 Intermediate breakwater construction and guard pit

To capture the sediment bypassing the end of the South breakwater that continues to feed the access channel (figure 2.4), a final work was carried out in the 2000s consisting in the realization of guard pit and an intermediate 260 m long breakwater. The purpose of the latter is to "guide" the sand to the guard pit where it will be temporarily stored, then dredged and released in front of beaches. The depth of the navigation channel allowing access to the port can therefore be maintained (figure 2.6).

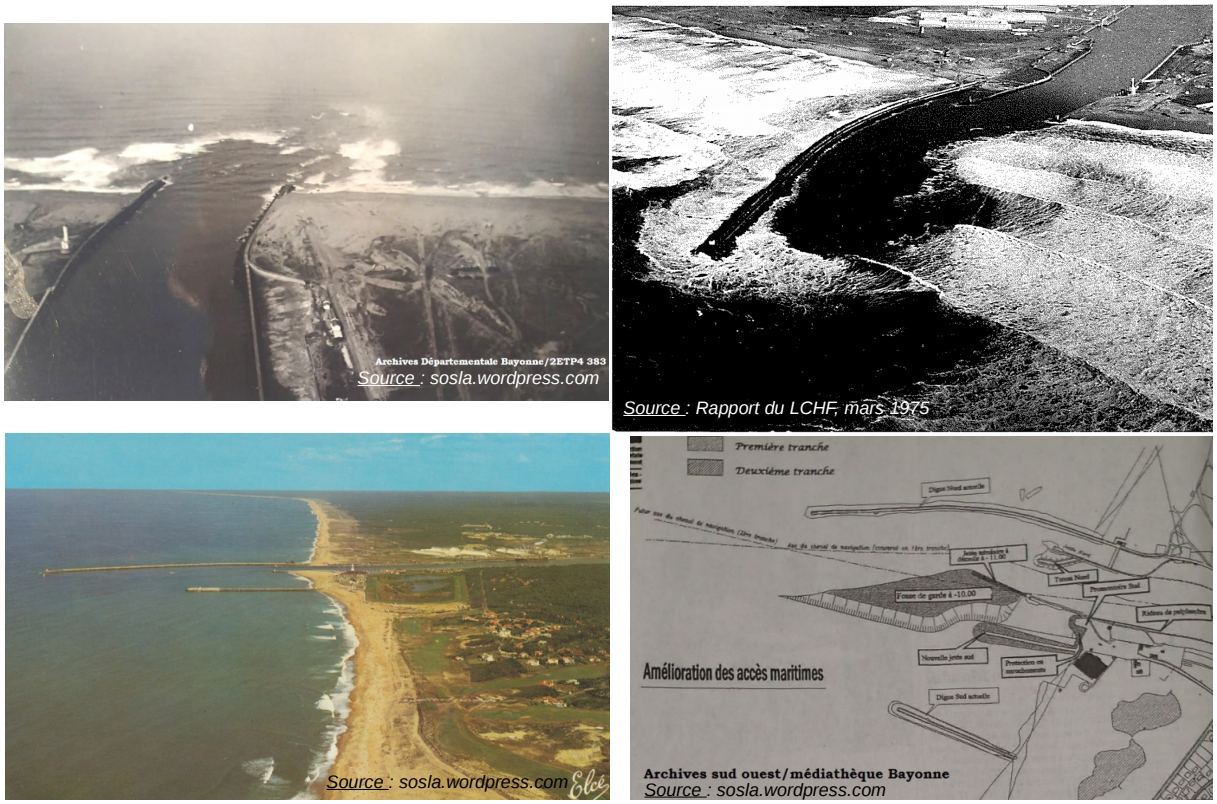

Figure 2.6 – (top left photo) Final position of the Adour mouth since 1900 after the construction of two jetties (taken in 1947). (top right photo) Mouth after the construction of the north breakwater in 1963-1965 and (bottom left photo) the south breakwater in 1975-1977. (bottom right photo) Work project of the middle breakwater and its "guard" pit (completed in 2000).

2.1.5 Sedimentary stock management

The north-south longshore coastal drift is very low in this area (Abadie et al., 2006). In addition, the construction of the northern breakwater prevented sediment supply in the river mouth from the longshore drift (Abadie et al., 2008). It should be noted that the sediment input from the river is negligible. Dredging and offshore storage of sand from nearby beaches have resulted in a deficit of sand volumes and a retreat of the coastline (Abadie et al., 2008). The underwater dredging sediment deposit peaking at -17 m, the sediments are not mobilized by the swell and their return to the coast is not possible. The deposit sediments, a mixture of sand (from beaches) and mud (from the river), are difficult to exploit. The recent acquisition of a dredger named Hondarra (start of operation in 2015) allows a reasoned, continuous and precise dredging of the port (in particular the depth at the quays (berth), the depth of the navigation channel and the guard pit). Dredged sediments are treated differently depending on their nature: mud from the river continues to be stored offshore in the deposit area while sand dredged in the guard pit

is put back in front of the beaches. These continuous dredging operations maintain the depth of port facilities and a relative stability of the coastline has been observed since 2015.

2.1.6 Current spatial configuration of Adour mouth

On the aerial photo (figure 2.7), we can see the spatial configuration of the Adour river mouth. The three breakwaters (North, middle and South) protect the port of Bayonne entrance against swell waves, lateral currents and silting of the waterway. The convergent, composed of two parallel jetties, narrows the river cross-section (160 m wide) in order to increase the flow velocity and to expel sediments during ebb tide. Just behind the convergent, concrete artificial beaches, called locally expansion area, are located on each river shore (figure 2.8). They were designed to promote the dissipation of waves entering the Adour. The convergent and the navigation channel are inclined at ~16°. At 900 m from the mouth, the first terminal of the river seaport (Tarnos) hosts heavy industry and concentrates more than 50% of the port activities. Further upstream, there are the Blancpignon and Saint-Bernard terminals at 3.5 and 4.5 km from the river mouth, respectively.

A marina (Port of Brise-Lames), a semi-enclosed water basin with an average depth of 2.5 m and a surface water area of ~0.05 km^2, is located on the left riverbank at 1.4 km from the river mouth. Its capacity is 425 pleasure boats (up to 16 m long) moored on 15 pontoons.

Figure 2.7 – Aerial photo of the Adour river mouth: (at the forefront, from left to right) north, middle and south breakwaters, (red lines) convergent and (purple lines) expansion areas. (black lines) River seaport terminals: (left) Tarnos, (lower right) Blancpignon and (upper right) Saint Bernard. (blue lines) Marina. Photo by Sophie Defontaine (2019), reproduced with permission.

Figure 2.8 – Expansion area (left bank) (2016).

2.2 Port of Bayonne: description and facilities

Port of Bayonne extends over the municipalities of Bayonne, Anglet and Boucau (Pyrénées-Atlantiques department) and the municipality of Tarnos (Landes department). It is composed of a deep-water commercial river seaport and a marina named port du Brise-Lames (semi-closed basin). The Nouvelle-Aquitaine region owns the seaport infrastructures (breakwaters, wharves, banks, ...) and its mission is to maintain them and to develop them to meet the needs of established companies and create new industrial and commercial activities. Bayonne & Basque Country Chamber of Commerce & Industry (CCI) is in charge of the economic activity of the seaport and ensures port operation by promoting and managing the economic tool.

The commercial seaport is located at the Adour river mouth and its administrative area extends 6.5 km upstream to the furthest downstream bridge on the Adour, which does not allow the passage of commercial vessels. The width of the Adour varies from 250 to 300 m with a maximum of 400 m at the turning zone and a minimum of 160 m at the river mouth (figure 2.1). The average water depth is maintained, by regular dredging operations, at 10 m with respect to chart datum, the lowest astronomical tide level. Total seaborne volume reached 2.35 million tons in 2018 of which 52% are importations and represented about 1000 vessels transiting through the port. Port of Bayonne is the third regional port after La Rochelle and Bordeaux ports (général au développement durable, 2018). Its main economic sectors are metalworking (one third of the total trade), fertilizer industry (21 % of the total trade, principally importation) and agri-food (17% of goods, mainly corn exportation). In addition, Port of Bayonne can manage varied traffic like bulk liquids (bitumen, hydrocarbon, and others), various bulk (forestry products), roro vessels and container vessels (Région Nouvelle-Aquitaine, 2018). The port activity is divided into 3 terminals, each with its own specialization: Tarnos terminal (heavy industries), Saint Bernard terminal (industrial logistics) and Blancpignon terminal (storage warehouses and containers handling). Port of Bayonne has recently developed its containerized trade activity in Blancpignon terminal by the construction of a 200 m long wharf in 2014 (Castel dock) with an expansion project planned in a few years. The future development and investment perspectives of the port industries are steel rolling and hydrocarbon processing. The recent acquisition of the Hondarra dredger in September 2015 allows regular maintenance of the navigation channel and wharf operating depths.

2.3 Exploitation issues

2.3.1 Surge motion of moored boat

During storm conditions, excessive surge motion (parallel to the dock) of moored cargo-type boats may occur at the river seaport terminal: the figures 2.9 and 2.10 present an example of the bulk carrier Nikolaos GS (February 16, 2018 between 8 and 10am (UTC+1)). The vessel has a length overall, a breadth extreme and a draught of 169 m, 27 m and 5.6 m, respectively and its gross tonnage and deadweight are 17000 t and 28600 t, respectively (according to the website `marinetraffic.com`).

Excessive surge motions of the vessel moored at the Tarnos terminal (with the bow facing upstream) occurred during ebb tide (low tide at 11:05 am, UTC+1), the horizontal displacements were about ten meters (figure 2.10). The offshore conditions measured at 50 m water depth at 9am (UTC+1) were: significant wave height of 4.3 m (Hs_{swell} = 4.07 m), peak period of 16.7 s (energy period Te = 14.2 s) and mean direction of 300°. To limit the displacement amplitude, two tugs pushed the vessel against the wharf on docking fenders.

Figure 2.9 – Surge motion of the moored bulk carrier Nikolaos GS, February 16, 2018 at 9am (UTC+1). To limit the movement amplitude, two tugs pushed the vessel against the wharf on docking fenders. The cargo was moored at Tarnos terminal with the bow facing upstream. The view was taken from the marina. Photo by Denis Morichon, reproduced with permission.

Snapshots in figure 2.10 correspond to a zero displacement speed. Between 0 and 3min10s, the boat literally went up the Adour, the displacement was opposite to the river flow. At 3min10s, the rear mooring lines (stern line and forward spring) stretched and were subjected to a considerable pressure, the boat then went back. At 6min38s, the front mooring lines (head line and aft spring) were subjected to higher pressures which had caused a break in the mooring system.

Figure 2.10 – Snapshots presenting the amplitude of moored boat surge motion. The lower pictures show the excessive tensions in the mooring lines, on the right picture (6min38s) a line was broken. Distances are estimated based on the 12 m gap between the docking fenders. Photos by Denis Morichon, reproduced with permission.

To limit the surge motions of moored boat, the port operator can require the use of additional steel mooring lines (installed by the port boaters) and deploy tugs to push the boat against the dock, or may impose the temporary relocation of the vessel upstream (usually at the Blancpignon terminal, 3.7 km from the river mouth). Generally these measures are accompanied by a survey of the various port teams. Such procedures lead to additional costs and delays in the transfer of goods. Furthermore, as in the case of the cargo ship Nikolaos, mooring lines can suddenly break and endanger people in the vicinity. In addition, despite the upstream ship relocation, extreme surge motions of moored boat may still occur. This phenomenon is a major problem in the operation of the commercial river seaport.

2.3.2 Seiche in the marina

During storm conditions, long-period oscillations have led to resonance of the marina. Significant horizontal currents then appear as well as significant vertical variations of the

free surface, particularly at the solid boundaries of the basin. Pleasure craft may collide and surveillance of mooring lines is required.

Figure 2.11 shows the free surface measured in the upstream basin of the marina. The offshore wave conditions at 3pm (UTC) were: significant wave height of 6.8 m (Hs_{swell} = 6.09 m), peak period of 15.4 s (energy period Te = 12.9 s) and mean direction of 298°. Significant oscillations are visible and the time series seems to correspond to a superposition of numerous periodic waves.

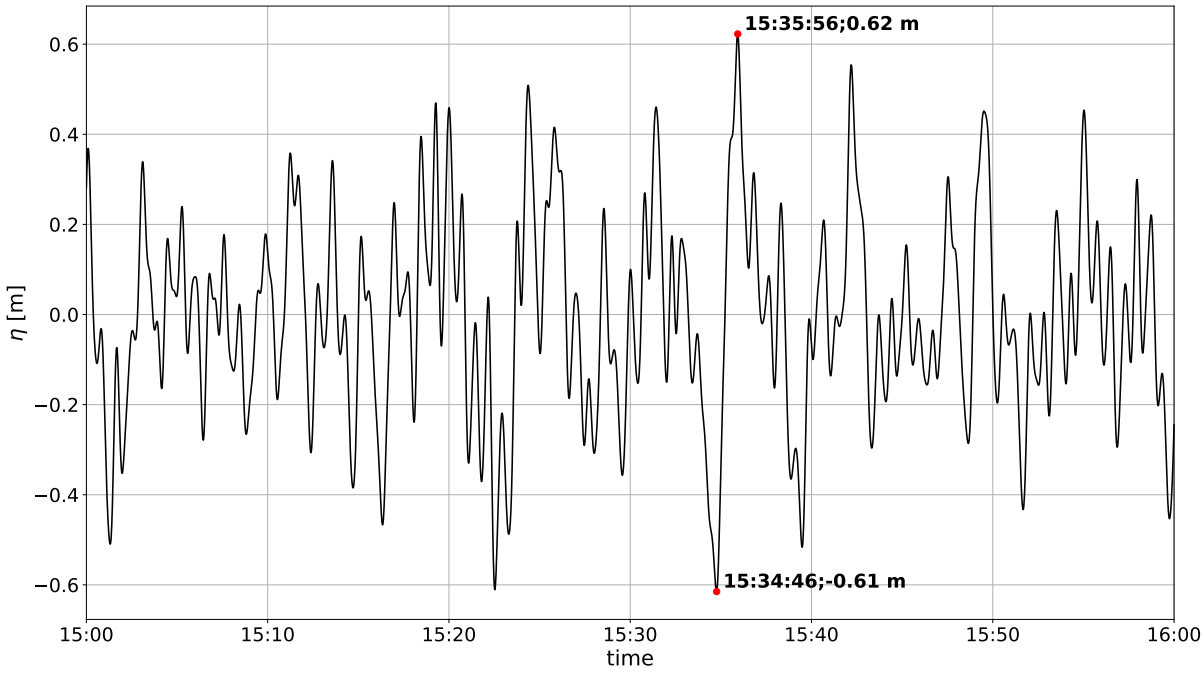

Figure 2.11 – Free surface timeserie (filtered in the 30 s-10 min period band) recorded on 24 March 2018 in the marina (upstream basin). Measurement by a pressure sensor. Time in UTC.

2.3.3 Navigation at the river mouth

Cargo navigation at the river mouth (port entry and exit operations) can be difficult because the trajectory to follow is complicated (S-shaped), counter-intuitive and sometimes hazardous. Following engine failure, the Spanish bulk carrier "Luno" ran aground on the southern breakwater on 5 February 2014 (storm Petra) while maneuvering through the mouth of the Adour river (source: Sud-Ouest newspaper). The Nouvelle-Aquitaine region is considering a project to redesign the river mouth configuration in the medium to long term.

2.4 Hydrodynamic characteristics at the river mouth

Port of Bayonne is located at the bottom of Bay of Biscay (Atlantic ocean). The tidal regime of the area is mesotidal. The mean sea level (MSL) and tidal range during spring tides are 2.53 m and 3.5 m, respectively (SHOM, 2014).

2.4.1 Wave climate

The southern part of the French Atlantic coast is exposed to very energetic swells in winter. The typical values of significant wave height (Hs) and peak period (Tp) are 4-8 m and 16-18 s respectively (Abadie et al., 2006) with a low directional variability represented by a mean wave direction of 300° with a 20° variation on both sides (figure 2.12). These energetic ocean waves are generated by winter storms that are strong extratropical cyclones associated with low pressure systems (and often strong winds) that track westward across the North Atlantic Ocean. In the last decades, a series of remarkable storm hit the french west coast, including Martin storm (1999) (Ulbrich et al., 2001), Klauss storm (2009) (Liberato et al., 2011), Xynthia storm (2010) (Kolen et al., 2013), Hercules storm (2014) (Masselink et al., 2016), Kurt storm (2017) (Bertin et al., 2018a; Bellafont et al., 2018a).

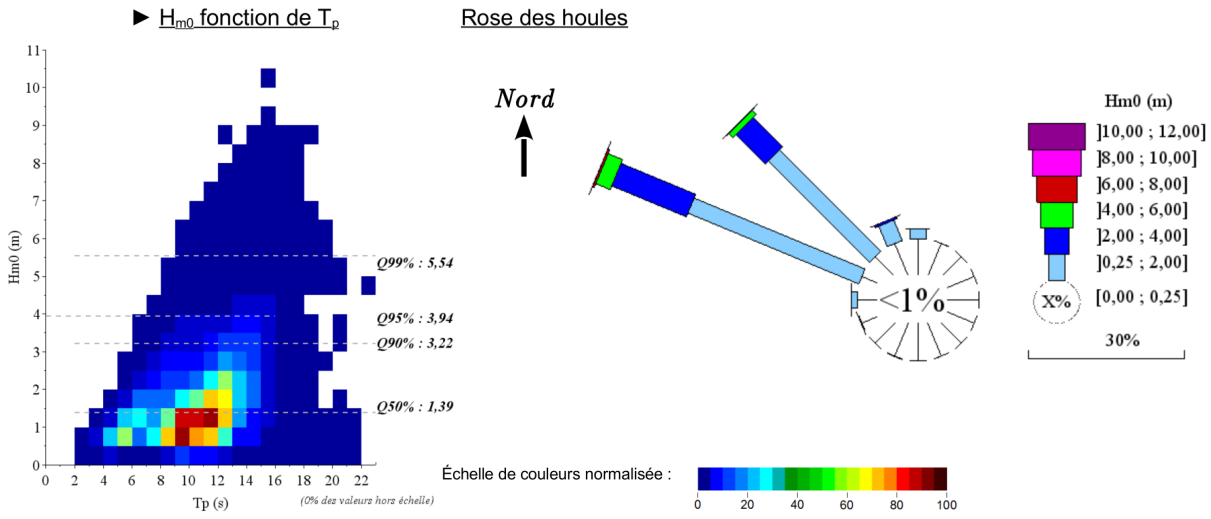

Figure 2.12 – Characteristics of offshore waves (at the wave buoy, point WB in the figure 2.1, 7 years of observations): (left panel) scatter plot of Hs and Tp and (right panel) compass rose of waves. Extract from synthesis report of CANDHIS (National Center for Archiving Swell Measurements), available on the following website: `http://candhis.cetmef.developpement-durable.gouv.fr`.

2.4.2 Nearshore current

Based on bathymetry dataset, Abadie et al. (2008) studied erosion and variation of sediment stock in the vicinity of the breakwaters and the neighboring beaches. They supplemented their study with numerical simulations to study the hydrodynamic of the area. Wave propagation, first simulated with a spectral wave model, forced a phase-resolving model that solved current generated by waves and tides (Briere et al., 2007). They found the same flow pattern as the LCHF's laboratory study (figure 2.4): the sheltering effect of the North breakwater induces cross-currents directed to the river mouth, whose magnitude is strongly dependent on the incident wave energy and water level.

The magnitude of spring tidal currents during flood and ebb tides is about 0.03 m/s in the study area close to the river mouth (Idier and Pedreros, 2005),

2.4.3 River flow

The Adour, a river located in the southwestern France, is about 300 km and its catchment area is about 17000 km^2. Its minimum, average annual and maximum discharges are 30, 300 and 3000 m^3/s, respectively. The river regime is pluvio-nival: the dominant regime is pluvial (rainfall in autumn and winter) supplemented by a nival contribution in spring (snow melt).

Defontaine et al. (2019) aimed to characterize the functioning of the lower estuary of the Adour river. Based on field experiments, the results show that the Adour lower estuary presents important variability in terms of hydrological regimes, from salt-wedge to partially mixed regimes depending on tidal and discharge conditions.

2.5 Conclusion

The Adour river mouth is characterized by a strong anthropogenic impact. The spatial configuration of the site is not fixed and still poses problems in terms of navigation at the mouth. Port of Bayonne, located at the river mouth, is composed of a commercial river seaport and a marina, which each have their own operating problems.

Abadie et al. (2008) and Briere et al. (2007) studies are only based on moderately energetic waves conditions. In addition, a spectral model was used for wave propagation that is not adapted to precisely solve diffraction at the vicinity of the breakwaters. No previous study has focused specifically on port agitation from the offshore generation of wave forcing and its propagation to the coast as well as its transformation in the river. Pons et al. (2008) numerically studied the marina behavior independently of external forcing.

Chapter 3

Method

3.1 Introduction

The detailed characterization of the response of a seaport exposed to external forcing and different incident waves types requires hydrodynamic measurements covering spatial scales of several kilometers and temporal scales from the second to several days. One solution is to use existing measuring devices, such as combining offshore wave buoy for measuring incident waves, and tide gauge for studying the water body response. However, tide gauge only provides single point measurements and partially covers the energy spectrum of water level oscillations. An another strategy consists in deploying a series of pressure sensors inside the seaport, at strategic locations, in order to get high-frequency data which are necessary to capture the full energy spectrum of water oscillations (Okihiro and Guza, 1996; Bellotti and Franco, 2011; López et al., 2012; Thotagamuwage and Pattiaratchi, 2014b).

Apart from tide gauge measurement, no data of water oscillations in port of Bayonne are available. In the framework of this thesis project, a field campaign was set up to record free surface oscillations in the Adour river mouth area in order to study the wave transformation in the river under different external forcing conditions, namely the incident short wave energy (from calm to energetic), the water level and the current caused by tidal phases and river discharge. In order to cover a wide range of external conditions, pressure sensors were deployed in the port over time periods of several months during winter periods. To supplement the punctual observations provided by the field campaign, a numerical wave model of port of Bayonne and its surrounding nearshore area was set-up, based on a Boussinesq-type model, to study the different stages of long wave propagations from their generation to their dissipation. Furthermore, the wave model is intended to provide a complementary tool to study the influence of port activities and facilities on IG waves characteristics.

In this chapter, the different types and sources of data are first presented, as well as the system developed to fix the pressure sensors in the port. Then, the methods for recovering free surface time series from pressure data are detailed as well as the method of reconstruction of bound IG waves spectrum from a wave buoy spectra. After an overview of the different wave models available, the Boussinesq-type wave model used is presented in the last part, as well as a validation case based on laboratory data (Suzuki et al., 2017).

3.2 Field data

3.2.1 Climatic conditions measurements

A directional wave buoy, moored in 50 m water depth at 7 km from the coastline, continuously records offshore wave conditions and provides a wind-sea and swell spectrum every 30 min. The Anglet buoy is managed and maintained by the national coastal in situ wave measurement network CANDHIS (National Center for Archiving Swell Measurements) in partnership with the UPPA. Three years of data are available (from January 27, 2016) with a measurement rate of 81%, due to summer maintenance or occasional data transmission problems.

Bayonne-Boucau tide gauge, located at 850 m from the river mouth, records the water level every minute (water level averaged over 15 s). It is managed by the SHOM and the Nouvelle-Aquitaine region council. The data are available on the SHOM website `data.shom.fr`.

Atmospheric pressure is measured every hour by a weather station located in Biarritz (~7 km from the study area) managed by Météo-France. The data are available on the website `meteociel.fr`

The river flow of the downstream part of the Adour, not directly measured by a permanent station, is obtained by summing the flow of its tributaries: Adour at Saint-Vincent-de-Paul, Luy (Saint-Pandelon), Gave de Pau (Bérenx), Gave d'Oloron (Escos), Bidouze (Saint-Palais) and Nive (Cambo-les-Bains). The data are available on the website `hydro.eaufrance.fr`.

3.2.2 Water elevation measurements

The offshore agitation data were supplemented by the deployment of pressure sensors in the river at relevant locations. Five pressure sensors, each with a sampling frequency of 1 Hz, were deployed in Port of Bayonne: a sensor, located close to the port entrance, recorded the river incoming waves (0.3 km from the mouth). Three sensors were deployed in the river seaport: two were positioned at the Tarnos terminal at European wharf

(1.4 km) and grain silos wharf (2.2 km), one was fixed at Blancpignon terminal (3.7 km) close to Castel wharf specialized in containerized trade activity (figure 3.1). These sensors were positioned in areas where goods transfers are important and therefore the presence of moored boats exposed to the risk of surge motion. The last sensor was deployed in the largest basin of the marina. Its position near a solid basin boundary is adapted to the measurement of vertical oscillations during seiche event due to the presence of a potential anti-node. In addition, as the two marina basins are connected by a 50 m width channel, the data are used to validate numerical model and study the impact of mesh size on simulation results.

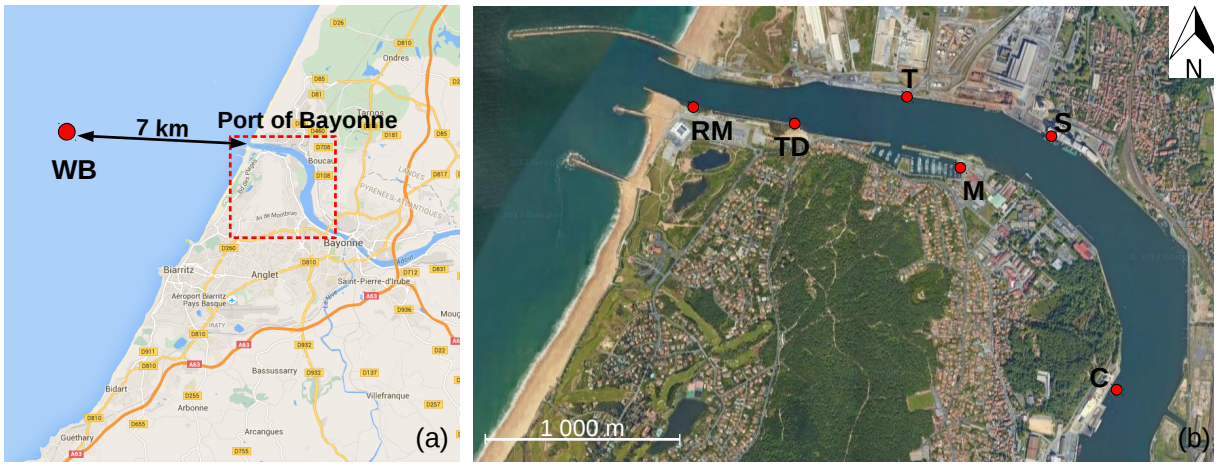

Figure 3.1 – Gauges locations: (WB) wave buoy, (TD) tide gauge. Pressure sensors: (RM) river mouth (0.3 km); river seaport: (T) Tarnos terminal, European wharf (1.4 km), (S) Tarnos terminal, corn silos wharf (2.2 km) and (C) Blancpignon terminal, Castel wharf (3.7 km); (M) right basin of the Marina. Bracketed figures are the distance of the sensor from the river mouth. Images source: google.maps.

Pressure sensor deployment procedure

Pressure sensors used in this study are RBRsolo D|Wave type. They measure the total pressure in a fluid up to 50 or 100 dBar (equivalent to a water height of 50 or 100 m), with a sampling frequency up to 2 Hz, an accuracy of 0.05 % and a time drift of 0.1 %/year in the measurement according to the constructor website (`rbr-global.com`). The capacity of the internal memory is 231 days (20 million measurements). Figure 3.2 presents the different sensor components. The measurement is made through a metal membrane that converts the applied pressure into electrical current, the calibration made by the sensor constructor allows to return to a measured pressure from the voltage current.

Figure 3.2 – Pressure sensor: (a) sensor inside, from left to right: battery, dehumidifier, on-board computer system, rubber rings for waterproofing; (b) outside protecting plastic structure. Total length and diameter: 21 cm and 2.54 cm.

Fixing device

A fixing device has been developed in collaboration with the Port of Bayonne staff in order to be able to maintain the pressure sensors on the dock access ladders throughout the campaign (figure 3.3). This device allows a great flexibility and speed in the sensors deployment (without nautical means), and therefore to target measurement points and/or specific events. The fixing device is made entirely of aluminum which is a light material with a good mechanical and corrosion resistance. It consists of a cylindrical tube with a length, diameter and thickness of 3 m, 3 cm and 3 mm respectively, in which the pressure sensor is inserted. The latter is held by a threaded rod bolted at its ends which passes through the aluminum tube. A metal hook can slide freely on the tube and be locked by a locking ring, a stopper is at each end of the tube.

The initial fixing device, providing the installation of the sensor head-up, was pierced to allow a good measurement (figure 3.3, d). During the first field campaign, one tube was damaged and deformed probably by an impact of a floating object. The device was then modified and the pressure sensor installed head-down in the tube (figure 3.3, a and b). A measurement comparison of the two devices was made over two high tide cycles and showed no difference.

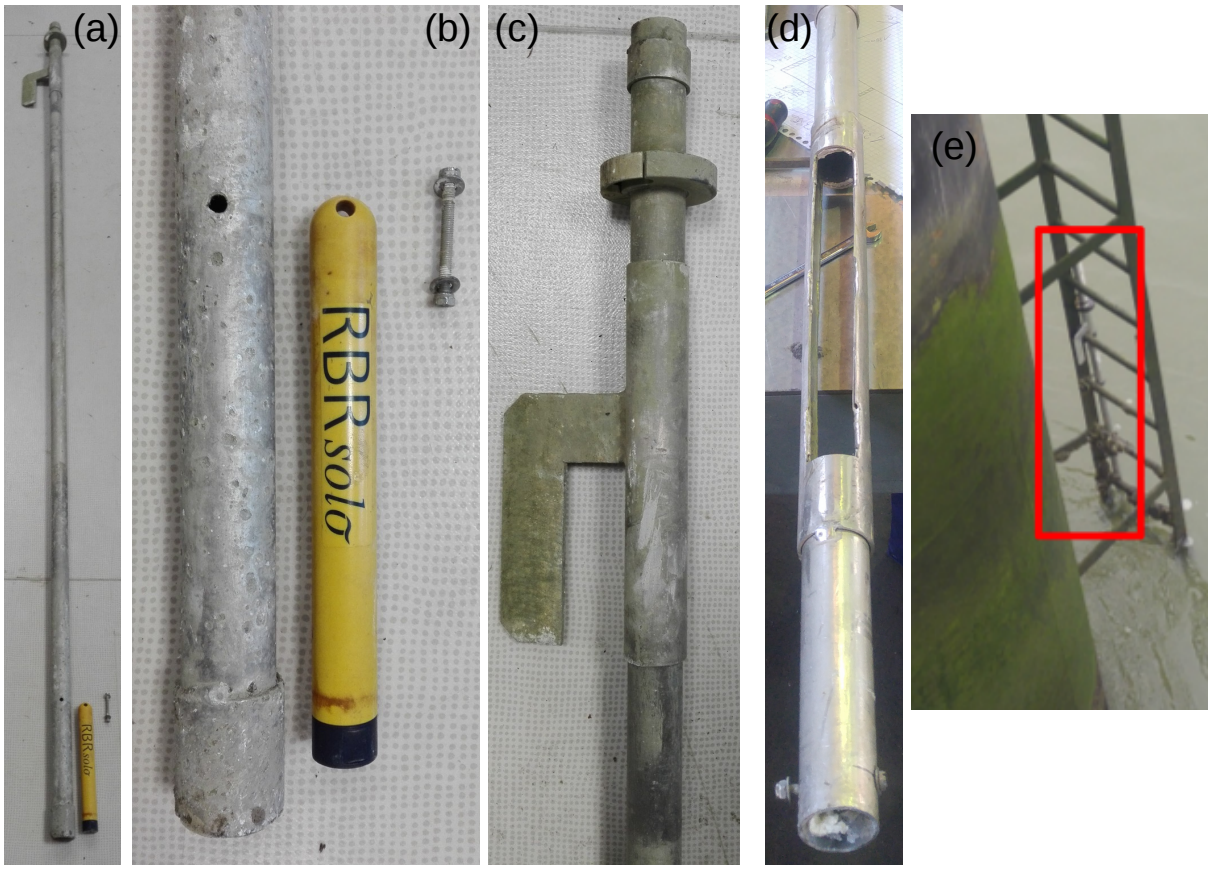

Figure 3.3 – Fixing device: (a) general view; (b) zoom on the bottom part, sensor inserted head-down in the tube and held by a bolted rod; (c) zoom on the upper part, locking ring and mobile metal hook; (d) initial configuration of the bottom part (fragility problem), head-up sensor; (e) device installed on a dolphin ladder.

River mouth fixing device

At the river mouth, port signal tower welcomes the pilots of port of Bayonne. A metal structure, providing access to pilot boats from the tower, is built on a concrete block, which makes a good anchor point for fixing a pressure sensor. This measurement point is relevant for the study because it is well exposed to incident waves that force harbor oscillations. The device is entirely made of stainless steel (mechanical and corrosion resistance) and fixed by means of anchor bolts to the concrete block (figure 3.4). The system is designed to withstand wave impacts since the river mouth can be a highly energetic area during storm events. A tube, in which the pressure sensor can slide, is welded to a plate of the same length. A welded corner piece covers the tube, increasing the strength and rigidity of the assembly. A cross at the bottom of the tube supports the pressure sensor while allowing water to pass through for measurement. A pressure sensor was machined at the head so that it could be threaded to a holding tube. The latter slides freely in the tube

and is blocked at the top of the device by a through bolt.

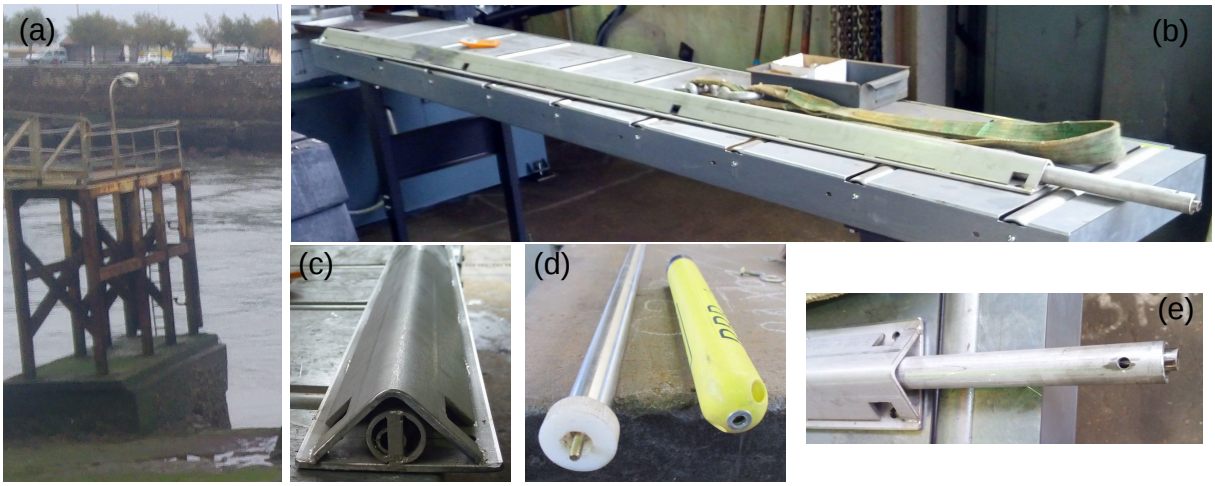

Figure 3.4 – Fixing device at the river mouth: (a) metal structure and concrete block support; (b) global view; (c) bottom part, plate, tube, corner piece, support cross; (d) holding tube bottom and machined sensor; (e) upper part, bolt hole.

Correction of time drift

Pressure sensors are equipped with internal clocks that drift about 60 s/year according to the manufacturer. A time drift control was carried out after each campaign: a pressure was applied at a specific time in order to cause a pressure jump on the recordings. The pressure sensors were rapidly immersed in a water bucket several times. The time of the pressure jump visible on the software must coincide with the time of immersion. The time drift can be corrected in a linear way by assuming a zero drift at the beginning of the measurement as the clock is synchronized, and a maximum drift at the end of the campaign.

Important data acquisition with a good spatial and temporal resolution is needed to study basin behavior under a large range of forcing conditions: energetic and calm conditions, role of the mesotidal environment, transformation in the river, etc. Continuous data acquisition was preferred to the burst method (partial data acquisition) because the time drift of the instruments internal clocks can lead to a desynchronization of the sensors between them and thus complicate the data analysis, especially over long measurement periods (several months). A 1 Hz sampling frequency was adopted since it is a good compromise between wave resolution (short and IG waves) and sensor capacity (battery and memory).

3.2.3 Recovering free surface elevation

Hydrostatic assumption

Pressure sensor records total pressure in the fluid (including atmospheric pressure). Pressure data are transformed into free surface time series by applying the hydrostatic pressure formula (3.1), whose application range is respected since the pressure sensors are located near the free surface (depth ~-1.5 m) and the wavefield is weekly nonlinear in the river.

$$h_H = \frac{P_{tot} - P_{atm}}{\rho g} \tag{3.1}$$

where h_H is the hydrostatic water depth, P_{tot} is the pressure recorded by the sensor, P_{atm} is the atmospheric pressure, ρ is the density of the fluid and g is the acceleration of gravity.
As the atmospheric pressure P_{atm} is measured every hour by the weather station, we considered that it varies linearly between two consecutive measurements and therefore that there was no sudden jump in atmospheric pressure, which is consistent near the coast. The acceleration of gravity g is assumed to be 9.81 m/s^2 and its variations with latitude and altitude are not taken into account.

The density ρ is considered constant over the entire water column and equal to 1000 kg/m^3 (freshwater density). This assumption leads to a maximum error level of 3 % if the measurement point is located exactly at the level of the density stratification and the water above is salty (saltwater density : 1030 kg/m^3). Even with the determination of the density at the sensor position (indirectly with a temperature and conductivity sensor for example), the assumption that the density is constant over the entire water column, equal to that at the sensor level, implies errors because the density is not determined over the entire water column.

Transfer function: linear wave theory

Bottom-mounted or underwater pressure transducers are commonly used for wave measurements and present many advantages. Pressure sensors are simple and robust devices, which are less expensive to use in the field, and are relatively protected due to their underwater deployment. However, pressure sensors do not directly record the free surface elevation. The hydrostatic assumption is the simplest way to recover free surface elevation and is relevant for describing long waves. For short waves, a commonly used method is the application of a transfer function derived from the linear wave theory (Tsai et al., 2005).

$$\zeta_H(t) = h_H(t) - h_0 \tag{3.2}$$

$$K_{p,L}(f, h_0, \delta_m) = \frac{\cosh[(h_0 + \delta_m)k(f)]}{\cosh[\delta_m k(f)]} \tag{3.3}$$

$$\omega^2 = gk \tanh(kh) \tag{3.4}$$

where $\zeta_H(t)$ is the hydrostatic elevation, h_0 is the the mean water depth above the sensor $h_0 = \overline{h_H(t)}$, $K_{p,L}$ is the pressure transfer function from linear wave theory (Tsai et al., 2005, equation 5), δ_m is the distance between the sensor and the bottom, h is the total water depth ($h = h_0 + \delta_m$), f is the wave frequency and ω its angular frequency ($\omega = 2\pi f$), k is the wavenumber determined from the linear dispersion relation (3.4).

The transfer function approach uses a linear relationship between the Fourier transforms $\mathcal{F}$ of the hydrostatic elevation ζ_H and the linear elevation reconstruction ζ_L (Oliveras et al., 2012):

$$\mathcal{F}(\zeta_L)(f) = \begin{cases} K_{p,L}(f)\mathcal{F}(\zeta_H)(f) & \text{si } f \leqslant f_c \\ \mathcal{F}(\zeta_H)(f) & \text{si } f > f_c \end{cases} \tag{3.5}$$

where $\mathcal{F}(\zeta_L)$ and $\mathcal{F}(\zeta_H)$ are the Fourier transforms of the linear elevation reconstruction ζ_L and the hydrostatic elevation ζ_H respectively and f_c is a cut-off frequency.
Then, the linear elevation reconstruction ζ_L is obtained from an inverse Fourier transform: $\zeta_L(t) = \mathcal{F}^{-1}(\mathcal{F}(\zeta_L))$.

A cut-off frequency has to be introduced to limit the application of the transfer function only to the low frequency part of the spectrum. First of all, the growth of the hyperbolic cosine function is very rapid and the transfer function no longer makes any "physical sense" for the high frequency part of the spectrum. In addition, as seen in the chapter state of the art (section 1.3.2), high frequency waves in the SW band correspond to higher harmonics of the peak SW frequency, that are generated by nonlinear interactions. These high frequency harmonic waves are phase-locked and bound to the primary short waves and travel at a celerity much larger than their intrinsic (linear) phase speed. Then, the linear dispersive relation (3.4) strongly overestimates their wavenumbers (Bonneton and Lannes, 2017), and the cosh function further amplifies these overestimations.

The Power Spectral Density (PSD), presented in section 3.2.4, of the linear elevation reconstruction can be directly determined from the PSD of the hydrostatic elevation by applying the squared transfer function. This method allows a direct calculation of the significant wave height of ζ_L and avoids an inverse Fourier transform operation to obtain

the time series of ζ_L.

$$PSD(\zeta_L)(f) = \begin{cases} K_{p,L}^2(f) PSD(\zeta_H)(f) & \text{si } f \leqslant f_c \\ PSD(\zeta_H)(f) & \text{si } f > f_c \end{cases} \tag{3.6}$$

where $PSD(\zeta_L)$ and $PSD(\zeta_H)$ are the power spectral densities of the linear elevation reconstruction and the hydrostatic elevation, respectively and f_c is the cut-off frequency.

Dispersion relation

The linear dispersion relation (3.4), used in the linear reconstruction method as well as in bound IG wave reconstruction (3.2.5), is solved with the iterative Newton-Raphson method which is a root-finding algorithm. It starts with an initial guess k_0 (3.9) for a root of the single-variable function f (3.7) defined for a real variable k whose derivative is $f'(k)$ (3.8). The algorithm consists to iterate the operation 3.10 (at the beginning $n = 0$) to find a better approximation of the root k_{n+1} than k_n until satisfying a convergence criterion (3.11).

The rate of convergence is quadratic, as $f'(k)$ is non-zero and $f''(k)$ is continuous (for all concerned k), if k_0 is sufficiently close to the seeking root. This condition can be roughly met by choosing the value closest to 0 of the two asymptotic solutions of k, namely the deep and shallow water conditions.

The convergence criterion (3.11) is based on the wavelength $L = 2\pi/k$ and ϵ is fixed to 0.01 m.

$$f(k) = gk \tanh(kh) - \omega^2 \tag{3.7}$$

$$f'(k) = g \tanh(kh) + \frac{gkh}{\cosh^2(kh)} \tag{3.8}$$

$$k_0 = \begin{cases} \omega^2/g & \text{deep water} \\ \omega/\sqrt{gh} & \text{shallow water} \end{cases} \tag{3.9}$$

$$k_{n+1} = k_n - \frac{f(k_n)}{f'(k_n)} \tag{3.10}$$

$$|2\pi/k_{n+1} - 2\pi/k_n| \leq \epsilon \tag{3.11}$$

The dispersion relation is a good candidate for this method. The algorithm, simple to code, gives accurate results quickly due the quadratic convergence. Other methods exist to solve the wave dispersion equation such as the direct and explicit solution proposed by Guo (2002), and more efficient numerical techniques such as a higher-order extension of

the Newton-Raphson technique (Newman, 1990).

Nonlinear reconstruction

Nonlinear effects increase close to the shoreline, the waves shape steepens and becomes asymmetric. A correct description of the wavefront is crucial for many coastal applications such as wave impacts, submersion and sediment transport. The linear transfer function is no longer suitable and a nonlinear reconstruction method is needed (Bonneton and Lannes, 2017). A nonlinear reconstruction method, easy to develop and implement in existing linear reconstruction routine, was proposed by Bonneton and Lannes (2017). It only adds two temporal derivatives of ζ_L, easily calculated from the Fourier transform $\mathcal{F}(\zeta_L)$.

Figure 3.5 illustrates the different methods to recover the free surface elevation from pressure measurement, namely the hydrostatic assumption, the fully dispersive linear and nonlinear reconstructions proposed in Bonneton and Lannes (2017). The wave field is bichromatic and propagates over a gently sloping bottom.

The spectral energy of ζ_H moves away from the direct measurement one with increasing frequency, the low frequency part as well as the first peak are well described by the hydrostatic assumption (3.5, left figure). The linear reconstruction corrects the spectral energy of ζ_H thanks to the transfer function. The second peak is well described by this method, but beyond the cut-off frequency the remaining peaks are underestimated. The nonlinear reconstruction, close to ζ_L before the cut-off frequency, is close to the direct measurement for the harmonic waves 3 and 4.

The lowest waves of the wave group are well reconstructed by the linear formula, but the crest elevation of the highest waves are underestimated (3.5, right figure). The nonlinear formula better described the elevation of the highest waves as well as the wave skewness.

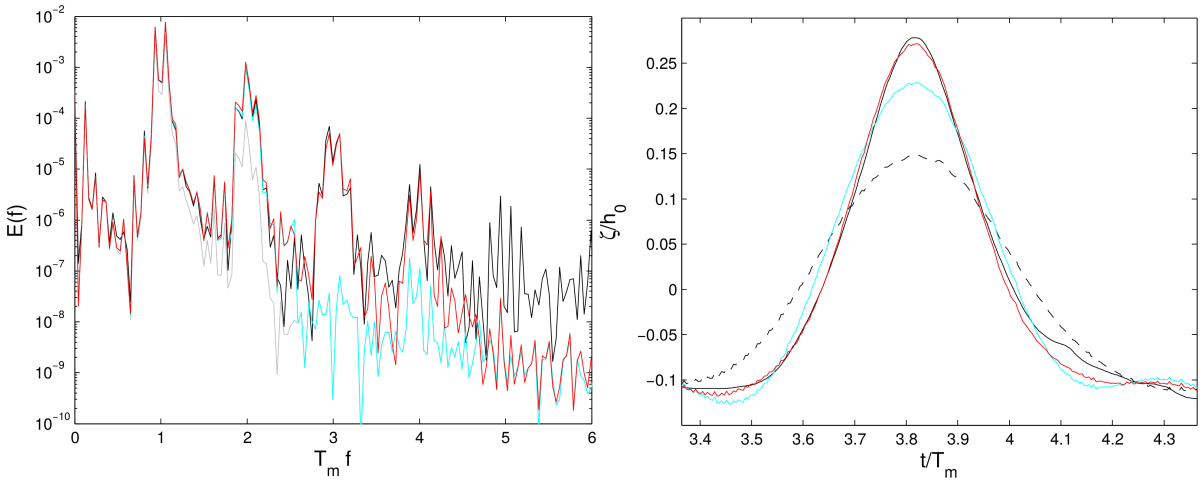

Figure 3.5 – Bi-chromatic waves, $f_1 = 0.5515\ Hz$, $f_2 = 0.6250\ Hz$, $T_m = \left(\frac{f_1+f_2}{2}\right)^{-1}$, $h_0 = 0.326\ m$, $\delta_m = 0.5\ cm$, and cut-off frequency $f_c = 1.5\ Hz$. (black line) Direct measurement of ζ; (grey and black dashed lines) hydrostatic elevation ζ_H; (cyan line) linear reconstruction ζ_L; (red line) nonlinear reconstruction ζ_{NL}. (left figure) Surface elevation energy density spectra $E(f)$ as a function of the dimensionless frequency $T_m f$. (right figure) Surface elevation time series, zoom on the highest wave of the wave group. Reproduced from Bonneton and Lannes (2017).

3.2.4 Spectral Analysis

A spectral analysis was performed to study the energy distribution in the different frequency bands as well as their spatial and temporal evolution.

The power spectral density (PSD) of the free surface is determined by the Welch (1967) method: the data are divided into 50% overlapping segments and a Hanning window is applied to each segment. The mean spectrum being related to the variance of the free surface, the associated confidence interval (CI) follows a Chi-square law (χ^2) of degree of freedom ν (3.12) (Thomson and Emery, 2014, equation 5.108).

$$\frac{\nu.s^2(f)}{\chi^2_{1-\alpha/2,\nu}} < \sigma^2(f) < \frac{\nu.s^2(f)}{\chi^2_{\alpha/2,\nu}} \tag{3.12}$$

where ν is the degree of freedom, σ^2 and s^2 are the true and calculated variances and α is the confidence coefficient taken at 5%.

In addition, the above interval applies to all frequencies f. It can be reduced to a unique interval if the spectrum is represented with a log scale. As the estimated spectrum approaches the real one, $\log(\sigma^2/s^2) \to 0$ and a single vertical confidence interval, valid for all frequencies, can be represented. Using a log scale representation, the confident interval

is reduced to:

$$CI = \left] \frac{\nu}{\chi^2_{1-\alpha/2,\nu}}; \frac{\nu}{\chi^2_{\alpha/2,\nu}} \right[\tag{3.13}$$

From these spectral densities, significant wave heights are calculated according to the formula (3.14) Holthuijsen (2007).

$$Hs = 4\sqrt{m_0} \tag{3.14}$$

$$m_0 = \int_{f_l}^{f_u} E(f)df \tag{3.15}$$

where Hs is the significant wave height, m_0 is the zeroth-order spectrum moment, f_l and f_u are the lower and upper limits of the integral.

Free surface oscillations in specific period bands can be determined by fixing the integration bounds of m_0. The so-called total significant wave height Hs is determined for $f_l = 0$ and $f_u = \infty$. Significant wave heights of short waves (SW), infragravity waves (IG) and very long waves (VLW) are computed by determining m_0 respectively for period intervals ranging from 5 to 30 s, 30 to 300 s, and 300 to 600 s. The discrete integral is calculated using the trapezoidal rule.
The tidal contribution is removed by considering a linear deviation of the signal (detrending) for time series of 2048 s (~34 min).

3.2.5 Bound IG waves reconstruction

Offshore wave buoys usually measure vertical and horizontal wave motions using accelerometers, one for each axis. For low frequency motion (period longer than 30 s), accelerations become very small and disappear in the sensor noise. As a result, wave buoys are not able to measure infragravity waves, but the bound IG waves component can be reconstructed from the short wave spectrum applying Hasselmann (1962) theory. Moreover, bound IG waves spectrum can be reconstructed from a short wave spectrum recorded by a pressure sensor in order to separate bound and free IG wave components (Herbers et al., 1994, 1995b).

Bound IG waves are generated by nonlinear interactions between first-order free short waves of nearly equal frequency and are phase-locked to the wave group. Considering an inviscid, incompressible, irrotational fluid in constant depth, bound IG waves induced by non-linear interaction of gravity waves can be determined by expanding the Euler waves equations and boundary conditions to second-order by a perturbation analysis (Stokes's method) (Longuet-Higgins and Stewart, 1962; Hasselmann, 1962).

Formulation

Bound wave components can be determined considering each pair of primary short waves in the spectrum and calculated the associated non-linear interactions through a coupling coefficient. Assuming that the short wave field is a linear sum of free waves with random phases, following Okihiro et al. (1992) formulation (equation 3), the infragravity bound sea surface spectrum $E_4(f_j)$ is:

$$E_4(f_j) = 2\delta f \sum_{n=n_{lo}}^{n_{hi}-j} \sum_{q=1}^{n_\theta} \sum_{r=1}^{n_\theta} eC^2 E(f_n, \theta_q) E(f_{n+j}, \theta_r) \delta\theta^2 \tag{3.16}$$

where $f_j = f_{n+j} - f_n$ is the bound wave frequency, $E(f_n, \theta_q)$ is the gravity wave frequency-directional spectrum, eC is the bound wave sea surface elevation coupling coefficient. δf and $\delta\theta$ are the frequency and directional resolutions of the short wave spectrum. $n_{lo}\delta f$ and $n_{hi}\delta f$ correspond to the lowest and highest gravity wave frequencies. $n_\theta = 360/\delta\theta$ is the number of directional bands at each frequency.

A primary wave is characterized by a frequency f_n and its corresponding angular frequency $\omega_n = 2\pi f_n$, by a spectral energy $E(f_n, \theta_q)$, and by a vector wavenumber $\overrightarrow{k_{n,q}} = (k_n \cos\theta_q; k_n \sin\theta_q)$ whose magnitude k_n is determined from the linear dispersion relation $\omega_n^2 = g k_n \tanh(k_n h)$ and direction is θ_q. The method to solve the linear dispersion relation is presented in the section 3.2.3.

Considering a pair of primary waves (f_n, θ_q) and (f_{n+j}, θ_r), the bound IG wave generated through nonlinear interactions has a wave frequency of $f_j = f_{n+j} - f_n$ and a vector wavenumber $\overrightarrow{\Delta k} = \overrightarrow{k_{n,q}} - \overrightarrow{k_{n+j,r}} = (\Delta k \cos\theta_b; \Delta k \sin\theta_b)$ whose magnitude Δk and direction θ_b are determined as follows :

$$\Delta k = \sqrt{k_n^2 + k_{n+j}^2 - 2k_n k_{n+j} \cos(\Delta\theta)} \tag{3.17}$$

$$\theta_b = \tan^{-1}\left(\frac{k_n \sin\theta_q - k_{n+j}\sin\theta_r}{k_n \cos\theta_q - k_{n+j}\cos\theta_r}\right) \tag{3.18}$$

where $\Delta\theta = |\theta_{n,q} - \theta_{n+j,r}|$ is the angle between the two considered primary waves.
The bound wave spectral energy is calculated via a sea surface elevation coupling coefficient eC defined as follows (Okihiro et al., 1992, equation 4a) and given by (Hasselmann, 1962; Sand, 1982).

$$\begin{aligned} {}_eC = &-\frac{g k_n k_{n+j}\cos\Delta\theta}{2\omega_n\omega_{n+j}} + \frac{(\omega_n^2 + \omega_{n+j}^2) - \omega_n\omega_{n+j}}{2g} - \frac{g\omega_j}{[g\Delta k \tanh(\Delta k h) - \omega_j^2]\omega_n\omega_{n+j}} \\ &\times \left\{ \omega_j \left[\frac{(\omega_n\omega_{n+j})^2}{g^2} + k_n k_{n+j}\cos\Delta\theta \right] - \frac{1}{2}\left[\frac{\omega_n k_{n+j}^2}{\cosh^2(k_{n+j}h)} - \frac{\omega_{n+j}k_n^2}{\cosh^2(k_n h)} \right] \right\} \end{aligned} \tag{3.19}$$

This method does not provide directional bound IG wave spectrum, the bound IG wave direction θ_b values being scattered, the directional resolution is coarse. Moreover, the bound wave spectrum can be written as a function of the bound IG frequency and direction $E_4(f_j, \theta_b)$. For a given bound wave component (f_j, θ_b) and after fixing a short wave component (f_n, θ_q), the method consists of determining the direction of the remaining short-wave θ_q with the equation 3.18, its frequency being given by the relation $f_j = f_{n+j} - f_n$ which allows to calculate k_{n+j} (Sand, 1982). This method is also limited by the resolution of the short wave spectrum δf and $\delta\theta$. As the spectrum is supposed to be continuous, interpolation is possible to improve its resolution, but would increase the computation time.

The equation 3.16 was selected and the spectrum resolution was adapted to maintain a good resolution of the bound IG waves with a reasonable computation time. First of all, the maximum period of $E4$ is imposed by the frequency step of the wave spectrum, a δf of 0.005 Hz imposes a 200 s max period of $E4$.

Directional energy distribution of buoy spectra

The spectrum provided by the buoy is determined by the method of Kuik et al. (1988) and for each frequency component, the power spectral density $E(f)$, the mean direction θ_m, the directional spread θ_{sd}, the skewness γ and the kurtosis δ are given. A frequency-direction spectrum needs to be reconstructed to be able to calculate the bound IG wave.

The directional energy distribution $D(\theta)$ (equation 3.20) was determined by a two-parameter function based on θ_m and θ_{sd}: the $\cos^{2s}$ model (Kuik et al., 1988) (equations 3.21 and 3.22), and the function used in the spectral model SWAN (equations 3.23 and 3.24) (team et al., 2007, appendix A, variable MS).

$$E(f, \theta) = E(f).D(\theta) \tag{3.20}$$

$$D_1(\theta) = A_1 \cos^{2s}\left(\frac{\theta - \theta_m}{2}\right) \tag{3.21}$$

$$s = \frac{2}{\theta_{sd}^2} - 1 \tag{3.22}$$

$$D_2(\theta) = A_2 \cos^{m}(\theta_m - \theta) \tag{3.23}$$

$$m = 0.6343\theta_{sd}^{-2.1905} \tag{3.24}$$

where the parametric functions D_1 and D_2 are respectively the $\cos^{2s}$ model and the SWAN function, A_1 and A_2 are normalization constants since $\int_0^{2\pi} D(\theta)d\theta = 1$, s and m are directional width parameters, all angles are in radian. The equation of m is obtained by a linear regression applied to the pairs of values (m, θ_{sd}) given in the table A.1 for θ_{sd} between 2° and 37.5°(team et al., 2007, appendix A) ($R^2 = 0.994$).

The exponentiation operation (x^b) with b a real power implies that x is a positive real number via the logarithm definition $x^b = e^{b \ln x}$, therefore only positive values of $\cos y$ are kept, so y is between 0 and π (mod 2π). This condition is met for D_1 by taking the absolute value of cosine before raised to the power of $2s$, while negative cosine values are to be excluded for D_2 before raised to the power of m. D_2 centered on θ_m is positive on the interval $[\theta_m - \pi/2, \theta_m + \pi/2]$ and zero otherwise, whereas D_1 centered on θ_m is positive on the interval $[0, 2\pi]$ (figure 3.6) and for $\theta_{sd} \geq 30°$ energy is present beyond $\theta_m \pm \pi/2$ (figure 3.7, c).

Figure 3.6 presents the directional energy distribution $D(\theta)$ given by the two parametric functions for different direction spreads θ_{sd}. For both parametric models, the directional energy distribution is assumed to be unimodal and symmetric around the mean direction, the directional spread θ_{sd} controls the shape of the function. In case of a superposition of two distinct wavefields, such as swells and sea waves, the distribution can be bimodal and Kuik et al. (1988) proposed a criterion based on the values of skewness γ and kurtosis δ to warn against this assumption (Kuik et al., 1988, equation 56). This criterion is relevant for the frequency transition between the two wavefields.

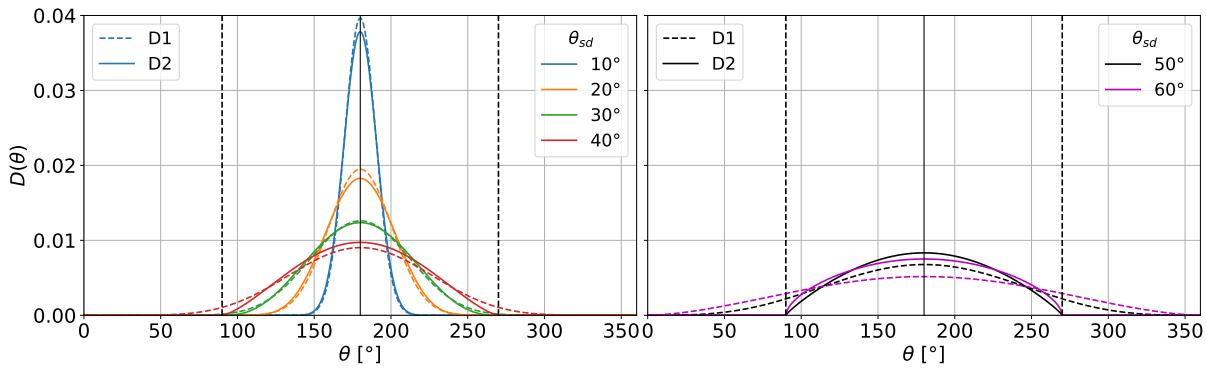

Figure 3.6 – Directional energy distribution $D(\theta)$ for (dashed lines) D_1 and (solid lines) D2 parametric functions and different directional spreads θ_{sd}. (Vertical solid line) mean direction $\theta_m = 180°$ and (vertical dashed lines) $\pm 90°$ around θ_m.

Figure 3.7 compares D_1 and D_2 functions, namely the maximum value D_{max} of $D(\theta)$ for $\theta = \theta_m$, the ratio of $D_{max,2}$ to $D_{max,1}$, and the integral of D_1 over the interval $[\theta_m - \pi/2; \theta_m + \pi/2]$.

For $\theta_{sd} \leq 40°$, D_1 and D_2 functions are very close with a difference of about 10% between the values of D_{max} (figure 3.6; figure 3.7, a and b), for D_1 function the energy is mainly in the interval $[\theta_m - \pi/2; \theta_m + \pi/2]$ (figure 3.7, c). For $\theta_{sd} \geq 40°$, differences between D_1 and D_2 are important and the energy distribution shape is flattened for the D_1 function, whereas the condition of D2 (positive energy in the interval $[\theta_m - \pi/2, \theta_m + \pi/2]$) imposes a limiting shape of the energy distribution. Typical directional spreading of wind

sea waves and swells being 30° and 10°, respectively (team et al., 2007), the application of any of the functions is not problematic for $\theta_{sd} \leq 40°$.

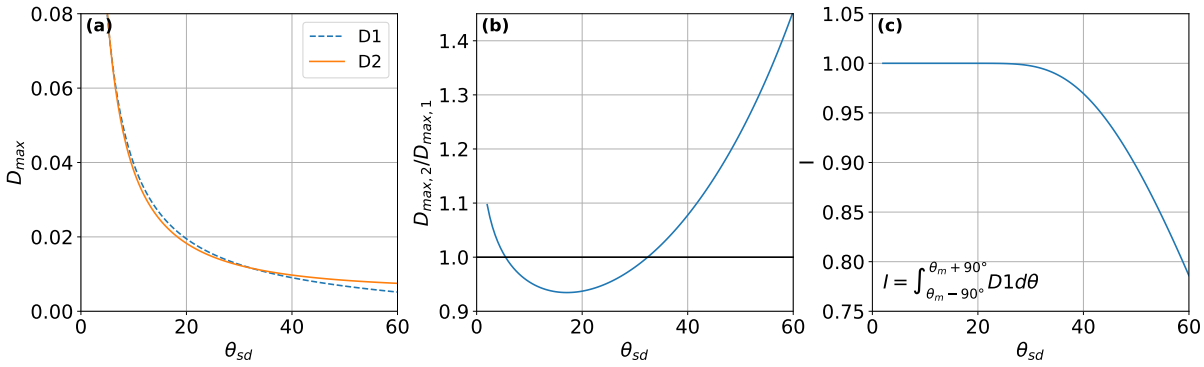

Figure 3.7 – Comparison between D_1 and D_2 parametric functions: (a) maximum value of D for $\theta = \theta_m$; (b) ratio of $D_{max,2}$ to $D_{max,1}$; and (c) integral of D_1 over the interval $[\theta_m - \pi/2; \theta_m + \pi/2]$.

The validation of the bound IG wave reconstruction method was based on the figure 2 of Okihiro et al. (1992) presenting bound wave spectra in several water depths (10, 40, 183 and 5000 m) forced by the same first-order SW waves spectrum whose directional distribution was determined by a $\cos^{2s}$ model with several directional spreads (0, 10, 40 and 160°) (figure 3.8).

For collinear primary waves $\theta_{sd} = 0°$, the bound IG spectra obtained with our Python routine and the one digitalized from Okihiro et al. (1992) are identical. For directionally spread waves $\theta_{sd} \neq 0°$, three directional resolutions $\delta\theta$ (10°, 5° and 3°) were selected in order to study the impact of $\delta\theta$ on bound IG reconstruction as well as on the computational time (table 3.1). For $\theta_{sd} = 10°$ (figure 3.8, b), the results given by the D_1 and D_2 parametric functions are very close. Some differences are visible for a 10 m water depth and $\delta\theta = 10°$, the curves are very close otherwise. For $\theta_{sd} = 40°$ and $\delta\theta \leq 5°$, the D_2 function gives the best results.

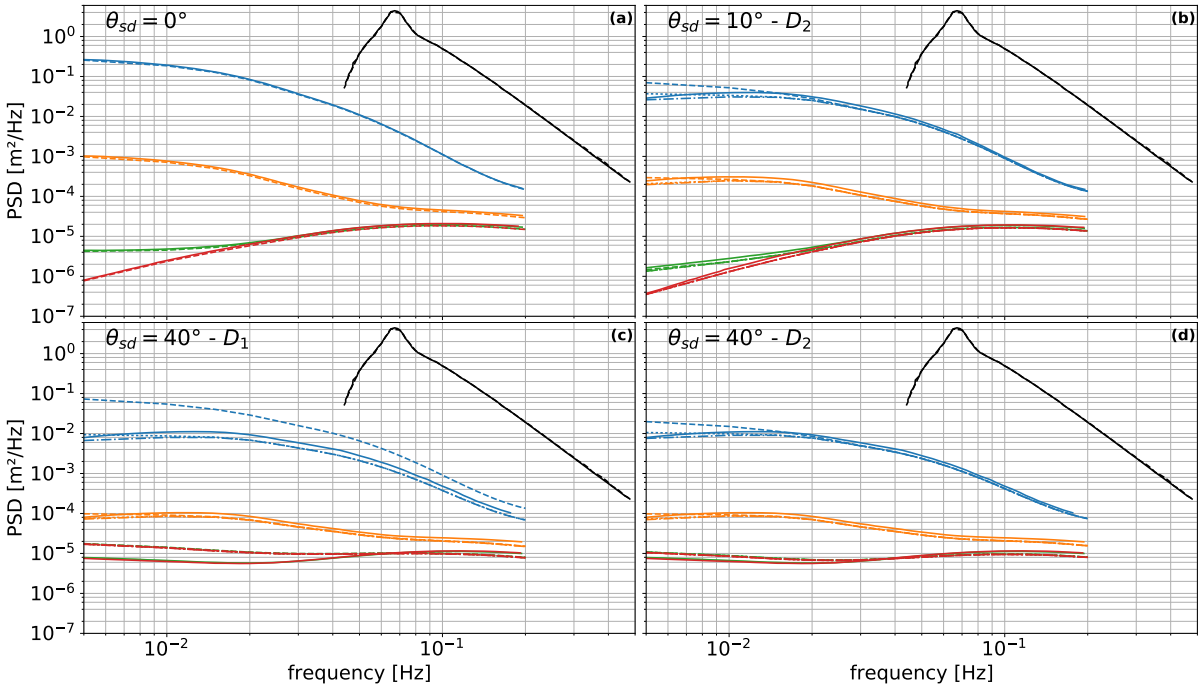

Figure 3.8 – Bound wave sea surface elevation spectra in depths of (blue line) 10 m, (orange line) 40 m, (green line) 183 m and (red line) 5000 m forced by the (black line) same first-order free wave energy spectrum. (Solid lines) reproduced from figure 2 of Okihiro et al. (1992), (discontinue lines) determined from our Python routine. (a) collinear SW waves $\theta_{sd} = 0°$; directionally spread waves (b) $\theta_{sd} = 10°$, (c,d) $\theta_{sd} = 40°$: directional resolution (dashed line) $\delta\theta = 10°$, (dotted line) $\delta\theta = 5°$, (dashdot line) $\delta\theta = 3°$. Parameter functions: (c) D1 and (b,d) D2.

$\delta\theta$	D_1	D_2
10°	3 s	1 s
5°	11 s	3 s
3°	38 s	8 s

Table 3.1 – Mean computational time of E_4 for θ_{sd} equal to 10° and 40° as a function of the spectrum directional resolution $\delta\theta$ and the parametric function.

The parametric function D_2 is faster than D_1 and gives better results. A directional resolution of 5° gives results similar to that of 3°, but the calculation time is divided by about 3 (table 3.1).

The bound IG reconstruction method was applied to the entire wave buoy database, the directional energy distribution was determined using the D_2 parametric function with a resolution $\delta\theta$ of 5°. The minimum period of E_4 was imposed to 20 s ($f_{max} = 0.05$ Hz), which reduces the calculation time to about 1 s for each buoy spectrum.

Limitations of the bound IG reconstruction method

The bound IG wave reconstruction is sensitive to the directional distributions, frequencies and energies of primary SW waves, and variations in water depths (Okihiro et al., 1992). The frequency and directional resolutions of the short wave spectrum (δf and $\delta\theta$) also affect the quality of the bound IG reconstruction. A small directional spreading in the primary waves induces a considerable reduction in the bound IG energy spectrum but thereafter directional spread becomes a less sensitive parameter (Bowers, 1993) (figure 3.9).

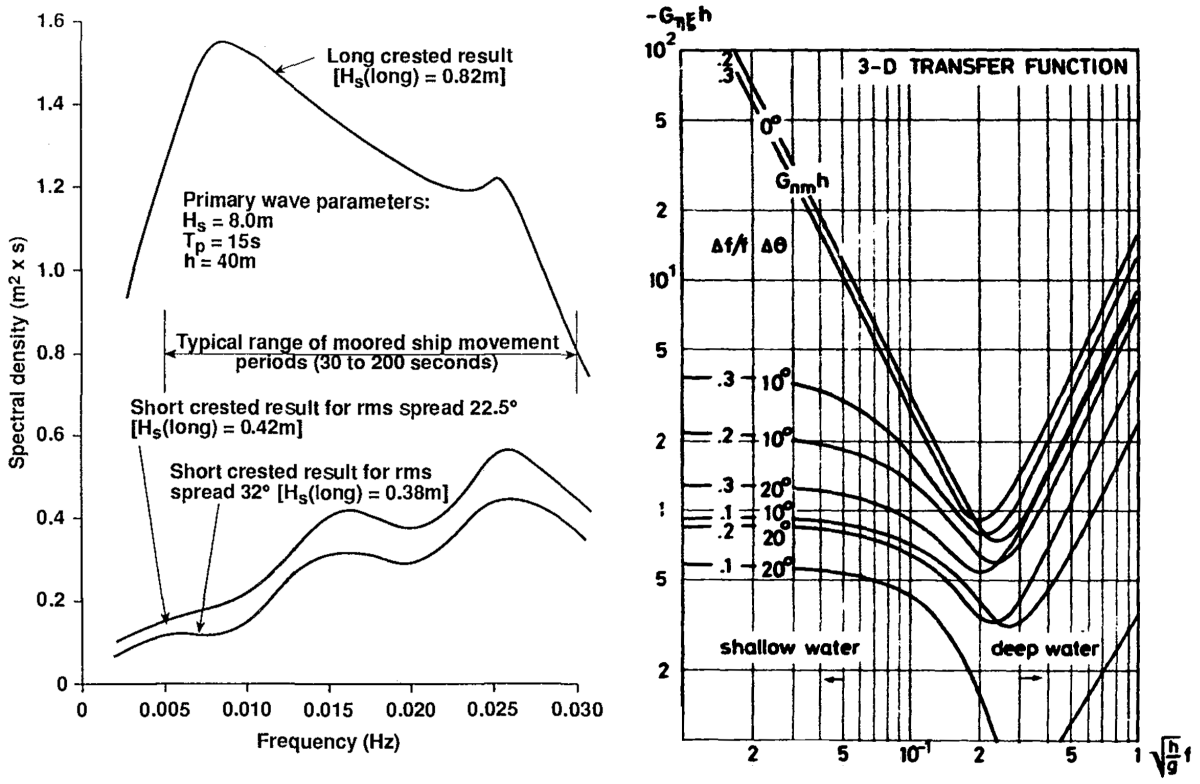

Figure 3.9 – (left figure) Bound IG spectrum reconstructed from a primary SW spectrum whose parameters are Hs = 8.0 m, Tp = 15 s and h = 40 m for different directional spreads: (long crested result) 0°, 22.5° and 32°. (right figure) Coupling coefficient ${}_eC$ (equation 3.19) for a wave group consisting of two frequencies $f_n = f$ and $f_{n+j} = \Delta f + f$ with an angle $\Delta\theta$ between one another. Left figure reproduced from Bowers (1993) and right figure modified from Sand (1982).

Buoy raw data are available, namely vertical and horizontal displacements, and other methods than a two-parameter function can be used for the estimation of directional wave spectra, such as four-parameter models (Van Heteren, 1983), maximum likelihood methods (Waals et al., 2009), maximum entropy methods (Hashimoto et al., 1995) or Bayesian methods (Hashimoto and Kobune, 1989). The toolbox of Matlab functions

DIWASP (DIrectional WAve SPectrum analysis) includes some of these methods.

The method of Hasselmann (1962) applies only to a flat seabed. But if the bed slope is rather gentle, the phase-locked IG wave has time to adjust itself to local depths, then the theory remains valid. Bowers (1993) estimated the additional bound IG wave amplitude due to varying water depth considering an uniform slopping bed (equations 3.25 and 3.26) and found that effects of bed slope are only important nearshore when the water depth is reduced, for high peak period of primary SW waves, and for steep bed slope. In addition, the Stokes expansion used by Hasselmann (1962) is only valid for weakly nonlinear waves, then not close to the surf zone where the waves become highly nonlinear. These two limitations reduce the range of applicability of the bound IG wave reconstruction method.

$$Hs_{bound,tot} = (1 + N^2)^{1/2} Hs_{bound,flat} \tag{3.25}$$

$$N = \frac{26.4 T_p^2 \tan \alpha}{h^{3/2}} \tag{3.26}$$

where N is the ratio of the additional bound IG wave amplitude due to varying water depth over the ($Hs_{bound,flat}$) flat bed bound IG amplitude, T_p is the pic period of primary SW waves, α is the constant seabed slope and $Hs_{bound,tot}$ is the significant total bound IG wave height.

3.3 Numerical wave model

The local measurements of water level oscillations carried out with the pressure sensors were supplemented by a numerical model in order to have a synoptic description of the waves field. The implemented model aims to simulate the transformation and propagation of waves from the open sea to the coast and then into the river, while taking into account the bathymetry effects, mainly the irregular bathymetry including an underwater sediment deposit and the harbor mouth configuration. It is necessary to compute short swell waves and their impacts on the navigation (currents characteristics at the river mouth) as well as on the distribution of wave energy in the vicinity of the breakwaters. Therefore the physical processes, which generate IG waves - in particular the non-linear interactions between short waves - has to be reproduced. The selected model has to be able to use the data from the wave buoy as input for its calculation, i.e. the wave forcing has to be based on the data from a measured wave spectrum. The numerical computation focuses on an energetic storm event. Considering the long-period swell characteristics of the area and the relatively shallow water depth of 50 m at the wave buoy, a numerical model based on

weakly dispersive governing equations is sufficient ($kh \approx 3$ or 4).

3.3.1 Type of wave models

Many types of numerical models exist depending for which physical processes as well as temporal and spatial resolution they are used. Also, different classes of wave models can be used to simulate the transformation of nearshore waves and their interaction with coastal structures.

Spectral wave models

For regional and large scales such as coastal waters, shelf seas, or even entire ocean basins, often only statistical properties of the waves are of interest. These can be modelled through a phase-averaging approach. The wave field needs to be homogeneous and stationary in the space and time interval considered. The wave spectrum represents the physically and statistically most meaningful phase-averaged characteristics of the waves (Holthuijsen, 2007). Spectral models are generally based on the spectral wave action balance equation. The two most widely used open-source spectral models are SWAN (team et al., 2007) and WAVEWATCH III (Tolman et al., 2014). Wave shoaling and refraction induced by the bathymetry and currents can be accurately simulated by spectral models. Diffraction processes can only be approximated due to the lack of pressure differentials in the free surface elevation (no wave phase). Partial or total reflexion against an obstacle can be handled. The input for spectral models is mostly a wind field. Parametric source terms generate wave energy from wind energy. Generally, this statistical approach is limited near the coast and for problems of the scale of a beach or port. A deterministic approach rather than a probabilistic approach is necessary. The deterministic approach, also called phase-resolving approach, calculates the actual free surface motion and particle speed of each individual wave with respect to changes in the bathymetry. In contrast to phase-averaged models many more details can be resolved such as wave-wave interaction, wave runup and inundation, as well as diffraction and reflection. One of the biggest advantages of phase-resolving models is their capability of being able to compute the transfer from short wave energy to long wave energy, i.e. the generation of IG-waves from wave breaking and other nonlinear processes.

Linear mild slope model

Models based on the linear mild-slope equation (Berkhoff (1972) equation) are of phase-resolving nature and commonly used in coastal engineering. The equation describes the combined effects of diffraction and refraction for waves propagating over bathymetry, as

well as refraction against coastal structures or boundaries such as breakwaters, beaches, or cliffs. Models are used to propagate linear monochromatic waves to the coast. For random waves, incident wave spectrum is first discretized into a sequence of frequencies and directions. Then, the steady wave state is computed for each pair, and the results are recombined to provide the random wave features. For harbor oscillation studies, a frequency scanning method designed to propagate monochromatic waves, whose periods cover a large interval, allows to determine the amplification factor for each period (Bellotti and Franco, 2011). The numerical model ARTEMIS (Agitation and Refraction with TElemac on a MIdSlope) (Aelbrecht, 1997) of the finite elements system of TELEMAC (`opentelemac.org`) is an example of such a model. Resonant properties of a water body can also be studied with Berkhoff's equation and directly computed by converting the time-depending problem into one of eigenvalues (Bellotti et al., 2012). The seiche module (Pons et al., 2008) of the numerical model Refonde (Debaillon et al., 2009) developed by CEREMA is one possibility.

Mild-slope equation models are usually used to study the behavior of an enclosed or semi-enclosed basin (Guillou and Chapalain, 2012), to design new basin configurations or to optimize short wave damping by structures and/or to limit the seiche amplitude in the basin. Models based on the linear mild-slope equation have limited applicabilities because the wave input is only based on monochromatic input waves and not on a full spectrum where waves nonlinearly interact with each other and with the bathymetry.

Surf beat models

Xbeach (mode surfbeat) was developed as a short-wave averaged but wave-group resolving model (Roelvink et al., 2009) - it is therefore also of phase-resolving nature. The variation of the free surface is simulated at the wave group scale (short wave envelope) and also the physical processes at the scale of IG waves. The short-wave motion is first solved using the wave action equation, then the variations of short-waves envelope are solved by the nonlinear (hydrostatic) shallow water equations. To analyse the IG wave generation mechanisms (moving breakpoint or bound wave shoaling), this two-step resolution allows to isolate one mechanism from the other (Bertin and Olabarrieta, 2016). Despite the elegant development of this model, it does not meet all our criteria by not solving the full free surface at the short wave scale.

Dispersive wave models

Both frequency dispersion and nonlinear effects play an important role in short wave propagation. Three main lengths are used to characterise a wave propagation problem: the wavelength L, the wave amplitude a, and the water depth h. The following dimensionless

parameters are respectively nonlinearity ϵ, frequency dispersion or shallowness μ, and wave steepness σ:

$$\epsilon=\frac{a}{h} \qquad \mu=\frac{h^2}{L^2} \qquad \sigma=\frac{a}{L}=\epsilon\sqrt{\mu}$$

The calculation of an additional non-hydrostatic pressure is a way to improve the frequency dispersion capacity in phase-resolving wave model based on the Nonlinear Shallow Water Equations. The hydrostatic pressure given by the nonlinear shallow water equations can be corrected with an additional governing equation for the vertical pressure. This approach is used in the SWASH model (Zijlema et al., 2011) and also the non-hydrostatic version of Xbeach. The computational domain can be divided into a fixed number of vertical layers and the frequency dispersion is improved by increasing the number of vertical layers: using two equidistant layers can be adequately retain progressive waves for $kh < \pi$.

An other way to handle short waves is the Boussinesq-type approach. Boussinesq-type equations are based on the Nonlinear Shallow Water Equations but terms including the lowest order effects of nonlinearity and frequency dispersion are added. The standard Boussinesq-type equations for variable water depth were first derived by Peregrine (1967) but were only applicable to relatively shallow water depths. Madsen et al. (1991) and Nwogu (1993) proposed new forms of Boussinesq-type equations to improve the frequency dispersion characteristics. For example, the concepts of Nwogu (1993) is based on a truncated series expansion of the horizontal velocity vector that is then substituted for the vertical velocity by using the irrotationality conditions $\frac{\partial u}{\partial z} = \frac{\partial w}{\partial x}$ and $\frac{\partial v}{\partial z} = \frac{\partial w}{\partial y}$, which expresses the vertical velocity in terms of a truncated series expansion of the horizontal velocities. Although the derivations of Madsen et al. (1991) and Nwogu (1993) are different, the linear dispersion properties are identical in both approaches. The so-called extended Boussinesq-type equations are ideally applicable to weakly nonlinear waves (Kirby, 1996). In addition, both sets of equations are not fully applicable to scenarios where the speed of currents exceeds the phase velocity of the individual waves (Chen et al., 1998). The BOSZ model (Roeber et al., 2010; Roeber and Cheung, 2012b) is based on the equations of Nwogu (1993) in conservative form.

Fully nonlinear Boussinesq-type wave models

Based on Nwogu (1993) approach, Wei et al. (1995) derived a set of fully nonlinear Boussinesq-type equations, which are the basis for the numerical model FUNWAVE (Kirby et al., 1998). The equations of Wei et al. (1995) are equivalent to the 2D fully nonlinear weakly dispersive equations derived by Green and Naghdi (1976) (Lannes and Bonneton, 2009). The numerical model UHAINA (recent development at the University

of Bordeaux) is based on the equations of Green and Naghdi (1976) (Filippini et al., 2018). More details on Boussinesq-type models can be found in Brocchini (2013).

3.3.2 Description of the BOSZ model

The capability of Boussinesq-type numerical models in handling the propagation and transformation of full wave spectra makes these models suitable tools for the computation of wave processes in the nearshore environment. The Boussinesq-type model BOSZ (Boussinesq Ocean and Surf Zone model) was developed for the computation of nearshore waves, wave-driven currents, infragravity oscillations, ship wake waves, near-field tsunamis and boulder/sediment transport (Roeber et al., 2010; Roeber and Cheung, 2012b; Roeber and Bricker, 2015; Li et al., 2018). In this study, the wave transformation from the wave buoy 06402 near Anglet to the river mouth of the Adour and into Port de Bayonne is investigated with BOSZ for a large swell scenario.

Governing equations

The governing equations are based on a conserved variable formulation of Nwogu (1993) equations (Roeber et al., 2010). Nwogu (1993) improved the accuracy of linear dispersion by expressing the velocity variable at an arbitrary reference depth z_α. The choice of z_α is affecting both linear and nonlinear wave properties with high sensitivity. Theoretically, the reference depth can be chosen over a wide range in depth, and it is technically possible to obtain an accurate match between the linear dispersion properties of Nwogu (1993) and Airy wave theory for $kh >> \pi$. However, it is difficult to optimise the dispersion properties for a range of kh-values instead of only for one particular wave period. It eventually comes down to finding a optimal compromise. Nwogu (1993) recommended a z_α-value of $-0.53h$. Recently, Simarro et al. (2013) recommended a value of $z_\alpha = -0.55502h$ as a better compromise between linear and nonlinear properties. On one side, the linear dispersion error increases for higher kh-values with a lower reference depth such as the one suggested by Simarro et al. (2013) but, on the other side, the shoaling properties can be improved due to the fact that the shoaling process is a group wave (long-wave) problem. The full mathematical derivation of the Nwogu (1993) equations is available in the appendix A.

Numerical formulation

The solution structure covers the Nonlinear Shallow Water Equations as a subset of the governing equations with a Finite Volume scheme based on a Total Variation Diminishing (TVD) reconstruction method of up to 5^{th} order and a HLLC Riemann solver. This

ensures robust and accurate computation of fast flows over irregular terrain including wet/dry boundaries such as encountered in the wave runup process. The frequency dispersion terms are based on a central-differential Finite Difference scheme (Roeber et al., 2010). The time integration is carried out with Runge-Kutta schemes of up to 4^{th} order allowing for adaptive time stepping. Due to the space-time derivatives that arise in the evolution variables of the momentum equations, systems of equations have to be solved to determine the flow speed in the x and y-directions at the end of each time step. The x and y systems are independent from each other with data-dependencies in only the x or y-direction, respectively. The numerical domain is discretized uniform rectangular cells and the simulations are integrated with an adaptive time step based on an initially defined Courant number (Cr) condition. The adaptive time step ensures that the Cr-condition is always satisfied even when fast flows arise over the course of the computation (e.g. during wave runup).

Wave breaking

Wave breaking is a challenging problem for dispersive depth-integrated models due to the parabolic nature of the dispersion terms, which do not strictly allow for discontinuous solutions. As the free surface steepens, the local nonlinearity increases, which is consequently balanced by the frequency dispersion terms. Depth-integrated models do not describe overturning of the free surface and thus cannot fully reproduce the wave breaking processes. Due to the absence of dissipative terms that mimic the turbulent dissipation effects of wave breaking, the governing equations of Boussinesq-type and also of non-hydrostatic models do not directly handle flow discontinuities arising at the leading edge of breaking waves or bores. However, the numerical solution can still provide physically meaningful results, if the potentially arising artifacts (in extreme cases even instabilities) near the wave front are counter-measured or avoided. BOSZ restricts the development of overshoots through local and momentary deactivation of the dispersion terms over a few grid cells along the breaking wave front. The deactivation can be based on a momentum gradient threshold, i.e. a geometric criterion, or alternatively a kinematic criterion based on a local free surface Froude number value. The use of conserved variables in the BOSZ governing equations allows for approximation of breaking waves as discontinuous flows. Conserved variables are essential for the correct computation of super-critical flows, since momentum conservation is a critical component for shock waves.

Based on a momentum gradient, which is similar to the evolution of the free surface over time, the dispersion terms are deactivated in every cell where the following criterion

is met:

$$|(Hu)_x| > B\sqrt{gH}$$
$$|(Hu)_y| > B\sqrt{gH}$$

where H is the total water depth, (u,v) are the horizontal flow velocities in x and y directions and B is taken to 0.5 based on comparison with experimental data (Roeber et al., 2010).
The query is checked in each time step and the model deactivates and reactivates dispersion on the fly. In cells with no dispersion, the solution is then purely based on the hydrostatic shallow water equations. The full Boussinesq-type solution is retained in all other cells. The deactivation of the dispersion is only local and it does not affect all cells between breaking wave and shoreline, which would be unnecessary. Even in the surf zone, it is possible that the solution is fully based on the Boussinesq-type solution and that no single cell is deactivated. The deactivation is solely dependent on the intensity of the momentum gradient (analogous to wave steepness) and it is well possible that the threshold in the above relation is not exceeded. This can be due to a relatively coarse grid, which in itself limits the steepness of the free surface, or due to relatively small waves.

An other strategy to identify wave breaking is based on free-surface Froude-Number criteria. Assuming quasi-hydrostatic flow conditions near the wave breaking front, the contribution of the dispersion terms in the governing equations is ignored momentarily in every cell where the Froude number (Fr) at the free surface exceeds an upper limit C_{B2}. The Froude number is calculated as $Fr = \sqrt{u^2 + v^2}/\sqrt{gH}$. In Nwogu (1993) equation, the flow velocity can be reconstructed at any level in depth through the prescribed velocity profile embedded in the governing equations. The equation of Nwogu (1993) is based on a Taylor series expansion of the horizontal velocity vector where the approximation of frequency dispersion results from the truncation of the series after second-order, which leads to a quadratic variation for the horizontal velocity over depth. With $z = \eta$, the free surface velocity is given by

$$\begin{aligned} u &= u_{z_\alpha} + \frac{1}{2}(z_\alpha^2 - z^2)[(u_{z_\alpha})_{xx} + (v_{z_\alpha})_{xy}] + (z_\alpha - z)[(hu_{z_\alpha})_{xx} + (hv_{z_\alpha})_{xy}] \\ v &= v_{z_\alpha} + \frac{1}{2}(z_\alpha^2 - z^2)[(u_{z_\alpha})_{xy} + (v_{z_\alpha})_{yy}] + (z_\alpha - z)[(hu_{z_\alpha})_{xy} + (hv_{z_\alpha})_{yy}] \end{aligned} \tag{3.27}$$

z_α is the reference depth at which the horizontal velocities are evaluated.
For $Fr > 1$, the flow is assumed to be supercritical and undular bores can develop. Around $Fr = 1.7 - 2.0$, hydraulic jumps form and the waves are clearly breaking.

Eddy viscosity An alternative to turning off the dispersion terms in cells where the threshold from the momentum gradient and/or Froude-number approach are exceeded is the inclusion of an additional dissipative terms in the momentum equations. This concept goes back to Zelt (1991) and was later improved by Kennedy et al. (2000). The idea is based on an eddy viscosity variable depending on the local shallow water celerity. The BOSZ model includes this option. If the eddy viscosity approach is chosen, dispersion remains active at all times and in all cells. The dissipative term is added to the momentum equation to counter-balance the potentially arising instabilities at the wave breaking front. Comparisons with experimental data have shown only very small differences between the eddy viscosity approach and the technique of deactivation of the dispersion terms.

Benchmark

The laboratory test conducted by Suzuki et al. (2017), specifically the test case WEN_004, was chosen as an additional validation of the BOSZ code to previously conducted validation efforts (see Roeber and Cheung, 2012a). The experiment from Suzuki et al. (2017) is a one-dimensional flume experiment. A wavemaker generated a wave spectrum at the left boundary of a 1 m deep flume sending out a series of swell waves with a peak period of 2 sec. At the right side of the flume, a sloping bottom was installed. Instead of a plane beach a abrupt step-type plateau was installed, which breaking waves were able to overtop (figure 3.11, bottom panel).

The input for the numerical model is the bathymetry of the wave tank configuration in 0.1 m grid spacing as well as the time series of the water level measured at a gauge near the wavemaker (Suzuki et al., 2017, figure 1). The flow velocity was not measures. Therefore the velocity in the boundary cell of BOSZ was calculated by linear long wave approximation. This approach is clearly not resulting in the most accurate flow velocity since the input water level time series results in non-hydrostatic pressure. However, the input waves are of relatively low dispersion $kh < \pi$ and a long wave assumption leads to a reasonable approximation of the flow speed.

The experiment is a useful test to examine how a numerical model propagates and transforms a full wave spectrum, including wave breaking and energy transfer into infragravity bands. The computed results by the BOSZ model are in very reasonable agreement with the data obtained by Suzuki et al. (2017) (figures 3.10 and 3.11). Wave gauges 3, 5, and 7 show the spectra derived from the observed time series over the flat and the sloping bottom of the tank. Wave gauges 8, 10, and 12 show the transformation of the spectral quantities after wave breaking. A strong change in spectral composition can be observed between gauge 7 and 8 where the waves break. The BOSZ model correctly reproduces the energy dissipation and transfer of gravity to infragravity energy during this process.

The model is able to accurately reproduce the energy distribution at all gauges even with a relatively coarse grid spacing of 0.1 m (figures 3.10 and 3.11). This confirms that the BOSZ model can handle the main surf zone processes without the need of excessively fine grid spacing. The additional results obtained from the same model setup but with inclusion of a dissipative eddy viscosity term instead of deactivation of the dispersion terms shows that both methods lead to consistent results (figure 3.10), which means that either method can be used to handle wave breaking scenarios in this kind of depth-integrated phase-resolving model.

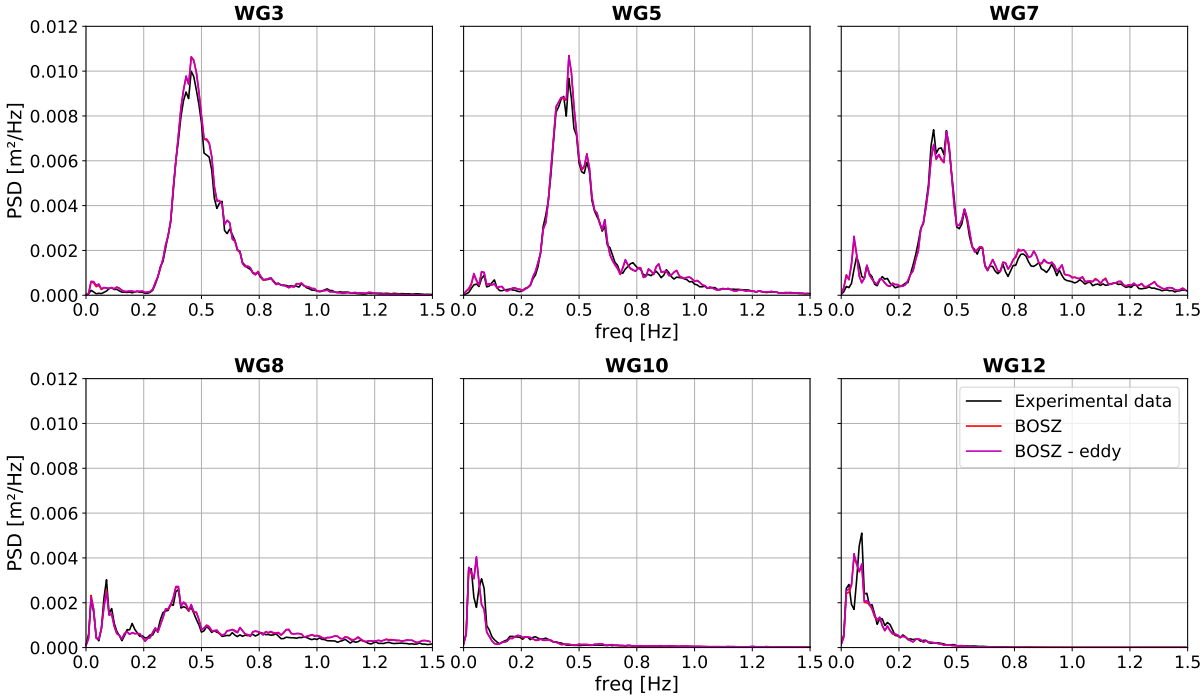

Figure 3.10 – Power spectral densities of (black lines) experimental and (purple and red lines) numerical data at different gauges whose locations are shown in figure 3.11 (bold figures). (purple lines) Dissipative eddy viscosity term instead of (red lines) deactivation of the dispersion terms. Test case WEN_004 (Suzuki et al., 2017).

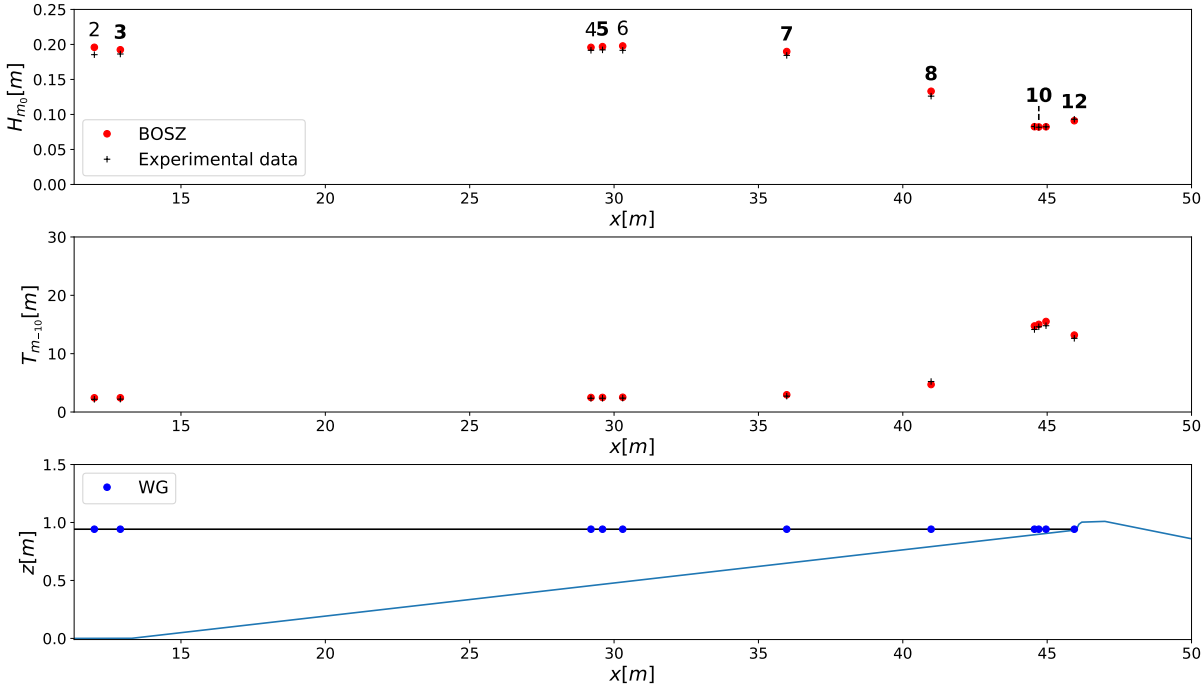

Figure 3.11 – (top) Significant wave height H_{m_0}, locations of wave gauges, (bold figures) locations where PSD are calculated in figure 3.10. (middle) Wave period $T_{m_{-10}}$. (red dots) BOSZ data, (black crosses) experimental data. (bottom) Numerical model domain and wave gauges positions.

Linking phase-averaged and phase-resolving models

The input for phase-resolving models applied to real-world scenarios is mostly based on an offshore waves spectrum either computed by a spectral model or recorded by a wave buoy. The wave generation in phase-resolving models is then based on the superposition principle of individual monochromatic waves each representing one component in frequency and direction of the entire input spectrum.

The lack of phase information is a limitation in connecting phase-averaged and phase-resolving models, since usually no information is provided on how the individual waves in a spectrum are locked to each other. The phase locking has an influence on the waves' nonlinear interactions with the bathymetry and between the individual waves. A common approach also used in BOSZ is to assign a random phase to each spectral component. Ideally, several wave fields have to be computed to provide a statistical representative of the input spectrum.

3.4 Conclusion

An autonomous measurement device complementary to the existing systems at the Port of Bayonne has been developed and implemented as part of a series of measurement campaigns to characterize the agitation of the study site for different energy and tidal conditions. A procedure for reconstructing the energy spectrum of incident waves in the IG frequency band, based on the Okihiro et al. (1992) method, has been developed to determine the properties of the incident bound IG waves during the measurement periods. This measurement effort, which consisted in targeting energy events over a three-year period, made it possible to acquire a unique set of data intended not only to study the behavior of IG waves in a river channel and a marina, but also to validate a numerical wave model based on the BOSZ code. The choice of this code, based on the resolution of Boussinesq-type equations, is motivated by the need for a numerical tool to describe both non-linear interactions and dispersive effects at wave scale in order to study IG wave transformation and interactions with coastal structures.

Chapter 4

Field Campaign

4.1 Introduction

In this chapter, we use a high frequency water level data set to investigate the respective contributions of incident short and long waves on the river seaport and marina oscillations. The data were collected during a three years field campaign to cover a wide range of climatic conditions. More specifically, the study aims to (1) identify the dominant oscillation periods in the river seaport and the marina, (2) identify the external forcing mechanisms, and (3) study the transformation of incident long waves during their propagation in the river.
The data set is presented in section 4.2. The procedure to analyze the pressure sensor measurements and to derive the characteristics of incident IG waves from an offshore wave buoy are described in section 4.3. Furthermore, the numerical code (REFONDE) used to compute the natural modes of oscillation that are compared with water level periods of oscillations measured in the marina is briefly described. The results are presented in section 4.4 and discussed in section 4.5. A general conclusion summarizing the main results of this chapter is drawn in the last section 4.6.

4.2 Data set

A series of field campaigns were launched to measure water level elevation in the port of Bayonne at different locations during three winters from 2016 to 2019. The measurements were carried out with five pressure sensors of 1 Hz sampling frequency. The sensor at the river mouth (0.3 km) is placed inside a stainless steel tube fixed on a concrete block accessible at low tide. The other sensors were fixed on dock access ladders located along the river seaport at 1.4, 2.2 and 3.7 km from the river mouth, and in the largest basin of the marina (figure 4.1). During each field campaign, the channel and marina sensors were

fixed at low tide to the ladders with a metal tube and plastic zip ties. This device allows a great flexibility in sensors deployment without using nautical means allowing to focus on specific events. The pressure sensors operating periods and malfunctions are listed in table 4.1. The pressure sensors network was complemented by a tidal gauge, permanently operated by the SHOM and located at 850 m upstream of the river mouth (figure 4.1). This tidal gauge records water level every minutes. Atmospheric pressure was measured every hour by a weather station located in Biarritz (~7 km from the study area). During the study period, incident offshore wave characteristics were measured by a directional wave buoy, moored in 50 m water depth at 7 km off the coast (figure 4.1). This waverider is part of the french coasts buoys network Candhis. It continuously records offshore wave conditions and provides wave spectrum every 30 min.

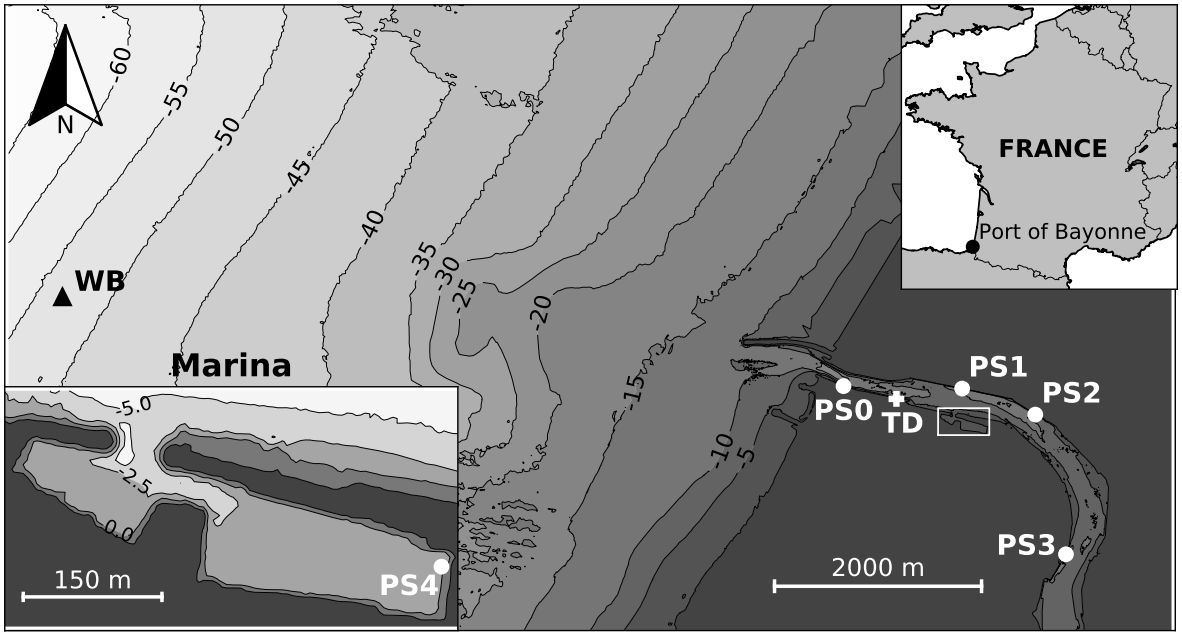

Figure 4.1 – Port of Bayonne and gauges locations: (WB) waverider buoy; (PS) pressure sensors (white dots): PS0 (river mouth), PS1-PS3 (river seaport) and PS4 (marina); and (TD) tide gauge. Zoom on the marina in the lower left corner (white rectangle on the map).

Gauge		PS0	PS1	PS2	PS3	PS4
Location		**0,3 km**	**1,4 km**	**2,2 km**	**3,7 km**	**Marina**
FC1 (2016)	Start	-	16/11	16/11	16/11	-
	End		30/11	30/11	30/11	
	Days		14	14	14	
FC2 (2017)	Start	-	12/01	12/01	12/01	-
	End		10/02	10/02	10/02	
	Days		29	29	29	
FC3 (2018)	Start	15/02	Lost gauge	15/02	15/02	08/03
	End	03/05		03/05	20/04	20/04
	Days	77		77	64	43
FC4 (2019)	Start	23/01	23/01	-	23/01	23/01
	End	13/06	22/03		22/03	22/03
	Days	168	57		57	57
Total	**Days**	**245**	**100**	**120**	**164**	**100**

Table 4.1 – Time covering of experimental data.

4.3 Methods

4.3.1 Water level analysis

Free surface elevation time series are computed from the pressure sensors data. Since the sensors are located near the free surface (depth ~-1.5 m) and waves are weakly nonlinear, water level is computed assuming hydrostatic pressure (Bonneton and Lannes, 2017). A spectral analysis of the water elevation time series is then performed to study the energy distribution in the different frequency bands. The tidal contribution is first removed by considering a linear deviation of the signal for time series of 2048 s. This 34-min record of long waves was chosen to be consistent with the time interval of the wave buoy measurements that we used to study the influence of incident waves on harbor oscillations. The filtered (PSD) power spectral density of the free surface is then determined using the Welch method (Welch, 1967), that consists in dividing the data into 50% overlapping segments and applying a Hanning window. The mean spectrum being related to the variance of the free surface, the associated (CI) confidence interval follows a (χ^2) Chi-square law of degree of freedom ν (Thomson and Emery, 2014, equation 5.108). Using a

log scale representation, the confident interval can be reduced to the equation 4.1.

$$CI = \left] \frac{\nu}{\chi^2_{1-\alpha/2,\nu}}; \frac{\nu}{\chi^2_{\alpha/2,\nu}} \right[\tag{4.1}$$

where α is the confidence coefficient taken at 5%.
Significant wave heights (Hs) can then be calculated from the PSD according to the formula 4.2 (Holthuijsen, 2007).

$$Hs = 4\sqrt{m_0} \tag{4.2}$$

where m_0 is the zeroth-order spectrum moment.
In our study, significant wave heights of short waves (SW), infragravity waves (IG) and very long waves (VLW) are computed by determining m_0 respectively for period intervals ranging from 5 to 30 s, 30 to 300 s, and 300 to 600 s.

4.3.2 Background energy spectrum determination

The periods of oscillation of a water basin are mainly related to the basin geometry rather than to the characteristics of external forcings (Rabinovich, 2009). By consequence, the natural topographic response of a water basin forced by long waves, also called background spectrum, is usually determined by computing water elevation density spectra for low incident waves energy (Marcos et al., 2009). In our study, calm and energetic conditions are discriminated using a threshold value based on the offshore incident wave energy flux given by:

$$F = Hs^2.Te \tag{4.3}$$

where Hs is the significant wave height and Te the energy period, measured at the wave buoy. Calm conditions correspond to periods when $F \leq F_{50}$, and energetic conditions to periods when $F \geq F_{95}$, with F_{50} and F_{95} corresponding to the 50th-quantile and the 95th-quantile, respectively. These two statistical values were computed from wave buoy data spanning over a multi-year period, which guarantees that these two values are well representative of the local sea state in our study area.

4.3.3 Natural periods of oscillation of the marina

The natural oscillation periods (NOP) of the marina are computed using the seiche module (Pons et al., 2008) of the Refonde numerical model (Debaillon et al., 2009) developped by the CEREMA. This approach is preferred to the application of the well known Merian's formula due to the complex geometry of the marina that is composed of two connected basins. It consists in converting the time-depending problem into eigen values using

the finite element approximation of the mild-slope equations (Berkhoff, 1972) assuming that shallow water condition is met. The eigenvalues, corresponding to the NOP, and eigenvectors, which are representative of the spatial distribution of standing waves, are then directly computed by an iteration method. The computational domain is defined by the bathymetry of the marina and the boundary conditions are specified along the contour lines by either fully reflection for solid boundaries or nodal line (or zero surface elevation) at the open sea boundary. The computed NOP are compared with the values obtained from the field measurements carried out in the marina with PS4.

4.3.4 Bound infragravity waves energy spectrum

The spectral characteristics of incident bound infragravity waves are estimated from short waves spectra measured at the wave buoy using the Hasselman's theory (Hasselmann, 1962). Indeed, considering an inviscid, incompressible, irrotational fluid in constant depth, bound IG waves induced by non-linear interaction of gravity waves can be determined by expanding the Euler waves equations and boundary conditions to second-order using a perturbation analysis as the Stokes's method (Longuet-Higgins and Stewart, 1962; Hasselmann, 1962). Assuming that the short waves field, including wind waves and swell, is a linear sum of free waves with random phases, the bound IG waves spectrum $E_4(f_j)$ can be computed according to (Okihiro et al. (1992) eq. 3) with the following formula:

$$E_4(f_j) = 2\delta f \sum_{n=n_{lo}}^{n_{hi}-j} \sum_{q=1}^{n_\theta} \sum_{r=1}^{n_\theta} eC^2 E(f_n, \theta_q) E(f_{n+j}, \theta_r) \delta\theta^2 \tag{4.4}$$

where $f_j = f_{n+j} - f_n$ is the j^{th} bound wave frequency, $E(f, \theta)$ is the gravity wave frequency-directional spectrum, eC is the bound wave sea surface elevation coupling coefficient (Okihiro et al. (1992) eq. 4a), δf and $\delta\theta$ are the frequency and directional resolutions. The symbols $n_{lo}\delta f$ and $n_{hi}\delta f$ correspond to the lowest and highest gravity wave frequencies. The number of directional bands at each frequency is given by $n_\theta = 360/\delta\theta$.

Raw wave buoy spectrum is integrated over the wave direction, and the frequency-direction spectrum is reconstructed using a parametric directional spreading function team et al. (2007) (appendix A, variable MS) and interpolated along $\delta\theta = 5°$ and $\delta f = 0.005\ Hz$. The minimum period of E_4 is set to 20 s and the maximum period is imposed by the frequency step, i.e 200 s.

4.4 Results

4.4.1 Total power density spectra of water levels

Power density spectra of 3-day water level time series were first computed, then averaged, for the pressure sensors installed along the channel harbor to determine the distribution of energy as a function of frequency bands. Six distinct peaks are clearly visible from 2h to 12h that correspond to the tidal frequencies with the highest energy peak reached at the semi-diurnal frequency (figure 4.2). On the contrary, no significant peak appears in the short and long waves frequency bands, except for PS4 deployed in the marina. Table 4.2 presents the significant wave heights H_{m0} determined from PSD in figure 4.2 for period lower than 2 h, as well as the (R_H) contribution of the frequency band to the variance of the free surface. In terms of energy distribution, most of the energy is concentrated in the tidal frequency band (table 4.2). For periods lower than 2h, the energy is mostly distributed between 5 s and 10 min. Energy in this frequency band reaches its maximum at the river mouth (32 cm at PS0) and decreases upstream down to 10 cm. Note that energy in the marina (PS4) is comparatively high as it reaches 21 cm. The contribution of the short waves, with periods lower than 30 s, to the variance of the tidally truncated free surface, is only significant at the river mouth ($R_{H,SW} = 54\%$). For the other pressure sensors installed in the river seaport, the energy is mainly concentrated in the infragravity bands ($30\ s < T < 300\ s$) with $R_{H,IG} > 70\%$. In the marina, the energy is quasi evenly distributed between the IG band and the very low frequency band ($5 < T < 10\ min$).

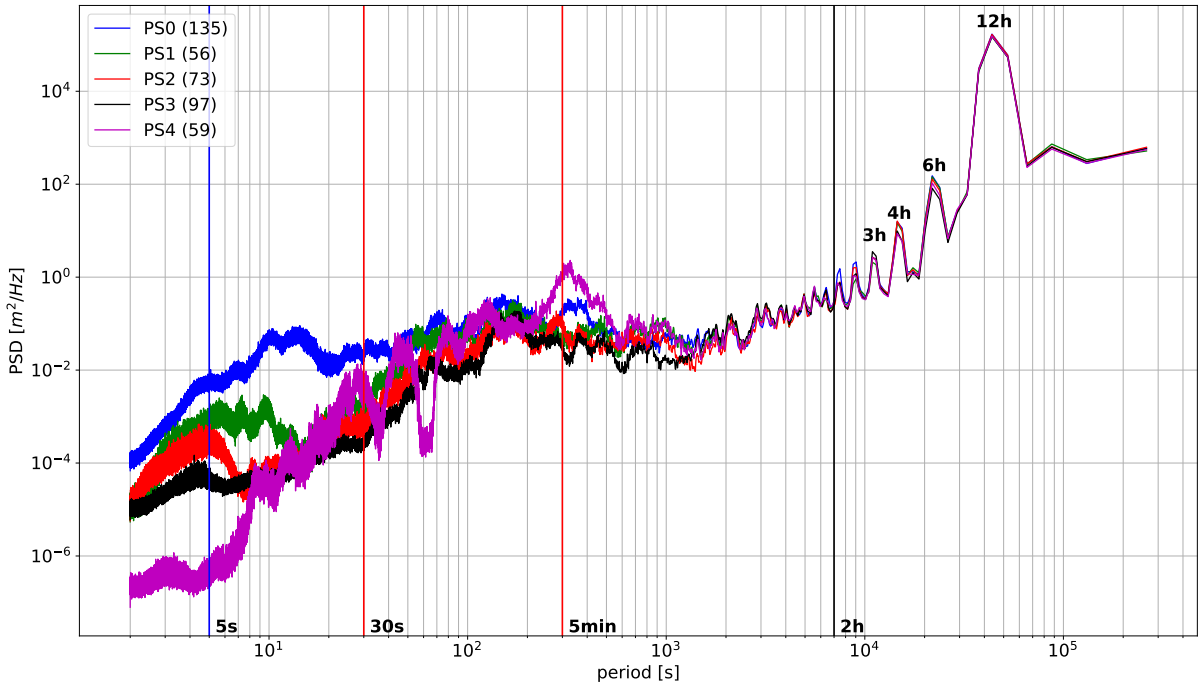

Figure 4.2 – Power spectral densities (PSD) at river sensors. The number of averaged spectra is indicated in brackets.

	Hs	**SW**		**IG**		**VLW**		$\mathbf{\Sigma R_H}$
		5-30s		30s-5min		5-10min		
	2s-2h	Hs	R_H	Hs	R_H	Hs	R_H	
PS0	0.32	0.24	54	0.19	35	0.06	4	93
PS1	0.16	0.05	8	0.14	74	0.04	6	88
PS2	0.11	0.02	4	0.10	72	0.03	9	85
PS3	0.10	0.01	2	0.09	76	0.03	8	85
PS4	0.21	0.03	2	0.15	53	0.13	40	95

Table 4.2 – Significant wave height (Hs) determined from PSD in figure 4.2 in different frequency bands for period<2h; $R_{H_{SW}} = m_{0,SW}/m_{0,p<2h}$.

4.4.2 Analysis of long waves

The analysis of energy spectra highlights that water level oscillations, both in the harbor channel and in the marina, are mostly driven by long waves with periods lower than 10 min. In the following, long waves energy spectra are thus analyzed in more details from 34 min time series. The influence of incident wave conditions is studied by comparing energy spectra computed for calm and energetic sea states, which were determined based

on the 50th and 95th-quantile of the offshore energy flux F_{50} and F_{95}, equal to 18 and 166 $m^2.s$ respectively.

Long wave energy evolution along the channel harbour

At the river mouth (PS0), most of the energy is concentrated in the SW band (R_{SW} = 50%) for energetic conditions, with a peak energy around 16 s. Significant wave height measured at PS0 reaches a maximum value of $Hs_{SW,max} = 1.3\ m$ during the study period, and the mean total significant wave heights is equal to 0.79 m (table 4.4).
The short wave Reduction Factor (RF) was computed to assess the efficiency of the breakwaters to dissipate incident short waves :

$$RF = \frac{Hs_{off} - Hs_{SW,PS0}}{Hs_{off}} \tag{4.5}$$

where RF is the short wave reduction factor, Hs_{off} is the offshore significant wave height and $Hs_{SW,PS0}$ is the short wave significant wave height at the river mouth. The minimum, mean and maximum values of RF are 75, 89 and 96% respectively for energetic events. The remaining energy in the SW band dissipates quickly as the short waves propagate in the river. Its contribution to the variance of the free surface becomes very low ($Hs_{SW,max} <$ 0.20 m and $R_{SW} < 10\%$ for PS1 to PS3).

During calm conditions, the energy in the IG period band is low and rather uniform for all river sensors and no energy peaks are visible in contrast to inside the marina (figure 4.3 and table 4.3). During energetic conditions ($F \geq F_{95}$), the IG energy level at the river mouth is high compared to the other river sensors. It represents 41% of the total energy measured at PS0 with a mean Hs_{IG} equal to 0.50 m, reaching an especially high value $Hs_{IG,max} = 1.0\ m$ (offshore conditions: $Hs = 6.1\ m$; $Te = 13.5\ s$). Upstream the river mouth, the mean energy in the IG band drops quickly since at PS1, only 1.1 km from PS0, Hs_{IG} is equal to 0.27 m, which corresponds to a dissipation rate of 47%. Once in the channel harbor, the contribution of the IG energy remains very high in particular during energetic conditions ($R_{IG} > 77\%$). It is worth noting that the dissipation rate of IG energy in the river is low. Indeed, Hs_{IG} only reduces of 8 cm between PS1 and PS3 (2.3 km), i.e. 30% dissipation for energetic conditions.

The energy distribution in the IG band displays a bi-modal distribution between band IG1 (30-100 s) and IG2 (100 s-5 min) (figure 4.3, center panel). At the river mouth (PS0), the energy is equally distributed between IG1 and IG2 ($Hs_{IG1} = 0.34\ m$ and $Hs_{IG2} = 0.36\ m$ during energetic conditions). This even distribution is conserved few kilometers from the river mouth at PS1 ($Hs_{IG1} = 0.17\ m$ and $Hs_{IG2} = 0.20\ m$). However, energy contribution of band IG1 decreases further upstream as it increases in band IG2.

Energy in band IG2 contributes to 43, 52 and 67% of the total energy at PS1, PS2 and PS3 respectively, while the energy contribution in band IG1 drops to 32, 23 and 15% respectively. Finally, the contribution of very long waves, with periods ranging between 300 and 600 s, contributes little to the river seaport oscillations: $Hs_{VLW} < 0.10\ m$ and $R_{VLW} < 5\%$.

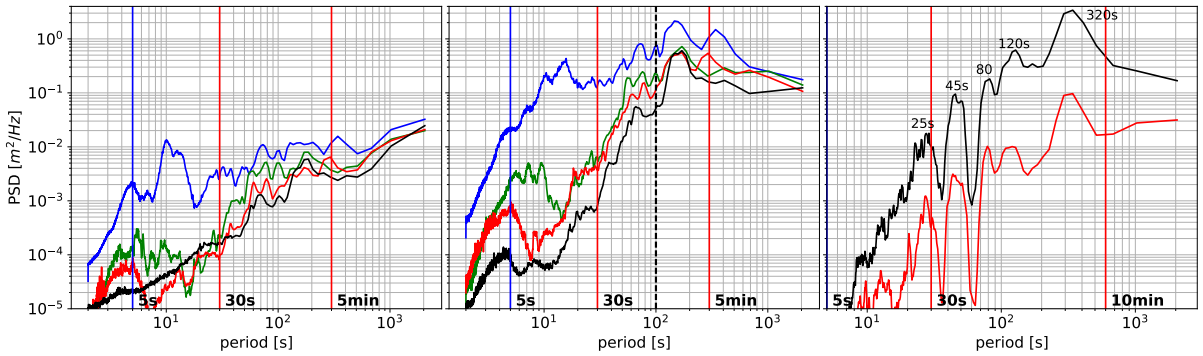

Figure 4.3 – PSD during calm and energetic conditions: (left) calm and (center) energetic conditions at river sensors (blue) PS0, (green) PS1, (red) PS2 and (black) PS3; right panel: (red) calm and (black) energetic conditions at the marina sensor (PS4) and resonant periods.

	Hs	**SW**		**IG**		**VLW**		**IG1**		**IG2**	
		5-30s		30s-5min		5-10min		30-100s		100s-5min	
	m	Hs	R	Hs	R	Hs	R	Hs	R	Hs	R
PS0	0.12	0.10	62	0.05	18	0.01	1	0.04	11	0.03	7
PS1	0.05	0.02	14	0.04	55	0.01	3	0.03	31	0.02	23
PS2	0.04	0.01	7	0.03	47	0.01	4	0.02	21	0.02	25
PS3	0.03	0.01	12	0.02	45	0.01	4	0.01	16	0.02	28
PS4	0.07	0.01	3	0.04	45	0.03	18	0.03	15	0.04	29

Table 4.3 – Hs during calm conditions (from PSD in figure 4.3). $R_{SW} = m_{0,SW}/m_0$.

	Hs	SW		IG		VLW		IG1		IG2	
		5-30s		30s-5min		5-10min		30-100s		100s-5min	
	m	Hs	R	Hs	R	Hs	R	Hs	R	Hs	R
PS0	0.79	0.56	50	0.50	41	0.13	3	0.34	19	0.36	20
PS1	0.31	0.08	8	0.27	77	0.06	4	0.17	32	0.20	43
PS2	0.27	0.05	3	0.24	77	0.07	6	0.13	23	0.19	52
PS3	0.21	0.02	1	0.19	83	0.05	6	0.08	15	0.17	67
PS4	0.38	0.05	2	0.28	52	0.18	22	0.13	11	0.24	40

Table 4.4 – Hs during energetic conditions (from PSD in figure 4.3). $R_{SW} = m_{0,SW}/m_0$.

Long wave energy inside the marina

The power density spectrum for the pressure sensor PS4 located in the marina includes several dominant frequency peaks (figure 4.3). During calm conditions, five distinct peaks are visible at 320, 120, 80, 45 and 25 s within the infragravity frequency band. For energetic conditions, the spectral energy distribution resembles the pattern observed for calm conditions with peaks at similar periods but amplified by a factor 10. During the study period, the significant wave height in the marina reached a maximum value of $Hs_{max} = 0.98\ m$, lower than the value at PS0 $Hs_{max} = 1.7\ m$, but higher than the one computed at PS1 ($Hs_{max} = 0.7\ m$), the presure sensor deployed in front of the marina entrance. Energy in the short wave frequency band is low with a 95th quantile of Hs_{SW} equal to 0.06 m, and a maximum value reaching 0.29 m. The majority of the energy is concentrated in the long wave frequency band ($30\ s < T < 10\ min$), in which it reached a very high value equal to 0.92 m.

The marina NOP were computed with the Refonde numerical model to compare with the dominant peaks in the background spectrum. In the computations, the open sea boundary is prescribed as a 100 m-radius circle centered on the marina entrance. In order to further analyze the functioning of the marina, complementary simulations were also carried out (results not shown here), which consisted in study each basin individually keeping an open boundary condition at the basins junction. The results of the computation show that the marina fundamental mode of oscillation (mode 0) or Helmholtz mode, has a period equal to 318 s that is close to the peak 320 s (figure 4.4). For this mode, a node is located at the entrance and an anti-node on the right bank of the right basin where the PS4 sensor was installed. The second peak 120 s is in the proximity of the second eigen mode, mode 1 (111 s). This mode is close to the fundamental mode of oscillation 99 s of the left basin functioning as an open-ended basin. The resonance of the left basin forces oscillations in the right one with two anti-nodes located on the opposite sides

of each basin and a node in the connection zone (figure 4.4). The third and forth NOP of the marina are similar to the two other energy peaks (80 s and 45 s). This two NOP correspond to the fundamental mode of oscillation of the right and left basins respectively, functioning as closed basin. Periods of energy peaks on the background spectrum, close to the eigen mode periods of the marina, are characteristic of external forcing amplification by a semi-closed basin geometry (Thotagamuwage and Pattiaratchi, 2014b). This results in Hs_{IG} and Hs_{VLW} values higher inside the marina than at PS1 located at the opposite river side in front of the marina entrance.

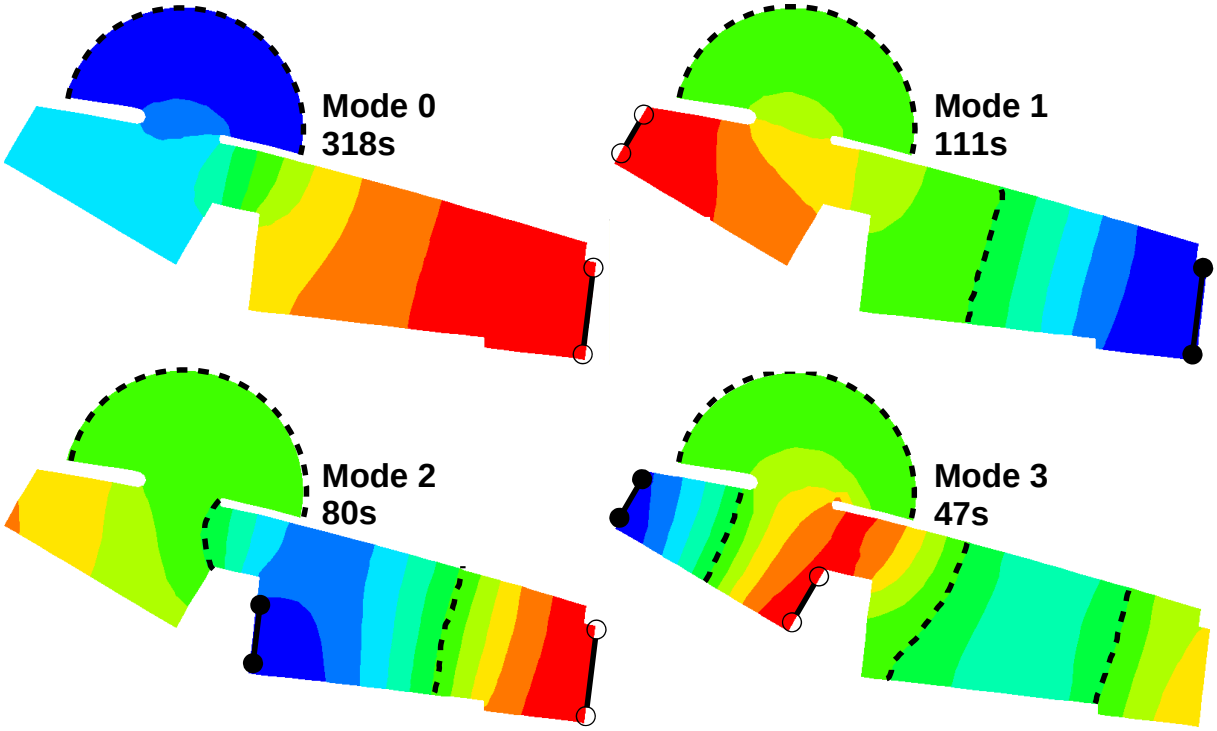

Figure 4.4 – The first four marina NRM: (circle-ended line) anti-node (filled and unfilled circles indicate anti-nodes out of phase) and (dashed line) node of the standing wave. An open sea boundary condition is applied at the 100 m-radius circle centered on the marina mouth and a closed boundary condition is applied otherwise. Water level = MSL. Color scales represent relative vertical oscillation amplitudes: amplitude is zero at a node and $|1|$ at anti-node with 1 and -1 for two anti-nodes out of phase.

4.4.3 Influence of water level and tidal phases

Influence on energy distribution along river

Water elevation data were filtered to study the influence of tidal level and river flow direction on the level of energy in the IG frequency band and its distribution between the IG1 and IG2 bands. Tidal signal, measured at the tidal gauge located near the river

mouth, was used to identify the different tidal stages in the all data base: high and low tides correspond to local extrema; flood and ebb tides correspond to an increasing or a decreasing of the signal respect to the average water level (2.65 m).
In a second step, average power density spectra were computed for series of 2 hours water elevation samples centered on high and low tides, and mid-tide during ebb and flood. For each pressure sensor, the mean significant wave heights in IG frequency band and in the two bands IG1 and IG2 were then computed and compared with the mean values computed over the entire time series. 10% of the most energetic events in terms of Hs were retained in order to target large port oscillations events while keeping a good statistical significance.

The mean significant wave heights of short waves ($T < 20\ s$) computed at the river mouth (PS0) are smaller at low tide ($Hs_{5\text{-}20s} = 0.47m$) than at high tide ($Hs_{5\text{-}20s} = 0.59m$) (figure 4.7). On the opposite, we noticed that IG waves have more energy at low tide (figure 4.5). Looking in more details, the amount of energy is higher in the IG2 band than the IG1 band. This difference is more pronounced at low tide. At locations PS1 and PS2, energy is still higher at low tide. Indeed, differences between Hs_{IG} computed at low and high tide remain fairly constant, equal to 16% for the two upstream sensors while it is 14% at PS0. This trend is reversed at PS3 where the energy is slightly higher at high tide in the IG, IG1 and IG2 bands. While the energy levels at PS0 are higher at low tide for the IG, IG1 and IG2 bands, they all decrease upstream until they reach the same level as those calculated at high tide.

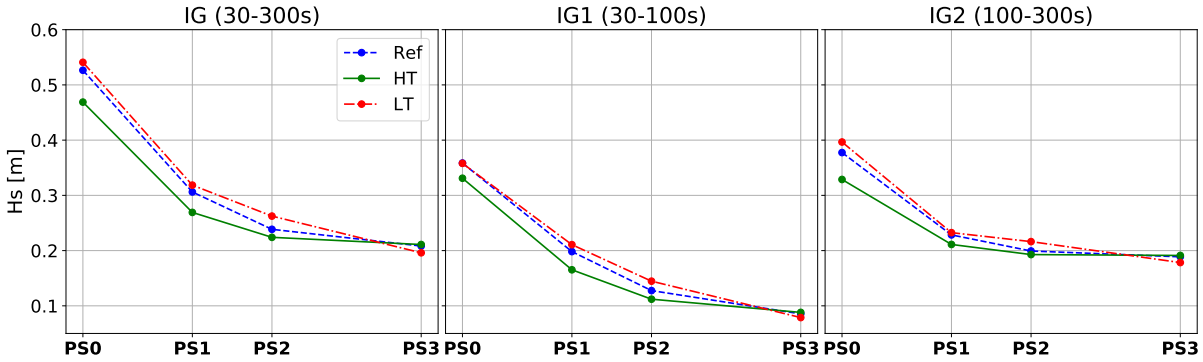

Figure 4.5 – Hs in infragravity frequency bands: IG, IG1 and IG2, calculated from figure 4.7. Influence of water level inside the channel harbor: (green, HT) high and (red, LT) low tide. The blue line (Ref) is the mean behavior considering all the data (reference scenario). The x-axis represents the distance between the sensors.

At the river mouth (PS0), the amount of energy in the IG band is independent of the tidal phase (figure 4.6). Similarly, Hs_{IG} does not vary between the ebb and flood tides in the IG1 band, as opposed to Hs_{IG2} that is smaller during ebb tide. Looking upstream,

we observe energy dissipation in the IG and IG1 bands whatever the phase of the tide. However, this decrease of energy is more pronounced during ebb tide when the long waves propagate against the river current. Focusing on the IG2 band, the upstream decrease of energy is only significant during ebb tide, while during the flood the energy is conserved between PS2 and PS3, which are 1.5 km apart.

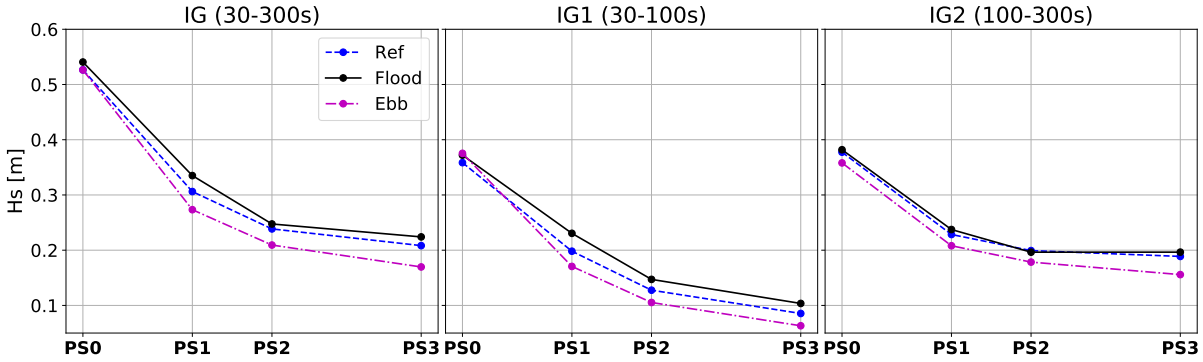

Figure 4.6 – Hs in infragravity frequency bands: IG, IG1 and IG2, calculated from figure 4.7. Influence of current: (black) flood and (magenta) ebb tide. The blue line (Ref) is the reference scenario. The x-axis represents the distance between the sensors.

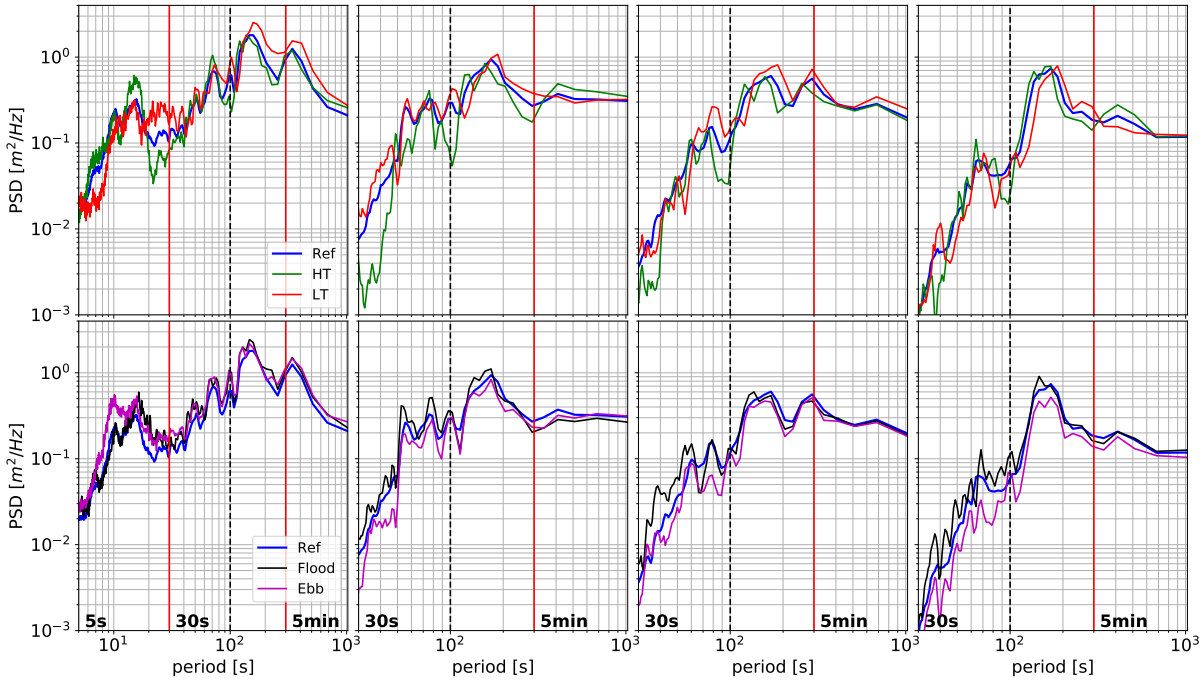

Figure 4.7 – Influence of water level inside the harbor (top panels): (green) high and (red) low tide. Influence of current (bottom panels): (black) flood and (magenta) ebb tide. The blue line is the mean behavior considering all the data (reference). Each column represents a river pressure sensor: from left to right PS0, PS1, PS2 and PS3. The 10% of the most energetic events (in terms of Hs) are considered for all scenarios.

Influence on the eigen modes of the marina

Power density spectra were also computed at PS4 for different water levels and tidal phases (figure 4.8). The overall patterns of energy distribution are similar at low and high tides with distinct energy peaks (figure 4.8, left panel). We also observe a shift of those peaks to lower periods at high tide. The tidal phase does not seem to influence the natural topographic response of the left basin of the marina where the PS4 sensor was deployed (figure 4.8, right panel). However, we notice an increase of energy during flood tide more or less pronounced for each peak.

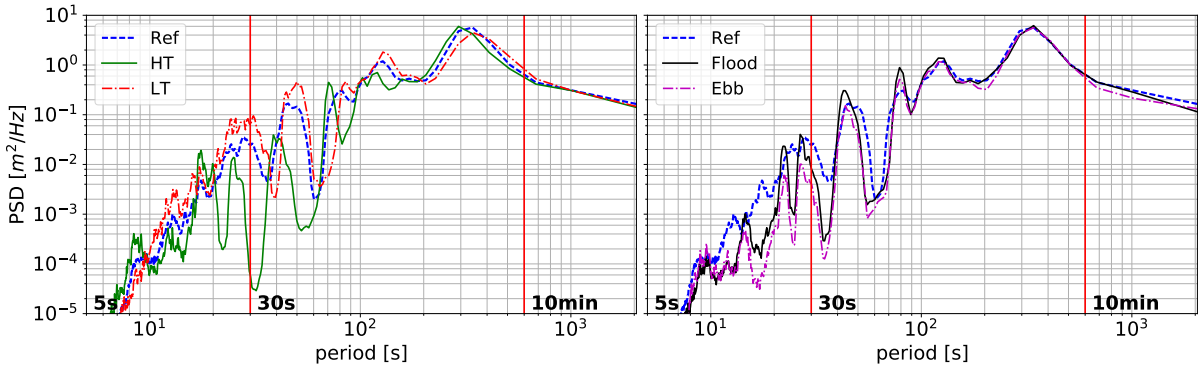

Figure 4.8 – PSD in the marina sensor (PS4): (blue) reference scenario; left panel (green, HT) high and (red, LT) low tides; and right panel (black) flood and (magenta) ebb tides.

4.4.4 Relation between long waves and incident waves

The significant wave height of incident bound infragravity waves Hs_{IG0}, computed from the wave buoy measurement using the Hasselmann's theory, was compared with energy computed in the IG band at the river mouth (PS0) to study the influence of offshore forcing to river harbor oscillations. Figure 4.9 shows strong positive correlation between Hs_{IG0} and $Hs_{IG,PS0}$ with the coefficient of determination r associated to the best linear fit revealing that 0.87% of the variability in $Hs_{IG,PS0}$ is determined by Hs_{IG0}. $Hs_{IG,PS0}$ variability is similarly explained by the offshore total significant wave height Hs ($r = 0.88\%$). The determination is improved when $Hs_{IG,PS0}$ is compared to swell significant wave height Hs_{swell} ($r = 0.93$), which indicates that IG waves at the river entrance are mainly forced by long period waves and that wind waves play a minor role on the water level oscillations.

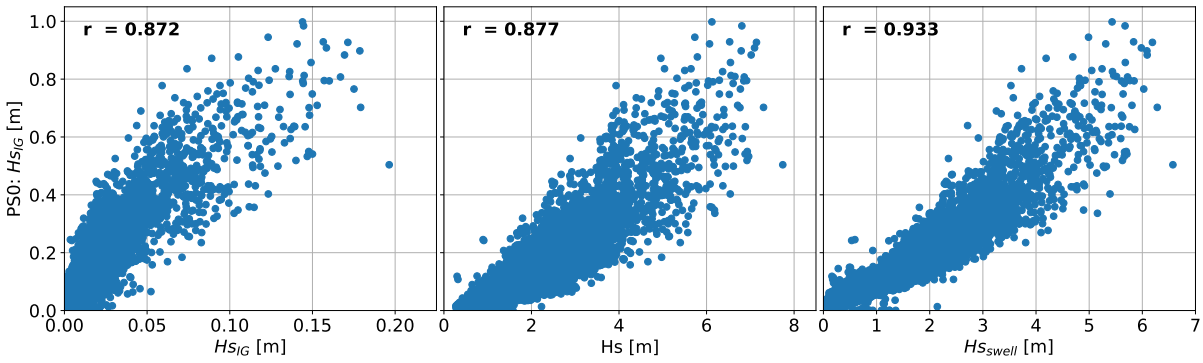

Figure 4.9 – Correlation coefficients between IG period oscillations at the river mouth (PS0) and offshore parameters: Hs_{IG}, bound IG amplitude; Hs, significant wave height; and Hs_{swell}, swell height ($p > 10$ s).

4.5 Discussion

This study is based on the analysis of an extensive set of water elevations data provided by local measurements carried out from the Adour river mouth up to the upstream part of Bayonne port. These measurements are complemented by offshore wave measurements that provide informations on incident wave forcings for various climatic conditions. The combination of these two set of data allows to point out the role of infragravity waves on the oscillation of both the marina and the channel harbour. However, the results of the field campaigns do not allow to analyze the mechanisms of incident long waves transformation during their nearshore propagation and their entering in the river. Nor do they fully explain the energy distribution in the infragravity frequency band at the river entrance and its evolution during the upstream propagation of the long waves. In this section, the results are discussed in relation to previous studies in order to improve the understanding of IG waves contribution to the functioning of both the marina and the channel harbor in a seaport configuration.

4.5.1 Marina oscillations

The pressure sensor measurements carried out in the marina at one location allowed to identify a series of energy peaks in the infragravity band. The measurements also highlight that the frequency of those peaks can vary with the tide. This result is consistent with the Merian's formula that shows that the eigen period of a semi-enclosed basin is inversely proportional to the square root of the water depth of a basin. While this formula can be applied to relatively simple basin, it is inappropriate to describe the complete functioning of complex geometric configurations like the marina. Indeed, the marina is divided into two connected basins that can interact with each other. In this case, our study confirmed that numerical modeling is necessary to separate the oscillation modes specific to each basins, to those corresponding to the coupling between them. Thus, the numerical simulations showed that the fundamental mode (period of ~5 min) corresponds to a semi-closed configuration of the whole basin, while the other higher modes, with smaller periods, correspond to coupled basin configurations. Consequently, a specific resonant mode of one basin will generate oscillations in the other. This finding is consistent to other studies performed on harbor with similar configurations (Thotagamuwage and Pattiaratchi, 2014b; Asano et al., 2010). Furthermore, the study highlighted that during offshore energetic conditions, the external IG wave forcing is amplified by the basin geometry, which can induce the generation of very large seiche events (maximum measured Hs up to ~1 m). The results of the numerical model indicate that the river may have a minor contribution on the marina behavior. Indeed, in the model set-up the open bound-

ary condition representing the marina entrance corresponds to an open sea condition, which is equivalent to ignoring the presence of the river. Despite this simplification, the eigen mode periods given by the model are very close to those visible on the background spectrum of the marina derived from the measurements.

4.5.2 Channel harbor oscillations

The measurements carried out along the river allowed to assess the efficiency of the defense structures of port of Bayonne to dampen incident short waves. Indeed, the study shows that incident short wave energy is reduced by ~90% at the sea port entrance (PS0). The remaining energy in the short wave period band is then quickly dissipated, the mean Hs_{SW} decreasing from 1.2 m at PS0 to 0.20 m at the first downstream quay of the commercial port (PS1). The study also highlighted that IG waves (30-300 s) control port agitation and represent about 80% of the variance of the free surface. During storm conditions, incoming IG waves can be very energetic and Hs_{IG} can reach values up to 1.0 m at the river mouth. As they enter the port, the IG waves propagate freely, without amplification, in the river, which acts as a wave guide. The measurements do not show the presence of a cross resonance phenomenon that could occur between river banks (Rabinovich, 2009). Assuming that the cross-section of the river is represented by a closed basin of 300 m long and 10 m deep, according to the Merian's formula, the period of the fundamental mode of the cross-section would be 60 s. It is reasonable to consider that if this phenomenon occurs it will be marginal and not very prejudicial to moored vessels.

4.5.3 Assessment of harbor operation conditions

Harbor structures are generally designed according to acceptable maximum harbor oscillations, defined in terms of Hs_{SW}, in order to guarantee safety conditions for harbor operations. Thus, in harbors, it is usually admitted that large boats can accept Hs_{SW} about 0.40 m for fishing boats and 0.70 m for general cargo (Thoresen, 2003). Recreational boats only tolerate Hs_{SW} of about 0.15 m. According to our study, these criteria are met in the navigation channel from the first quay. However, excessive surge movements of cargo-type moored vessels have occurred on several occasions (figures 2.9 and 2.10) causing a cessation of loading operations and sometimes leading to a sudden break in the mooring lines. If we consider a traditional mooring system, a typical natural period of a large ship would be around 1 min or slightly more, which is the infragravity frequency band. This suggests that incident IG waves penetrating in the port Bayonne can be responsible for the observed extreme surge motions of moored vessels. Considering the dissipation of energy in the IG period bands, this suggests that the upstream part of

the port, which is used as a retreat zone, is not totally safe. Indeed, the measurements at PS3 show that if the boat natural period is in the IG1 period band (30-100 s), vessel may be safe as dissipation of energy in this band is significant between PS1 and PS3. On the opposite, if the boat natural period is in the IG2 period band (100-300 s) the dissipation is much lower and the resonant phenomenon may occur. In the latter case, boat relocation would be inefficient as the boat will still be exposed to long wave forcing, even at 3.7 km from the river mouth.

4.5.4 Incident IG waves

During the study periods, wave conditions were dominated by energetic swells with long periods (between 14 and 20 s) and narrow banded energy spectrum. These wave conditions are favorable for the generation of bound IG waves (Okihiro et al., 1992). Indeed, Hs_{IG} of several dozen centimeters were estimated from the wave buoy measurements carried out in 50 m depth (figure 4.9).

Dominant IG wave generation mechanism

Previous studies have shown that the normalized bed slope β_b (equation 4.6) is a good indicator to identify the dominant mechanisms for the generation of IG waves (Battjes et al., 2004). Indeed it was shown that for $\beta_b < 0.3$ the shoreline has a mild-slope regime for which the bound wave shoaling mechanism is dominant over the moving breakpoint mechanism (Van Dongeren et al., 2007).

$$\beta_b = \frac{h_x T}{2\pi}\sqrt{\frac{g}{h_b}} \tag{4.6}$$

where h_x is the bed slope, T is the period of IG (or low-frequency) waves and h_b is the mean breaking depth.
Considering a cross-shore profile representative of the offshore bathymetry between the wave buoy (50 m) and the head of the North breakwater we have computed β_b to determine the dominant IG waves generation process in the nearshore zone. The slope of the considered profile is very gentle (0.7%). Considering that wave breaking is depth controlled, we consider that $h_b = 10\ m$, which is the depth right in front of the north breakwater. If we take the upper limit of IG wave band $T = 300\ s$, we can compute the maximum $\beta_{b,max} \approx 0.33$ from equation 4.6. This maximum value, close to 0.3, suggests that in our configuration the shoreline has a mild-slope regime indicating that the generation of IG waves during the incident waves propagation toward the river mouth is dominated by non-linear energy transfers.

Shoreward propagation of IG waves

When wave groups propagate shoreward on sloping bottom, energy are transfered from short waves to the bound IG wave due to a phase lag occurring between the short wave envelope and the bound IG wave. The resulting growth in amplitude of bound IG wave appears to be frequency dependent (Battjes et al., 2004; de Bakker et al., 2013) (section 1.3.1). The phase lag increases with higher short-wave peak periods and with lower water depths, but the effects of the group period and the bottom slope are not unequivocal (Guérin et al., 2019). Considering the 0.7% average slope of the nearshore zone, the phase lag is expected to increase with higher incident group periods during the shoaling phase (Guérin et al., 2019, figure 8). As a consequence, the growth in amplitude of the bound IG waves should be higher for IG2 band than for IG1. In the surf zone, the incoming IG waves can still receive energy from short waves through nonlinear energy interactions (section 1.3.2). For gentle bed slope, energy transfers can occur from high to low IG frequencies, in other word from IG1 to IG2 periods (De Bakker et al., 2016b) (figure 1.9). Despite a lower offshore bound IG amplitude, IG2 seems to have a higher amplitude growth rate during the shoaling phase due to a higher phase lag between the short wave envelope and the bound IG wave (Guérin et al., 2019). In the surf zone, energy transfer still occurs from SW to IG waves, and potentially from IG1 to IG2 (De Bakker et al., 2016b) which would further increase the energy differences between these two period bands.

Other parameters: water level variation and ambient current

Water level variation due tidal modulation affects the dynamic of IG2 waves whose spectral energy and period increase at low tide (figure 4.7, PS0). At the head of the North breakwater where short waves are considered starting to break, the shoaling zone appears to be longer at low tide. In addition, the local reduction in water depth caused by the deposit of dredged material increases wave non-linearity and could favor this phenomenon. Unlike IG2 waves, IG1 is not very affected by tidal modulation (figure 4.7, PS0), except for the 20-40 s period band where strong differences are visible during high and low tides. This phenomenon, independent of the river current, is probably due to local amplification effects and seems to be controlled by a threshold water level at high tide.

The ambient current seems to have a limited impact on the generation of IG waves (figure 4.7). The nearshore current is mainly generated by the tide and the river that flows into the ocean. On the one hand, the magnitude of spring tidal currents during flood and ebb tides is about 0.03 m/s in the study area (Idier and Pedreros, 2005). On the other hand, the river flows into the ocean and the northern breakwater tends to direct the current southward (figure 2.4), which affects its amplitude in the nearshore zone.

Thus, the nearshore currents are too weak in the area of generation and propagation of IG waves to affect them.

4.5.5 Transformation of IG waves along the river

The measurements carried out in the river channel have shown that the incident IG waves gradually loss energy as they propagate upstream from PS0 to PS3. At the river mouth most of the short waves energy is dissipated by breakwaters, so nonlinear energy transfers from SW to IG waves reduce, and IG waves no longer gain energy by this phenomenon once in the river: they propagate as free waves and gradually dissipate.

Wave transformation in the converging zone: between PS0 and PS1

Regardless of IG period band (IG1 or IG2) and tidal phase, the largest decrease in Hs between two consecutive points is observed between PS0 and PS1, about 1 km apart: Hs_{PS1} is between 50 and 60% of Hs_{PS0} (table 4.4, figures 4.5 and 4.6). This decrease can be partially explained by the river width variation between PS0 and PS1. Indeed, the river width is about 160 m and 260 m at PS0 and PS1, respectively and wave energy (i.e wave height) will adjust to geographic variations (i.e. river cross-section) in order to maintain a constant energy flux between PS0 and PS1. This can be substantiated by considering the (F) energy flux for long waves that propagate in an open-channel (Green, 1838; Holthuijsen, 2007):

$$F = E\|\overrightarrow{c_{g,rel}} + \vec{U}\|b \tag{4.7}$$

where E is the wave energy per unit crest length and per unit time, $\|\vec{c}_{g,rel} + \vec{U}\|$ is the transport velocity of the wave energy and b is the cross-section width. E is equal to $1/8\rho g H^2$ where ρ is the water density, g is the gravitational acceleration and H is the wave height. $\overrightarrow{c_{g,rel}}$ is the relative group velocity vector ($\overrightarrow{c_{g,rel}}$ is taken normal to the wave crest and its magnitude is $\sqrt{gh}$), $\vec{U}$ is the depth-averaged ambient current velocity vector.

The ambient current is firstly neglected ($\|\vec{U}\| = 0$) as the reduction in Hs is observed regardless of tidal phase. The river bottom slope being very low, the water depth is considered identical at PS0 and PS1. The wave energy transport velocity is therefore the same at both points. Assuming that the energy flux is conserved between PS0 and PS1, the channel section variation should induce a 20% upstream decrease in Hs. This value, lower than the observations, suggests that a loss of wave energy occurs between these two points. In addition to friction dissipation, the spatial configuration of the river mouth may also contribute to wave energy dissipation. The convergent and the waterway are inclined at ~16° and this angle promotes the propagation of incoming waves toward concrete artificial beaches (figures 2.7 and 2.8), which may also contribute to the

dissipation of entering IG waves.

Effect of the current. In order to specifically study the effect of river current on wave transformation, measurements during flow and ebb tides, whose average water level is identical, are used (figures 4.6 and 4.7). At PS0, significant wave height of incoming IG waves (i.e wave energy) is comparable at flood and ebb tide. However, the Hs decrease between PS0 and PS1 is higher during ebb than flood tide. As the water level variation amplitude is comparable for the considered ebb and flow events, it is reasonable to assume that the dissipation rate should be about the same. We therefore assume that the observed differences of Hs are related to the river current, and especially its propagation direction. Indeed, an ambient current modifies the wave energy transport velocity (equation 4.7), and assuming a co-directional river flow, the wave energy flux is higher during flood ($\overrightarrow{c_{g,rel}} \cdot \vec{U} = 0$) than during ebb ($\overrightarrow{c_{g,rel}} \cdot \vec{U} = \pi/2$) for identical wave energy and current magnitude. So at PS0, the wave energy flux is greater during flood than during ebb tides. Moreover, the widening of the river cross-section at PS1 leads to a decrease in the current magnitude ($\|\vec{U}\|$). To conserve the energy flux between PS0 and PS1, the wave energy (i.e Hs_{IG}) will increase (decrease) during flood (ebb) to balance the decrease (increase) in the wave energy transport velocity. This increase of energy during flood could explain why the loss of energy is weaker than during ebb tide.

Doppler shift. In presence of an ambient current, the dispersion relation is affected by the Doppler shift (Holthuijsen, 2007) and transforms to:

$$\omega_a = \sigma + kU_n \tag{4.8}$$

where ω_a and σ are the absolute and relative angular frequencies (σ respects the linear dispersion relationship, $\sigma^2 = gk\tanh(kh)$), k is the wavenumber, U_n is the component of the current in the wave direction.

For the same absolute frequency (measured by a sensor), a current opposite to the waves propagation causes an increase in wave energy since the wave action $A = E/\sigma$ is conserved in the presence of a current field instead of the wave energy E.

At PS0, an energy increase is visible only for short waves during ebb tide; for $p > 30$ s, the ebb and flood spectra are very close (figure 4.7, bottom left panel). The Doppler shift mainly affects SW waves and has a little or no effect on long waves. Indeed, the wavenumber k is inversely proportional to the wave period according to the shallow water theory and becomes very low for IG period band considering the 10 m water depth of the river.

Upstream IG wave propagation: PS1 to PS3

During the upstream propagation in the river from PS1 to PS3, IG2 loses little energy in contrast to IG1 that undergoes a significant energy decrease (figure 4.3, center panel and table 4.4). This bi-modal behavior is not explicable by the conservation of wave energy flux in the river (equation 4.7), which modifies long wave energy regardless of period. Moreover, the river cross-section variation is low from PS1 to PS3 and its effects on wave energy are considered as a secondary process. The energy variation in the river is thus likely to be due to energy dissipation by friction or nonlinear energy transfers.

The river acts as a wave guide and its S-shape could favor wave energy concentration at river banks through combined effects of refraction due to river bathymetry and reflexion process. In addition, sediment accumulations caused by river processes induce a water depth reduction at river banks. These two phenomena lead to local wave non-linearity increases at river bank and potentially wave energy reductions that seem to affect IG1 more than IG2.

At PS0, incoming IG waves have more energy at low tide (mainly in IG2 period band); at PS3, the differences of PSD at high and low tides are very small and even IG energy is higher at high tide (figure 4.5). A lower water depth favoring energy dissipation and nonlinear energy transfers, energy decrease in the river is higher at low tide.
The differences in Hs observed at PS1 between flow and ebb tides are "conserved" between PS1 and PS3, except for IG2 at PS3 (figure 4.6). As the ambient current magnitude is low compared to the relative group velocity (equation 4.7) in the considered zone, differences in wave height remain identical between flood and ebb tides.

4.6 Conclusion

This study is based on an intensive measurement campaign conducted over 3 consecutive winters (2016-2019). Five pressure sensors were deployed in Port of Bayonne: one at the river mouth measuring the incoming waves, three in the Adour river (river seaport) to study the evolution of IG waves in the river and one in the marina recording the seiche. A directional swell buoy continuously measured the offshore agitation conditions. These data were used to study the intrinsic behavior of each harbor and their response to different external forcing scenarios: calm and energetic offshore incident waves, high and low tides, and flood and ebb. In addition, a numerical model, based on harmonic analysis method, was used to study the natural resonance mode of the marina.

Port of Bayonne is directly exposed to very energetic swells. At the harbor mouth, two main breakwaters effectively dampen the incident short waves (5-30 s). The remaining SW energy is strongly dissipated by the spatial configuration of the river mouth (expan-

sion area) and the navigation criteria in terms of Hs_{SW} are met in the channel harbor. The infragravity (IG) waves (30-300 s) control port agitation and represent the main part of the variance of the free surface (80%). As they enter the harbor, the IG waves no longer receive energy from SW waves and propagate freely without amplification in the river which acts as a wave guide.

A converging zone, characterized by a narrowing of the river cross-section, is present between the river mouth and the first harbor dock. The widening of the river section at the first dock leads to a decrease in wave energy (~20%) regardless of long wave period and tidal phase. Concrete artificial beaches located on both sides of the converging zone could also contribute to a further wave energy reduction. In the presence of an ambient current, the widening of the river cross-section leads to an increase in wave energy at the first dock when the direction of current and incoming waves is the same (i.e flood).

During the upstream propagation in the river, IG wave energy presents a bi-modal behavior between IG1 (30-100 s) and IG2 (100-300 s) period bands: IG1 undergoes a significant energy decrease, unlike IG2 that loses little energy. We suspect that the river geometry —channel S-shape and river bathymetry —is responsible for IG wave dissipation and has greater impact on IG1 than IG2 energy reduction.

The Marina is a semi-enclosed basin, and the periods of its fundamental (period of ~5 min) and harmonic modes are in the IG period band. The amplification of the energetic external forcing by the basin geometry can generate large seiche events ($Hs \approx 1\ m$).

The typical natural period of a cargo-type moored vessel is 1 min or more and can be in the IG period band. The resonance can lead to a significant surge motion of the boat (parallel to the dock) and possibly to a sudden snapping of mooring lines. Sometimes adopted by the port authorities, the retreat movement consisting in moving the vessel upstream can be insufficient if its resonance period is in the IG2 (100-300 s) period band. Indeed, as IG2 loses little energy during its propagation in the river, the boat can remain exposed even several kilometers from the river mouth.

Offshore incident energetic swells favor the generation of second-order bound IG waves. During the shoaling phase, the gentle slope of neighboring beaches allows to significant energy transfers from short wave to bound IG wave and therefore their growth in amplitude. In this mild-slope regime, the bound IG wave shoaling mechanism is dominant over the moving breakpoint mechanism for the generation of IG waves. The tide and river currents are too small in the bound IG waves generation area to have any impact. Despite a lower offshore bound IG amplitude according to Hasselmann (1962) theory, IG2 could have a higher amplitude growth rate during the shoaling phase due to a higher phase lag between the short wave envelope and the bound IG wave for this gentle bed slope environment (Guérin et al., 2019). In addition, the local reduction in water depth

caused by the deposit of dredged material could favor this phase lag and accentuate it at low tide. In the surf zone, energy transfer can still occurs from SW to IG waves, and potentially from IG1 to IG2 (De Bakker et al., 2016b) which would further increase the energy differences between these two period bands.

Chapter 5

Estimation of harbor oscillations from offshore bulk wave parameters

5.1 Introduction

In this chapter, we propose to study the oscillations of a series of French seaports located along the Atlantic ocean and the English channel. This work is based on the analysis of an extensive set of water elevation data provided by the French tide gauge network, called RONIM. It is part of a collaborative work performed with the SHOM that led to the writing of an article, currently under revision in the Natural Hazards journal (since May 2019). First, the data are analyzed to determine the periods of oscillations of harbors of different configurations and wave climate exposures, and compared with the natural modes of oscillations computed with REFONDE (section 4.3.3). Offshore wave characteristics computed at each site by the SHOM, with the spectral wave model WaveWatch III (WW3), are then used to study the contribution of incident bound IG waves to ports functioning. In the last section of the chapter, empirical formulations are developed and tested for each site, including port of Bayonne, to estimate harbor oscillations in the low frequency band based on offshore bulk wave parameters

5.2 Oscillation of seaports of the RONIM network

5.2.1 Study sites

The northern and western coasts of France offer a large variety of harbor configurations. They include military, commercial and fishing ports that differ in terms of size, type of protection, number of basins and level of exposure to ocean forcing. Along these coasts, the tidal range is generally high with a semi-diurnal tide ranging from macro-tidal to meso-tidal regimes. This study focuses on 16 harbors, belonging to the RONIM network, numbered in an anti-clockwise direction (figure 5.1). The French tide gauge network, called RONIM, is operated by the SHOM (Naval Hydrographic and Oceanographic Service) and covers a large part of the French metropolitan and overseas coasts. The network is now mainly composed of permanent radar tide-gauges, whose water level measurement time-series are available on the REFMAR website (`http://data.shom.fr`) with a 1 min period sampling. Although tide gauges are adapted to tidal measurement, we wanted to exploit the temporal and spatial extent of the data. Harbor characteristics are indicated in table 5.1. Average water depth (d) and mean sea level (MSL) in harbors are referenced to the chart datum (lowest astronomical tide). The tidal range (TR) is indicated for spring tides. The harbor geometry is described by the surface water area (S), the basin aspect ratio (q), defined as the ratio between the width (l) and the length (L) of a basin.

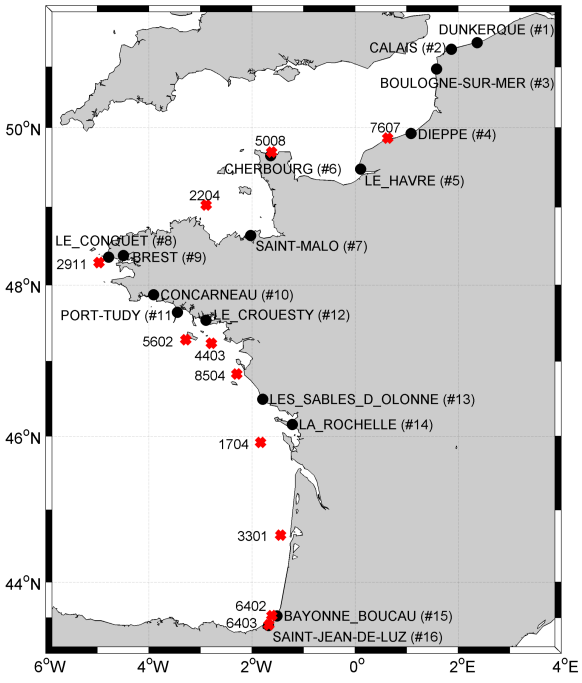

Figure 5.1 – Study site positions in black circle and wave buoys in red cross.

Hauts de France (#1-3) - North Sea

The three first harbors are characterized by a macro-tidal regime with tidal range that can reach up to 7.75 m (Boulogne-sur-mer #3). Their geometry is complex with a multitude of basins connected in permanence or only occasionally by locks. The eastern part of the port of Dunkerque (#1) is composed of a square outer port and a very elongated inner port (Trystram Channel). Port of Calais (#2) is composed of a deep water harbour and a smaller and shallower inner port (Bassin Henri Ravisse). Port of Boulogne-sur-mer (#3) is located in an artificial roadstead (Rade Carnot) and composed of a deep rectangular basin (quai de l'Europe). Wave exposure is highly dependent on harbor entrance orientation. The sea-state in this area is dominated by short waves, with wind wave of West-South-West and a residual swell of North, with periods which generally do not exceed 10 s. The significant wave height can reach 3 meters.

Normandie (#4-6) - English Channel

The harbors in this area are characterized by a macro-tidal regime with tidal range that can reach up to 8.5 m (Dieppe #4). The configurations of these 3 harbors are very different. Port of Dieppe (#4) is composed with an outer port connected with a small elongated channel to the marina and inner port. Port of Le Havre (#5), located in Seine river mouth, is very large and is composed of an outer port prolongated with 2 elongated basins in deep water. Port of Cherbourg (#6) is located in an artificial roadstead (Grande rade, S= 13 km^2). Harbor activities (military and commercial operations) are located in the Petite rade (S=2.8 km^2). The military area is composed of three rectangular basins: Napoleon III Basin, Charles X Basin and a fore-port, where the tide gauge is located. These 3 ports are located in the English Channel, where waves are generated by the local wind and are characterized by a high directional spread. Port #5 is mainly exposed to waves with directions West-north-west and North-west, while port #6 is exposed to waves with directions from East to West passing by North. In this area, maximum wave height and wave period can reach 4.5 m and 16 s respectively.

Bretagne (#7-12) - Celtic Sea

The harbors #7-12 are characterized by a macro-tidal regime: tidal range is mainly between 4.2 m (#10) and 5.9 m (#9) with a maximum value of 10.7 m for port of Saint-Malo #7. Port of Saint-Malo (#7) is located slightly downstream of a tidal power station in Rance river. It is composed of a small and shallow outer harbor providing access to basins through locks. Port of Le Conquet (#8), small and shallow, is located at the mouth of the Ria River (generally dry at low tide). Port of Brest (#9), located in a large natural

roadstead (Rade de Brest), is a large deep-water military port. The port is backed by the Penfeld River that is now closed upstream and channeled. Port of Concarneau (#10), small and shallow, is located in a bay (Baie de la Forêt). Small islands (Glénan Islands) are present offshore. Port-Tudy (#11), small and shallow, is located on the island of Groix between the island and the continent. A tidal basin is present in the port that is closed at low tide to keep boats afloat. Port of Le Crouesty (#12), also small and shallow, is located in the bay of Quiberon delimited by the peninsula of the same name and the Belle-île Island located offshore. These ports are subject to energetic swell whose main directions are West and West-north-west. Maximum wave height and wave period can reach values up to 13 m and 18 s respectively.

Pays de la Loire (#13) and Nouvelle Aquitaine (#14-16)

The last four southern harbors are located in the Pays de la Loire and Nouvelle Aquitaine. Except for the Bayonne harbor (#15) that is located along the Adour river, the three other harbors are semi-enclosed basins. The tidal regime is meso-tidal with a maximum tide range at La Rochelle (TR = 5.45 m). Port of Sables d'Olonne (#13) is composed of a narrow navigation channel giving access to two rectangular shallow basins and to a deeper tidal basin. Port of La Rochelle (#14), located behind the islands of Ré and Oléron, is a large deep-water port with a tidal basin. Port of Bayonne-Boucau (#15) is a deep-water channel harbor located near the mouth of the Adour River. Port of Saint-Jean de luz (#16) is a small marina located in a bay (S=2 km^2) sheltered by breakwaters. This part of the Atlantic coast is mainly exposed to West-north-west wave with maximum significant wave heights and wave periods reaching more than 8 meters and 18 s offshore from the island of Oléron.

5.2.2 Tide gauge data analysis

Seven years of tidal gauge measurement data, from the 1^{st} of December 2009 to the 1^{st} of April 2017, were selected (figure 5.2). Sea level measurement are first filtered using a 2 hours Butterworth high-passed filter in order to suppress tidal signal. The resulting sea level high-frequency oscillations represent agitation within the long wave (LW) frequency band corresponding to common eigen periods of harbors and bays (2 min $\leq$ T $\leq$ 100 min). A data cleaning method was carried out to remove spikes and gaps present in the measurement. Spikes are identified and suppressed when data exceed three times the standard deviation computed over 2 hours. Gaps lower than one hour are filled by a cubic spline interpolation. Usually, this automatic method works quite well, but some sea-level data required the removing of long measurement periods displaying too many spikes and

Harbours	MSL (m)	TR (m)	Basins name	S (km^2)	L (km)	q	d (m)
Dunkerque	3.24	5.45	Outer port	0.90	1.0	0.90	13.5
			Trystram Channel (TG)	0.36	1.9	0.10	6.0
Calais	4.03	6.50	Deep water harbour	0.73	2.2	0.15	9.0
			Bassin Henri Ravisse (TG)	0.23	1.25	0.15	9.0
Boulogne	4.91	7.75	Artificial roadstead	4.35	2.2	0.90	7.5
			Deep water harbour (TG)	0.3	1.0	0.30	7.5
Dieppe	4.94	8.55	Outer harbour (TG)	0.34	1.5	0.15	4.5
Le Havre	4.96	6.75	Deep water basins	1.44	3.0	0.16	14.0
			Outer harbour (TG)	0.30	0.75	0.53	10.0
Cherbourg	3.87	5.30	Grande rade	12.8	8.0	0.20	7.5-13.5
			Petite rade	2.81	1.5	1.25	7.0
			Fore-port (TG)	0.06	0.25	1	7.0
Saint-Malo	6.76	10.7		0.21	0.65	0.50	4.0
Le Conquet	3.98	5.75		0.10	0.4	0.65	2.0
Brest	4.13	5.9	Rade de Brest	170.0	17-25	0.6-0.3	17-50
			Military port	2.70	3.0	0.30	11.0
			Penfield river (TG)	0.31	2.5	0.05	8.0
Concarneau	3.06	4.2		0.35	1.0	0.35	4.0
Port-Tudy	3.19	4.25		0.04	0.3	0.45	2.5
Le Crouesty	3.29	4.55		0.20	1.0	0.20	2.0
Les Sables d'Olonne	3.2	4.45		0.43	1.7	0.15	2.0
La Rochelle	3.9	5.1		0.4	1.0	0.4	9.0
Bayonne-Boucau	2.53	3.5	Channel harbour (TG)	2.11	6.5	0.05	8.0
Saint-Jean de Luz	2.51	3.75	Bay (TG)	1.90	1.9	0.53	5.0
			Socoa marina	0.02	0.27	0.25	1.0

Table 5.1 – Harbour characteristics: (MSL) mean sea level and (TR) spring tide range; for each basins: (S) surface water area, (L) length, (q) basin aspect ratio, and (d) depth respect to the chart datum, (TG) tide-gauge location basin.

dating errors, such as Calais, Les Sables d'Olonne and Saint-Jean de Luz tide gauges. Moreover, the tide-gauge of Boucau-Bayonne is subject to siltation of the stilling well that perturbs measurements at low tide. These low tide data are suppressed, reducing drastically available data for this harbor.

From the filtered and cleaned sea-level data, power density spectra (PSD) are calculated over 4 consecutive days, using a Hanning window with a 50% overlapping data. Significant wave heights (H_{LW_h}) are calculated from these PSD in the 2-100 min period band according to equation 3.14. In addition, Hs in the 2-7 min period band (H_{LF_h}) is computed to estimate the contribution of (LF) low frequency waves. Background spectrum is computed by averaging the PSD observed during calm periods, which are identified when Hs is lower than the ($H^{95}_{LW_h}$) 95^{th} quantile of Hs time series. These averaged spectra highlight the main resonant modes for each site and are used to identify the dominant seiche periods. Similarly, energetic spectrum is computed by averaging the PSD observed during the most energetic conditions, which are identified when $H_{LW_h} > H^{95}_{LW_h}$.

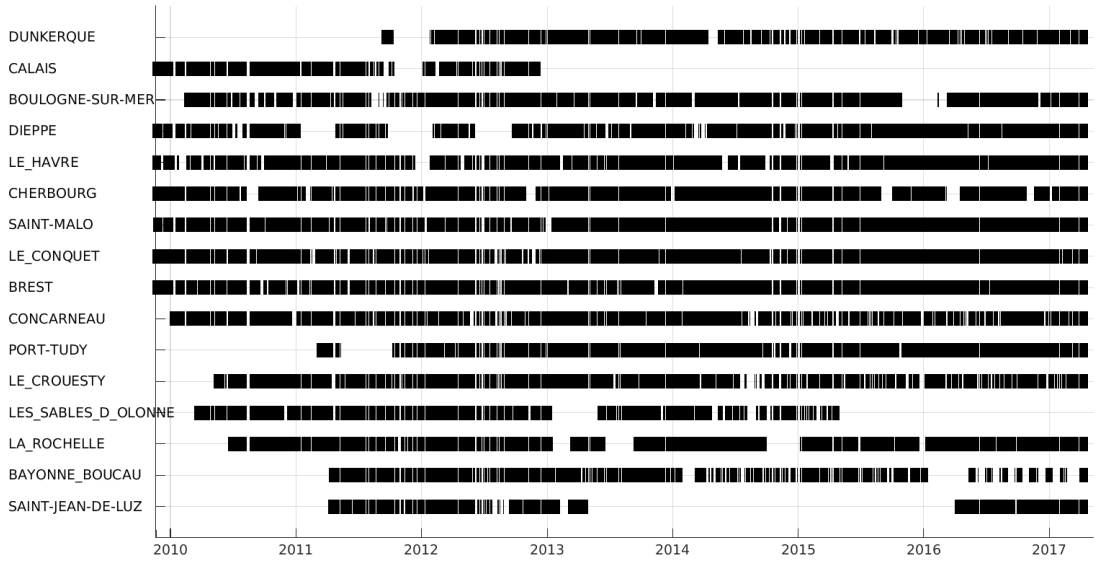

Figure 5.2 – Available tide-gauges sea-level data measurements.

5.2.3 Determination of harbor resonant periods

Figure 5.3 presents for each site the background energy spectrum, the total averaged spectrum and the energy spectrum computed for the most energetic conditions. Resonant periods highlighted on the background spectra appear as broadened peaks. This is explained by the large range of tidal sea-level variations, which can reach up to 10 m during spring tides in this macro-tidal area, and affect basin resonant periods. Resonant periods determined from the spectral analysis give characteristics of sea level oscillation frequencies only at the location of the tide gauge. To assess whether the tide gauge was representative of the basin behavior, basin eigenmodes were determined with the Refonde numerical model (section 4.3.3). The model was applied to most of the study sites except for Dieppe, Saint-Malo, Le Conquet and Concarneau for which no accurate bathymetry was available and for port of Bayonne, located inside a river, for which no upstream reflected boundary condition can be defined. Computed eigen periods are consistent with those identified with spectral analysis, although some resonant periods are not detected on spectral analysis due to specific tide-gauge location. Resonant periods for the first four eigen modes issued from numerical modelling are available in the table 5.2.

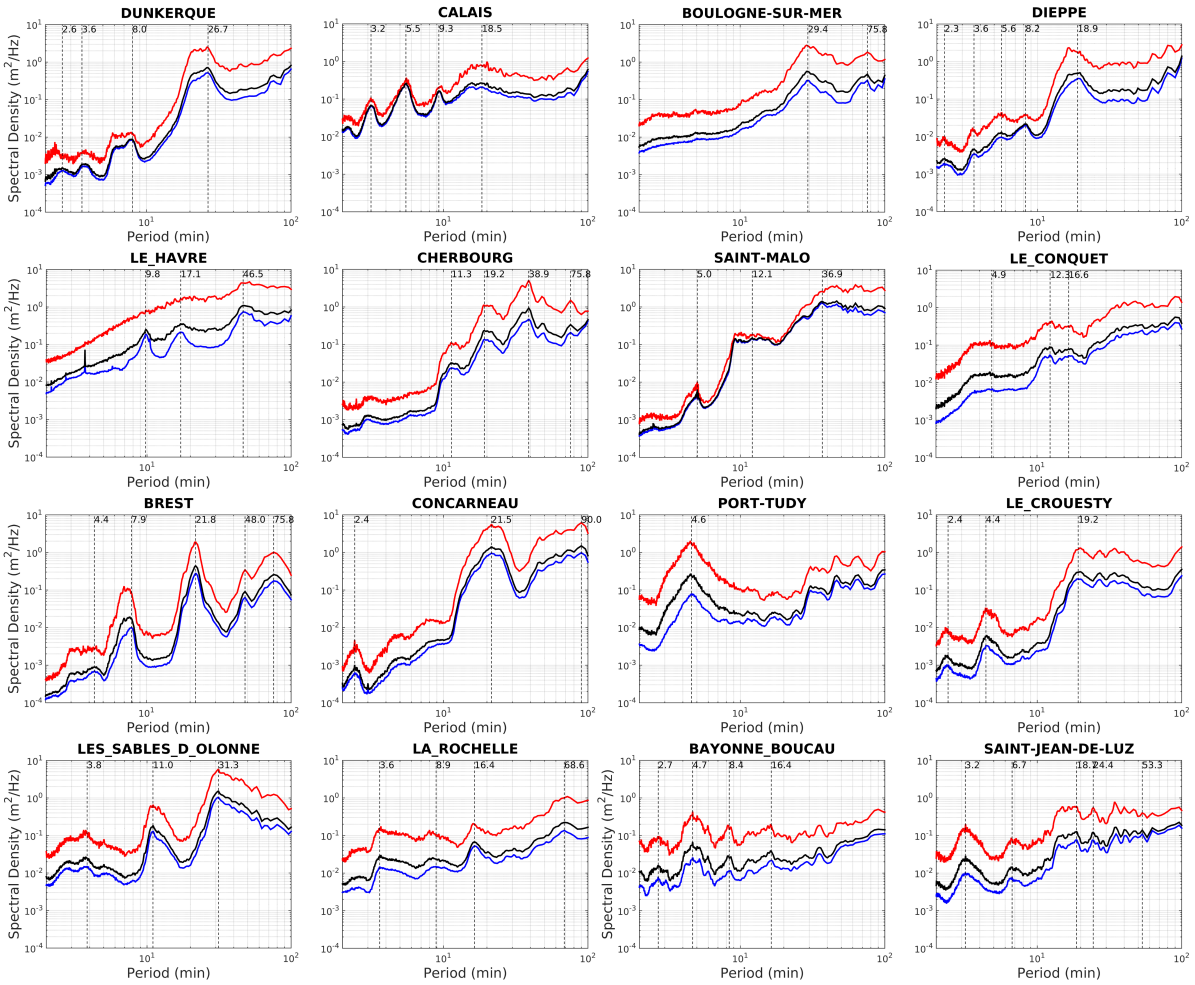

Figure 5.3 – Averaged power density spectra computed over 4 days (Total in black), during calm weather condition (Background in blue) and energetic condition (red).

Spectral energy distribution depends on harbor configuration. Power density spectra show that harbors with a large part of energy in ($2\ min \leq T \leq 7\ min$) LF frequency band are relatively small-scale harbors as Le Conquet ($L = 400\ m$), Port-Tudy ($L = 300\ m$), or deep-water harbors as Calais ($d = 11.5\ m$), Le Havre ($d = 10\ m$), La Rochelle ($L = 1000\ m$ and $d = 9\ m$) and Bayonne ($d = 8\ m$). Larger scale and shallower harbors, as Dunkerque, Dieppe or Brest, show a large part of energy in the very long frequency (VLF) band ($7\ min \leq T \leq 24\ min$). Some of identified resonance modes are not due to harbor basins but to the neighboring environment that can induce longer resonant periods ($T > 24\ min$). This is the case for ports of Boulogne-sur-Mer and Cherbourg located in artificial roadsteads, port of Brest settled in a natural roadstead, and ports of Concarneau, Le Crouesty and Saint-Jean de Luz positioned in bays. For open estuary harbors, as Bayonne, oscillation periods are not due to along-estuary basin resonance but rather to local resonances. The simple and small scale configuration of Port-Tudy induces

Harbours	$H_{LW_h}^{95}$ (cm)	$H_{LW_h}^{max}$ (cm)		Eigen periods (min)				
				mode 1	mode 2	mode 3	mode 4	mode 5
Dunkerque	11.2	92		26.7			6.3-7.9	3.6
				23.8	*9.6*	*7.3*	*6.5*	
Calais	14.8	67		18.5	9.3	5.5	3.2	
				12.3	*8.6*	*4.8*	*3.9*	
Boulogne-sur-Mer	12.4	82	75.8	29.4				
				19.6	*13.5*	*10.6*	*9.4*	*7.2*
Dieppe	12.8	52		18.9		3.6-8.2	2.2	
Le Havre	17.6	122		46.5		17.1	9.8	
				46.5	*16.6*	*10.3*	*8.6*	*6.4*
Cherbourg	11.2	89	38.9	19.2	11.3			
				27.0	*16.5*	*14.0*	*12.1*	*9.7*
Saint-Malo	17.1	50	36.9	9.0-14.0	5.0			
Le Conquet	12.1	67		12.3-16.6		4.8		
Brest	7.6	38	75.8 48.0	21.8			7.7	3-4.4
			134.0 56.0	*20.1*	*15.8*	*8.2*	*6.9*	*5.9*
Concarneau	18.6	70		21.5			2.4	
Port-Tudy	17.1	112		4.6				
				4.9	*2.6*	*1.8*	*0.9*	
Le Crouesty	10.4	48		18.9		4.5	2.4	
				17.9	*6.1*	*4.7*	*2.8*	*2.2*
Les Sables d'Olonne	16.6	61		31.3	11.0		3.8	
				32.3	*12.0*	*6.4*	*5.5*	*3.9*
La Rochelle	10.0	39	68.6	16.4	8.6		3.6	
				17.1	*5.7*	*3.2*	*1.9*	
Bayonne-Boucau	14.6	38		16.4	8.4	4.7	2.7	
Saint-Jean de Luz	10.2	28	31.0 24.0	16.0-18.7		6.7		3.2
				11.2	*7.0*	*5.8*	*4.7*	*3.7*

Table 5.2 – Long wave significant height maximum ($H_{LW_h}^{max}$) and eigen periods computed for each harbors from spectral analysis and numerical model (in italic), the first column corresponds to resonance of neighboring environment.

a unique broadened peak on the background spectrum, which is centered around 4.6 min and extending from 3 to 6 min. PSD of Saint-Malo presents a significant amount of energy in the VLF, which is unexpected for this small-scale harbor ($L = 325\ m$). A tidal power plant located slightly upstream of the harbor could have an influence on harbor oscillations.

5.2.4 Mechanisms for generation of harbor oscillations

Nearshore spectral wave model

Offshore wave characteristics are determined for each site at a point located slightly further offshore in front of the harbor entrance with the third generation spectral wave model WaveWatch III® v4.18 (WW3) (Tolman et al., 2014). Waves buoys measurements whose positions are presented in figure 5.1 are used to validate the WW3 model results by comparing modeled sea state parameters (H_s and $T_{m0,1}$) with waves buoys measurements, from the 1^{st} of October 2013 to 31^{st} of March 2017. The validation is based on statistic values and the comparisons show the ability of WW3 to reproduce short-waves characteristics. Scores for H_s show generally coefficients of determination (r^2) higher that 0.8. For $T_{m0,1}$, results are particularly weak for buoys 7607 and 5008 with respective r^2 of 0.54 and 0.47 (figure 5.1). These results show that short wave periods occurring in the English Channel mainly driven by wind sea are not well reproduced by WW3. For the other points, scores for $T_{m0,1}$ are good with r^2 greater than 0.80.

Role of incident bound IG waves

Incident bound IG waves energy is estimated from the offshore wave spectra using the method of Okihiro et al. (1992) based on the second-order nonlinear theory of Hasselmann (1962) (section 3.2.5). Modeled gravity wave spectra are interpolated along $\delta\theta = 5°$ and $\delta f = 1/300\ Hz$. The (H_{IG_i}) incident IG waves significant height is given by integrating bound IG energy over the IG period band (30 s-5 min). Correlation coefficients between H_{IG_i} and H_{LW_h} (2-100 min) are given in table 5.3. Results generally show poor correlations, except for the small-scale harbor of Port-Tudy with a significant correlation coefficient of 83% and, to a lesser extent, for Le Havre, Le Conquet, La Rochelle and Bayonne with correlation coefficients about 75%. On the opposite, correlation coefficients between H_{IG_i} and harbor significant wave height H_{IG_h} (2-5 min) give much better results in most cases than considering H_{LW_h}. They reach 80% (table 5.3) for Le Conquet, Brest, Port-Tudy and Les Sables d'Olonne. Correlation coefficients computed using H_{LF_h} are quiet similar and sometimes better than with H_{IG_h}. These results show clearly that harbor oscillations in the IG band are mainly induced by incident bound IG waves forced

by short waves, but also that the influence of bound waves can be extended to the Low Frequency band (LF) up to 7 minutes depending on harbor resonant periods. This results was previously assessed by López et al. (2012) and Gawehn et al. (2016).

Harbors	Correlation coefficient (r)				
	LW 2-100min	IG 2-5min	LF 2-7 min	VLF 7-24 min	ULF 24-100 min
Dunkerque	0.43	0.45	0.48	0.43	0.35
Boulogne-sur-Mer	0.59	0.77	0.78	0.60	0.43
Dieppe	0.57	0.70	0.72	0.47	0.55
Le Havre	0.73	0.65	0.71	0.71	0.67
Cherbourg	0.54	0.77	0.78	0.50	0.51
Saint-Malo	0.28	0.49	0.44	0.14	0.28
Le Conquet	0.73	**0.82**	**0.83**	0.72	0.48
Brest	0.68	**0.83**	0.78	0.64	0.57
Concarneau	0.48	0.72	0.75	0.45	0.43
Port-Tudy	**0.83**	**0.82**	**0.82**	0.78	0.62
Le Crouesty	0.60	0.74	0.79	0.45	0.50
Les Sables d'Olonne	0.71	**0.80**	**0.81**	0.71	0.49
La Rochelle	0.76	0.71	0.72	0.69	0.63
Bayonne-Boucau	0.76	0.70	0.71	0.77	0.68
Saint-Jean de Luz	0.63	0.55	0.55	0.61	0.51

Table 5.3 – Correlation coefficient (r) between H_{IG_i} and harbor significant wave height in different period bands. Correlation coefficients higher than 0.8 are in bold.

5.3 Estimation of harbor oscillations using offshore wave parameters

In the previous section, it was shown that small harbor oscillations are strongly correlated with incident IG bound waves. In the following, we propose to develop an empirical formulation based on the Bowers (1993) formulation to estimate those oscillations directly from offshore wave statistical parameters. The approach relies on the determination of a set of optimal free parameters by seeking the best agreement between the (H_{-_p}) predicted significant wave height and (H_{-_h}) those measured in the harbor with the tide-gauges. Symbol '_' refers to the frequency band (LF or LW) thereafter considered for harbor significant wave heights used to adjust the empirical formulation. This relation is given by :

$$H_{-_p} = k\frac{H_s^{\alpha}T_{m0,1}^{\beta}}{d^{\gamma}}, \tag{5.1}$$

where the offshore incident wave characteristics are the (H_s) significant short wave height, the ($T_{m0,1}$) mean period, and d is the water depth. The symbols α, β and γ are the free parameters to be determined for a study site for a considered harbor oscillations frequency band.

5.3.1 Application to seaports of the RONIM network

Estimation of harbor long wave significant wave height (H_{LW_h})

The correlation coefficients between the long wave significant wave height measured (H_{LW_h}) and computed with equation 5.1 (H_{LW_p}) are shown in figure 5.4 as a function of the energy ratio between energy in the LF frequency band (ϵ_{LF_h}) and energy in the LW frequency band (ϵ_{LW_h}). This figure shows that the correlation coefficients increase with the energy ratio. Good correlations ($r > 0.8$) were found between offshore short waves parameters and harbors oscillations for ports where LF waves represent a significant part of the long waves energy ($\epsilon_{LF_h}/\epsilon_{LW_h} > 0.4$), such as Port-Tudy, Bayonne and La Rochelle. Harbor oscillations in LF period band are mainly induced by incident bound IG waves which are directly or indirectly generated by short-wave groups (section 1.3.1), that explains these good correlations. For ports where the LF period band has only a small contribution to the total spectral energy ($\epsilon_{LF_h}/\epsilon_{LW_h} < 0.1$), correlations with offshore short wave forcing are weak ($r < 0.7$), such as ports of Dunkerque (# 1), Brest (#9), Cherbourg (#6), Dieppe (#4), Concarneau (#10), Le Crouesty (#12). Oscillations in these ports are possibly generated by other mechanisms such as atmospheric processes or (less likely given the temporal extent of the data) tsunamis (section 1.2.2) (Okihiro and Guza, 1996; López et al., 2012; De Jong et al., 2003; Tappin et al., 2013). The contribution of LF period band is intermediate in the five remaining ports ($0.1 < \epsilon_{LF_h}/\epsilon_{LW_h} < 0.4$). Harbor oscillations in Boulogne-sur-Mer and Saint-Jean de Luz are weakly correlated with offshore short wave parameters ($r < 0.7$). In these two ports, the tide gauge is located at the entrance of port basins and predominantly records longer oscillations of the surroundings, namely the artificial roadstead for the first port and the sheltered bay for the second, in front of those of the ports (figure 5.3). Ports of Le Havre, les Sables d'Olonne and Le Conquet present high correlations with offshore short waves parameters ($r > 0.7$). Oscillations in these ports seem to have a mixed character with influences both from the incident short waves and other driving agents such as meteorological processes (López et al., 2012) .

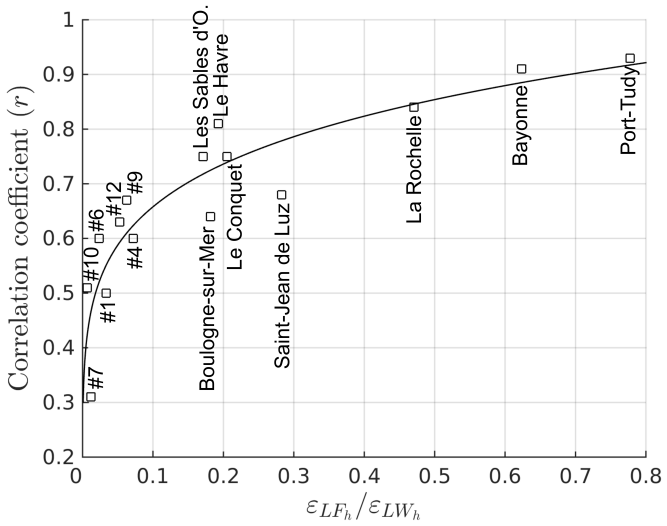

Figure 5.4 – Correlation coefficients between H_{LW_h} and H_{LW_p} as a function of the ratio of energy $\epsilon_{LF_h}/\epsilon_{LW_h}$ (black squares). Line represents an exponential fit.

Estimation of harbor low frequency significant wave height (H_{LF_h})

The six ports with the highest correlation ($r > 0.7$, figure 5.4) have been selected for the development of an empirical formula in order to predict LF harbor oscillations based on offshore incident wave characteristics. Dispersion diagrams between H_{LF_h} and H_{LF_p} (equation 5.1) are shown in figure 5.5 as well as (Q-Q) quantile-quantile diagrams. Except for port of Le Havre, correlation coefficients are higher than 90%. Regressions are relatively good with points centered around the fitting line as shown by the Q-Q plot following in most cases the line $y = x$. However for port of la Rochelle, predictive values seem to underestimate harbor oscillations for extreme events.

Except for port of Le Havre, the retained ports are located on the Atlantic facade and harbor oscillations in LF period band can be reasonably estimated and predicted using offshore short waves parameters. For Port-Tudy, harbor oscillations are mainly caused by LF period band ($\epsilon_{LF_h}/\epsilon_{LW_h} \approx 80\%$) and H_{LF_p} is a good indicator of a potential seiche hazard. As presented in the chapter 4, port of Bayonne faces energetic incident IG waves that are mainly responsible for harbor oscillations. IG waves can generate seiche in the marina and problems of keeping boats docked in the river seaport, H_{LF_p} is then related to a potential risk for port operations. The LF period band is responsible for about 50% for port of la Rochelle but only 20% of the total spectral energy for the other ports. However, the offshore agitation parameters remain a good indicator of the LW port oscillations ($r > 0.7$, figure 5.4), and H_{LF_p} and/or H_{LW_p} can be relevant for harbor operation management.

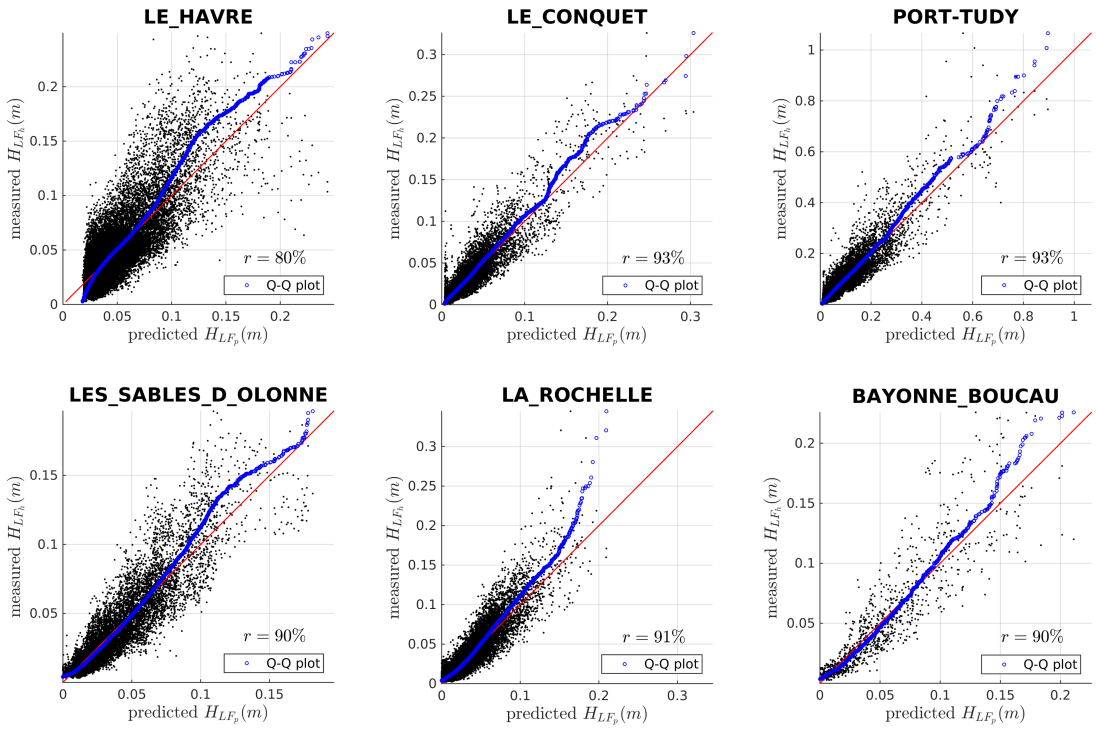

Figure 5.5 – Dispersion diagrams of harbour LF wave heights H_{LF_h} and predicted wave heights H_{LF_p}. Blue circles represent the Quantile-Quantile plot.

5.3.2 Application to port of Bayonne

Tide gauges whose primary purpose is tidal measurement are mainly configured for a 1 min or 10 min data acquisition and are generally equipped with a stilling well to mechanically filter high frequency waves (swells and seiches) (Simon and Manley, 2013). Thus, even with a 1 Hz sampling frequency, tide gauge measurements remain incomplete for the whole infragravity period band. For port of Bayonne, the measurement point at the river mouth, directly exposed to waves, is ideal for measuring incident waves at high frequency (1 Hz) in contrast to tide gauge. To complete this study for port of Bayonne, a statistical model is applied to our dataset and consists to find an empirical relationship for the harbor oscillations in IG period band at the river mouth Hs_{IG} (i.e incoming IG waves) in terms of offshore incident short waves parameters and water level. This model also allows to study the influence of these parameters on the incoming IG waves amplitude and constitutes the first step in the development of an IG hazard prediction system, whose purpose is to improve port operations management.

Methods

The empirical relationship was determined by the simple and multiple linear regression approach with least-squares method for parameter estimation (Lafaye de Micheaux et al., 2013) and its mathematical form was inspired by the one proposed by Bowers (1993) (equation 5.1):

$$Hs_{IG,mod} = \alpha \prod_i X_i^{x_i} \tag{5.2}$$

where $Hs_{IG,mod}$ is the fitting value, X are the explanatory variables, α and x are the model parameters. The linear regression is simple for $i = 1$ or multiple for $i > 1$.
A variable change was used to remain within the framework of linear regression and the logarithm operation was applied to all variables. In order to evaluate the performance of the model, model parameters were estimated from a partial data set. The remaining independent data are used to test the model accuracy. To choose the explanatory variables in the regression model, we applied the forward selection approach with F-tests, Akaike information criterion (AIC) and adjusted R-squared (R^2) as model fit criteria (Lafaye de Micheaux et al., 2013). The AIC is a relative estimator of the quality of statistical models and provides a means for model selection: the lower the model AIC, the better its quality. The forward selection method consists to minimize the AIC for each added explanatory variable to the model. The root-mean-square error (RMSE) between Hs_{IG} and $Hs_{IG,mod}$ was also determined. A binary classification method was used to study the model performance, namely its sensitivity and precision, which were respectively estimated through the true positive rate (TPR) and the positive predictive value (PPV) defined as

$$TPR = \frac{TP}{TP + FN} \qquad PPV = \frac{TP}{TP + FP} \tag{5.3}$$

where TP, FN and FP are true positive, false negative and false positive respectively.
The continuous values of the model are made binary by defining a cutoff threshold equal to the 95th percentile of Hs_{IG}.

Results

The incident wave parameters, determined from the frequency spectrum of the Anglet buoy, can be divided into 3 types, namely the wave height, period and direction. The wave height is evaluated by the (Hs or H_{m0}) total significant wave height, the Hs of wind sea waves determined for a period p lower than 10 s , and the Hs of swell waves determined for $p > 10$ s. The wave period is evaluated by the ($T_{m0,1}$ and $T_{m0,2}$) mean periods, the (Te or $T_{m-1,0}$) energetic period, and the (Tp) peak period. The wave direction is characterized by the (Dm) mean direction and the (Dsd) mean directional spreading. The (WL) water

level in the river is also an independent variable available for the model. Data from the winter months of (FC) field campaigns 3 and 4 until February 2019 (4322 observations) are used to set up the models. An additional set of data, obtained between February 4 and June 12 2019 (5292 observations), is used to test the predictive qualities of the most performing statistical model. For all F-test, F-value are significant since the maximum associated p-value equal to 0.02% is lower than 5%. The table 5.5 presents the formula of $Hs_{IG,mod}$ and the parameter estimations of the models.

Model	**Explanatory variables**	**AIC**	**R^2**	**RMSE (m)**
1	Hs_{swell}	-11289.8	0.8850	0.059
	Hs	-8672.6	0.7892	0.073
2	Hs ; Te	-13161.5	0.9254	0.046
3	Hs ; Te ; Dm	-13797.0	0.9356	0.042
4	Hs ; Te ; Dm ; WL	-13809.0	0.9358	0.042

Table 5.4 – Selection of explanatory variables and model scores: (AIC) Akaike information criterion, (RMSE) root-mean-square error and R-squared for a one-explanatory-variable model or adjusted R-squared for a multiple-explanatory-variable model.

The best univariate model is with Hs_{swell} that integrates information on the wave period. However, no other explanatory variable can be added to the model at the risk of redundancy in the data (table 5.4). As the second best univariate model is with Hs, Hs is selected and the forward method is continued. The next added variable provides information on the waves period and the most effective variable is Te in front of $T_{m0,1}$, $T_{m0,2}$ and Tp with AIC equal to -11961.6, -11108.2 and -10934.1 respectively. With Hs and Te as explanatory variables, this model is more efficient than the one with only Hs_{swell} and R_a^2 is equal to 92.54%. The mean direction further improves the prediction model (in front of Dsd with AIC of -13209) and this 3-variable model has an R_a^2 equal to 93.56%. Finally, the water level in the river improves very slightly the regression model.

Figure 5.6 shows the scatter plot of Hs_{IG} and $Hs_{IG,mod}$ for the selected models as well as the fitting line and the 95%-level interval of prediction. To apply a binary classification, a cutoff threshold, set at the 95th percentile of Hs_{IG} equal to 0.47 m, is used to transform the Hs data in boolean data. The 3 presented models are accurate (PPV = ~85%). However, the univariate model is not sensitive (TPR = 30%), the values of Hs_{IG} are very underestimated by the model and during false negative, Hs_{IG} can be high (3 events with $Hs_{IG} > 0.80\ m$). Two explanatory variables (Hs and Te) improves the sensitivity of the model (TPR = ~63%) and the points of the scatter plot are better centered around the fitting line. Three explanatory variables (Hs, Te and Dm) further improve the model sensibility (TPR = 72%) and its robustness since the interval of prediction is narrower and

Hs_{IG} during false negative is reduced (second maximum value of 0.65 m). The addition of the explanatory variable WL slightly improves the statistical model and the variation of FN, TP and FP is 1 for all of them.

From statistical model 4, figure 5.7 shows the effects of the variation of Dm and WL on $Hs_{IG,mod}$ respect to the average mean direction of incident short waves (300°) and the mean sea level (2.5 m). The water level has little impact on $Hs_{IG,mod}$: the maximum increase at low tide is 4.5% compared to a maximum decrease of 2% at high tide, however its impact is more marked at low tide. The role of the mean direction of the incident short waves has much more influence on $Hs_{IG,mod}$: a decrease (increase) of 10°in the mean direction leads to an increase (decrease) of about 10% of $Hs_{IG,mod}$.

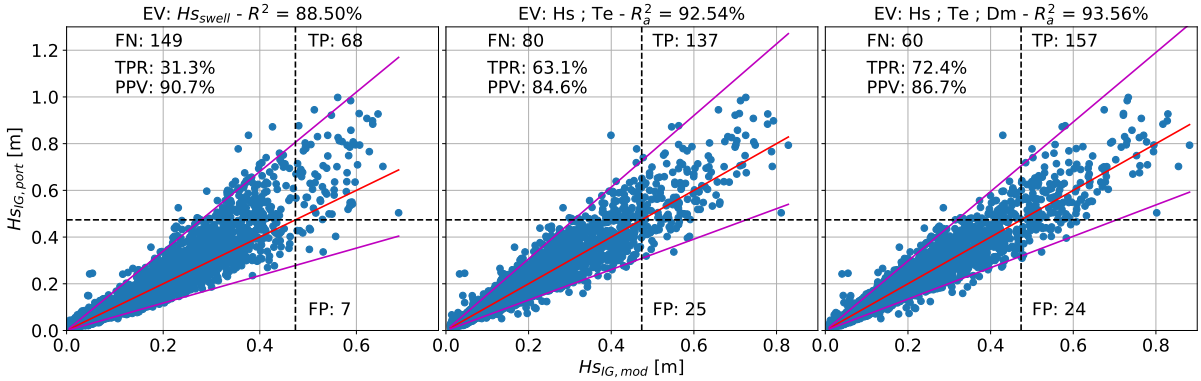

Figure 5.6 – Statistical models 1, 2 and 3: scatter plot of $Hs_{IG,port}$ and $Hs_{IG,mod}$ (4322 observations). EV referees to explanatory variables. (Magenta lines) 95%-level interval of prediction ; (red line) fitting line (equation $y = x$) ; (black dashed lines) cutoff threshold: 95th percentile of $Hs_{IG,port}$ equal to 0.47 m. Coefficient of determination: R-squared (R^2) or adjusted R-Squared (R_a^2). Model evaluation (binary classification): numbers of (FN) false negative ; (TP) true positive ; (FP) false positive ; (TPR) true positive rate ; (PPV) positive predictive value.

Model	$\mathbf{Hs_{IG,mod}}$	$\log(\alpha)$	β	γ	δ	ϵ
1	$\alpha Hs_{swell}^{\beta}$	-2.371	1.060			
	αHs^{β}	-3.077	1.398			
2	$\alpha Hs^{\beta} Te^{\gamma}$	-6.592	1.140	1.632		
3	$\alpha Hs^{\beta} Te^{\gamma} Dm^{\delta}$	8.613	1.191	1.606	-2.667	
4	$\alpha Hs^{\beta} Te^{\gamma} Dm^{\delta} WL^{\epsilon}$	8.661	1.192	1.608	-2.672	-0.028

Table 5.5 – Empirical formula and corresponding free parameters value for 4 regression models.

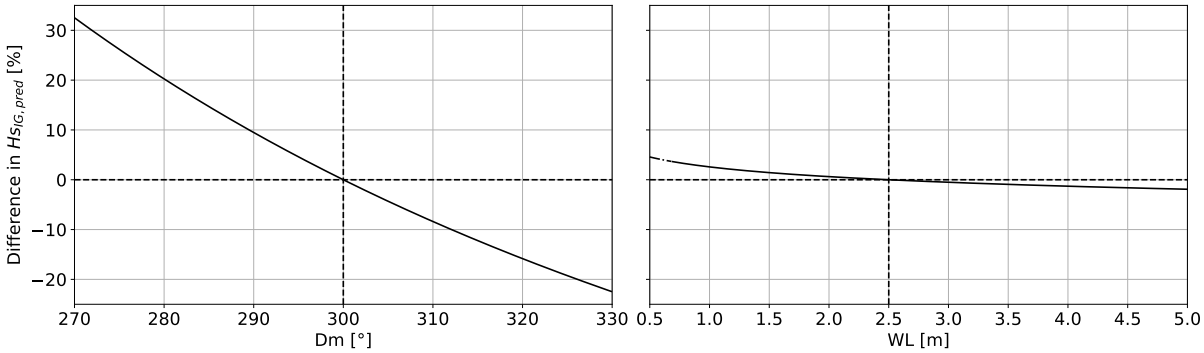

Figure 5.7 – Effects of (Dm) mean direction and (WL) water level on $Hs_{IG,mod}$ from model 4: positive values are augmentations. Reference values: (Dm) average of mean direction and (WL) mean sea level. Dashed line is unobserved values.

Discussion

Despite the small variation in the mean direction of the incident waves, this parameter improves the quality of the statistical model and the prediction of the incident IG waves (figure 5.6). Short waves coming further West than the average mean direction (300°) generate larger IG waves at the river mouth (figure 5.7). For incident wave directions in the range of 270-280°, the deposit of dredged material, aligned with the harbor entrance, favors the concentration of wave energy on the port mouth by a refraction phenomenon (Bellafont et al., 2018b). For directions higher than 300°, the port entrance is directly protected from incident waves by the North breakwater, which seems to limit the generation of IG waves in the vicinity of the Adour entrance. In addition, the river mouth could be in the less energetic refraction zone of the deposit. The water level as explanatory variable has a slightly effect on the prediction of incident IG waves. Its effect, asymmetrical around the MSL, is more pronounced at low tide (figure 5.7).

The best explanatory variable providing information about the waves period is Te in front of $T_{m0,1}$, $T_{m0,2}$ and Tp. In contrast to the peak period Tp based on a unique spectrum data, the energy period Te takes into account the shape and the frequency distribution of the spectral energy (as well as $T_{m0,1}$ and $T_{m0,2}$). Te through the -1 order moment with which it is calculated gives more weight to the low frequencies of the spectrum, involved in the generation of IG waves.

Time series of Hs_{IG} and $Hs_{IG,mod}$

To evaluate the models, figure 5.6 individually displays the pairs (Hs_{IG} ; $Hs_{IG,mod}$) without taking into account the time period of a storm event (generally extended from 12 to 24 h). Figure 5.8 presents in a complementary way the data in temporal domain. Each point is

generally part of a multi-hour storm event which is anticipated by the statistical model. No group of points seems outlier and far from the regression curve, which is consistent with the figure 5.6.

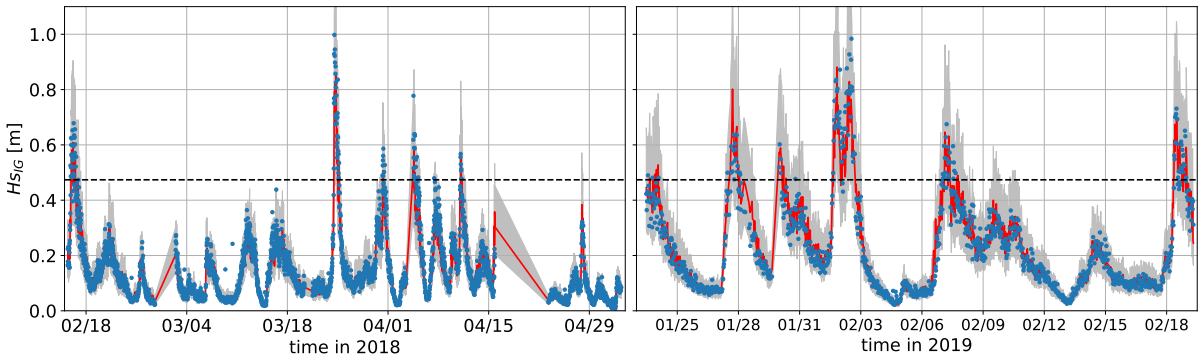

Figure 5.8 – Time series of (blue dots) $Hs_{IG,port}$ and (red line) $Hs_{IG,mod}$ from statistical model 3, (black dashed lines) 95th percentile of $Hs_{IG,port}$ equal to 0.47 m, (grey surface) interval of prediction. (left panel) Field campaign 3 and (right panel) field campaign 4. Gaps are due to the lack of data from the wave buoy.

Predictive capability of the model

Figure 5.9 presents the time series of $Hs_{IG,port}$ and $Hs_{IG,mod}$ for the data not used to determine the model parameters, from February 4 to June 12 2019 (5292 observations). Five events above the threshold of the ($Hs^{95}_{IG,port}$) 95th percentile of $Hs_{IG,port}$ occurred during this period. Three are clearly identified by the statistical model with $Hs_{IG,mod}$ above $Hs^{95}_{IG,port}$. For the other two, the predictive curve is above the threshold but the real values are underestimated. Overall, the trends are well captured by the model and it is interesting to note that no false positive event occurred.

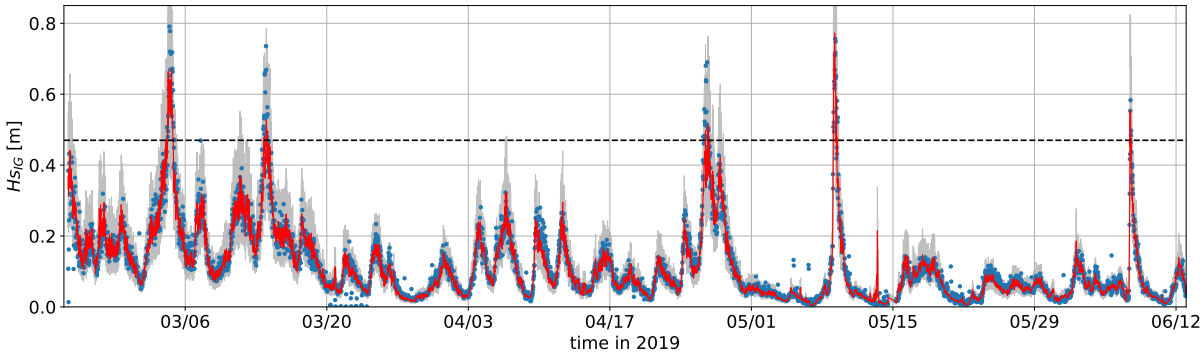

Figure 5.9 – Test of the statistical model 3 with data not used to set up the model: time series of (blue dots) $Hs_{IG,port}$ and (red line) $Hs_{IG,mod}$ from statistical model 3, (black dashed lines) 95th percentile of $Hs_{IG,port}$ equal to 0.47 m, (grey surface) interval of prediction.

Seiche hazard indicator in the marina

Figure 5.10 shows the links between IG oscillations at the river mouth and marina oscillations in the IG period band as well as in the extended period band of IG+VLW (30-600 s) for FC3 and winter FC4 data. For the field campaign 3 (figure 5.10, a), the relationship is quite linear between IG oscillations at the river mouth and in the marina, whereas the scatter plot is spread out around the fitting curve for FC4 (figure 5.10, b). This is due to mud silting of the marina pressure sensor, which caused a "signal damping" since the pressure applied to the gauge membrane is reduced. The siltation changed over time and some sudden variations (pressure jump) are visible in the data. Dredging operations were carried out shortly before FC3 in the marina, that is why the sensor was not affected by this problem. However, the relationship between marina oscillations in the IG and IG+VLW period bands remains quite similar and linear for FC3 and FC4 (figure 5.10, c and d). IG oscillations at the river mouth is a good indicator of the marina oscillations in the IG period band but also in the extended period band (IG+VLW) that includes the fundamental mode of the marina. So, $Hs_{IG,mod}$ can be used as an indicator of marina seiche hazard. By combining the FC3 data (figure 5.10, a and c), the linear relationship is $Hs_{IG+VLW,marina} = Hs_{IG,PS0}$ with a R^2 of 0.965 and a RMSE of 0.045 m.

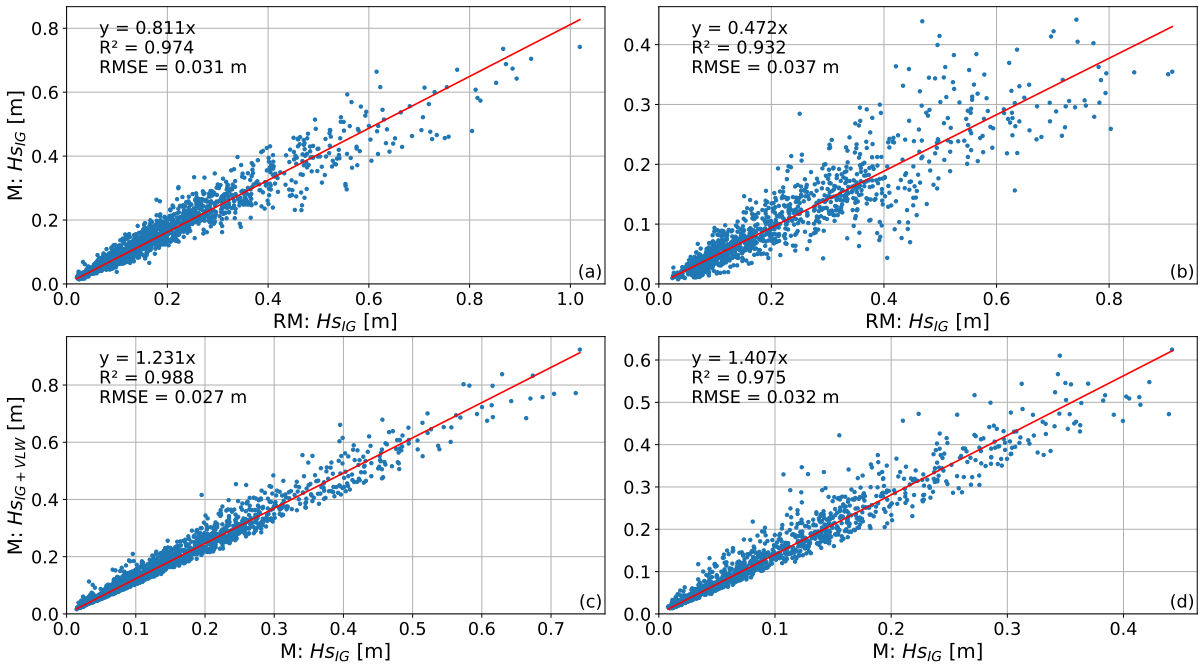

Figure 5.10 – (a,b) Scatter plot of IG (30-300 s) wave height in the (M) marina and at the (RM) river mouth. (c, d) Scatter plot of wave height in the marina in IG period band and in IG+VLW (30-600 s) period band. (a, c) field campaign 3 (1809 observations) and (b, d) field campaign 4 (1132 observations).

Application of the model to all available buoy data

Figures 5.11 and 5.12 present $Hs_{IG,mod}$ time series resulting of the application of the statistical model 3 formula to all available buoy data and the most important events of the years 2017 and 2018.

The archived warning bulletins for potential risk of waves and submersion issued from météo France can be a way to identify energetic and problematic events. Of the six winter events identified in 2017 and 2018, three are classified as a level of 3 out of 4 risk for waves and submersion, such as (a) Kurt, Leiv and Marcel storms event and (d) Carmen and Eleanor storms event. However, the risk of submersion depends on the water level mainly influenced by the tide. (c) Bruno storm, which occurred during neap tide, was classified as a 2 out of 4 risk in spite of the intensity of the offshore incident swell waves and the potential IG oscillations in the port.

Continuous data acquisition system maintained during the generally less energetic spring and summer periods may be relevant and justified, as shown by the Miguel storm occurred in June and identified as an important event by the statistical model (figure 5.12).

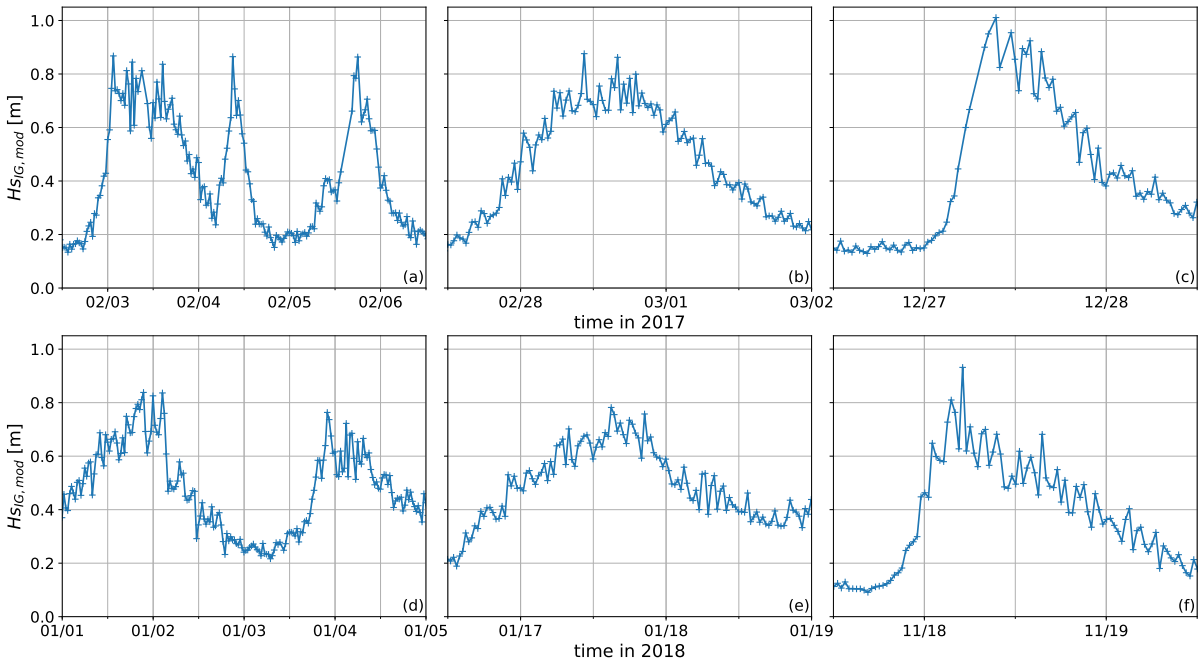

Figure 5.11 – Statistical model 3 applied to all available buoy data and selection of the most important events. (a, b, d) publication of a warning bulletin from météo France for potential risk of waves and submersion (level 3 of 4) (Source: `http://vigilance-public.meteo.fr/`). (a) Kurt, Leiv and Marcel storms, (c) Bruno storm, (d) Carmen and Eleanor storms.

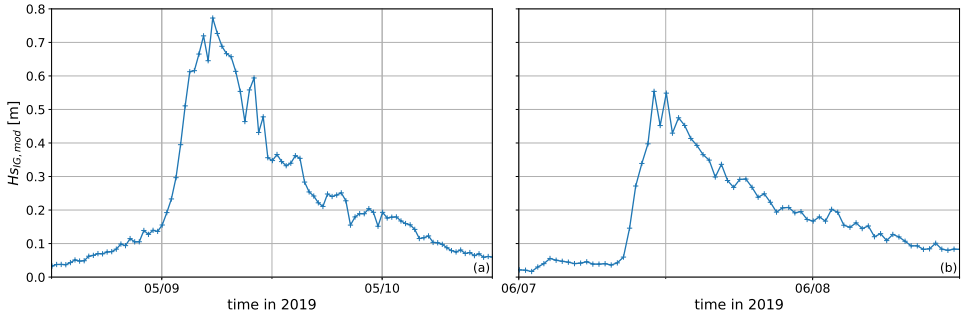

Figure 5.12 – Important values of $Hs_{IG,mod}$ during May and June. (b) Miguel storm.

5.4 Conclusion

Tide gauge data can be used to characterize port behavior and to identify resonance periods of harbor basins or of the port neighboring environment such as bay or roadstead. In some cases, tide measurement can be representative of the global port oscillations in the low frequency band (2-7 min) as for Port-Tudy, and therefore be used to estimate harbor oscillations from offshore bulk wave parameters. However, tide gauges do not provide a measurement of the whole IG period band (30-300s) due to their sampling period of 1 or 10 min and the presence of a stilling well which mechanically filters these waves that can interfere with tide measurement.

The deployment of sensors is generally needed to complete the tidal data and specifically record harbor oscillations. From pressure sensor data, a statistical model was developed for port of Bayonne to predict the IG wave height at the river mouth from offshore incident short waves bulk parameters. The latter are simulated in real time by spectral wave models (as WW3) that forecast the sea state over a few days with a good accuracy. Considering the quality of the statistical model, a predictive alert system can be developed. To make this system operational, the predicted hazard has to be related to potential consequences (financial, human,...) in order to assess the risk. The empirical formula can also be integrated into a more global monitoring system (see González-Marco et al., 2008).

Chapter 6

Numerical study

6.1 Introduction

In this chapter, we use a Boussinesq-type wave model to study the generation and transformation of incident waves, their interaction with port activities as well as their transformation and dissipation in the river. It is based on the BOSZ code presented in the section 3.3.2 of chapter 3. This model allows to describe both non-linear interactions and dispersive effects at wave scale. The numerical study focuses on a storm event selected from the database described in chapter 4. It aims to determine the spatial and frequency distribution of the incident wave energy from the nearshore zone to the upstream part of the Adour river during energetic conditions. The numerical model is specifically intended to investigate the bi-modal distribution of IG wave energy in the river (chapter 4) and the impact of a dredged material deposit on the nearshore transformation of incident waves. Furthermore, a new river mouth configuration is simulated in order to study the influence of coastal structure on IG waves characteristics in the river.

First, the storm Hugo that occurred in March 23, 2018 is presented. This storm was selected as it is representative of a one-year return period storm in the study area. The model setup and its validation are presented in section 6.2. The model results are then analyzed through maps of significant wave heights considering several frequency bands, namely short (SW, 6-30 s) and infragravity (IG, 30-300 s) period bands, and the two sub-period bands IG1 (30-100 s) and IG2 (100-300 s) highlighted in chapter 4. Table 6.1 shows the different numerical cases used in this chapter. The results are compared with the current situation, taken as reference case.

	Reference case	
Case 0	Current configuration	One-year return period storm
	Transformation of IG waves along the river	
Case 1	Influence of the marina	Marina removed
Case 2	Bottom friction dissipation	Zero bottom friction in the Adour
Case 3	Cross-section profile (river bathymetry) Geometry of the channel (S-shape)	Uniform bathymetry in the Adour Zero bottom friction in the Adour
	Influence of the nearshore bathymetry	
Case 4	Impact of a dredging deposit	Deposit removed
	Influence of the Adour river mouth configuration	
Case 5	New configuration of river mouth	South breakwater extended

Table 6.1 – Numerical cases: their aims and differences from the reference case (case 0).

6.2 Validation of the numerical model

Figure 6.1 shows the sensor positions for the selected field campaign FC3.

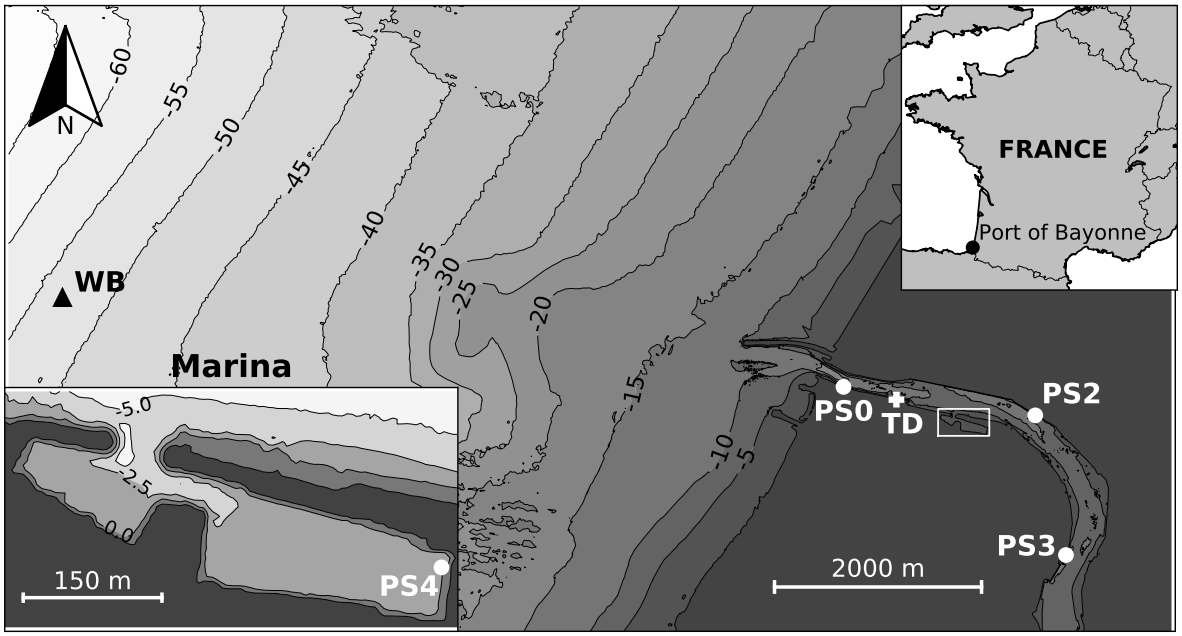

Figure 6.1 – Port of Bayonne and gauges locations: (WB) waverider buoy; (PS) pressure sensors (white dots): PS0 (river mouth), PS2-PS3 (river seaport) and PS4 (marina); and (TD) tide gauge. The sensor PS1 was lost during the field campaign FC3 (chapter 4 and table 4.1). Zoom on the marina in the lower left corner (white rectangle on the map).

6.2.1 Energetic event: Hugo storm

During the storm event, from 24 to 25 March 2018, the offshore significant wave height and peak period reached maximum values of 6 m and 18 s respectively (figure 6.2, a). Figure 6.2 shows the response of port of Bayonne to external forcing and *Hs* in the channel harbor (PS2) and in the marina (PS4). The contribution of short waves (5-30 s) in harbor oscillations is low ($Hs_{SW} < 0.15\ m$) unlike IG waves whose significant heights Hs_{IG} reach values of 0.47 m for an *Hs* of 0.55 m in the channel harbor and a Hs_{IG} of 0.95 m for an *Hs* of 1.07 m in the marina. The period band of Hs_{IG} has been extended to 600 s for the marina in order to include the period of basin's fundamental mode (chapter 4).

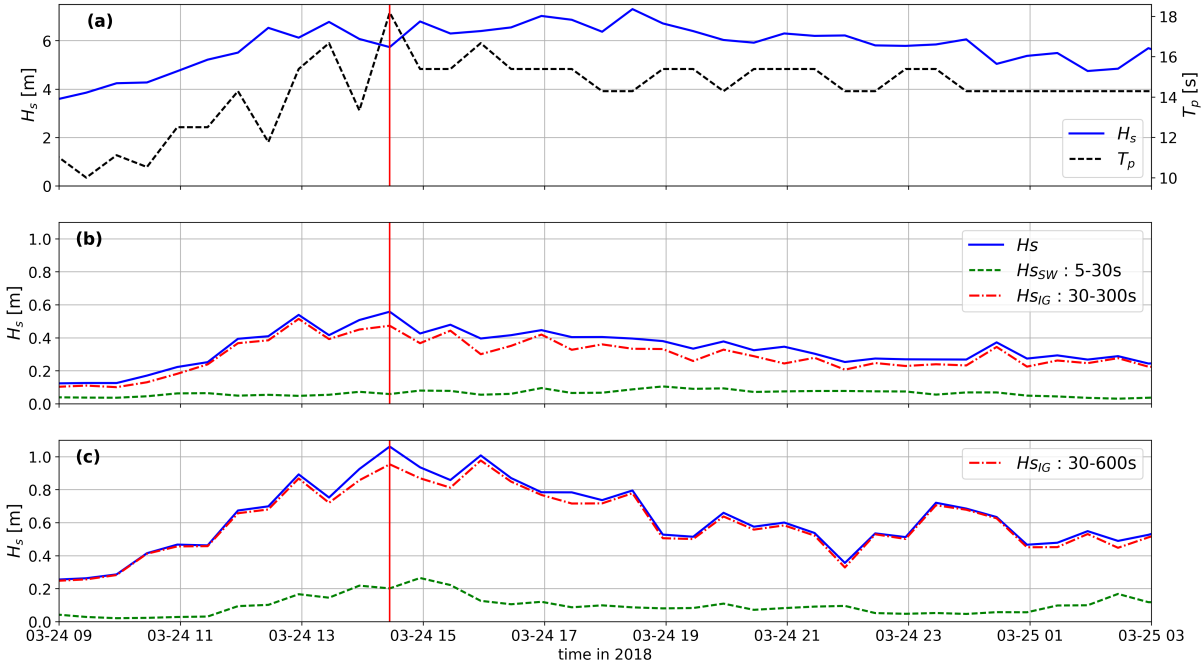

Figure 6.2 – Storm event: (a) *Hs* and *Tp* at the offshore wave buoy; (b) *Hs* in the river (PS2) and (c) *Hs* in the marina (PS4). The red vertical line corresponds to the simulated event.

To study the waves transformation during the propagation in the river, power spectral densities (PSD) at the pressure sensors are presented in figure 6.3 (18h of data). From these densities, significant wave heights are calculated and the contribution of the different period bands to the variance of the free surface is expressed as a ratio of m_0 ($R_{SW} = m_{0,SW}/m_0$) (table 6.2). Despite a *Hs* greater than 5 m at the wave buoy, Hs_{SW} is equal to 1 m at the port mouth (PS0). In the river, the remaining energy dissipates quickly and its contribution to the variance of the free surface is low: $Hs_{SW} < 0.10\ m$ and $R_{SW} < 5\%$ for PS2 to PS4. The contribution of IG waves to the variance of the free surface is rather low (~30%) at the port mouth but Hs_{IG} is equal to 0.7 m. In the river seaport, the

IG energy is very high ($R_{IG} > 80\%$) and dissipates slightly: only 6 cm in terms of *Hs* between PS2 (2.2 km) and PS3 (3.7 km), i.e. 20% dissipation. The very long waves (VLW), with a period between 300 and 600 s, have a weak part in the channel harbor oscillations: $Hs_{VLW} < 0.15\ m$ and $R_{VLW} < 6\%$ for PS0-PS3. In the marina, the PSD has several peaks that are characteristic of amplification by basin geometry and correspond to the eigen mode periods of the marina (chapter 4). The main peak is related to the fundamental (Helmholtz) mode with period of 330 s, a broad peak is visible at 125 and 80 s, and three peaks are more marked at 45, 27 ans 22 s.

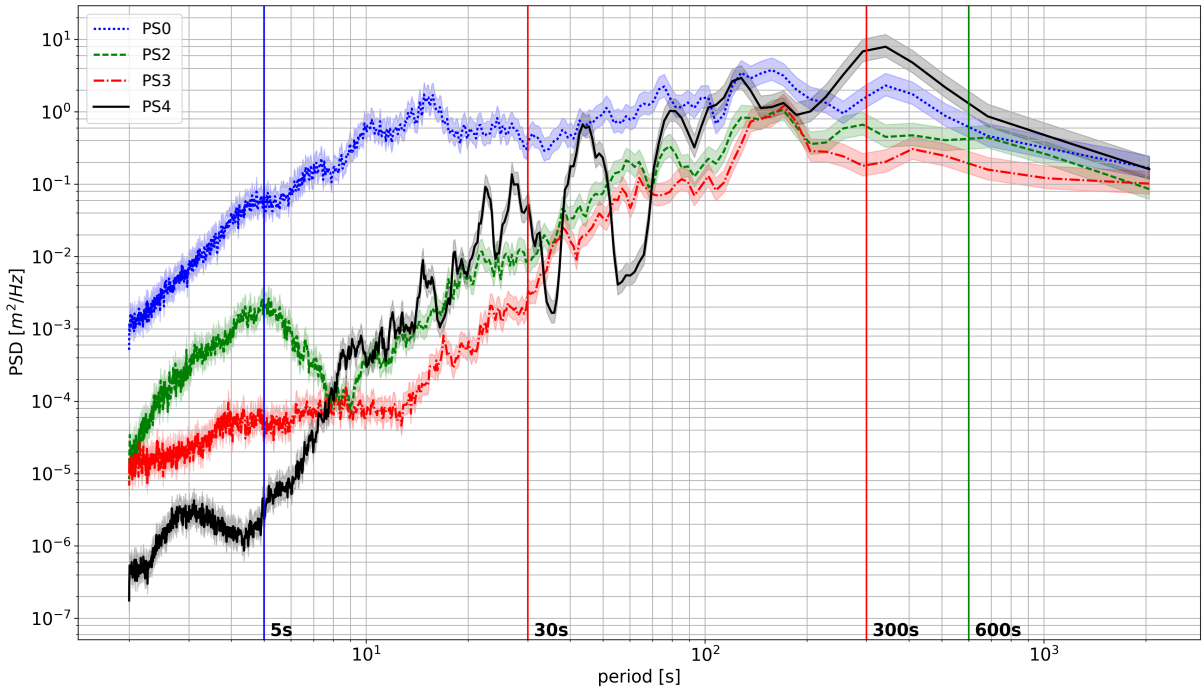

Figure 6.3 – Power spectral densities (PSD) at pressure sensors and confidence intervals (CI).

	Hs	**SW**		**IG**		**VLW**	
		5-30s		30-300s		300-600s	
	m	Hs (m)	R (%)	Hs (m)	R (%)	Hs (m)	R (%)
PS0	1.28	0.99	61	0.72	32	0.16	2
PS2	0.35	0.07	4	0.31	79	0.08	6
PS3	0.27	0.02	1	0.25	86	0.06	6
PS4	0.67	0.12	3	0.53	62	0.28	17

Table 6.2 – Hs in different period bands calculated from PSD (figure 6.3) and contribution (R) of the different period bands to the variance of the free surface (%).

6.2.2 Model setup

The numerical domain extended 8 km seaward to include the offshore wave buoy (water depth of 50 m), and covered 8.5 km of coast (centered on the harbor mouth) (figure 6.4). The upstream boundary of the Adour river is 11 km upstream of the river mouth. A sponge condition is applied at the domain boundaries. The mesh is composed of square cells, ~50% of which are wet. Two grid resolutions are chosen, 6.5 and 10 m, to study the effect of mesh size in terms of computation time and simulation performance (table 6.3). With a 20 ° clockwise rotation of the domain, the western boundary is almost oriented perpendicular to the average direction of forcing. The seabed materials in the study area are essentially fine sand with some mud in the river. Rocky outcrops have been identified 2 km south of the mouth of the Adour River (Augris and Clabaut, 2001). From these data, a Manning coefficient was taken equal to 0.015 s/m^3 over the whole domain, corresponding to sand grain with diameter 0.3 mm (Arcement and Schneider, 1989), and an arbitrary factor of 10 is applied in the breakwaters area to take into account their effect on short waves dissipation with their rubble-mound armor layers.

The model simulation period is 4 hours, the first 30 minutes are used to initialize the model. The remaining 3h30 are divided into 30 min segments and their power spectral densities are average. The selected event is therefore simulated seven times. Since no phase information is provided in the input spectrum, BOSZ model assigns a random phase to each spectral component and therefore several simulations are required to correctly reproduce the input spectrum. Since the Boussinesq-type equations have only limited dispersion capabilities, the shortest waves are eliminated from the input spectrum. BOSZ model defines the ratio of wavelength to water depth (μ) that controls the high frequency tail of the spectrum. The truncated energy is redistributed over the remaining frequency to maintain the overall energy of the spectrum. The ratio μ is taken to 1.5, thus waves with a period of less than ~7 s are eliminated from the spectrum (applying the linear dispersion relation for a 50 m water depth). Since the individual waves are generated for a specific water depth, the first 100 offshore cells have constant depth and no friction. Wave breaking is handled by deactivating the dispersion terms along the breaking wave front using a momentum gradient threshold (section 3.3.2).

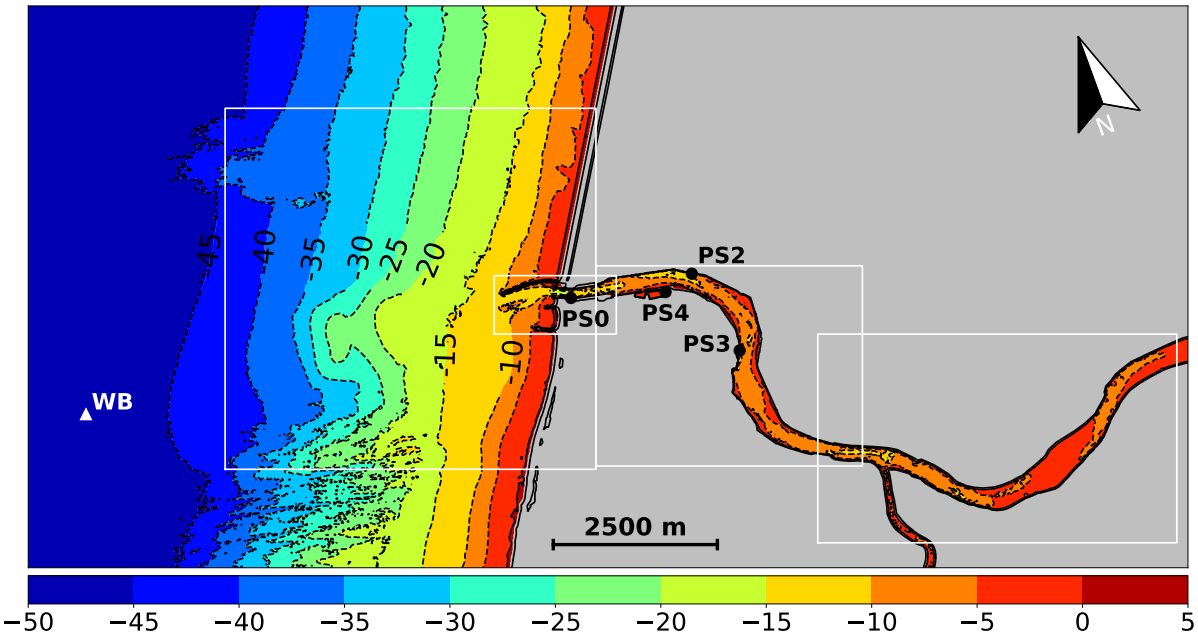

Figure 6.4 – Numerical domain and sensor locations. The first 100 offshore cells are flat. Dry cells are in grey. (white rectangles) Four areas for Hs maps: nearshore zone, river mouth ara, ports area and upstream part of the Adour river.

Grid resolution	m	**10**	**6.5**
Cells	millions	1.5	3.5
Wet cells	%	49	47
Computational time	days	1	3.5
12 cores: Intel Xeon x5675 @ 3,06 GHz			

Table 6.3 – Numerical domain characteristics and computational time.

6.2.3 Selected event

The effects of river flow and tide are neglected. To respect this hypothesis, the numerical study focuses on the event of 24 March 2018 from 14:30 to 15:00 (UTC) at low tide: the mean water level was 1.97 m respect to chart datum with a standard deviation of 0.05 m, and the Adour flow (430 m^3/s) was slightly higher than the mean annual river flow. The wave characteristics measured offshore were: *Hs*, *Tp*, direction at the peak and directional spreading at the peak equals to 5.7 m, 18 s, 299 ° and 19 ° respectively. The BOSZ model is forced with a frequency-direction spectrum reconstructed from wave buoy measurements using a parametric directional spreading function (team et al., 2007)(section 3.2.5).

6.2.4 Measurement and model result comparison

The power spectral densities from the measured and simulated water level time series are presented in figure 6.5 for the channel harbor and in figure 6.6 for the marina. At PS0, short waves energy is globally underestimated and particularly for periods of less than 12 s. This can be due to the effect of local wind not taken into account in the model and to the cut-off period of 7 s on the input spectrum. For the other sensors (PS2 and PS3), the energy in short wave period band is very low and can be neglected ($Hs_{SW} < 0.05\ m$).

Spatial variation and frequency distribution of IG waves (30-300 s) are well reproduced by the model for the channel harbor sensors (PS0 to PS3) and for the two grid resolutions (6.5 and 10 m): the shapes of computed spectral energy from BOSZ agree well with the measurements. But, the underestimation of spectral energy for periods higher than 290 s results in a 10% difference in the Hs_{IG} values for the 6.5 m mesh size and for the sensors in the channel harbor (underestimation for PS0 and PS2, and overestimation for PS3): the differences of Hs_{IG} are from 0.03 m to 0.10 m. For the 10 m mesh size, the Hs_{IG} values are underestimated by about 20% for PS0 and PS2 and 10% for PS3: the differences of Hs_{IG} are from 0.03 m to 0.15 m.

At PS4 (the marina), the 45 s peak is well reproduced by the model as well as the broad peak between 50 and 200 s. The underestimation of energy at peaks at 290 and 450 s results in significant differences of Hs: 20% and 40% for 6.5 and 10 m grid resolution respectively. The sensor PS4 is used to study the impact of the mesh size on simulation results, as the width of the channel between the two basins is 50 m (figure 6.1). The spectral energy differences between the two meshes are small for periods greater than 40 s. Comparisons of spectra in the IG period band show that the BOSZ model can reproduce the generation of IG by ocean forcing and their transformation during propagation in the river.

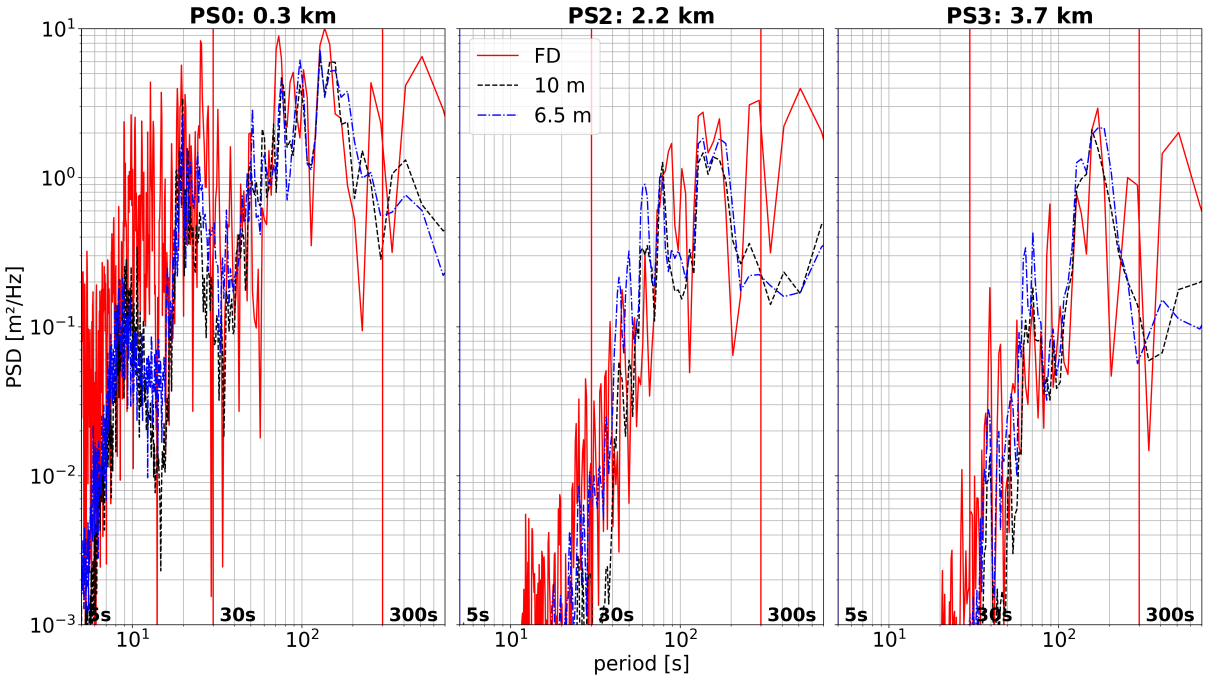

Figure 6.5 – Power spectral densities for (FD) measured and simulated data with the two grid resolutions (10 and 6.5 m), in the channel harbor (PS0 to PS3).

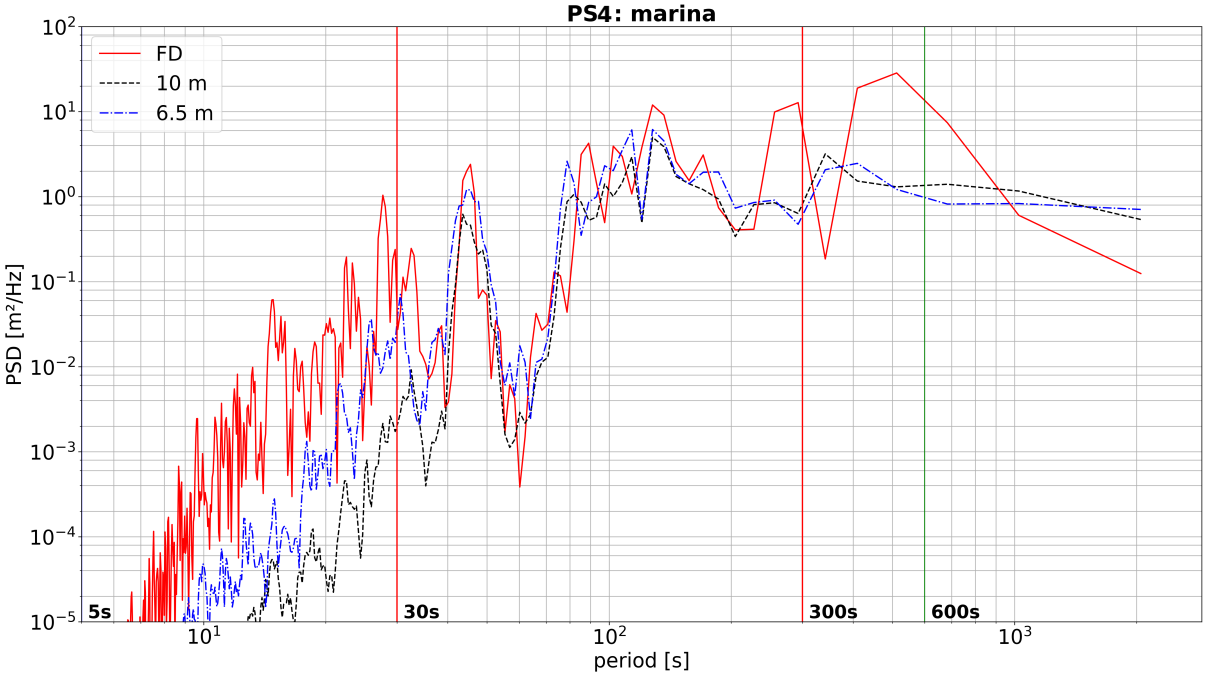

Figure 6.6 – Power spectral densities for (FD) measured and simulated data with the two grid resolutions (10 and 6.5 m), in the marina (PS4).

	Hs			SW (5-30 s)			IG (30-300 s)				
				Hs (m)			Hs (m)			Diff (%)	
	Meas.	6.5m	10m	Meas.	6.5m	10m	Meas.	6.5m	10m	6.5m	10m
PS0	1.62	1.06	1.00	1.22	0.63	0.57	0.94	0.83	0.79	-12	-17
PS2	0.56	0.44	0.38	0.06	0.03	0.02	0.47	0.42	0.35	-12	-25
PS3	0.37	0.36	0.30	0.02	0.01	0.01	0.31	0.34	0.29	10	-7
PS4	1.06	0.68	0.56	0.20	0.05	0.01	0.77	0.62	0.49	-19	-37

Table 6.4 – Hs in different period bands calculated from PSD (figures 6.5 and 6.6).

6.3 Current configuration of the Adour mouth and its vicinity (case 0)

In this section, maps of significant wave heights are determined for the (CC) current configuration in several frequency bands: short (6-30 s) and infragravity (30-300 s) period bands as well as in IG1 (30-100 s) and IG2 (100-300 s) period bands. For each point of the mesh, *Hs* is calculated from power spectral densities. Free surface time series were saved with a 3 s period sampling.

6.3.1 Nearshore zone

The considered nearshore zone extends 5.5 km seaward and its north and south limits are 1.5 km from the domain boundaries to limit disturbances in data (figure 6.4). Figure 6.7 presents *Hs* in SW and IG period bands. The bathymetry contour lines are indicated in the maps and are respect to chart datum.

Areas of high energy concentrations in the SW period band can be seen on the map. At the dredging deposit, Hs_{SW} increases and reaches values greater than 6 m for a -15 m depth. Further north in an area not influenced by the deposit, Hs_{SW} is between 4 and 4.5 m for a -15 m depth. On both sides of the deposit, Hs_{SW} is between 2.5 and 3.5 m. Further south at the level of a rock outcrop, an increase in Hs_{SW} is visible, which reach values greater than 5.5 m. For a depth between -10 and -7.5 m, a rapid decrease in Hs_{SW} occurs due to the depth-limited short wave breaking.

Energy in the infragravity bands (IG, IG1 and IG2), presented in the *Hs* maps, correspond to the superposition of waves of different natures, namely incident bound IG waves, cross-shore propagating free IG waves (leaky waves and IG waves generated by the moving breakpoint mechanism), and alongshore propagating free IG waves (edge waves) (section 1.3.1). Aligned with the deposit in the vicinity of the river mouth, an increase in

Hs_{IG} is visible, which reach values greater than 1 m for depths between -12.5 and -10 m. In this area, the bedslope is gentler compared to the neighboring beaches. Further north in the area not influenced by the deposit, a faster increase of Hs_{IG} is noticeable with the depth reduction in the shoaling zone (up to -12.5 m), Hs_{IG} is between 0.70 and 0.85 m before the short wave breaking zone. At the coastline, an energy concentration in the IG band occurs with $Hs_{IG} > 1.3\ m$ due to wave reflexion processes.

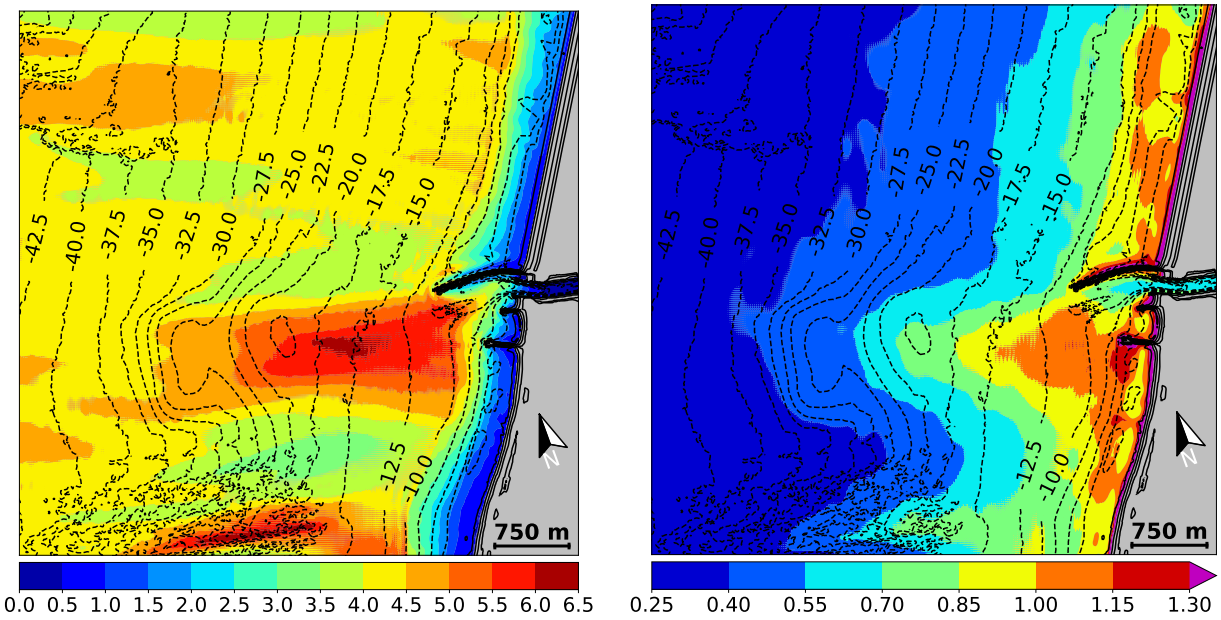

(a) Hs_{SW} (b) Hs_{IG}

Figure 6.7 – Maps of Hs in SW (6-30 s) and IG (30-300 s) period bands (unit: m). Current configuration of the area. (dotted lines) Contour lines (m respect to chart datum). Grid resolution = 10 m.

Figure 6.7 presents *Hs* in IG1 and IG2 period bands. Overall, IG1 has the same spatial energy distribution as IG (figure 6.7). In the nearshore zone, IG2 wave energy is lower than the one in IG1. However, close to the south breakwater, Hs_{IG2} reaches values between 0.7 and 0.8 m for depths between -7.5 and -5 m. Stationary or pseudo-stationary waveforms could be distinguished both cross-shore and alongshore. However, these map representations do not allow precise and relevant analyses of this phenomenon.

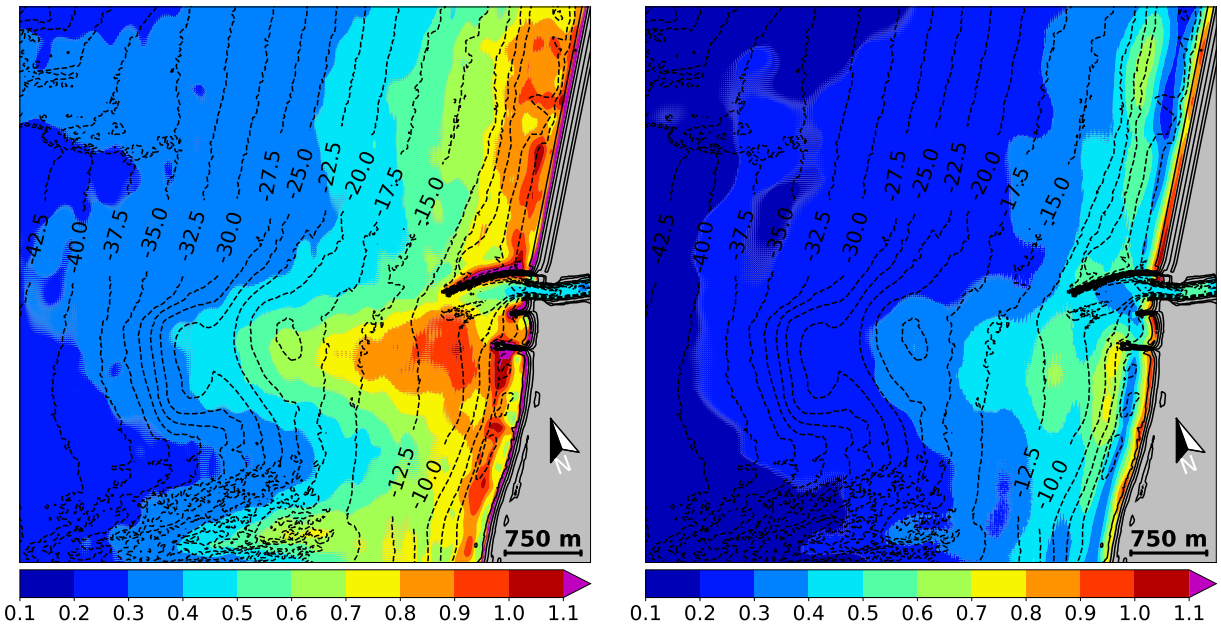

(a) Hs_{IG1} (b) Hs_{IG2}

Figure 6.8 – Maps of Hs in IG1 (30-100 s) and IG2 (100-300 s) period bands (unit: m). Current configuration of the area. (dotted lines) Contour lines (m respect to chart datum). Grid resolution = 10 m.

6.3.2 River mouth

The river mouth zone allows to study the waves transformation in the vicinity of the breakwaters and their penetration into the port (figure 6.4). Figure 6.9 presents *Hs* in SW and IG period bands. A rapid reduction in the SW energy is visible in the breakwaters area with an incoming $Hs_{SW} < 0.5\ m$ into the river. In addition, SW enters the area near the navigation channel with Hs_{SW} between 3.5 and 4 m at 250 m from the port entrance. At the level of the beaches, a rapid reduction in Hs_{SW} occurs from a depth of -10 m at the beginning of the surf zone.

At the head of the North breakwater (-10 m), the significant wave height of the incident IG wave is between 1.0 and 1.1 m. From this depth, a rapid and regular energy reduction is visible as far as the port entrance, where Hs_{IG} is between 0.6 and 0.7 m.

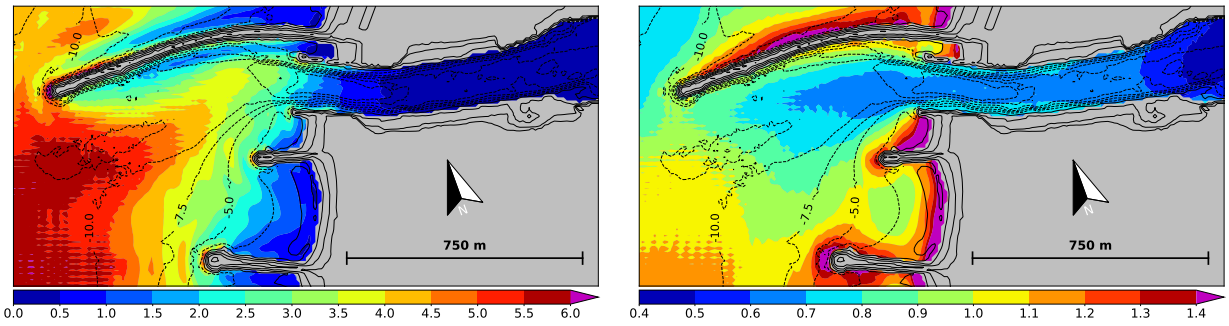

(a) Hs_{SW} (b) Hs_{IG}

Figure 6.9 – Maps of Hs in SW (6-30 s) and IG (30-300 s) period bands (unit: m). Current configuration of the area. (dotted lines) Contour lines (m respect to chart datum). Grid resolution = 10 m.

Figure 6.10 presents *Hs* in IG1 and IG2 period bands. IG1 presents the same pattern as IG. The incident IG1 wave height is between 0.9 and 1 m and a regular energy reduction occurs until the port entrance, where Hs_{IG1} is between 0.4 and 0.5 m. The variation in IG2 energy is low in the river mouth area with $0.4 < Hs_{IG2} < 0.5\ m$. An area of lower energy is visible between the head of the intermediate breakwater and the middle of the north one ($0.3 < Hs_{IG2} < 0.4\ m$). In the converging zone at the port entrance, the wave energy in IG1 and IG2 is similar with a significant wave height between 0.4 and 0.5 m.

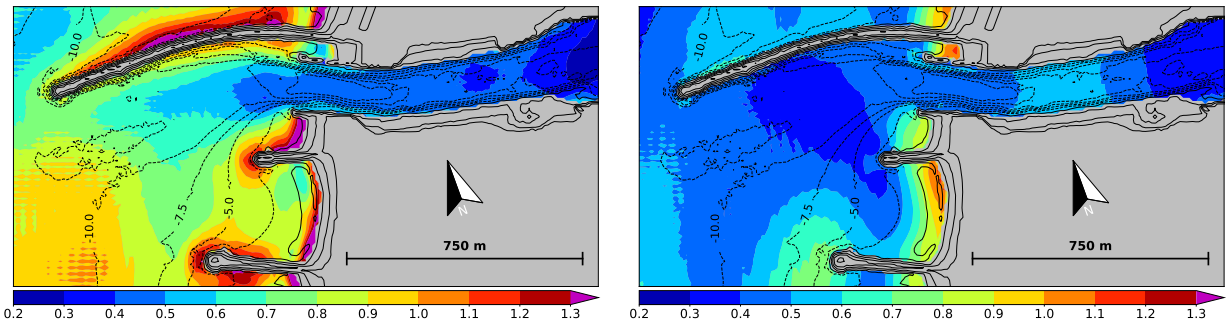

(a) Hs_{IG1} (b) Hs_{IG2}

Figure 6.10 – Maps of Hs in IG1 (30-100 s) and IG2 (100-300 s) period bands (unit: m). Current configuration of the area. (dotted lines) Contour lines (m respect to chart datum). Grid resolution = 10 m.

6.3.3 Ports area

Ports area focuses on the marina and the river seaport, whose upstream administrative limit extends 6 km from the river mouth (figure 6.4). Figure 6.11 presents *Hs* in IG period

band in the river and Hs_{tot} in the marina. Wave energy in the SW period band is very low with Hs_{SW} about 0.15 m at the end of the converging zone and $Hs_{SW} < 0.05\ m$ beyond. IG waves control the harbor oscillations since the maps of Hs_{tot} and Hs_{IG} are very similar (not shown).

At the end of the converging zone, Hs_{IG} is between 0.4 and 0.5 m. Over a distance of 300 m, Hs_{IG} loses 0.1 m and an additional 0.1 m over 450 m. From the beginning of the sinuosity of the river, Hs_{IG} is between 0.2 and 0.3 m to the upstream part of the river seaport.

Oscillations in the marina result of the superposition of the different natural resonance modes of the basins. The mode 1 of the marina presented in the figure 4.4 is clearly visible on the Hs_{tot} map, an anti-node is located at the left basin boundary where $Hs_{tot} > 1.0\ m$. The fundamental mode, whose pattern is less visible on the map, seems less captured by the model (figure 6.6).

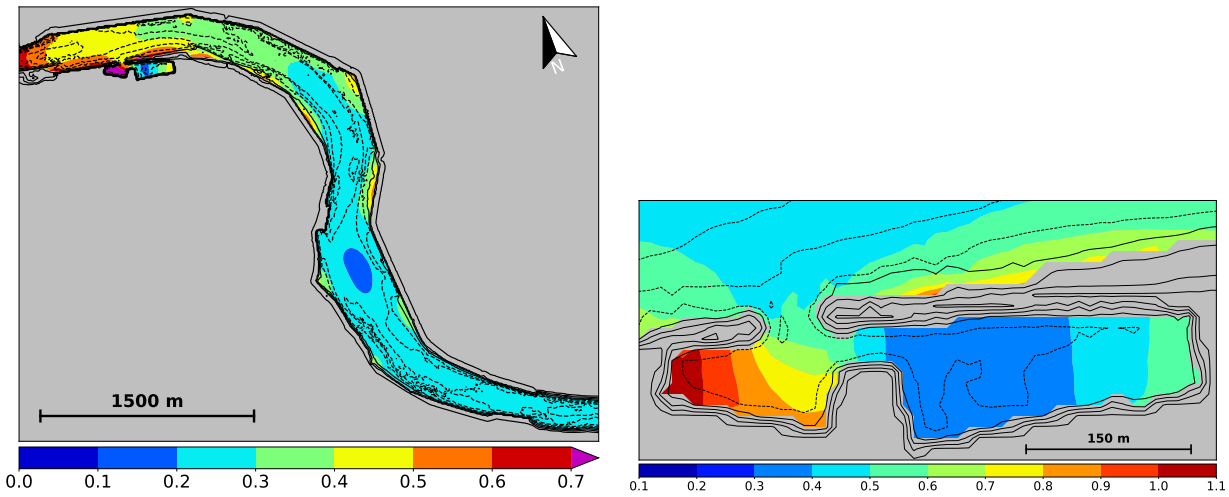

(a) Hs_{IG} (b) Hs_{tot}

Figure 6.11 – Maps of Hs in IG (30-300 s) period band and Hs_{tot} (6-2048 s) in the marina (unit: m). Current configuration of the area. (dotted lines) Contour lines (m respect to chart datum). Grid resolution = 10 m.

Figure 6.12 presents Hs in IG1 and IG2 period bands. From the end of the converging zone, IG1 loses a lot of energy in the river. At the beginning of the sinuosity of the river, Hs_{IG1} is lower than 0.1 m. A wave energy concentration is visible on the riverbanks.

Over 1.5 km from the end of the converging zone, Hs_{IG2} loses 0.1 m and is globally greater than 0.2 m from the beginning of the sinuosity of the river to the upstream part of the river seaport.

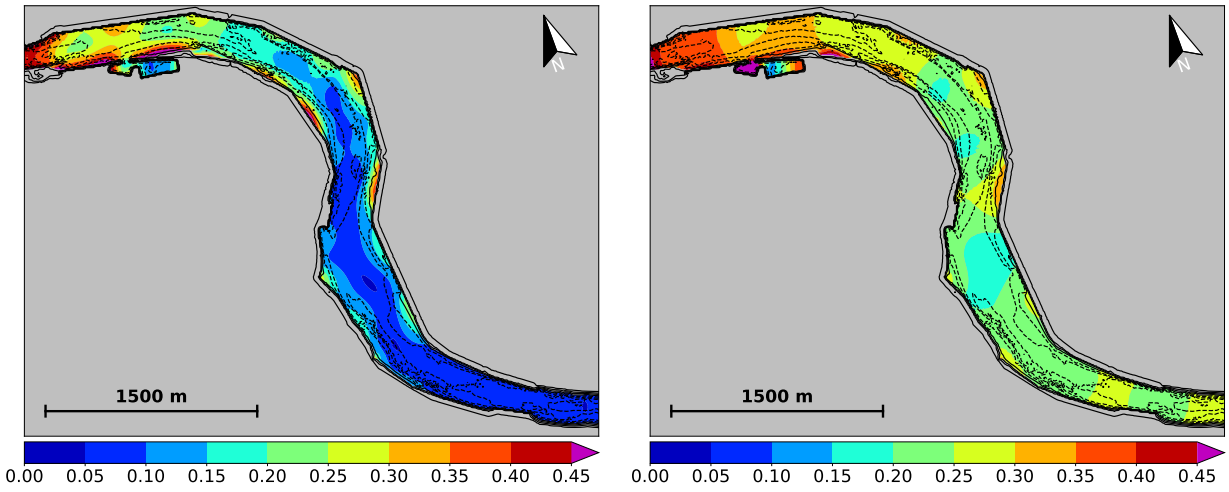

(a) Hs_{IG1} (b) Hs_{IG2}

Figure 6.12 – Maps of Hs in IG1 (30-100 s) and IG2 (100-300 s) period bands (unit: m). Current configuration of the area. (dotted lines) Contour lines (m respect to chart datum). Grid resolution = 10 m.

6.3.4 Upstream part of the Adour river

Figure 6.13 presents *Hs* in IG1 and IG2 period bands in the upstream part of the Adour and where the Nive river flows into the Adour (figure 6.4). In this area, the energy in IG1 band is low with $Hs_{IG1} < 0.1\ m$. A concentration of energy is visible on the riverbanks. In the upstream part of Adour, Hs_{IG1} is lower than 0.05 m

At the river seaport limit, Hs_{IG2} is greater than 0.2 m and loses only 0.05 m over a distance of 2.5 km. In the upstream part of Adour as well as in the Nive river, Hs_{IG2} is between 0.10 and 0.15 m. A local standing wave pattern seems to be visible with two anti-nodes located on the riverbanks.

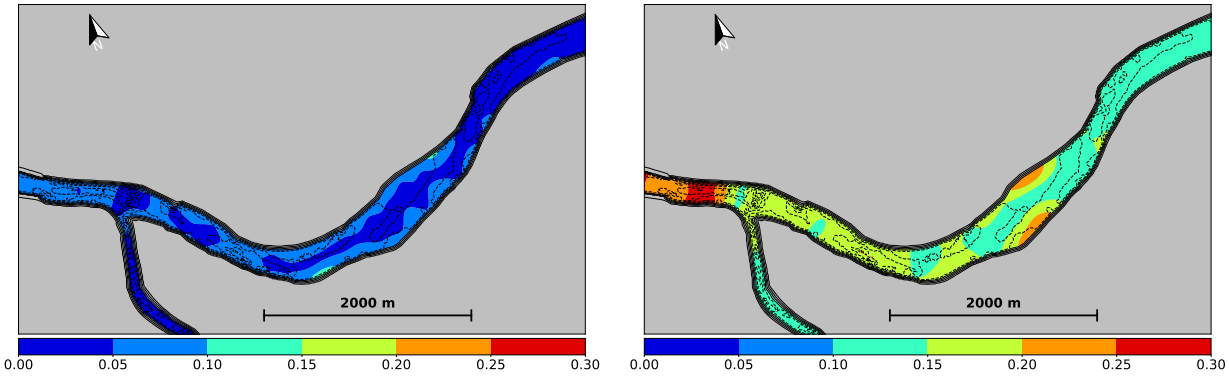

(a) Hs_{IG1} (b) Hs_{IG2}

Figure 6.13 – Maps of Hs in IG1 (30-100 s) and IG2 (100-300 s) period bands (unit: m). Current configuration of the area. (dotted lines) Contour lines (m respect to chart datum). Grid resolution = 10 m.

6.4 Transformation of IG waves along the river in ports area

To study the transformation of IG waves in ports area, different processes were isolated — effects of the marina, bottom friction dissipation and river geometry — by modifying the numerical domain, namely the bathymetry or bottom friction conditions (table 6.1). The input wave spectrum is however the same for all cases to keep the same wave field and phase locking. Numerical results are compared to the current configuration.

6.4.1 Influence of the marina (case 1)

Figure 6.14 shows the relative differences of Hs in IG1 and IG2 period bands without the marina. In front of the marina, a local amplification of IG1 results of the marina resonance (figure 4.4): a node characterized by a reduction in Hs is located at the marina mouth; anti-nodes are located on the opposite river bank and in the marina (not visible). A small reduction in Hs_{IG1} is noticeable upstream. Downstream of the marina, small amplifications of Hs_{IG2} are visible; upstream, reductions in Hs_{IG2} are rather uniform. The marina has only local effects on IG waves and is not responsible for the strong energy differences in IG1 and IG2 period bands.

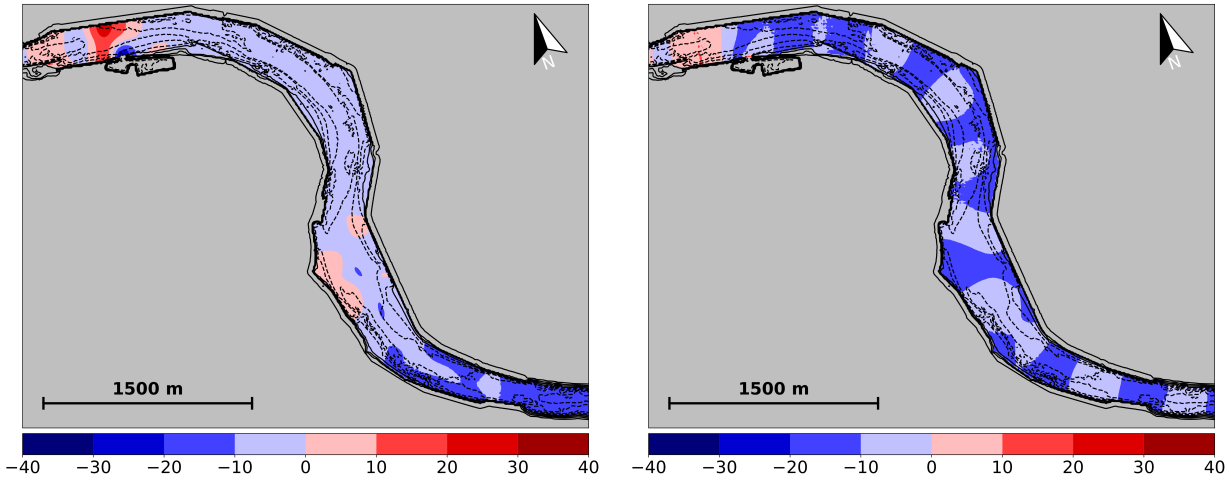

(a) Differences of Hs_{IG1}

(b) Differences of Hs_{IG2}

Figure 6.14 – Map of differences of Hs in (a) IG1 (30-100 s) and (b) IG2 (100-300 s) (unit: %), positive values correspond to increases. Configuration without the marina. Grid resolution = 10 m.

6.4.2 Effect of bottom friction dissipation (case 2)

Figure 6.15 shows the relative differences of Hs in IG1 and IG2 period bands without bottom friction in the river. Dissipation by bottom friction is low in ports area (±5%) and similarly affects IG1 and IG2 period bands. The Adour river bed, composed of sand and mud (Augris and Clabaut, 2001), has low bottom friction. The results are consistent with previous studies on IG waves dissipation in sandy beach environments (section 1.3.2).

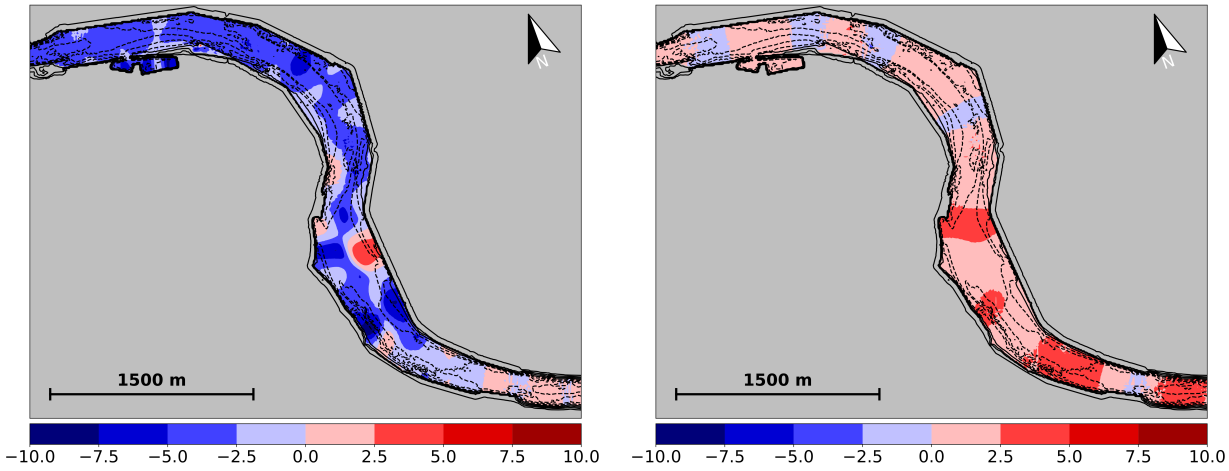

(a) Differences of Hs_{IG1} (b) Differences of Hs_{IG2}

Figure 6.15 – Map of differences of Hs in (a) IG1 (30-100 s) and (b) IG2 (100-300 s) (unit: %), positive values correspond to increases. Configuration without bottom friction in the Adour. Grid resolution = 10 m.

6.4.3 Effect of river cross-section profile and channel geometry (case 3)

In addition to the conditions of case 2, an uniform bathymetry is applied in the river from the river widening. Figure 6.16 presents Hs differences in IG1 and IG2 period bands. Strong differences between IG1 and IG2 energy are visible. IG1 is strongly affected by the river bathymetry and undergoes large dissipation during its upstream propagation; Hs_{IG2} differences compared to the current configuration are uniform, with an average reduction about 20%.

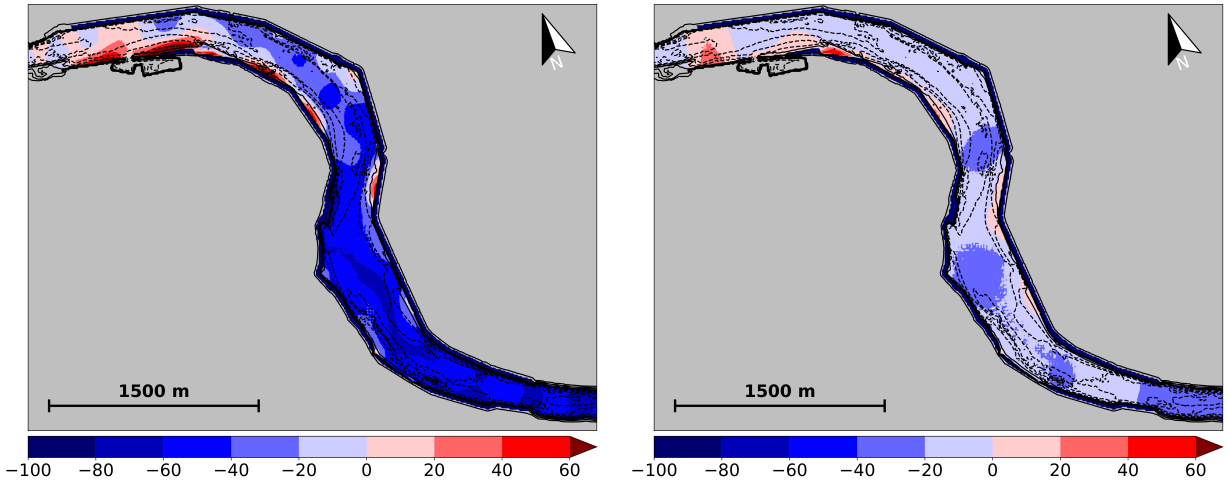

(a) Differences of Hs_{IG1} (b) Differences of Hs_{IG2}

Figure 6.16 – Map of differences of Hs in IG1 (30-100 s) and IG2 (100-300 s) period band (unit: %), positive values correspond to increases. Configuration with a uniform river bathymetry without bottom friction. Grid resolution = 10 m.

Figure 6.17 shows *Hs* in the IG1 and IG2 period bands for case 3. River acts as a wave guide, but the S-shape of the channel affects IG wave propagation in the river. From 2 km upstream, the cross-sectional distribution of IG1 energy presents strong gradients with energy increase at river bank (mainly outer curve) and energy reduction in the middle of the river. IG2, less affected by the river meandering, has a more uniform cross-sectional energy repartition.

Dissipation by bottom friction being negligible in the river, nonlinear energy transfer is thus expected as the main energy dissipation mechanism of IG waves in the river (section 1.3.2). The S-shaped channel favors energy concentration at river banks where sediments accumulate due to river processes. Local increase in wave non-linearity favors the steepening of IG waves and nonlinear energy transfer from low to high wave frequencies. As Hs_{IG1} is greater than Hs_{IG2} at river bank, nonlinearity and steepness of IG1 are greater: non-linear transfers are thus likely to occur from IG1 to higher wave frequencies (potentially to SW band) where wave energy is then dissipated.

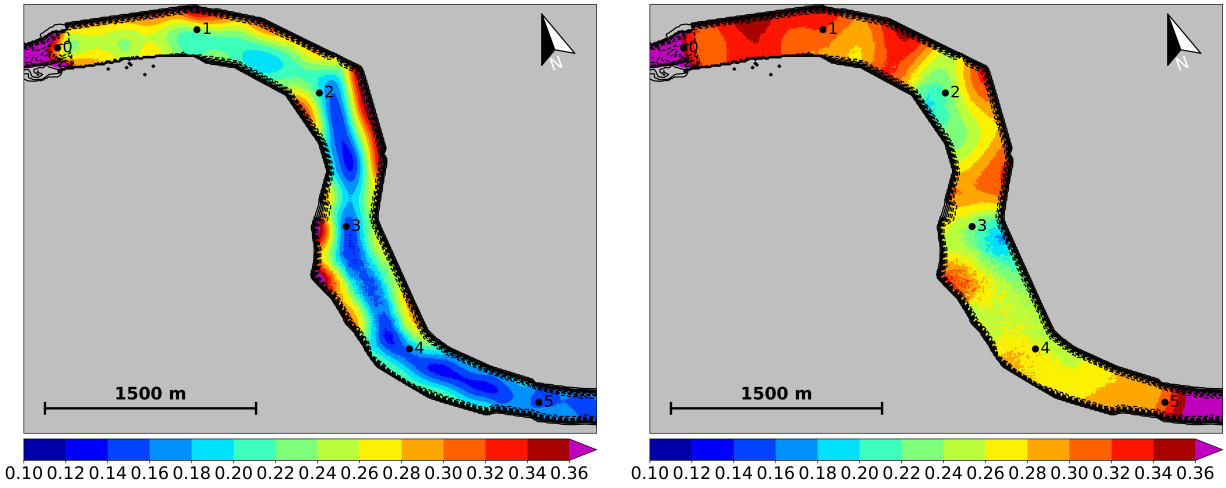

(a) Hs_{IG1} (b) Hs_{IG2}

Figure 6.17 – Map of Hs in IG1 (30-100 s) and IG2 (100-300 s) period bands (unit: m). Grid resolution = 10 m. Dots represent distances in kilometers from the first port wharf.

6.5 Influence of the deposit of dredged material (case 4)

The deposit of dredged material is visible at depths between -35.0 and -17.5 m and located between 2.5 and 3.5 km from the coastline. To study its effects on waves transformation, it is removed from the numerical domain and replaced by an uniform slope (SD configuration), namely the initial bathymetry of the area. All other input parameters are identical. *Hs* without the deposit as well as relative differences of *Hs* are presented in the following figures.

6.5.1 Nearshore zone

Figure 6.18 shows *Hs* in the SW period band as well as relative differences with the current configuration. The energy in the short wave period band is more uniform in the nearshore zone without the deposit, and Hs_{SW} is between 4.0 and 4.5 m outside the surf zone. South of the zone, an area with SW energy concentration is still visible at the level of rock outcrops, Hs_{SW} is locally greater than 6.0 m. In the vicinity of the river mouth, a small increase in Hs_{SW} is visible with values between 4.5 and 5.0 m.
Map of Hs_{SW} differences shows that the deposit of dredged material concentrates the energy of incident short waves on the port mouth. In the deposit trail, Hs_{SW} increases by about 25% and decreases by 15-20% on either side of the deposit. The deposit impacts the energy distribution of incident waves at the coast through refraction processes and

seems to concentrate the waves energy in the port mouth for the simulated event.

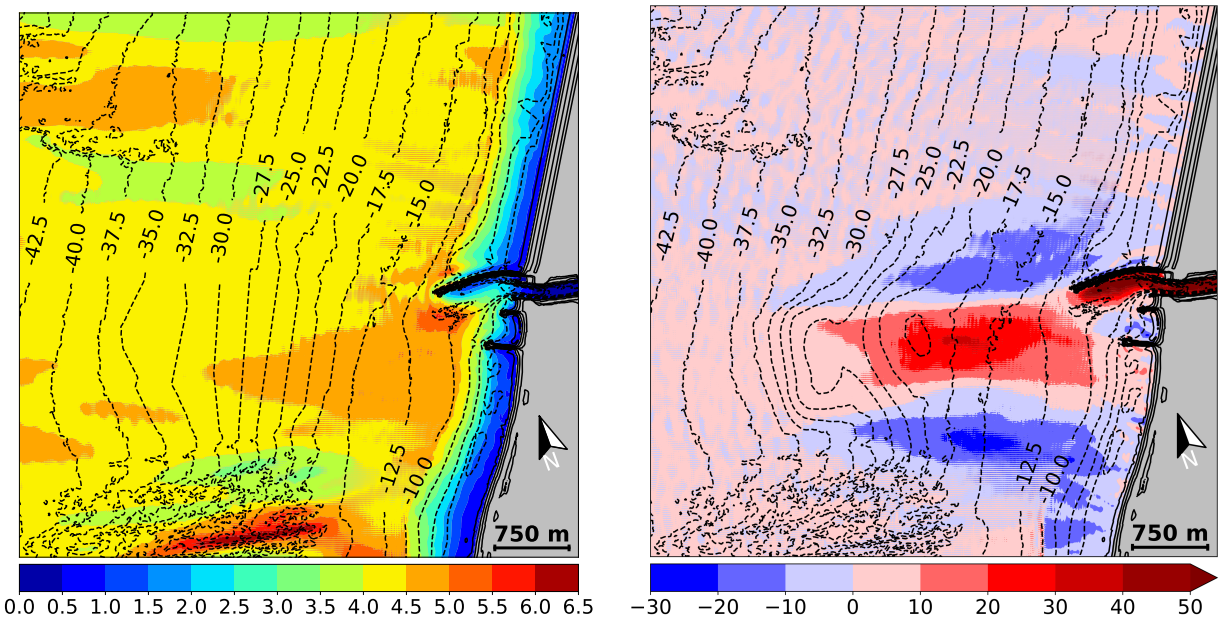

(a) Hs_{SW} (b) Differences of Hs_{SW}

Figure 6.18 – (a) Map of Hs in SW (6-30 s) period band (unit: m). (b) Map of differences of Hs (unit: %), positive values correspond to increases, formula: (CC-SD)/SD. Configuration (SD) without the deposit. (dotted lines) Contour lines (m respect to chart datum). Grid resolution = 10 m.

Figure 6.19 presents *Hs* in IG1 and IG2 period bands as well as the *Hs* differences compared to the current configuration. As for the SW band, the wave energy in IG1 is more uniform in the nearshore zone without the deposit. IG2 seems to be slightly affected by its presence.

Map of differences shows that at the top of the deposit Hs_{IG1} increases by about 40% and decreases by 10-20% on either side of the deposit (particularly in the south). IG2 seems less affected by the deposit, which leads to an increase in Hs_{IG2} between 10 and 30%.

The refraction due to the deposit affects IG1 and to a lesser extent IG2. In addition to this process, the reduction in water depth by the deposit increases the non-linearity of the incident short waves, and possibly the generation of IG waves (and especially IG1 according to the map).

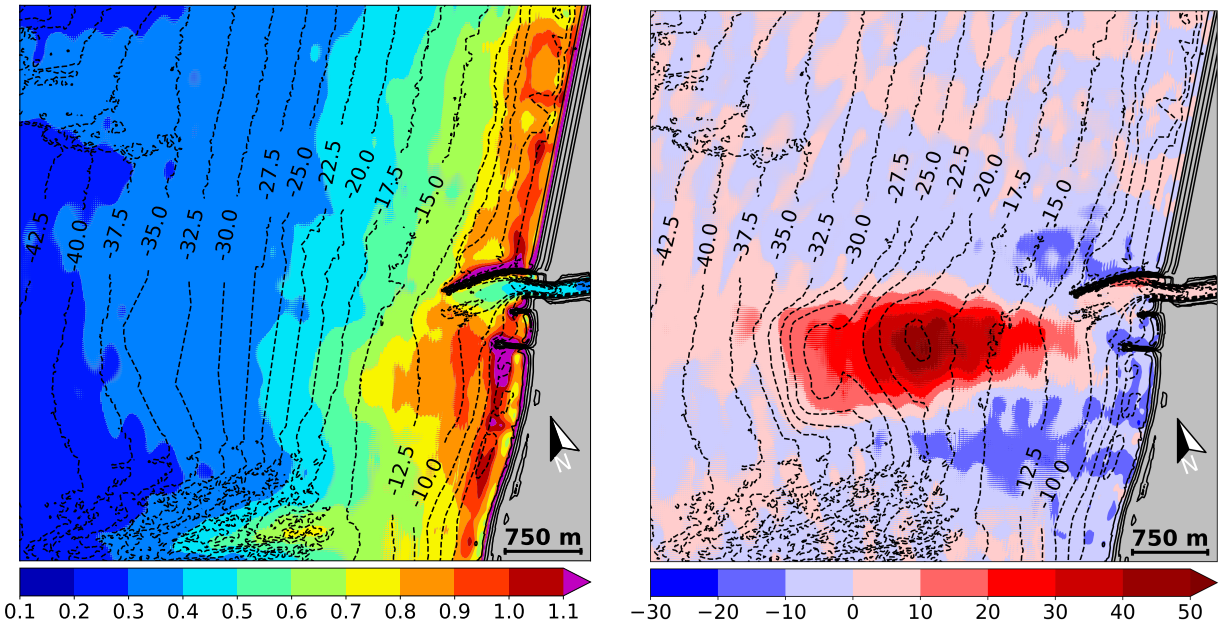

(a) Hs_{IG1} (b) Differences of Hs_{IG1}

(c) Hs_{IG2} (d) Differences of Hs_{IG2}

Figure 6.19 – (a, c) Maps of Hs IG1 (30-100 s) and IG2 (100-300 s) period bands (unit: m). (b, d) Maps of differences of Hs (unit: %), positive values correspond to increases, formula: (CC-SD)/SD. Configuration (SD) without the deposit. (dotted lines) Contour lines (m respect to chart datum). Grid resolution = 10 m.

6.5.2 River mouth

Figure 6.20 presents *Hs* in the SW period band as well as relative differences in *Hs*. At a depth of -10 m, Hs_{SW} is between 4 and 4.5 m without the deposit compared to 5 and 5.5 m for the current configuration. The SW waves intrusion into the area near the mouth is weaker, the access channel appears to be less exposed to short waves. At the north breakwater and close to the navigation channel, an increase in Hs_{SW} greater than 40% is visible and caused by the deposit. The incoming SW is still lower than 0.5 m in the converging zone without the deposit.

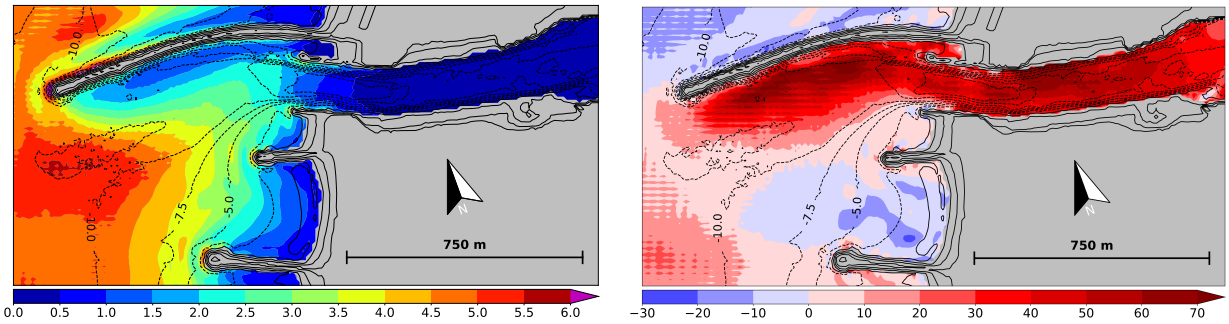

(a) Hs_{SW} (b) Differences of Hs_{SW}

Figure 6.20 – (a) Map of Hs in SW (6-30 s) period band (unit: m). (b) Map of differences of Hs (unit: %), positive values correspond to increases, formula: (CC-SD)/SD. Configuration (SD) without the deposit. (dotted lines) Contour lines (m respect to chart datum). Grid resolution = 10 m.

Figure 6.21 presents *Hs* in the IG1 and IG2 period bands as well as relative differences in *Hs*. Globally, the spatial wave energy repartition in IG1 and IG2 bands is comparable to the current configuration. In the converging zone at the port entrance, the wave energy in IG1 and IG2 is still similar, with a significant wave height between 0.4 and 0.5 m. Although an increase between 0 and 20% can be observed in the river mouth area, the amplitude of incoming IG waves in the port appears to be little impacted by the presence of the deposit.

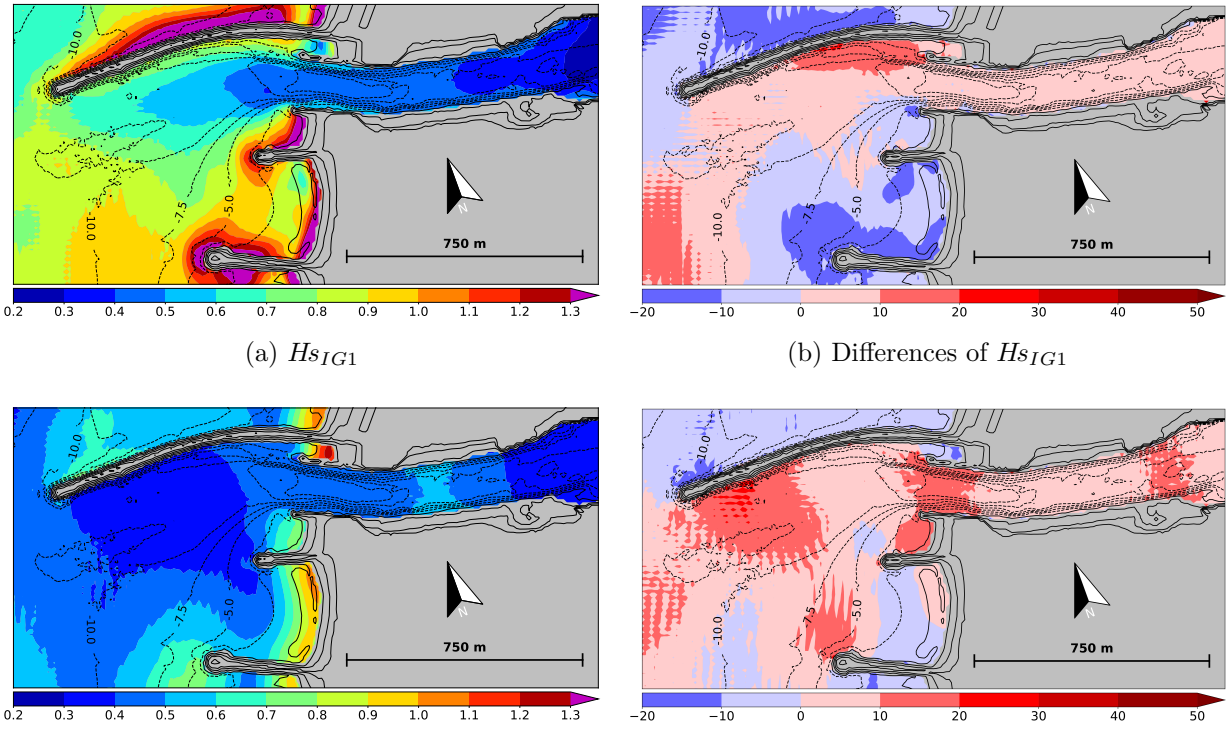

(a) Hs_{IG1} (b) Differences of Hs_{IG1}

(c) Hs_{IG2} (d) Differences of Hs_{IG2}

Figure 6.21 – (a, c) Maps of Hs IG1 (30-100 s) and IG2 (100-300 s) period bands (unit: m). (b, d) Maps of differences of Hs (unit: %), positive values correspond to increases, formula: (CC-SD)/SD. Configuration (SD) without the deposit. (dotted lines) Contour lines (m respect to chart datum). Grid resolution = 10 m.

6.5.3 Ports area

Figure 6.22 presents *Hs* in the IG period band as well as relative differences in *Hs*. Globally, the spatial IG wave energy repartition is comparable to the current configuration, with a global increase in Hs_{IG} between 0 and 10% in the river.

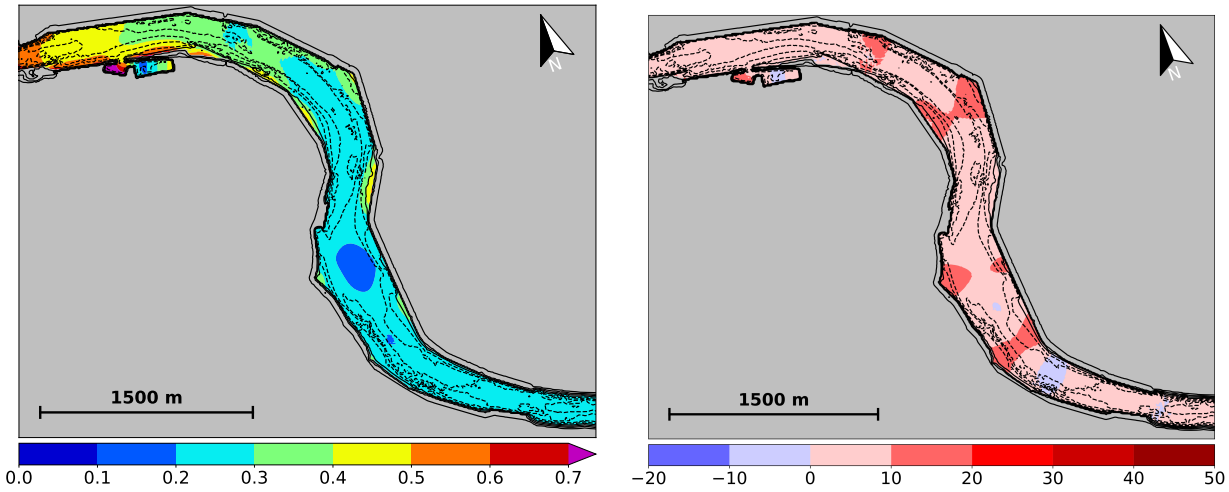

(a) Hs_{IG} (b) Differences of Hs_{IG}

Figure 6.22 – (a) Map of Hs in IG (30-300 s) period band (unit: m). (b) Map of differences of Hs (unit: %), positive values correspond to increases, formula: (CC-SD)/SD. Configuration (SD) without the deposit. (dotted lines) Contour lines (m respect to chart datum). Grid resolution = 10 m.

Figure 6.23 shows Hs_{tot} in the marina as well as relative differences in Hs. The significant wave height at the left basin boundary is between 0.8 and 0.9 m against 1.0 and 1.1 m for the current configuration. An increase of Hs_{tot} between 10 and 20% is observed in the left basin of the marina due to the presence of the deposit.

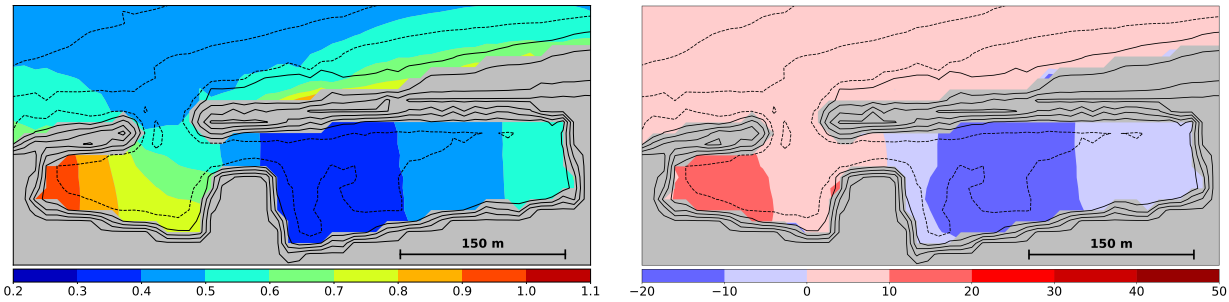

(a) Hs_{tot} (b) Differences of Hs_{tot}

Figure 6.23 – (a) Map of Hs_{tot} (6-2048 s) in the marina (unit: m). (b) Map of differences of Hs (unit: %), positive values correspond to increases, formula: (CC-SD)/SD. Configuration (SD) without the deposit. (dotted lines) Contour lines (m respect to chart datum). Grid resolution = 10 m.

6.6 Influence of the Adour river configuration: concave extension (case 5)

A new spatial configuration of the river mouth was simulated. It consists of a 350 m long concave extension of the current South breakwater in order to ensure a 350 m width harbor opening and thus create an outer harbor basin (DC configuration). This configuration was proposed in a former laboratory study carried out in the 1970s on a scale model to design the South breakwater (figure 2.3).

6.6.1 Nearshore zone

Figure 6.24 presents *Hs* in the SW and IG period bands as well as relative differences in *Hs*. The new configuration has little or no impact on the wave field in the nearshore zone both in the SW and IG period bands. Differences are only visible in the river mouth area. The neighboring south beaches are not affected by the extension in the SW bands, while an increase between 10 and 20% in Hs_{IG} is visible close to the south breakwater.

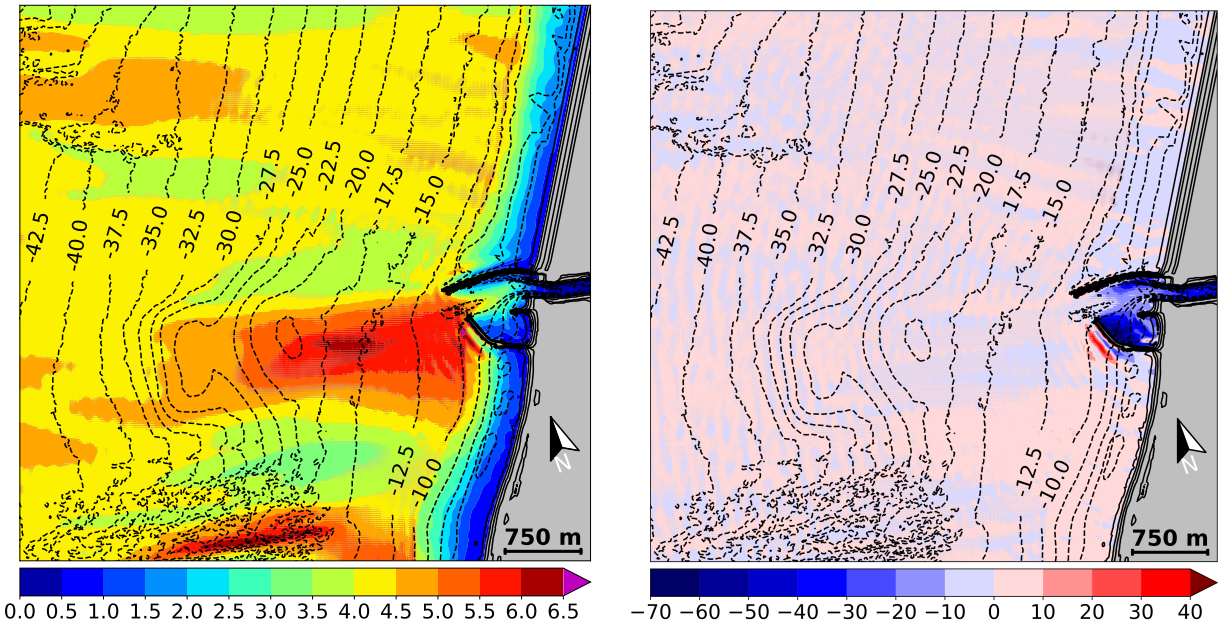

(a) Hs_{SW}

(b) Differences of Hs_{SW}

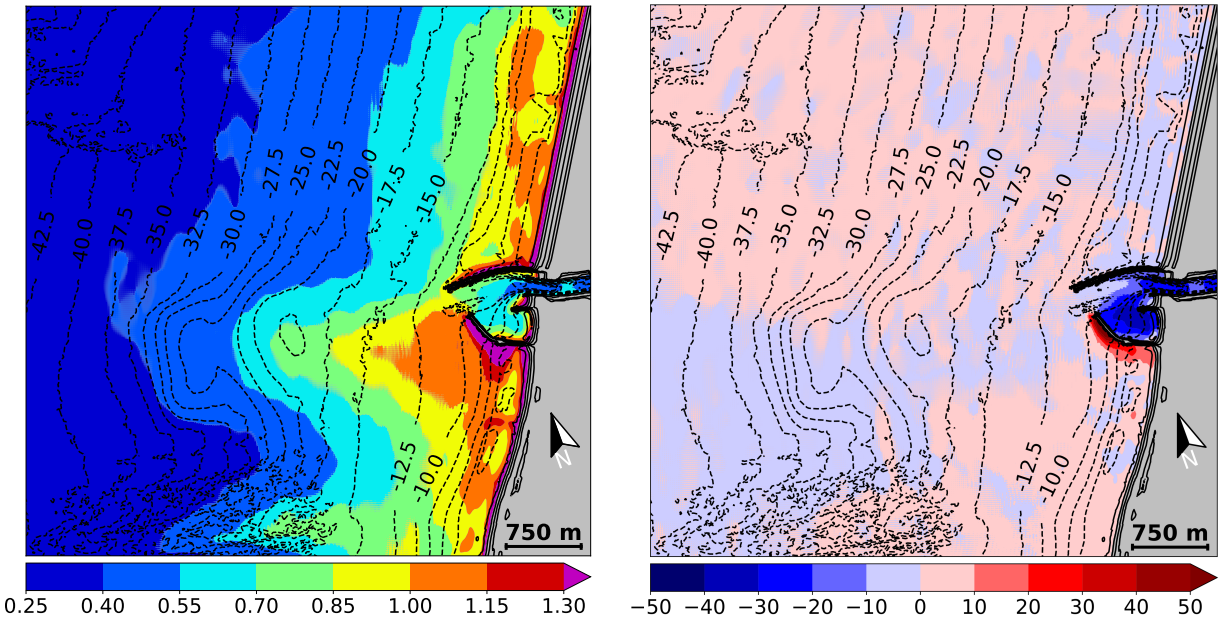

(c) Hs_{IG}

(d) Differences of Hs_{IG}

Figure 6.24 – (a, c) Map of Hs in SW (6-30 s) and in IG (30-300 s) period band (unit: m). (b, d) Map of differences of Hs (unit: %), positive values correspond to increases, formula: (DC-CC)/CC. Configuration (DC) with the concave extension of the South breakwater. (dotted lines) Contour lines (m respect to chart datum). Grid resolution = 10 m.

6.6.2 River mouth

Figure 6.25 presents *Hs* in the SW period band as well as relative differences in *Hs*. Short waves intrusions are still visible at the new port entrance. The extension has little effect (reduction of $Hs_{SW} < 10\%$) over 250 m from the entrance, then a reduction between 10 and 20% occurs up to the river access channel. At 350 m from the river access channel, Hs_{SW} is between 3.0 and 3.5 m. Reductions of more than 30% in Hs_{SW} are visible in the lower part of the North breakwater. A significant reduction in Hs_{SW} behind the new extended south breakwater ensures an overall area with $Hs_{SW} < 1.5\ m$
Reflection process occurs against the new structure, with areas where $Hs_{SW} > 6\ m$. The presence of the deposit, through the SW energy concentration phenomenon described above, would have an economical impact on any project to extend or modify the river mouth configuration, since the wave efforts on the structure would be higher.

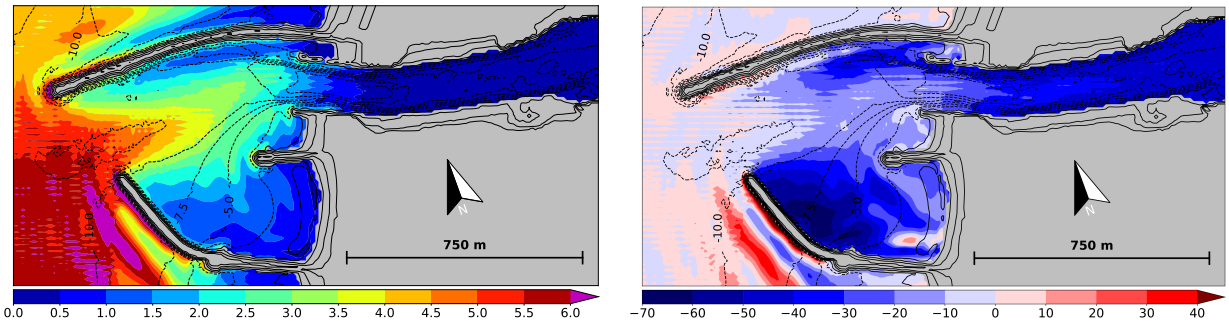

(a) Hs_{SW} (b) Differences of Hs_{SW}

Figure 6.25 – (a) Map of Hs in SW (6-30 s) period band (unit: m). (b) Map of differences of Hs (unit: %), positive values correspond to increases, formula: (DC-CC)/CC. Configuration (DC) with the concave extension of the South breakwater. (dotted lines) Contour lines (m respect to chart datum). Grid resolution = 10 m.

Figure 6.26 presents *Hs* in the IG1 and IG2 period bands as well as relative differences in *Hs*. From the new port entrance to 250 m from the river navigation channel, a reduction of Hs_{IG1} between 0 and 10% occurs. From this distance, the incoming IG1 wave height is reduced between 10 and 20%. Behind the structure, a significant energy reduction of IG1 ensures an area where $Hs_{IG1} < 0.5\ m$, even if an energy increase is visible at the solid boundaries of the outer harbor basin. The reflections of the incident IG1 waves against the new structure lead to Hs_{IG1} greater than 1.3 m.
From 250 m from the new port entrance, a significant reduction of Hs_{IG2} between 20 and 30% occurs. With the new configuration, the significant wave heights in IG1 and IG2 are between 0.3 and 0.4 m in the river converging zone.

The creation of the outer harbor basin seems to promote the generation of local resonance modes, as shown by the increase in IG energy at solid basin boundaries probably due to the presence of stationary wave anti-node.

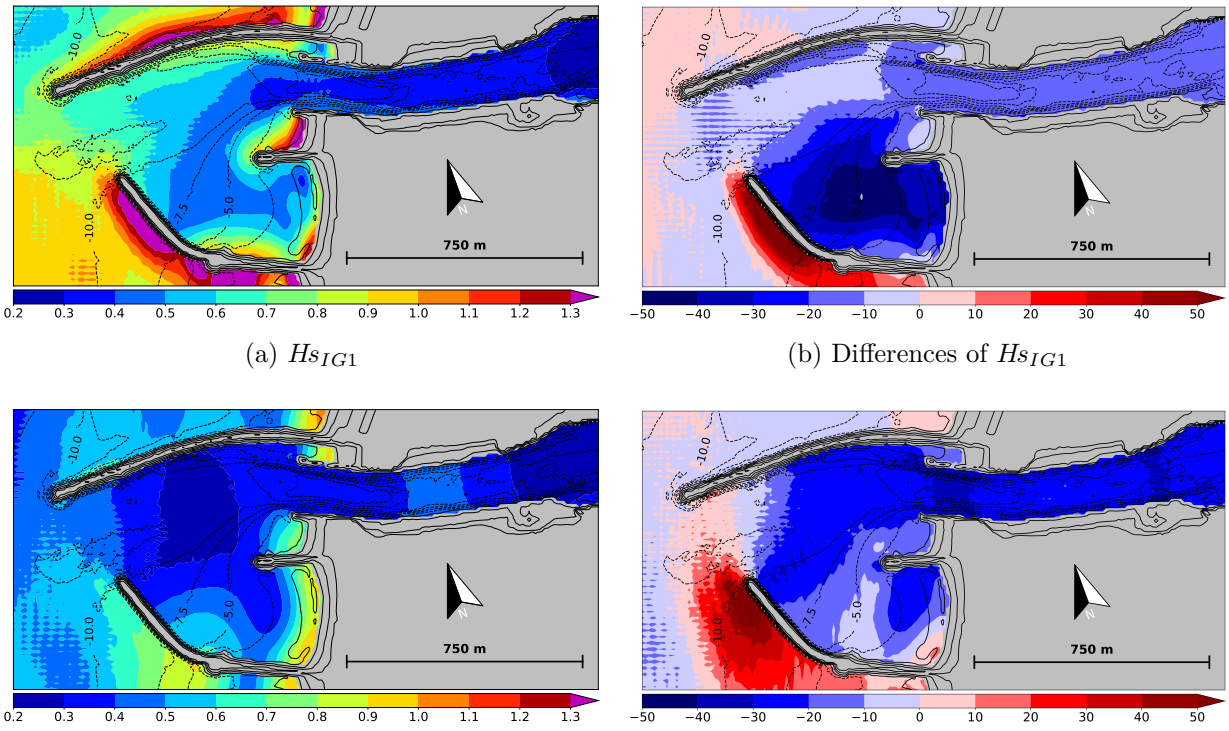

(a) Hs_{IG1} (b) Differences of Hs_{IG1}

(c) Hs_{IG2} (d) Differences of Hs_{IG2}

Figure 6.26 – (a, c) Map of Hs in IG1 (30-100 s) and IG1 (100-300 s) period band (unit: m). (b, d) Map of differences of Hs (unit: %), positive values correspond to increases, formula: (DC-CC)/CC. Configuration (DC) with the concave extension of the South breakwater. (dotted lines) Contour lines (m respect to chart datum). Grid resolution = 10 m.

6.6.3 Ports area

Figure 6.27 shows *Hs* in the IG1 and IG2 period bands as well as relative differences in *Hs*. The overall behavior of IG1 and IG2 in the river is similar to the current configuration. The incident wave energy reduction in IG1 and IG2 bands, induced by the new mouth configuration, is maintained in the river.

IG1 rapidly loses energy in the river and a reduction in Hs_{IG1} between 10 and 20% is observed in the river. From the beginning of the sinuosity of the rive, Hs_{IG2} is between 0.15 and 0.20 m and a reduction in Hs_{IG2} between 20 and 30% is observed in the river.

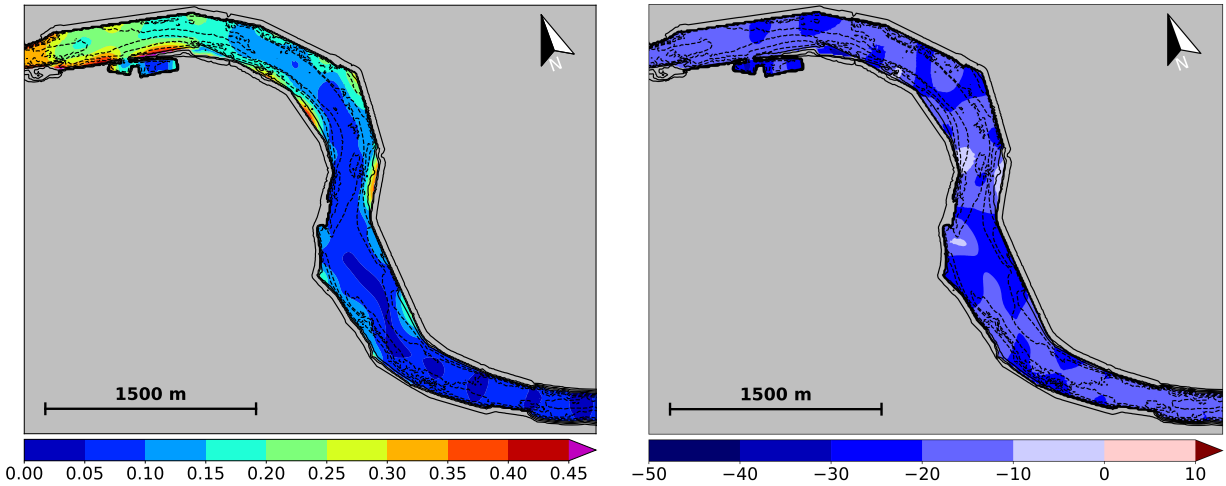

(a) Hs_{IG1} (b) Differences of Hs_{IG1}

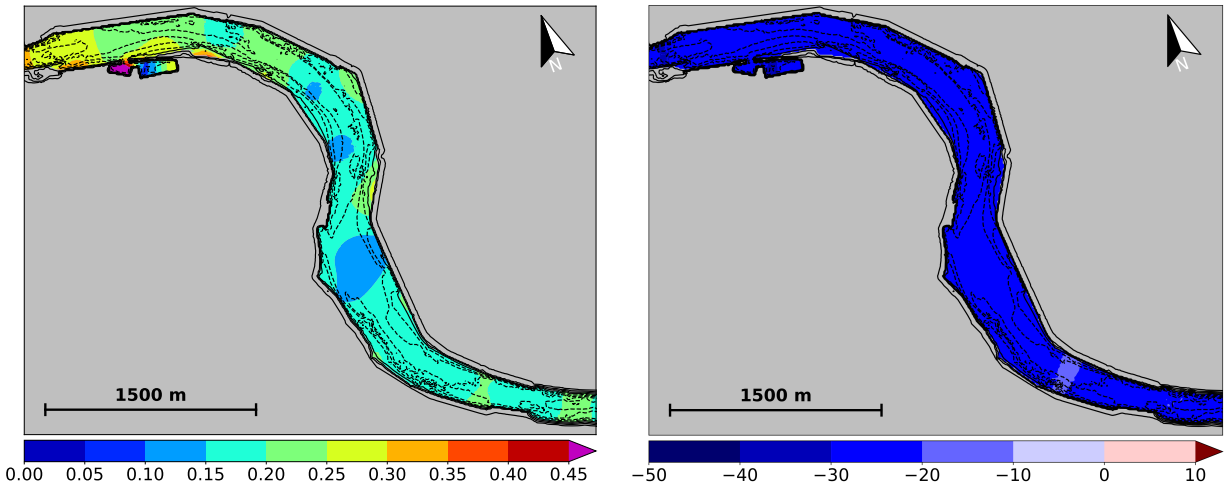

(c) Hs_{IG2} (d) Differences of Hs_{IG2}

Figure 6.27 – (a, c) Map of Hs in IG1 (30-100 s) and IG1 (100-300 s) period band (unit: m). (b, d) Map of differences of Hs (unit: %), positive values correspond to increases, formula: (DC-CC)/CC. Configuration (DC) with the concave extension of the South breakwater. (dotted lines) Contour lines (m respect to chart datum). Grid resolution = 10 m.

Figure 6.28 shows Hs_{tot} in the marina as well as relative differences in Hs. The IG wave energy reduction in the river has a favorable effect on the reduction of the seiches amplitude in the marina: Hs_{tot} at the left basin boundary is between 0.7 and 0.8 m. A reduction between 20 and 30% is observed in the left basin.

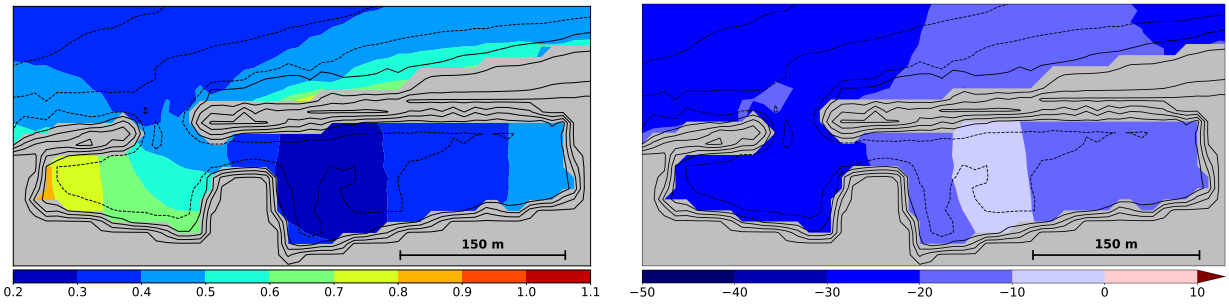

(a) Hs_{tot} (b) Differences of Hs_{tot}

Figure 6.28 – (a) Map of Hs_{tot} (6-2048 s) in the marina (unit: m). (b) Map of differences of Hs (unit: %), positive values correspond to increases, formula: (DC-CC)/CC. Configuration (DC) with the concave extension of the South breakwater. (dotted lines) Contour lines (m respect to chart datum). Grid resolution = 10 m.

6.6.4 Upstream part of the Adour river

Figure 6.29 shows Hs in the IG1 and IG2 period bands as well as relative differences in Hs. As for the current configuration, the energy in IG1 is low in the upstream part of the Adour and $Hs_{IG1} < 0.05\ m$. The IG2 energy reduction is maintained in the upstream part and Hs_{IG2} is between 0.10 and 0.15 m.

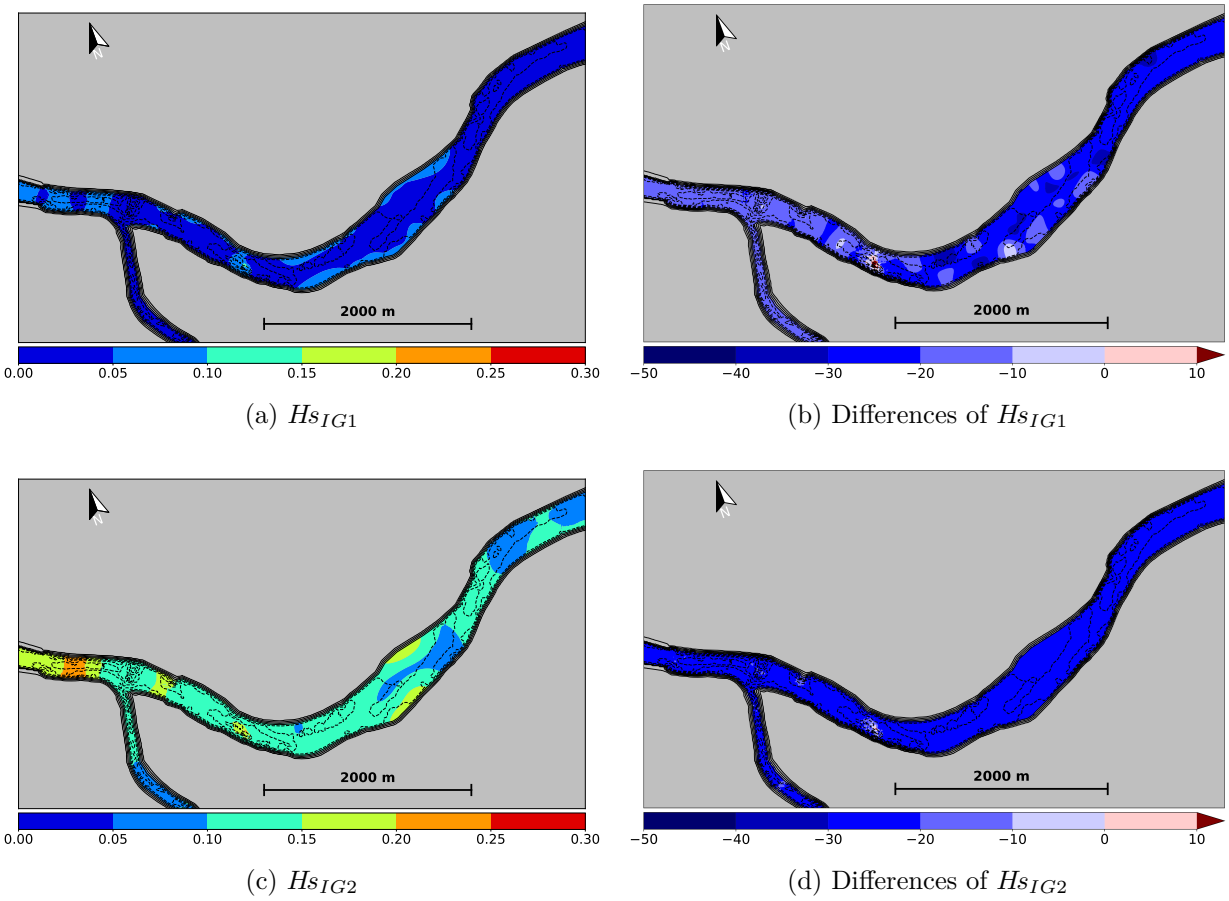

(a) Hs_{IG1} (b) Differences of Hs_{IG1}

(c) Hs_{IG2} (d) Differences of Hs_{IG2}

Figure 6.29 – (a, c) Map of Hs in IG1 (30-100 s) and IG1 (100-300 s) period band (unit: m). (b, d) Map of differences of Hs (unit: %), positive values correspond to increases, formula: (DC-CC)/CC. Configuration (DC) with the concave extension of the South breakwater. (dotted lines) Contour lines (m respect to chart datum). Grid resolution = 10 m.

6.7 Conclusion

The BOSZ model was first validated by comparing experimental and numerical results during a one-year return period storm event. Comparisons of spectra show that the model can reproduce the generation of IG waves associated with the incident short waves and their transformation in the river, even with a relatively coarse mesh (10 m grid resolution).

The numerical study confirms the results of the field campaign analysis (chapter 4). The breakwaters at the port mouth efficiency protect the port against incoming short waves and IG waves control port agitation. For the simulated event, the significant wave heights in IG1 and IG2 period bands are similar and about 0.4 m at the first harbor dock located 1.4 km from the river mouth. However, IG1 loses a lot of energy during the river

propagation, and after a distance of 2.5 km Hs_{IG1} is lower than 0.1 m. In contrast, Hs_{IG2} is greater than 0.1 m even at a distance of 10 km, for the simulated event.

To investigate the bi-modal energy distribution of IG period band, several numerical cases were simulated to study the contribution of the marina, the bottom friction and the channel geometry (i.e S-shape and river bathymetry) on the transformation and dissipation of IG waves in the river. The marina has only a local effect on IG waves: its basin resonance leads to the formation of an anti-node located on the opposite river bank; small reductions in IG1 and IG2 are noticeable upstream. Dissipation by bottom friction is negligible in the river due the nature of Adour river bed material (sand and mud). Channel geometry is the main parameter explaining the strong differences in IG1 and IG2 energy. The S-shape of the channel affects IG wave propagation in the river. Cross-sectional distribution of IG1 energy presents strong gradients with energy increase at river bank, where sediments accumulate due to river processes. The resulting local increase in non-linearity and steepness of IG1 favors non-linear transfers from IG1 to higher wave frequencies (potentially to SW band), where wave energy is dissipated. In contrast to IG1, IG2 is less affected by the meandering shape of the channel and the river bathymetry and loses less energy during its upstream propagation

The numerical simulations show that the deposit of dredged material concentrates the energy of incident short waves on the port mouth by refraction process. In the deposit trail, Hs_{SW} increases by about 25% and decreases by 15-20% on either side of the deposit, for the simulated event. At the north breakwater and close to the navigation channel, an increase in Hs_{SW} greater than 40% accentuates the mechanical stresses on the structure and can disrupt navigation procedures. The refraction due to the deposit also affects IG1 and to a lesser extent IG2, but the amplitude of incoming IG waves in the port appears to be little impacted by the presence of the deposit, for the simulated event.

A new spatial configuration of the river mouth was simulated and was based on the laboratory study carried out in the 1970s on a scale model to design the South breakwater (section 2.1.3). The current South breakwater is extended by a 350 m long concave part. By keeping the same input parameters, the numerical results show that this configuration has a favorable impact on the reduction of harbor oscillations. Hs_{SW} is reduced by about 15% in the navigation channel for the simulated event. The amplitude of incoming IG waves in the port is also reduced by about 15% for Hs_{IG1} and about 25% for Hs_{IG2} for the simulated event. This reduction, maintained during the propagation in the river, could reduce the seiche amplitude in the marina and reduce the risk of surge motion of moored ships in the seaport. The amplitude of IG2 upstream of the river is also reduced. It should be noted that the creation of an outer harbor basin promotes the generation of local resonance modes.

The position of a dredging disposal area seems to be crucial and can have an impact on wave energy distribution at the coastline. For the simulated event, the deposit favors the concentration of short wave energy on port structures and has an impact on incident IG waves. Simulations with different incident wave directions could complete this study and determine the effect of the deposit under different wave conditions.
Simulations over a whole tidal cycle would make it possible to study the influence of water level variation and tidal currents on the IG dynamics in the nearshore zone as well as in the river.

Chapter 7

Conclusion

This study investigated the dynamics of infragravity (IG) waves in river seaports based on water levels measurements and numerical simulations using a Boussinesq-type wave model. Port of Bayonne constitutes the study site. It was selected as it is representative of a seaport located nearby a river mouth in a mesotidal environment. It is exposed to very energetic incident swells during storm events, which are favorable to the generation of significant IG waves. A small adjacent marina is located on a riverbank at the entrance of the harbor.

The main objectives of the study were to characterize the functioning of port of Bayonne including the mechanisms of generation and dissipation of infragravity waves, and their interactions with port activities such as dredging operations and port infrastructures.

An intensive measurement campaign was conducted over 3 consecutive winters (2016-2019). Five pressure sensors were deployed in Port of Bayonne: one at the river mouth measuring the incoming waves, three in the Adour river (river seaport) to study waves evolution in the river and one in the marina recording the seiche. A directional swell buoy continuously measured the offshore agitation conditions. This unique set of data covers a large range of external forcing scenarios: calm and energetic offshore incident waves, different water level and tide phases.

The local measurements of water level oscillations were supplemented by a numerical model validated using the field measurements. A phase-resolving Boussinesq-type wave model, BOSZ model, was used to simulate the propagation and transformation of waves from the open sea to the coast and then into the river. Such a wave model describes both non-linear interactions and dispersive effects at wave scale and allows to study the IG wave transformation and interactions with coastal structures.

7.1 Functioning of port of Bayonne

The incident short waves (SW) (5-30 s) are efficiently damped at the harbor mouth by two main breakwaters. The maximum wave height in this period band recorded at the river mouth was 1.3 m. The remaining SW energy is strongly dissipated in the river ($Hs_{SW,max} < 0.2\ m$). IG waves (30-300 s) control port agitation and represent the main part of the variance of the free surface (80%), a maximum Hs_{IG} of 0.7 m was recorded at 1.4 km from the river mouth. As they enter the harbor, the IG waves no longer receive energy from SW waves and propagate freely without amplification in the river which acts as a wave guide.

The marina is a semi-enclosed basin, and the periods of its fundamental (period of ~5 min) and harmonic modes are in the IG period band. The amplification of the energetic external forcing by the basin geometry can generate large seiche events ($Hs \approx 1\ m$). The marina, divided into two connected basins which interact with each other, has a complex geometric configuration. A numerical model, based on harmonic analysis method, was used to study the natural resonance mode of the marina and to isolate the oscillation modes, which are specific to each basins and to the coupling between them.

The typical natural period of a cargo-type moored vessel is 1 min or more which falls into the IG frequency band. The resonance of this oscillating system can lead to a significant surge motion (parallel to the dock) of the boat moored in the river seaport and possibly to a sudden snapping of mooring lines.

At the Adour river entrance, two parallel jetties reduce the river cross-section with the aim to increase the ebb flow velocity and limit silting. At the first harbor dock, the river cross-section increases, which results in a reduction of incident wave energy across all frequency bands. At the river mouth, the wave energy is very similar during ebb and flood tides, but the flood current, in the same direction of wave propagation, leads to a higher incoming wave energy flux. Moreover, the widening of the river cross-section between the converging zone and the first quay leads to a decrease in the magnitude of flow velocity, the wave energy therefore increases during flood to balance the decrease in the energy propagation velocity.

7.2 IG waves propagation in a river channel

The energy distribution in the IG band displays a bi-modal distribution between band IG1 (30-100 s) and IG2 (100 s-5 min). Unlike IG1, IG2 loses little or no energy during the propagation in the river.

At low tide the incoming IG waves have more energy than at high tide (mainly in IG2

period band). These differences are conserved up to about 3.5 km from the river mouth and reversed beyond that.
The simulation of a one-year return-period storm event ($Hs = 6\ m$ and $Tp = 18\ s$) shows that the significant wave height is about 0.4 m for IG1 and IG2 at the first harbor dock located 1.4 km from the river mouth. Over a distance of 2.5 km, Hs_{IG1} is lower than 0.1 m while Hs_{IG2} is greater than 0.1 m at a distance of 10 km.
To investigate the bi-modal energy distribution of IG period band, several numerical cases were simulated to study the contribution of the marina, the bottom friction and the channel geometry (i.e S-shape and river bathymetry) on the transformation and dissipation of IG waves in the river. The marina has only a local effect on IG waves: its basin resonance leads to the formation of an anti-node located on the opposite river bank. Dissipation by bottom friction is negligible in the river due the nature of Adour river bed material (sand and mud). Channel geometry is the main parameter explaining the strong differences in IG1 and IG2 energy. The S-shape of the channel affects IG wave propagation in the river. Cross-sectional distribution of IG1 energy presents strong gradients with energy increase at river bank, where sediments accumulate due to river processes. The resulting local increase in non-linearity and steepness of IG1 seems to favor non-linear transfers from IG1 to higher wave frequencies (potentially to SW band), where wave energy is dissipated. In contrast to IG1, IG2 is less affected by the meandering shape of the channel and the river bathymetry and loses less energy during its upstream propagation
The results of this study suggest that dredging operations in the river can affect IG wave propagation and could favor their dissipation in the river.

7.3 IG wave generation mechanisms

The nearshore area of port of Bayonne, characterized by gentle slopes (~1%), presents a mild-slope regime according to the classification of Van Dongeren et al. (2007). The generation of IG waves is therefore mainly due to the bound IG wave shoaling mechanism than the moving breakpoint mechanism. The coast is exposed to incident energetic swells that favor the generation of bound IG waves. During the shoaling phase, the gentle slope of the nearshore area allows significant energy transfers from short wave to bound IG and therefore their growth in amplitude. These two effects result in a significant infragravity wave energy at the coast.
The tide and river currents are small in the bound IG wave generation area and seem to have only limited impact on the incoming IG waves' amplitude recorded at the river mouth.

7.4 IG waves interactions with port activities

An underwater sediment deposit is located between 2.5 and 3.5 km from the coast and peaks at -17 m. It is made of material from various dredging operations of the port entrance. The simulation of the one-year return-period storm event shows that the deposit concentrates the energy of incident short waves on the port mouth by refraction process. In the deposit trail, Hs_{SW} increases by about 25% and decreases by 15-20% on either side of the deposit, for the simulated event. At the north breakwater and close to the navigation channel, an increase in Hs_{SW} greater than 40% accentuates the mechanical stresses on the structure and can disrupt navigation procedures. The refraction due to the deposit also affects IG1 and to a lesser extent IG2. However, the total significant wave height of incoming IG waves in the port appears to be little impacted by the presence of the deposit, for the simulated event.
The results of this study suggest that the position of a dredging disposal can be critical as it can favor the concentration of short wave energy on port structures as well as have an impact on incident IG waves.

A new spatial configuration of the river mouth was simulated. It consists of a 350 m long concave extension of the current South breakwater in order to ensure a 350 m width harbor opening and thus create an outer harbor basin. This configuration was proposed in a former laboratory study carried out in the 1970s on a scale model to design the South breakwater. By keeping the same input parameters, the numerical results show that this configuration has a favorable impact on the reduction of harbor oscillations. Hs_{SW} is reduced by about 15% in the navigation channel for the simulated event. The amplitude of incoming IG waves in the port is also reduced by about 15% for Hs_{IG1} and about 25% for Hs_{IG2}. This reduction, maintained during the propagation in the river, could reduce the seiche amplitude in the marina and reduce the risk of surge motion of moored ships in the seaport. The amplitude of IG2 upstream of the river is also reduced. It should be noted that the creation of an outer harbor basin promotes the generation of local resonance modes.
Spatial configuration of a river mouth could reduce the incoming IG wave amplitude in the port.

7.5 Further work

Further research can be undertaken to complete and extend this study.

7.5.1 Further numerical simulations

The numerical simulations of a storm event, characteristic of annual storm conditions, was performed for a constant water level neglecting the effect of the tide. It would be interesting to extend the results of this study by considering different storm scenario in order to complement the understanding of the behavior of the system during extreme wave conditions such as a ten-year or centennial return period storm event. Simulations over a complete tidal cycle would make it possible to study the influence of water level variation and tidal currents on the IG dynamics both on their generation in the nearshore zone and on their propagation and dissipation in the river. Finally, the impact of global climate change could also be studied.

7.5.2 Influence of the ambient current

Recent studies (Defontaine et al., 2019) have shown that during high river flow and tidal range, the Adour river can be strongly stratified due to the development of pycnocline. This scenario generally occurs when there is a flooding risk upstream of the river. In our study, the stratification of the Adour river was not considered. This questions the influence of a sheared flow on the propagation of long waves. In future work, it would be interesting to consider the following questions :

- What is the impact of a stratified environment on the upstream propagation of IG waves in a river ?
- What is the contribution of IG waves to upstream flooding? Can they be responsible for exceeding the safety thresholds?

7.5.3 Surge motion of moored boat

The excessive surge motions of cargo-type moored vessel occurring in the seaport result from the interaction between long waves and vessel. Generally, this problem is addressed numerically by coupling a wave model to a dynamic model (Van Der Molen et al., 2006). This problem could be managed by directly integrating floating objects into a fluid model and particularly in depth-integrated Boussinesq-type wave models.

7.5.4 Predictive alert systems

In the same way as the national tide gauge network, a sustainability network of a high-frequency acquisition data could be dedicated to the measurement of harbor oscillations. Associated with the real-time sea state data provided by wave buoys, this continuous data

acquisition would allow the development of effective predictive system of harbor oscillations.

In this study, only a basic empirical formulation was developed based on multi-linear regression method. Other methods could be used to establish the statistical model, such as nonparametric method or the use of intermediate analytical variable for the long waves generation (Stiassnie and Drimer, 2006). Statistical tools can also be used such as artificial neural network (López and Iglesias, 2013) or bayesian network (Poelhekke et al., 2016). Such methods present a high potential but require a lot of data covering a wide range of external conditions to be adjusted and calibrated. The databases could be completed with results from wave models.

These predictive systems could be integrated into a more global monitoring system (González-Marco et al., 2008) of which it can be the first level. As a 2nd level of the monitoring system, waves models could be initiated to determine the whole wave field. In the near future, Boussinesq-type numerical models could be implemented in an operational approach because computing times are continuously reduced (development on GPUs for example) (Tavakkol and Lynett, 2017).

Appendix A

Derivation of the set of Boussinesq-type equations proposed by Nwogu (1993)

A.1 Leibniz integral rule

$$\frac{d}{dx}\left(\int_{a(x)}^{b(x)} f(x,t)dt\right) = f(x,b(x)).\frac{d}{dx}b(x) - f(x,a(x)).\frac{d}{dx}a(x) + \int_{a(x)}^{b(x)} \frac{\partial}{\partial x}f(x,t)dt$$

A.2 Nondimensional variables

$$\begin{array}{llll} x'=lx & u'=\varepsilon\sqrt{gh_0}u & \eta'=a_0\eta & t'=\frac{l}{\sqrt{gh_0}}t \\ y'=ly & v'=\varepsilon\sqrt{gh_0}v & h'=h_0h & \\ z'=h_0z & w'=\frac{\varepsilon}{\mu}\sqrt{gh_0}w & p'=\rho g a_0 p & \end{array}$$

$$\text{Nonlinearity: } \varepsilon = \frac{a_0}{h_0}$$

$$\text{Frequency dispersion: } \mu = \frac{h_0}{l}$$

A.3 Continuity equation (CE)

$$
\begin{aligned}
u'_{x'} + v'_{y'} + w'_{z'} = 0 &\iff \frac{\varepsilon\sqrt{gh_0}}{l}u_x + \frac{\varepsilon\sqrt{gh_0}}{l}v_y + \frac{\varepsilon}{\mu h_0}\sqrt{gh_0}w_z = 0 \\
&\iff u_x + v_y + \overbrace{\frac{l}{\mu h_0}}^{=1/\mu^2} w_z = 0 \\
&\iff \boxed{\mu^2(u_x + v_y) + w_z = 0} \ \textbf{(3)}
\end{aligned}
$$

A.4 Euler's equations of motion on x an y

$$
\begin{aligned}
& u'_{t'} + u'u'_{x'} + v'u'_{y'} + w'u'_{z'} + \frac{1}{\rho}p'_{x'} = 0 \\
\iff & \frac{\varepsilon g h_0}{l}u_t + \frac{\varepsilon^2 g h_0}{l}uu_x + \frac{\varepsilon^2 g h_0}{l}vu_y + \frac{\varepsilon^2 g}{\mu}wu_z + \frac{g a_0}{l}p_x = 0 \\
\iff & \frac{h_0}{l\varepsilon}u_t + \frac{h_0}{l}uu_x + \frac{h_0}{l}vu_y + \frac{1}{\mu}wu_z + \frac{a_0}{\varepsilon^2 l}p_x = 0 \\
\iff & \frac{\mu^2}{\varepsilon}u_t + \mu^2 uu_x + \mu^2 vu_y + wu_z + \overbrace{\frac{a_0\mu}{\varepsilon^2 l}}^{=\frac{1}{\varepsilon}\frac{a_0}{l}\frac{h_0}{l}\frac{h_0}{a_0}=\frac{\mu^2}{\varepsilon}} p_x = 0 \\
\iff & \boxed{\mu^2 u_t + \varepsilon\mu^2 uu_x + \varepsilon\mu^2 vu_y + \varepsilon wu_z + \mu^2 p_x = 0} \ \textbf{(4) and (5)}
\end{aligned}
$$

A.5 Euler's equations of motion on z

$$
\begin{aligned}
& w'_{t'} + u'w'_{x'} + v'w'_{y'} + w'w'_{z'} + \frac{1}{\rho}p'_{z'} + g = 0 \\
\iff & \varepsilon g \overbrace{\frac{h_0}{\mu l}}^{=1} w_t + \varepsilon^2 g\frac{h_0}{\mu l}uw_x + \varepsilon^2 g\frac{h_0}{\mu l}uw_y + g\frac{\varepsilon^2}{\mu^2}ww_z + g\frac{a_0}{h_0}\frac{\partial p}{\partial z} + g = 0 \\
\iff & \boxed{\varepsilon w_t + \varepsilon^2 uw_x + \varepsilon^2 vw_y + \frac{\varepsilon^2}{\mu^2}ww_z + \varepsilon p_z + 1 = 0} \ \textbf{(6)}
\end{aligned}
$$

A.6 Irrotationality condition (IC)

$$\begin{aligned} u_z &= w_x \\ v_z &= w_y \quad \textbf{(7)} \\ w_x &= u_z \end{aligned}$$

A.7 Dynamic boundary condition at the free surface (DBC) at the free surface

$$\text{at } z = \varepsilon\eta\text{: } p = 0 \quad \textbf{(8)}$$

A.8 Kinematic boundary condition (KBC) at the free surface

$z' = \eta'(x, y, t) \iff h_0 z = a_0 \eta \iff z = \varepsilon\eta$

$$\begin{aligned} & w'\Big|_{z'=\eta'} = \eta'_{t'} + u'\Big|_{z'=\eta'}\eta'_{x'} + v'\Big|_{z'=\eta'}\eta'_{y'} \\ \iff & \frac{\varepsilon}{\mu}\sqrt{gh_0}w\Big|_{z=\varepsilon\eta} = \frac{a_0}{l}\sqrt{gh_0}\eta_t + \varepsilon\sqrt{gh_0}u\Big|_{z=\varepsilon\eta}\frac{a_0}{l}\eta_x + \varepsilon\sqrt{gh_0}v\Big|_{z=\varepsilon\eta}\frac{a_0}{l}\eta_y \\ & \qquad\qquad \overbrace{\qquad\qquad}^{\frac{a_0}{l}\frac{\mu}{\varepsilon}=\frac{a_0}{l}\frac{{h_0}^2}{la_0}=\mu^2} \\ \iff & w\Big|_{z=\varepsilon\eta} = \qquad \mu^2 \qquad \eta_t + \varepsilon\mu^2 u\Big|_{z=\varepsilon\eta}\eta_x + \varepsilon\mu^2 v\Big|_{z=\varepsilon\eta}\eta_y \\ \iff & \boxed{\text{at } z = \varepsilon\eta\text{: } w = \mu^2\eta_t + \varepsilon\mu^2 u\eta_x + \varepsilon\mu^2 v\eta_y} \quad \textbf{(9)} \end{aligned}$$

A.9 Kinematic boundary condition (KBC) at the seabed

$z' = -h'(x, y) \iff h_0 z = -h_0 h \iff z = -h$

$$\begin{aligned} & u'\Big|_{z'=-h'}h'_{t'} + v'\Big|_{z'=-h'}h'_{y'} + w'\Big|_{z'=-h'} = 0 \\ \iff & \varepsilon\sqrt{gh_0}\frac{h_0}{l}u\Big|_{z=-h}h_x + \varepsilon\sqrt{gh_0}\frac{h_0}{l}v\Big|_{z=-h}h_y + \frac{\varepsilon}{\mu}\sqrt{gh_0}\frac{h_0}{l}w\Big|_{z=-h} = 0 \\ \iff & w\Big|_{z=-h} + \mu^2 u\Big|_{z=-h}h_x + \mu^2 v\Big|_{z=-h}h_y = 0 \\ \iff & \boxed{\text{at } z = -h\text{: } w + \mu^2 u h_x + \mu^2 v h_y = 0} \quad \textbf{(10)} \end{aligned}$$

A.10 Integration of the continuity equation over the water depth

$$\int_{-h}^{\varepsilon\eta} \mu^2(u_x + v_y) + w_z \; d\zeta = 0$$

Leibniz integral rule: $\dfrac{\partial}{\partial x}\displaystyle\int_{-h}^{\varepsilon\eta} u \; d\zeta = \int_{-h}^{\varepsilon\eta} u_x \; d\zeta + \varepsilon u\Big|_{z=\varepsilon\eta}\eta_x + u\Big|_{z=-h}h_x$

$$\iff \boxed{\int_{-h}^{\varepsilon\eta} u_x \; d\zeta = \frac{\partial}{\partial x}\int_{-h}^{\varepsilon\eta} u \; d\zeta - \varepsilon u\Big|_{z=\varepsilon\eta}\eta_x - u\Big|_{z=-h}h_x}$$

The same for v: $\boxed{\displaystyle\int_{-h}^{\varepsilon\eta} v_y \; d\zeta = \frac{\partial}{\partial y}\int_{-h}^{\varepsilon\eta} v \; d\zeta - \varepsilon v\Big|_{z=\varepsilon\eta}\eta_y - v\Big|_{z=-h}h_y}$

$$\boxed{\int_{-h}^{\varepsilon\eta} w_z \; d\zeta = w\Big|_{z=\varepsilon\eta} - w\Big|_{z=-h}}$$

KBC at the free surface: $w\Big|_{z=\varepsilon\eta} - \varepsilon\mu^2\left(u\Big|_{z=\varepsilon\eta}\eta_x + v\Big|_{z=\varepsilon\eta}\eta_y\right) = \mu^2\eta_t$

KBC at the seabed: $-w\Big|_{z=-h} - \mu^2\left(u\Big|_{z=-h}h_x + v\Big|_{z=-h}h_y\right) = 0$

Finally: $\boxed{\dfrac{\partial}{\partial x}\displaystyle\int_{-h}^{\varepsilon\eta} u \; d\zeta + \frac{\partial}{\partial y}\int_{-h}^{\varepsilon\eta} v \; d\zeta + \eta_t = 0}$ **(11)**

A.11 Integration of the Euler's equations on x an y over the water depth

$$\int_{-h}^{\varepsilon\eta} \mu^2 u_t + \varepsilon\mu^2 u u_x + \varepsilon\mu^2 v u_y + \varepsilon w u_z + \mu^2 p_x \; d\zeta = 0$$

Leibniz integral rule: $\dfrac{\partial}{\partial t}\displaystyle\int_{-h}^{\varepsilon\eta} u \; d\zeta = \int_{-h}^{\varepsilon\eta} u_t \; d\zeta + \varepsilon u\Big|_{z=\varepsilon\eta}\eta_t + v\Big|_{z=-h}\overbrace{h_t}^{=0}$

$$\iff \boxed{\int_{-h}^{\varepsilon\eta} \mu^2 u_t \; d\zeta = \mu^2\frac{\partial}{\partial t}\int_{-h}^{\varepsilon\eta} u \; d\zeta - \varepsilon\mu^2 u\Big|_{z=\varepsilon\eta}\eta_t}$$

Leibniz integral rule: $\dfrac{\partial}{\partial y}\displaystyle\int_{-h}^{\varepsilon\eta} uv\ d\zeta = \int_{-h}^{\varepsilon\eta} u_y v\ d\zeta + \int_{-h}^{\varepsilon\eta} uv_y\ d\zeta + \varepsilon(uv)\Big|_{z=\varepsilon\eta}\eta_y + (uv)\Big|_{z=-h}h_y$

$$\iff \boxed{\int_{-h}^{\varepsilon\eta} \varepsilon\mu^2 vu_y\ d\zeta = \varepsilon\mu^2\frac{\partial}{\partial y}\int_{-h}^{\varepsilon\eta} uv\ d\zeta - \varepsilon\mu^2\int_{-h}^{\varepsilon\eta} uv_y\ d\zeta - (\varepsilon\mu)^2(uv)\Big|_{z=\varepsilon\eta}\eta_y - \varepsilon\mu^2(uv)\Big|_{z=-h}h_y}$$

Integration by parts: $(uw)_z = uw_z + wu_z$

$$\iff \int \frac{\partial}{\partial z}(uw)\ d\zeta = \int uw_z\ d\zeta + \int wu_z\ d\zeta$$
$$\iff \int_{-h}^{\varepsilon\eta} wu_z\ d\zeta = \Big[uw\Big]_{-h}^{\varepsilon\eta} - \int_{-h}^{\varepsilon\eta} uw_z\ d\zeta$$
$$\iff \boxed{\int_{-h}^{\varepsilon\eta} \varepsilon wu_z\ d\zeta = \varepsilon(uw)\Big|_{z=\varepsilon\eta} - \varepsilon(uw)\Big|_{z=-h} - \varepsilon\int_{-h}^{\varepsilon\eta} uw_z\ d\zeta}$$

$$-\varepsilon\mu^2\int_{-h}^{\varepsilon\eta} uv_y\ d\zeta - \varepsilon\int_{-h}^{\varepsilon\eta} uw_z\ d\zeta = -\int_{-h}^{\varepsilon\eta} \varepsilon u\overbrace{\Big[\mu^2 v_y + w_z\Big]}^{=-\mu^2 u_x\ \textbf{(CE)}}\ d\zeta$$
$$= \int_{-h}^{\varepsilon\eta} \varepsilon\mu^2 uu_x\ d\zeta$$

Leibniz integral rule: $\dfrac{\partial}{\partial x}\displaystyle\int_{-h}^{\varepsilon\eta} u^2\ d\zeta = \int_{-h}^{\varepsilon\eta} 2uu_x\ d\zeta + \varepsilon u^2\Big|_{z=\varepsilon\eta}\eta_x + u^2\Big|_{z=-h}h_x$

$$\iff \boxed{2\varepsilon\mu^2\int_{-h}^{\varepsilon\eta} uu_x\ d\zeta = \varepsilon\mu^2\frac{\partial}{\partial x}\int_{-h}^{\varepsilon\eta} u^2\ d\zeta - (\varepsilon\mu)^2u^2\Big|_{z=\varepsilon\eta}\eta_x - \varepsilon\mu^2u^2\Big|_{z=-h}h_x}$$

$$-\varepsilon\mu^2(uv)\Big|_{z=-h}h_y - \varepsilon(uw)\Big|_{z=-h} - \varepsilon\mu^2u^2\Big|_{z=-h}h_x = -\varepsilon u\Big|_{z=-h}\overbrace{\left[w\Big|_{z=-h} + \mu^2 u\Big|_{z=-h}h_x + \mu^2 v\Big|_{z=-h}h_y\right]}^{=0\ \textbf{(KBC at } z=-h\textbf{)}}$$
$$=0$$

$$
\begin{aligned}
&-\varepsilon\mu^2 u\Big|_{z=\varepsilon\eta}\eta_t - (\varepsilon\mu)^2(uv)\Big|_{z=\varepsilon\eta}\eta_y + \varepsilon(uw)\Big|_{z=\varepsilon\eta} - (\varepsilon\mu)^2 u^2\Big|_{z=\varepsilon\eta}\eta_x \\
&= -\varepsilon u\Big|_{z=\varepsilon\eta}\overbrace{\left[-w\Big|_{z=\varepsilon\eta} + \mu^2\eta_t + \varepsilon\mu^2 u\Big|_{z=\varepsilon\eta}\eta_x + \varepsilon\mu^2 v\Big|_{z=\varepsilon\eta}\eta_y\right]}^{=0 \text{ (KBC at } z=\varepsilon\eta)} \\
&= 0
\end{aligned}
$$

Leibniz integral rule: $\dfrac{\partial}{\partial x}\displaystyle\int_{-h}^{\varepsilon\eta} p\ d\zeta = \int_{-h}^{\varepsilon\eta} p_x\ d\zeta + \varepsilon\overbrace{p\Big|_{z=\varepsilon\eta}}^{=0 \text{ (DBC at } z=\varepsilon\eta)}\eta_x + p\Big|_{z=-h}h_x$

$$
\Longleftrightarrow \boxed{\int_{-h}^{\varepsilon\eta}\mu^2 p_x\ d\zeta = \mu^2\frac{\partial}{\partial x}\int_{-h}^{\varepsilon\eta} p\ d\zeta - \mu^2 p\Big|_{z=-h}h_x}
$$

Finally:

$$
\boxed{\frac{\partial}{\partial t}\int_{-h}^{\varepsilon\eta} u\ d\zeta + \varepsilon\frac{\partial}{\partial x}\int_{-h}^{\varepsilon\eta} u^2\ d\zeta + \varepsilon\frac{\partial}{\partial y}\int_{-h}^{\varepsilon\eta} uv\ d\zeta + \frac{\partial}{\partial x}\int_{-h}^{\varepsilon\eta} p\ d\zeta - p\Big|_{z=-h}h_x = 0} \quad \textbf{(12)}
$$

$$
\boxed{\frac{\partial}{\partial t}\int_{-h}^{\varepsilon\eta} v\ d\zeta + \varepsilon\frac{\partial}{\partial x}\int_{-h}^{\varepsilon\eta} uv\ d\zeta + \varepsilon\frac{\partial}{\partial y}\int_{-h}^{\varepsilon\eta} v^2\ d\zeta + \frac{\partial}{\partial y}\int_{-h}^{\varepsilon\eta} p\ d\zeta - p\Big|_{z=-h}h_y = 0} \quad \textbf{(13)}
$$

A.12 Integration of the Euler's equations on z over the water depth from an arbitrary depth z to the free surface

$$
\int_{z}^{\varepsilon\eta} \varepsilon w_t + \varepsilon^2 u w_x + \varepsilon^2 v w_y + \frac{\varepsilon^2}{\mu^2} w w_z + \varepsilon p_z + 1\ d\zeta = 0
$$

Leibniz integral rule: $\dfrac{\partial}{\partial t}\displaystyle\int_{z}^{\varepsilon\eta} w\ d\zeta = \int_{z}^{\varepsilon\eta} w_t\ d\zeta + \varepsilon w\Big|_{z=\varepsilon\eta}\eta_t - w\overbrace{z_t}^{=0}$

$$
\Longleftrightarrow \boxed{\int_{z}^{\varepsilon\eta}\varepsilon w_t\ d\zeta = \varepsilon\frac{\partial}{\partial t}\int_{z}^{\varepsilon\eta} w\ d\zeta - \varepsilon^2 w\Big|_{z=\varepsilon\eta}\eta_t}
$$

Leibniz integral rule:

$$\frac{\partial}{\partial x}\int_z^{\varepsilon\eta} uw\ d\zeta = \int_z^{\varepsilon\eta} uw_x\ d\zeta + \int_z^{\varepsilon\eta} u_x w\ d\zeta + \varepsilon(uw)\Big|_{z=\varepsilon\eta}\eta_x - uw\overbrace{z_x}^{=0}$$

$$\iff \boxed{\int_z^{\varepsilon\eta} \varepsilon^2 uw_x\ d\zeta = \varepsilon^2\frac{\partial}{\partial x}\int_z^{\varepsilon\eta} uw\ d\zeta - \varepsilon^2\int_z^{\varepsilon\eta} u_x w\ d\zeta - \varepsilon^3(uw)\Big|_{z=\varepsilon\eta}\eta_x}$$

$$\implies \boxed{\int_z^{\varepsilon\eta} \varepsilon^2 vw_y\ d\zeta = \varepsilon^2\frac{\partial}{\partial y}\int_z^{\varepsilon\eta} vw\ d\zeta - \varepsilon^2\int_z^{\varepsilon\eta} v_y w\ d\zeta - \varepsilon^3(vw)\Big|_{z=\varepsilon\eta}\eta_y}$$

$$-\varepsilon^2\int_z^{\varepsilon\eta} u_x w\ d\zeta - \varepsilon^2\int_z^{\varepsilon\eta} v_y w\ d\zeta = -\varepsilon^2\int_z^{\varepsilon\eta}\frac{w}{\mu^2}\overbrace{\left(\mu^2 u_x + \mu^2 v_y\right)}^{=-w_z\ \textbf{(CE)}}\ d\zeta$$

$$= \frac{\varepsilon^2}{\mu^2}\int_z^{\varepsilon\eta} ww_z\ d\zeta$$

Classic integral rule: $\boxed{2\frac{\varepsilon^2}{\mu^2}\int_z^{\varepsilon\eta} ww_z\ d\zeta = \frac{\varepsilon^2}{\mu^2}w^2\Big|_{z=\varepsilon\eta} - \frac{\varepsilon^2}{\mu^2}w^2}$

$$-\varepsilon^2 w\Big|_{z=\varepsilon\eta}\eta_t - \varepsilon^3(uw)\Big|_{z=\varepsilon\eta}\eta_x - \varepsilon^3(vw)\Big|_{z=\varepsilon\eta}\eta_y = -\varepsilon^2 w\Big|_{z=\varepsilon\eta}\overbrace{\left[\eta_t + \varepsilon u\Big|_{z=\varepsilon\eta}\eta_x + \varepsilon v\Big|_{z=\varepsilon\eta}\eta_y\right]}^{=\frac{1}{\mu^2}w|_{z=\varepsilon\eta}\ \textbf{(KBC at } z=\varepsilon\eta\textbf{)}}$$

$$= -\frac{\varepsilon^2}{\mu^2}w^2\Big|_{z=\varepsilon\eta}$$

$$\int_z^{\varepsilon\eta} p_z\ d\zeta = \overbrace{p\Big|_{z=\varepsilon\eta}}^{=0\ \textbf{(DBC at } z=\varepsilon\eta\textbf{)}} - p$$

$$\iff \boxed{\int_z^{\varepsilon\eta} \varepsilon p_z\ d\zeta = -\varepsilon p}$$

$$\boxed{\int_z^{\varepsilon\eta} 1\ d\zeta = \varepsilon\eta - z}$$

$$\boxed{p = \eta - \frac{z}{\varepsilon} + \frac{\partial}{\partial t}\int_z^{\varepsilon\eta} w\ d\zeta + \varepsilon\frac{\partial}{\partial x}\int_z^{\varepsilon\eta} uw\ d\zeta + \varepsilon\frac{\partial}{\partial y}\int_z^{\varepsilon\eta} vw\ d\zeta - \frac{\varepsilon}{\mu^2}w^2} \quad \textbf{(14)}$$

A.13 Integration of the continuity equation over the water depth from the seabed

$$\int_{-h}^{z} \mu^2(u_x + v_y) + w_z\ d\zeta = 0$$

Leibniz integral rule: $\dfrac{\partial}{\partial x}\int_{-h}^{z} u\ d\zeta = \int_{-h}^{z} u_x\ d\zeta + u\overbrace{z_x}^{=0} + u\Big|_{z=-h} h_x$

$$\Longleftrightarrow \boxed{\int_{-h}^{z} \mu^2 u_x\ d\zeta = \mu^2\frac{\partial}{\partial x}\int_{-h}^{z} u\ d\zeta - \mu^2 u\Big|_{z=-h} h_x}$$

$$\Longrightarrow \boxed{\int_{-h}^{z} \mu^2 v_y\ d\zeta = \mu^2\frac{\partial}{\partial y}\int_{-h}^{z} v\ d\zeta - \mu^2 v\Big|_{z=-h} h_y}$$

Classic integral rule: $\boxed{\int_{-h}^{z} w_z\ d\zeta = w\ -w\Big|_{z=-h}}$

$$-w\Big|_{z=-h} - \mu^2\left(u\Big|_{z=-h} h_x + v\Big|_{z=-h} h_y\right) = 0 \ \textbf{(KBC at z=-h)}$$

Finally: $\boxed{w = -\mu^2\left(\dfrac{\partial}{\partial x}\int_{-h}^{z} u\ d\zeta + \dfrac{\partial}{\partial y}\int_{-h}^{z} v\ d\zeta\right)}$ **(15)**

For $z = -h(x, y)$:

$$w = -\mu^2\left(u\Big|_{z=-h} h_x + \int_{-h}^{z} u_x\ d\zeta + v\Big|_{z=-h} h_y + \int_{-h}^{z} v_y\ d\zeta\right)$$

$$\Longrightarrow\ w\Big|_{z=-h} = -\mu^2\left(u\Big|_{z=-h} h_x + v\Big|_{z=-h} h_y\right) \ \textbf{(KBC at z=-h)}$$

A.14 Taylor series of a function $f(x)$ at a real a

$$\begin{aligned} f(x) &= \sum_{n=0}^{+\infty} \frac{f^{(n)}(a)}{n!}(x-a)^n \\ &= f(a) + (x-a)f'(a) + \frac{(x-a)^2}{2}f''(a) + \frac{(x-a)^3}{6}f^3(a) + O((x-a)^4) \end{aligned}$$

A.15 Taylor series of u at $z = -h$

$$\boxed{\boldsymbol{u} = \boldsymbol{u}\Big|_{z=-h} + (z+h)\boldsymbol{u_z}\Big|_{z=-h} + \frac{(z+h)^2}{2}\boldsymbol{u_{zz}}\Big|_{z=-h} + \boldsymbol{E} \text{ with } \|\boldsymbol{E}\| = O((z+h)^3)} \quad \textbf{(16)}$$

A.16 Derived from the horizontal components (u and v) of the velocity with respect to z

Irrotationality condition:

$$\begin{aligned} & u_z = w_x \\ \iff & u_z = \frac{\partial}{\partial x}\left[-\mu^2 \left(\frac{\partial}{\partial x}\int_{-h}^{z} u \, d\zeta + \frac{\partial}{\partial y}\int_{-h}^{z} v \, d\zeta \right) \right] \end{aligned}$$

Leibniz integral rule (2 times):

$$\begin{aligned} & -\mu^2 \frac{\partial^2}{\partial x^2}\int_{-h}^{z} u \, d\zeta \\ = & -\mu^2 \frac{\partial}{\partial x}\left(\int_{-h}^{z} u_x \, d\zeta + u\overbrace{z_x}^{=0} + u\Big|_{z=-h} h_x \right) \\ = & -\mu^2 \left(\int_{-h}^{z} u_{xx} \, d\zeta + u_x \overbrace{z_x}^{=0} + u_x\Big|_{z=-h} h_x + u\Big|_{z=-h} h_{xx} + \left(u\Big|_{z=-h}\right)_x h_x \right) \end{aligned}$$

Leibniz integral rule (2 times):

$$
\begin{aligned}
&-\mu^2 \frac{\partial^2}{\partial x \partial y} \int_{-h}^{z} v \, d\zeta \\
&= -\mu^2 \frac{\partial}{\partial x} \left(\int_{-h}^{z} v_y \, d\zeta + v \overbrace{z_y}^{=0} + v\Big|_{z=-h} h_y \right) \\
&= -\mu^2 \left(\int_{-h}^{z} v_{xy} \, d\zeta + v_y \overbrace{z_x}^{=0} + v_y\Big|_{z=-h} h_x + v\Big|_{z=-h} h_{xy} + \Big(v\Big|_{z=-h}\Big)_x h_y \right)
\end{aligned}
$$

$$
\begin{aligned}
\boldsymbol{u_b} &= \Big(u\Big|_{z=-h}; v\Big|_{z=-h}\Big) \\
\frac{\partial}{\partial x}\big(\boldsymbol{u_b}.\nabla h\big) &= \frac{\partial}{\partial x}\Big(u\Big|_{z=-h} h_x + v\Big|_{z=-h} h_y\Big) \\
&= \Big(u\Big|_{z=-h}\Big)_x h_x + \Big(v\Big|_{z=-h}\Big)_x h_y + u\Big|_{z=-h} h_{xx} + v\Big|_{z=-h} h_{xy}
\end{aligned}
$$

$$
\begin{aligned}
\big(\nabla.\boldsymbol{u}\big)\Big|_{z=-h} &= u_x\Big|_{z=-h} + v_y\Big|_{z=-h} \\
\implies h_x\big(\nabla.\boldsymbol{u}\big)\Big|_{z=-h} &= h_x\Big(u_x\Big|_{z=-h} + v_y\Big|_{z=-h}\Big)
\end{aligned}
$$

$$
\boxed{u_z = -\mu^2 \left[\int_{-h}^{z} u_{xx} + v_{xy} \, d\zeta + \frac{\partial}{\partial x}\big(\boldsymbol{u_b}.\nabla h\big) + h_x\big(\nabla.\boldsymbol{u}\big)\Big|_{z=-h} \right]}
$$

The same for v:

$$
\boxed{v_z = -\mu^2 \left[\int_{-h}^{z} u_{xy} + v_{yy} \, d\zeta + \frac{\partial}{\partial y}\big(\boldsymbol{u_b}.\nabla h\big) + h_y\big(\nabla.\boldsymbol{u}\big)\Big|_{z=-h} \right]}
$$

For $z = -h(x,y)$:

$$u_z\Big|_{z=-h(x,y)} = -\mu^2\left[\frac{\partial}{\partial x}\Big(\boldsymbol{u_b}.\nabla h\Big) + h_x\Big(\nabla.\boldsymbol{u}\Big)\Big|_{z=-h}\right]$$

$$v_z\Big|_{z=-h(x,y)} = -\mu^2\left[\frac{\partial}{\partial y}\Big(\boldsymbol{u_b}.\nabla h\Big) + h_y\Big(\nabla.\boldsymbol{u}\Big)\Big|_{z=-h}\right]$$

$$\Longrightarrow \boxed{\boldsymbol{u_z}\Big|_{z=-h(x,y)} = -\mu^2\left[\nabla\Big(\boldsymbol{u_b}.\nabla h\Big) + \nabla h\Big(\nabla.\boldsymbol{u}\Big)\Big|_{z=-h}\right]} \textbf{ (17)}$$

A.17 Vertical velocity w

$$w = -\mu^2\left(\frac{\partial}{\partial x}\int_{-h}^{z} u\ d\zeta + \frac{\partial}{\partial y}\int_{-h}^{z} v\ d\zeta\right) \textbf{ (15)}$$

$$-\mu^2\frac{\partial}{\partial x}\int_{-h}^{z} u\ d\zeta = -\mu^2\frac{\partial}{\partial x}\int_{-h}^{z} \overbrace{u\Big|_{z=-h} + (z+h)u_z\Big|_{z=-h} + ...}^{\textbf{(16)}}\ d\zeta$$

$$= -\mu^2\frac{\partial}{\partial x}\Big[(z+h)u\Big|_{z=-h}\Big] - \mu^2\frac{\partial}{\partial x}\Big[\frac{(z+h)^2}{2}u_z\Big|_{z=-h}\Big] + O(\mu^6)$$

$$= -\mu^2\frac{\partial}{\partial x}\Big[(z+h)u\Big|_{z=-h}\Big] + \mu^4\frac{\partial}{\partial x}\left\{\frac{(z+h)^2}{2}\left[\frac{\partial}{\partial x}\Big(\boldsymbol{u_b}.\nabla h\Big) + h_x\Big(\nabla.\boldsymbol{u}\Big)\Big|_{z=-h}\right]\right\} + O(\mu^6)$$

$$-\mu^2\frac{\partial}{\partial y}\int_{-h}^{z} v\ d\zeta = -\mu^2\frac{\partial}{\partial y}\Big[(z+h)v\Big|_{z=-h}\Big] + \mu^4\frac{\partial}{\partial y}\left\{\frac{(z+h)^2}{2}\left[\frac{\partial}{\partial y}\Big(\boldsymbol{u_b}.\nabla h\Big) + h_y\Big(\nabla.\boldsymbol{u}\Big)\Big|_{z=-h}\right]\right\} + O(\mu^6)$$

$$\boxed{w = -\mu^2\nabla.\Big[(z+h)\boldsymbol{u_b}\Big] + \mu^4\nabla.\left\{\frac{(z+h)^2}{2}\left[\nabla\Big(\boldsymbol{u_b}.\nabla h\Big) + \nabla h\Big(\nabla.\boldsymbol{u}\Big)\Big|_{z=-h}\right]\right\} + O(\mu^6)} \textbf{ (18)}$$

A.18 Equation (19) from the seabed

$$
\begin{aligned}
\text{Classic integral rule: } & \int_{-h}^{z} u_z \, d\zeta = u - u\Big|_{z=-h} \\
\text{Irrotationality condition: } & \int_{-h}^{z} u_z \, d\zeta = \int_{-h}^{z} w_x \, d\zeta \\
\implies & u - u\Big|_{z=-h} = \int_{-h}^{z} w_x \, d\zeta \\
\implies & v - v\Big|_{z=-h} = \int_{-h}^{z} w_y \, d\zeta \\
\iff & \boxed{\boldsymbol{u} - \boldsymbol{u_b} = \int_{-h}^{z} \nabla w \, d\zeta} \quad \textbf{(19)}
\end{aligned}
$$

$$
\begin{aligned}
& w = -\mu^2 \nabla . \Big[(z+h) \boldsymbol{u_b} \Big] + O(\mu^4) \quad \textbf{(18)} \\
\iff \; & w = -\mu^2 \Big\{ \frac{\partial}{\partial x} \Big[(z+h) u\Big|_{z=-h} \Big] + \frac{\partial}{\partial y} \Big[(z+h) v\Big|_{z=-h} \Big] \Big\} + O(\mu^4) \\
\implies \; & w_x = -\mu^2 \Big\{ \frac{\partial^2}{\partial x^2} \Big[(z+h) u\Big|_{z=-h} \Big] + \frac{\partial^2}{\partial x \partial y} \Big[(z+h) v\Big|_{z=-h} \Big] \Big\} + O(\mu^4)
\end{aligned}
$$

$$
\begin{aligned}
(uv)_{xx} &= u_{xx} v + 2 u_x v_x + u v_{xx} \\
(uv)_{xy} &= u_{xy} v + u_x v_y + u_y v_x + u v_{xy}
\end{aligned}
$$

$$
\begin{aligned}
\frac{\partial^2}{\partial x^2} \Big[(z+h) u\Big|_{z=-h} \Big] &= h_{xx} u\Big|_{z=-h} + 2 h_x \Big(u\Big|_{z=-h} \Big)_x + (z+h) \Big(u\Big|_{z=-h} \Big)_{xx} \\
\frac{\partial^2}{\partial x \partial y} \Big[(z+h) v\Big|_{z=-h} \Big] &= h_{xy} v\Big|_{z=-h} + h_x \Big(v\Big|_{z=-h} \Big)_y + h_y \Big(v\Big|_{z=-h} \Big)_x + (z+h) \Big(v\Big|_{z=-h} \Big)_{xy}
\end{aligned}
$$

$$
\begin{aligned}
\nabla . \boldsymbol{u_b} &= \Big(u\Big|_{z=-h} \Big)_x + \Big(v\Big|_{z=-h} \Big)_y \\
\implies \frac{\partial}{\partial x} \big(\nabla . \boldsymbol{u_b} \big) &= \Big(u\Big|_{z=-h} \Big)_{xx} + \Big(v\Big|_{z=-h} \Big)_{xy}
\end{aligned}
$$

$$\nabla.\Big(h\boldsymbol{u_b}\Big) = \frac{\partial}{\partial x}\Big(hv\Big|_{z=-h}\Big) + \frac{\partial}{\partial y}\Big(hv\Big|_{z=-h}\Big)$$

$$\implies \frac{\partial}{\partial x}\Big[\nabla.\Big(h\boldsymbol{u_b}\Big)\Big] = \frac{\partial^2}{\partial x^2}\Big(hv\Big|_{z=-h}\Big) + \frac{\partial^2}{\partial x \partial y}\Big(hv\Big|_{z=-h}\Big)$$

$$\iff \frac{\partial}{\partial x}\Big[\nabla.\Big(h\boldsymbol{u_b}\Big)\Big] = h_{xx}u\Big|_{z=-h} + 2h_x\Big(u\Big|_{z=-h}\Big)_x + h\Big(u\Big|_{z=-h}\Big)_{xx}$$
$$+h_{xy}v\Big|_{z=-h} + h_x\Big(v\Big|_{z=-h}\Big)_y + h_y\Big(v\Big|_{z=-h}\Big)_x + h\Big(v\Big|_{z=-h}\Big)_{xy}$$

$$w_x = -\mu^2 z\frac{\partial}{\partial x}\Big(\nabla.\boldsymbol{u_b}\Big) - \mu^2\frac{\partial}{\partial x}\Big[\nabla.\Big(h\boldsymbol{u_b}\Big)\Big] + O(\mu^4)$$

The same for w_y: $w_y = -\mu^2 z\frac{\partial}{\partial y}\Big(\nabla.\boldsymbol{u_b}\Big) - \mu^2\frac{\partial}{\partial y}\Big[\nabla.\Big(h\boldsymbol{u_b}\Big)\Big] + O(\mu^4)$

$$\boxed{\nabla w = -\mu^2 z\nabla\Big(\nabla.\boldsymbol{u_b}\Big) - \mu^2\nabla\Big[\nabla.\Big(h\boldsymbol{u_b}\Big)\Big] + O(\mu^4)}$$

$$\boldsymbol{u} = \boldsymbol{u_b} + \int_{-h}^{z}\nabla w\ d\zeta$$

$$\iff \boxed{\boldsymbol{u} = \boldsymbol{u_b} - \mu^2\Big(\frac{z^2}{2} - \frac{h^2}{2}\Big)\nabla\Big(\nabla.\boldsymbol{u_b}\Big) - \mu^2(z+h)\nabla\Big[\nabla.\Big(h\boldsymbol{u_b}\Big)\Big] + O(\mu^4)} \quad \textbf{(20)}$$

A.19 Pressure p

$$p = \eta - \frac{z}{\varepsilon} + \frac{\partial}{\partial t}\int_z^{\varepsilon\eta} w\ d\zeta + O(\mu^4 + \epsilon^2)$$

$$w = -\mu^2\nabla.\Big[(z+h)\boldsymbol{u_b}\Big] + O(\mu^4) \quad \textbf{(18)}$$

$$\iff w = -\mu^2\Big\{\frac{\partial}{\partial x}\Big[(z+h)u\Big|_{z=-h}\Big] + \frac{\partial}{\partial y}\Big[(z+h)v\Big|_{z=-h}\Big]\Big\} + O(\mu^4)$$

$$\iff w = -\mu^2\Big\{h_x u\Big|_{z=-h} + h_y v\Big|_{z=-h} + (z+h)\Big[\Big(u\Big|_{z=-h}\Big)_x + \Big(v\Big|_{z=-h}\Big)_y\Big]\Big\} + O(\mu^4)$$

$$\implies \int_z^{\varepsilon\eta} w\ d\zeta = \mu^2\Big\{z\Big(h_x u\Big|_{z=-h} + h_y v\Big|_{z=-h}\Big) + \Big(\frac{z^2}{2} + hz\Big)\Big[\Big(u\Big|_{z=-h}\Big)_x + \Big(v\Big|_{z=-h}\Big)_y\Big]\Big\} + O(\mu^4 + \epsilon^2)$$

$$\frac{\partial}{\partial t}\int_z^{\varepsilon\eta} w\, d\zeta = \mu^2\left\{z\left[h_x\left(u\Big|_{z=-h}\right)_t + h_y\left(v\Big|_{z=-h}\right)_t\right]+\left(\frac{z^2}{2}+hz\right)\left[\left(u\Big|_{z=-h}\right)_{xt} + \left(v\Big|_{z=-h}\right)_{yt}\right]\right\}+O(\mu^4+\epsilon^2)$$

$$\begin{aligned}
\boldsymbol{u_{bt}} &= \left(\left(u\Big|_{z=-h}\right)_t;\left(v\Big|_{z=-h}\right)_t\right)\\
\implies \nabla.\boldsymbol{u_{bt}} &= \left(u\Big|_{z=-h}\right)_{xt} + \left(v\Big|_{z=-h}\right)_{yt}\\
\implies \nabla.\left(h\boldsymbol{u_{bt}}\right) &= \frac{\partial}{\partial x}\left[h\left(u\Big|_{z=-h}\right)_t\right] + \frac{\partial}{\partial y}\left[h\left(v\Big|_{z=-h}\right)_t\right]\\
\iff \nabla.\left(h\boldsymbol{u_{bt}}\right) &= h_x\left(u\Big|_{z=-h}\right)_t + h\left(u\Big|_{z=-h}\right)_{xt} + h_y\left(v\Big|_{z=-h}\right)_t + h\left(v\Big|_{z=-h}\right)_{yt}
\end{aligned}$$

$$\frac{\partial}{\partial t}\int_z^{\varepsilon\eta} w\, d\zeta = \mu^2\left[z\nabla.\left(h\boldsymbol{u_{bt}}\right) + \frac{z^2}{2}\nabla.\boldsymbol{u_{bt}}\right] + O(\mu^4+\epsilon^2)$$

$$\boxed{p = \eta - \frac{z}{\varepsilon} + \mu^2 z\nabla.\left(h\boldsymbol{u_{bt}}\right) + \mu^2\frac{z^2}{2}\nabla.\boldsymbol{u_{bt}} + O(\mu^4+\epsilon^2)} \quad \textbf{(21)}$$

A.20 Vertical velocity w expressed in term of u_α

$$\boldsymbol{u_\alpha} = \left(u\Big|_{z=z_\alpha(x,y)};v\Big|_{z=z_\alpha(x,y)}\right)$$

$\boxed{w = -\mu^2\nabla.\left[(z+h)\boldsymbol{u_\alpha}\right] + O(\mu^4)}$ see A.17

$$w = -\mu^2\left[h_x u\Big|_{z=z_\alpha} + (z+h)\left(u\Big|_{z=z_\alpha}\right)_x + h_y v\Big|_{z=z_\alpha} + (z+h)\left(v\Big|_{z=z_\alpha}\right)_y\right] + O(\mu^4)$$

$$w = -\mu^2\left\{z\left[\overbrace{\left(u\Big|_{z=z_\alpha}\right)_x + \left(v\Big|_{z=z_\alpha}\right)_y}^{\nabla.\boldsymbol{u_\alpha}}\right] + \overbrace{h_x u\Big|_{z=z_\alpha} + h\left(u\Big|_{z=z_\alpha}\right)_x + h_y v\Big|_{z=z_\alpha} + h\left(v\Big|_{z=z_\alpha}\right)_y}^{\nabla.(h\boldsymbol{u_\alpha})}\right\} + O(\mu^4)$$

$$\boxed{w = -\mu^2\nabla.(h\boldsymbol{u_\alpha}) - \mu^2 z\nabla.\boldsymbol{u_\alpha} + O(\mu^4)} \quad \textbf{(22)}$$

A.21 Horizontal velocity expressed in term of u_α

$$\boxed{\nabla w = -\mu^2 z\nabla\left(\nabla.\boldsymbol{u_\alpha}\right) - \mu^2\nabla\left[\nabla.\left(h\boldsymbol{u_\alpha}\right)\right] + O(\mu^4)}$$ see A.18

$$\boldsymbol{u} = \boldsymbol{u_\alpha} + \int_{z_\alpha}^{z} \nabla w \; d\zeta$$

$$\iff \boxed{\boldsymbol{u} = \boldsymbol{u_\alpha} + \mu^2\Big(\frac{z_\alpha^2}{2} - \frac{z^2}{2}\Big)\nabla\Big(\nabla.\boldsymbol{u_\alpha}\Big) + \mu^2(z_\alpha - z)\nabla\Big[\nabla.\Big(h\boldsymbol{u_\alpha}\Big)\Big] + O(\mu^4)} \quad \textbf{(22)}$$

A.22 Pressure p expressed in term of z_α

$$\boldsymbol{u_{\alpha t}} = \Big(\Big(u\Big|_{z=z_\alpha}\Big)_t ; \Big(v\Big|_{z=z_\alpha}\Big)_t\Big)$$

$$\boxed{p = \eta - \frac{z}{\varepsilon} + \mu^2 z\nabla.\Big(h\boldsymbol{u_{\alpha t}}\Big) + \mu^2\frac{z^2}{2}\nabla.\boldsymbol{u_{\alpha t}} + O(\mu^4 + \epsilon^2)} \text{ see A.19 } \textbf{(24)}$$

A.23 Synthesis

$$u = u\Big|_{z=z_\alpha} + \mu^2\Big[\Big(\frac{z_\alpha^2}{2} - \frac{z^2}{2}\Big)\frac{\partial}{\partial x}\Big(\nabla.\boldsymbol{u_\alpha}\Big) + (z_\alpha - z)\frac{\partial}{\partial x}\Big[\nabla.(h\boldsymbol{u_\alpha})\Big]\Big] + O(\mu^4) \quad \textbf{(23)}$$

$$v = v\Big|_{z=z_\alpha} + \mu^2\Big[\Big(\frac{z_\alpha^2}{2} - \frac{z^2}{2}\Big)\frac{\partial}{\partial y}\Big(\nabla.\boldsymbol{u_\alpha}\Big) + (z_\alpha - z)\frac{\partial}{\partial y}\Big[\nabla.(h\boldsymbol{u_\alpha})\Big]\Big] + O(\mu^4) \quad \textbf{(23)}$$

$$w = -\mu^2\nabla.(h\boldsymbol{u_\alpha}) - \mu^2 z\nabla.\boldsymbol{u_\alpha} + O(\mu^4) \quad \textbf{(22)}$$

$$p = \eta - \frac{z}{\varepsilon} + \mu^2 z\nabla.\Big(h\boldsymbol{u_{\alpha t}}\Big) + \mu^2\frac{z^2}{2}\nabla.\boldsymbol{u_{\alpha t}} + O(\mu^4 + \epsilon^2) \quad \textbf{(24)}$$

$$\frac{\partial}{\partial x}\int_{-h}^{\varepsilon\eta} u \; d\zeta + \frac{\partial}{\partial y}\int_{-h}^{\varepsilon\eta} v \; d\zeta + \eta_t = 0 \quad \textbf{(11)}$$

$$\frac{\partial}{\partial t}\int_{-h}^{\varepsilon\eta} u \; d\zeta + \varepsilon\frac{\partial}{\partial x}\int_{-h}^{\varepsilon\eta} u^2 \; d\zeta + \varepsilon\frac{\partial}{\partial y}\int_{-h}^{\varepsilon\eta} uv \; d\zeta + \frac{\partial}{\partial x}\int_{-h}^{\varepsilon\eta} p \; d\zeta - p\Big|_{z=-h} h_x = 0 \quad \textbf{(12)}$$

$$\frac{\partial}{\partial t}\int_{-h}^{\varepsilon\eta} v \; d\zeta + \varepsilon\frac{\partial}{\partial x}\int_{-h}^{\varepsilon\eta} uv \; d\zeta + \varepsilon\frac{\partial}{\partial y}\int_{-h}^{\varepsilon\eta} v^2 \; d\zeta + \frac{\partial}{\partial y}\int_{-h}^{\varepsilon\eta} p \; d\zeta - p\Big|_{z=-h} h_y = 0 \quad \textbf{(13)}$$

A.24 Continuity equation

$$\int_{-h}^{\varepsilon\eta} u\ d\zeta = (\varepsilon\eta+h)u\Big|_{z=z_\alpha} + \mu^2\Bigg\{\Big[\frac{z_\alpha^2}{2}(\varepsilon\eta+h) - \Big(\frac{\varepsilon^3\eta^3}{6}+\frac{h^3}{6}\Big)\Big]\frac{\partial}{\partial x}\Big(\nabla.\boldsymbol{u_\alpha}\Big) + \Big[z_\alpha(\varepsilon\eta+h) - \Big(\frac{\varepsilon^2\eta^2}{2}-\frac{h^2}{2}\Big)\Big]\frac{\partial}{\partial x}\Big(\nabla.(h\boldsymbol{u_\alpha})\Big)\Bigg\} + O(\mu^4)$$
$$= (\varepsilon\eta+h)u\Big|_{z=z_\alpha} + \mu^2\Bigg\{h\Big(\frac{z_\alpha^2}{2}-\frac{h^2}{6}\Big)\frac{\partial}{\partial x}\Big(\nabla.\boldsymbol{u_\alpha}\Big) + h\Big(z_\alpha+\frac{h}{2}\Big)\frac{\partial}{\partial x}\Big[\nabla.(h\boldsymbol{u_\alpha})\Big]\Bigg\} + O(\mu^4+\varepsilon^2)$$

$$\int_{-h}^{\varepsilon\eta} v\ d\zeta = (\varepsilon\eta+h)v\Big|_{z=z_\alpha} + \mu^2\Bigg\{h\Big(\frac{z_\alpha^2}{2}-\frac{h^2}{6}\Big)\frac{\partial}{\partial y}\Big(\nabla.\boldsymbol{u_\alpha}\Big) + h\Big(z_\alpha+\frac{h}{2}\Big)\frac{\partial}{\partial y}\Big[\nabla.(h\boldsymbol{u_\alpha})\Big]\Bigg\} + O(\mu^4+\varepsilon^2)$$

$$\boxed{\frac{\partial}{\partial x}\int_{-h}^{\varepsilon\eta} u\ d\zeta + \frac{\partial}{\partial y}\int_{-h}^{\varepsilon\eta} v\ d\zeta + \eta_t = 0} \quad \textbf{(11)}$$

$$\boxed{\eta_t + \nabla.\Big[(\varepsilon\eta+h)\boldsymbol{u_\alpha}\Big] + \mu^2\nabla.\Bigg\{h\Big(\frac{z_\alpha^2}{2}-\frac{h^2}{6}\Big)\nabla\Big(\nabla.\boldsymbol{u_\alpha}\Big) + h\Big(z_\alpha+\frac{h}{2}\Big)\nabla\Big[\nabla.(h\boldsymbol{u_\alpha})\Big]\Bigg\} = 0} \quad \textbf{(25a)}$$

A.25 Horizontal momentum equations

$$\boxed{\frac{\partial}{\partial t}\int_{-h}^{\varepsilon\eta} u\ d\zeta + \varepsilon\frac{\partial}{\partial x}\int_{-h}^{\varepsilon\eta} u^2\ d\zeta + \varepsilon\frac{\partial}{\partial y}\int_{-h}^{\varepsilon\eta} uv\ d\zeta + \frac{\partial}{\partial x}\int_{-h}^{\varepsilon\eta} p\ d\zeta - p\Big|_{z=-h}h_x = 0} \quad \textbf{(12)}$$

$$\text{Leibniz integral rule: } \frac{\partial}{\partial x}\int_{-h}^{\varepsilon\eta} p\ d\zeta = \int_{-h}^{\varepsilon\eta} p_x\ d\zeta + \varepsilon\eta_x \overbrace{p\Big|_{z=\varepsilon\eta}}^{=0\ \textbf{(DBC)}} + h_x p\Big|_{z=-h}$$
$$\implies \frac{\partial}{\partial x}\int_{-h}^{\varepsilon\eta} p\ d\zeta - p\Big|_{z=-h}h_x = \int_{-h}^{\varepsilon\eta} p_x\ d\zeta$$

$$p = \eta - \frac{z}{\varepsilon} + \mu^2 z\nabla.\Big(h\boldsymbol{u_{\alpha t}}\Big) + \mu^2\frac{z^2}{2}\nabla.\boldsymbol{u_{\alpha t}} + O(\mu^4+\epsilon^2)$$
$$\implies p_x = \eta_x + \mu^2 z\frac{\partial}{\partial x}\Big[\nabla.\Big(h\boldsymbol{u_{\alpha t}}\Big)\Big] + \mu^2\frac{z^2}{2}\frac{\partial}{\partial x}\Big(\nabla.\boldsymbol{u_{\alpha t}}\Big) + O(\mu^4+\epsilon^2)$$
$$\implies \int_{-h}^{\varepsilon\eta} p_x\ d\zeta = (\varepsilon\eta+h)\eta_x - \mu^2\frac{h^2}{2}\frac{\partial}{\partial x}\Big[\nabla.\Big(h\boldsymbol{u_{\alpha t}}\Big)\Big] + \mu^2\frac{h^3}{6}\frac{\partial}{\partial x}\Big(\nabla.\boldsymbol{u_{\alpha t}}\Big) + O(\mu^4+\epsilon^2)$$

$$\frac{\partial}{\partial t}\int_{-h}^{\varepsilon\eta} u\ d\zeta = \frac{\partial}{\partial t}\Big[(\varepsilon\eta+h)u\Big|_{z=z_\alpha}\Big] + \mu^2\frac{\partial}{\partial t}\left\{\left(\frac{z_\alpha^2 h}{2}-\frac{h^3}{6}\right)\frac{\partial}{\partial x}\big(\nabla.\boldsymbol{u_\alpha}\big)+\left(z_\alpha h+\frac{h^2}{2}\right)\frac{\partial}{\partial x}\big[\nabla.(h\boldsymbol{u_\alpha})\big]\right\}$$
$$+O(\mu^4+\varepsilon^2)$$
$$= \frac{\partial}{\partial t}\Big[(\varepsilon\eta+h)u\Big|_{z=z_\alpha}\Big] + \mu^2\left\{\left(\frac{z_\alpha^2 h}{2}-\frac{h^3}{6}\right)\frac{\partial^2}{\partial x\partial t}\big(\nabla.\boldsymbol{u_\alpha}\big)+\left(z_\alpha h+\frac{h^2}{2}\right)\frac{\partial^2}{\partial x\partial t}\big[\nabla.(h\boldsymbol{u_\alpha})\big]\right\}$$
$$+O(\mu^4+\varepsilon^2)$$

$$\frac{\partial^2}{\partial x\partial t}\big(\nabla.\boldsymbol{u_\alpha}\big) = \frac{\partial^2}{\partial x\partial t}\Big[\big(u\big|_{z=z_\alpha}\big)_x+\big(v\big|_{z=z_\alpha}\big)_y\Big] = \big(u\big|_{z=z_\alpha}\big)_{xxt}+\big(v\big|_{z=z_\alpha}\big)_{xyt}$$
$$\frac{\partial}{\partial x}\big(\nabla.\boldsymbol{u_{\alpha t}}\big) = \frac{\partial}{\partial x}\Big[\big(u\big|_{z=z_\alpha}\big)_{xt}+\big(v\big|_{z=z_\alpha}\big)_{yt}\Big] = \big(u\big|_{z=z_\alpha}\big)_{xxt}+\big(v\big|_{z=z_\alpha}\big)_{xyt}$$
$$\boxed{\frac{\partial^2}{\partial x\partial t}\big(\nabla.\boldsymbol{u_\alpha}\big) = \frac{\partial}{\partial x}\big(\nabla.\boldsymbol{u_{\alpha t}}\big)}$$
$$\frac{\partial^2}{\partial x\partial t}\big[\nabla.(h\boldsymbol{u_\alpha})\big] = \frac{\partial^2}{\partial x\partial t}\left[\frac{\partial}{\partial x}\big(hu\big|_{z=z_\alpha}\big)+\frac{\partial}{\partial y}\big(hv\big|_{z=z_\alpha}\big)\right] = \big(hu\big|_{z=z_\alpha}\big)_{xxt}+\big(hv\big|_{z=z_\alpha}\big)_{xyt}$$
$$\frac{\partial}{\partial x}\big[\nabla.(h\boldsymbol{u_{\alpha t}})\big] = \frac{\partial}{\partial x}\left\{\frac{\partial}{\partial x}\Big[h\big(u\big|_{z=z_\alpha}\big)_t\Big]+\frac{\partial}{\partial y}\Big[h\big(v\big|_{z=z_\alpha}\big)_t\Big]\right\} = \big(hu\big|_{z=z_\alpha}\big)_{xxt}+\big(hv\big|_{z=z_\alpha}\big)_{xyt}$$
$$\boxed{\frac{\partial^2}{\partial x\partial t}\big[\nabla.(h\boldsymbol{u_\alpha})\big] = \frac{\partial}{\partial x}\big[\nabla.(h\boldsymbol{u_{\alpha t}})\big]}$$

$$\frac{\partial}{\partial t}\int_{-h}^{\varepsilon\eta} u\ d\zeta = \frac{\partial}{\partial t}\Big[(\varepsilon\eta+h)u\Big|_{z=z_\alpha}\Big] + \mu^2\left\{\left(\frac{z_\alpha^2 h}{2}-\frac{h^3}{6}\right)\frac{\partial}{\partial x}\big(\nabla.\boldsymbol{u_{\alpha t}}\big)+\left(z_\alpha h+\frac{h^2}{2}\right)\frac{\partial}{\partial x}\big[\nabla.(h\boldsymbol{u_{\alpha t}})\big]\right\}$$
$$+O(\mu^4+\varepsilon^2)$$

$$\frac{\partial}{\partial t}\int_{-h}^{\varepsilon\eta} u\ d\zeta + \frac{\partial}{\partial x}\int_{-h}^{\varepsilon\eta} p\ d\zeta - p\Big|_{z=-h}h_x = \varepsilon\eta_t u\Big|_{z=z_\alpha} + (\varepsilon\eta+h)\big(u\big|_{z=z_\alpha}\big)_t + (\varepsilon\eta+h)\eta_x$$
$$+\mu^2 h\left\{\frac{z_\alpha^2}{2}\frac{\partial}{\partial x}\big(\nabla.\boldsymbol{u_{\alpha t}}\big)+z_\alpha\frac{\partial}{\partial x}\big[\nabla.(h\boldsymbol{u_\alpha})\big]\right\}+O(\mu^4+\varepsilon^2)$$

$$(uvw)_x = w(uv)_x + uvw_x$$

$$\begin{aligned} \varepsilon u^2 &= \varepsilon (u|_{z=z_\alpha})^2 + O(\mu^4 + \varepsilon^2) \\ \implies \varepsilon \frac{\partial}{\partial x} \int_{-h}^{\varepsilon\eta} u^2 \, d\zeta &= \varepsilon \frac{\partial}{\partial x} \Big[(\varepsilon\eta + h)(u|_{z=z_\alpha})^2 \Big] \\ &= \varepsilon u|_{z=z_\alpha} \frac{\partial}{\partial x} \Big[(\varepsilon\eta + h) u|_{z=z_\alpha} \Big] + \varepsilon h u|_{z=z_\alpha} \Big(u|_{z=z_\alpha} \Big)_x + O(\mu^4 + \varepsilon^2) \end{aligned}$$

$$\begin{aligned} \varepsilon uv &= \varepsilon u|_{z=z_\alpha} v|_{z=z_\alpha} + O(\mu^4 + \varepsilon^2) \\ \implies \frac{\partial}{\partial y} \int_{-h}^{\varepsilon\eta} \varepsilon uv \, d\zeta &= \varepsilon \frac{\partial}{\partial y} \Big[(\varepsilon\eta + h) u|_{z=z_\alpha} \, v|_{z=z_\alpha} \Big] + O(\mu^4 + \varepsilon^2) \\ &= \varepsilon u|_{z=z_\alpha} \frac{\partial}{\partial y} \Big[(\varepsilon\eta + h) v|_{z=z_\alpha} \Big] + \varepsilon h v|_{z=z_\alpha} \Big(u|_{z=z_\alpha} \Big)_y + O(\mu^4 + \varepsilon^2) \end{aligned}$$

$$\begin{aligned} \varepsilon \eta_t &= -\varepsilon \nabla . \Big[(\varepsilon\eta + h) \boldsymbol{u_\alpha} \Big] + O(\varepsilon\mu^2) \quad \textbf{(25a)} \\ \implies \varepsilon \eta_t u|_{z=z_\alpha} &= -\varepsilon u|_{z=z_\alpha} \nabla . \Big[(\varepsilon\eta + h) \boldsymbol{u_\alpha} \Big] + O(\varepsilon\mu^2) \end{aligned}$$

$$\frac{\partial}{\partial y} \int_{-h}^{\varepsilon\eta} \varepsilon u^2 \, d\zeta + \frac{\partial}{\partial y} \int_{-h}^{\varepsilon\eta} \varepsilon uv \, d\zeta + \varepsilon \eta_t u \Big|_{z=z_\alpha} = \varepsilon h \Big[u|_{z=z_\alpha} \Big(u|_{z=z_\alpha} \Big)_x + v|_{z=z_\alpha} \Big(u|_{z=z_\alpha} \Big)_y \Big] + O(\mu^4 + \varepsilon^2)$$

$$(\boldsymbol{u_\alpha} . \nabla) \boldsymbol{u_\alpha} = \left(u|_{z=z_\alpha} \frac{\partial}{\partial x} + v|_{z=z_\alpha} \frac{\partial}{\partial y} \right) \begin{pmatrix} u|_{z=z_\alpha} \\ v|_{z=z_\alpha} \end{pmatrix} = \begin{pmatrix} u|_{z=z_\alpha} \Big(u|_{z=z_\alpha} \Big)_x + v|_{z=z_\alpha} \Big(u|_{z=z_\alpha} \Big)_y \\ u|_{z=z_\alpha} \Big(v|_{z=z_\alpha} \Big)_x + v|_{z=z_\alpha} \Big(v|_{z=z_\alpha} \Big)_y \end{pmatrix}$$

$$\begin{aligned} &\frac{\partial}{\partial t} \int_{-h}^{\varepsilon\eta} u \, d\zeta + \varepsilon \frac{\partial}{\partial x} \int_{-h}^{\varepsilon\eta} u^2 \, d\zeta + \varepsilon \frac{\partial}{\partial y} \int_{-h}^{\varepsilon\eta} uv \, d\zeta + \frac{\partial}{\partial x} \int_{-h}^{\varepsilon\eta} p \, d\zeta - p\Big|_{z=-h} h_x = 0 \quad \textbf{(12)} \\ \iff & (\varepsilon\eta + h) \Big(u\Big|_{z=z_\alpha} \Big)_t + (\varepsilon\eta + h)\eta_x + \mu^2 h \left\{ \frac{z_\alpha^2}{2} \frac{\partial}{\partial x} \Big(\nabla . \boldsymbol{u_{\alpha t}} \Big) + z_\alpha \frac{\partial}{\partial x} \Big[\nabla . (h \boldsymbol{u_\alpha}) \Big] \right\} \\ & + \varepsilon h \Big[u|_{z=z_\alpha} \Big(u|_{z=z_\alpha} \Big)_x + v|_{z=z_\alpha} \Big(u|_{z=z_\alpha} \Big)_y \Big] + O(\mu^4 + \varepsilon^2) = 0 \end{aligned}$$

$$\mu^2(\varepsilon\eta + h) = \mu^2 h + O(\varepsilon\mu^2)$$
$$\varepsilon(\varepsilon\eta + h) = \varepsilon h + O(\varepsilon^2)$$

$$\boxed{\Big(u|_{z=z_\alpha}\Big)_t + \eta_x + \varepsilon\Big[u|_{z=z_\alpha}\Big(u|_{z=z_\alpha}\Big)_x + v|_{z=z_\alpha}\Big(u|_{z=z_\alpha}\Big)_y\Big] + \mu^2\left\{\frac{z_\alpha^2}{2}\frac{\partial}{\partial x}\Big(\nabla.\boldsymbol{u_{\alpha t}}\Big) + z_\alpha\frac{\partial}{\partial x}\Big[\nabla.(h\boldsymbol{u_\alpha})\Big]\right\} = 0}$$

$$\boxed{\Big(v|_{z=z_\alpha}\Big)_t + \eta_y + \varepsilon\Big[u|_{z=z_\alpha}\Big(v|_{z=z_\alpha}\Big)_x + v|_{z=z_\alpha}\Big(v|_{z=z_\alpha}\Big)_y\Big] + \mu^2\left\{\frac{z_\alpha^2}{2}\frac{\partial}{\partial y}\Big(\nabla.\boldsymbol{u_{\alpha t}}\Big) + z_\alpha\frac{\partial}{\partial y}\Big[\nabla.(h\boldsymbol{u_\alpha})\Big]\right\} = 0}$$

$$\boxed{\boldsymbol{u_{\alpha t}} + \nabla\eta + \varepsilon(\boldsymbol{u_\alpha}.\nabla)\boldsymbol{u_\alpha} + \mu^2\left\{\frac{z_\alpha^2}{2}\nabla\Big(\nabla.\boldsymbol{u_{\alpha t}}\Big) + z_\alpha\nabla\Big[\nabla.(h\boldsymbol{u_\alpha})\Big]\right\} = 0} \quad \textbf{(25b)}$$

Bibliography

Abadie, S., Butel, R., Mauriet, S., Morichon, D., and Dupuis, H. (2006). Wave climate and longshore drift on the south aquitaine coast. *Continental Shelf Research*, 26(16):1924 – 1939.

Abadie, S. M., Brière, C., Dubranna, J., Maron, P., and Rihouey, D. (2008). Erosion generated by wave-induced currents in the vicinity of a jetty: case study of the relationship between the adour river mouth and anglet beach, france. *Journal of Coastal Research*, pages 59–69.

Aelbrecht, D. (1997). Artemis 3.0: A finite element model for predicting wave agitation in coastal areas and harbours including dissipation. *WIT Transactions on The Built Environment*, 30.

André, G., Marcos, M., and Daubord, C. (2013). Detection method of meteotsunami events and characterization of harbour oscillations in western mediterranean. In *Coastal Dynamics 2013 conference proceedings*, pages 83–92.

Arcement, G. J. and Schneider, V. R. (1989). Guide for selecting manning's roughness coefficients for natural channels and flood plains.

Asano, T., Yamashiro, T., and Kakinuma, T. (2010). Field observations of seiche events in a t-shape bay of kami-koshiki island, japan.

Augris, C. and Clabaut, P. (2001). *Cartographie géologique des fonds marins côtiers: exemples le long du littoral français*. Editions Quae.

Baldock, T. and Huntley, D. (2002). Long–wave forcing by the breaking of random gravity waves on a beach. In *Proceedings of the Royal Society of London A: Mathematical, Physical and Engineering Sciences*, volume 458, pages 2177–2201. The Royal Society.

Battjes, J., Bakkenes, H., Janssen, T., and Van Dongeren, A. (2004). Shoaling of subharmonic gravity waves. *Journal of Geophysical Research: Oceans*, 109(C2).

Bellafont, F., Morichon, D., Roeber, V., André, G., and Abadie, S. (2018a). Oscillations portuaires forcées par les ondes infra-gravitaires dans un chenal de navigation.

Bellafont, F., Morichon, D., Roeber, V., André, G., and Abadie, S. (2018b). Infragravity period oscillations in a channel harbor near a river mouth. *Coastal Engineering Proceedings*, 1(36):8.

Bellotti, G. (2007). Transient response of harbours to long waves under resonance conditions. *Coastal engineering*, 54(9):680–693.

Bellotti, G., Briganti, R., Beltrami, G. M., and Franco, L. (2012). Modal analysis of semi-enclosed basins. *Coastal Engineering*, 64:16–25.

Bellotti, G. and Franco, L. (2011). Measurement of long waves at the harbor of marina di carrara, italy. *Ocean Dynamics*, 61(12):2051–2059.

Berkhoff, J. (1972). *Computation of Combined Refraction-Diffraction*, chapter 24, pages 471–490.

Bertin, X., Bruneau, N., Breilh, J.-F., Fortunato, A. B., and Karpytchev, M. (2012). Importance of wave age and resonance in storm surges: The case xynthia, bay of biscay. *Ocean Modelling*, 42:16–30.

Bertin, X., De Bakker, A., Guerin, T., Chataigner, T., Martins, K., and Coulombier, T. (2018a). Transferts d'énergie et réflexion des ondes infra-gravitaires au niveau d'une plage dissipative.

Bertin, X., de Bakker, A., van Dongeren, A., Coco, G., André, G., Ardhuin, F., Bonneton, P., Bouchette, F., Castelle, B., Crawford, W. C., et al. (2018b). Infragravity waves: from driving mechanisms to impacts. *Earth-Science Reviews*.

Bertin, X. and Olabarrieta, M. (2016). Relevance of infragravity waves in a wave-dominated inlet. *Journal of Geophysical Research: Oceans*, 121(8):5418–5435.

Biésel, F. (1952). Equations generales au second ordre de la houle irreguliere. *La Houille Blanche*, (3):372–376.

Bonneton, P. and Lannes, D. (2017). Recovering water wave elevation from pressure measurements. *Journal of Fluid Mechanics*, 833:399–429.

Bowen, A. J. and Inman, D. L. (1971). Edge waves and crescentic bars. *Journal of Geophysical Research*, 76(36):8662–8671.

Bowers, E. (1993). Low frequency waves in intermediate water depths. In *Coastal Engineering 1992*, pages 832–845.

Bricker, J. D. and Roeber, V. (2015). Mechanisms of damage during typhoon haiyan: storm surge, waves, and 'tsunami-like'surf beat. In *Proceedings of the 36th IAHR World Congress*, volume 28.

Briere, C., Abadie, S., Bretel, P., and Lang, P. (2007). Assessment of telemac system performances, a hydrodynamic case study of anglet, france. *Coastal engineering*, 54(4):345–356.

Brocchini, M. (2013). A reasoned overview on boussinesq-type models: the interplay between physics, mathematics and numerics. *Proceedings of the Royal Society A: Mathematical, Physical and Engineering Sciences*, 469(2160):20130496.

Chen, G.-Y., Chien, C.-C., Su, C.-H., and Tseng, H.-M. (2004). Resonance induced by edge waves in hua-lien harbor. *Journal of oceanography*, 60(6):1035–1043.

Chen, Q., Madsen, P. A., Schäffer, H. A., and Basco, D. R. (1998). Wave-current interaction based on an enhanced boussinesq approach. *Coastal Engineering*, 33(1):11–39.

Contardo, S. and Symonds, G. (2013). Infragravity response to variable wave forcing in the nearshore. *Journal of Geophysical Research: Oceans*, 118(12):7095–7106.

De Bakker, A., Brinkkemper, J., Van der Steen, F., Tissier, M., and Ruessink, B. (2016a). Cross-shore sand transport by infragravity waves as a function of beach steepness. *Journal of Geophysical Research: Earth Surface*, 121(10):1786–1799.

De Bakker, A., Herbers, T., Smit, P., Tissier, M., and Ruessink, B. (2015). Nonlinear infragravity–wave interactions on a gently sloping laboratory beach. *Journal of Physical Oceanography*, 45(2):589–605.

de Bakker, A., Tissier, M., Marieu, V., Sénéchal, N., Ruju, A., Lara, J., and Ruessink, B. (2013). Infragravity wave propagation and dissipation on a low-sloping laboratory beach. In *Proceedings of the Conference on Coastal Dynamics*, pages 443–452.

De Bakker, A., Tissier, M., and Ruessink, B. (2014). Shoreline dissipation of infragravity waves. *Continental Shelf Research*, 72:73–82.

De Bakker, A., Tissier, M., and Ruessink, B. (2016b). Beach steepness effects on nonlinear infragravity-wave interactions: A numerical study. *Journal of Geophysical Research: Oceans*, 121(1):554–570.

de Bont, J., Van Der Molen, W., Van Der Lem, J., Ligteringen, H., Mühlenstein, D., and Howle, M. (2010). Calculations of the motions of a ship moored with moormaster units.

De Jong, M. and Battjes, J. (2004). Low-frequency sea waves generated by atmospheric convection cells. *Journal of Geophysical Research: Oceans*, 109(C1).

De Jong, M., Holthuijsen, L., and Battjes, J. (2003). Generation of seiches by cold fronts over the southern north sea. *Journal of Geophysical Research: Oceans*, 108(C4).

Debaillon, P., Sergent, P., and Orcel, O. (2009). Refonde v2.6. Notice théorique, Centre d'Etudes Techniques Maritime et Fluviales. (In French).

Defontaine, S., Sous, D., Morichon, D., Verney, R., and Monperrus, M. (2019). Hydrodynamics and spm transport in an engineered tidal estuary: The adour river (france). *Estuarine, Coastal and Shelf Science*, 231:106445.

Eckart, C. (1951). Surface waves on water of variable depth. *Wave report nr. 100, SIO reference 51-12*.

Elgar, S. and Guza, R. (1985). Observations of bispectra of shoaling surface gravity waves. *Journal of Fluid Mechanics*, 161:425–448.

Elgar, S., Herbers, T., Okihiro, M., Oltman-Shay, J., and Guza, R. (1992). Observations of infragravity waves. *Journal of Geophysical Research: Oceans*, 97(C10):15573–15577.

Elzinga, T., Iribarren, J., and Jensen, O. (1993). Movements of moored ships in harbours. In *Coastal Engineering 1992*, pages 3216–3229.

Filippini, A. G., De Brye, S., Perrier, V., Marche, F., Ricchiuto, M., Lannes, D., and Bonneton, P. (2018). Uhaina: A parallel high performance unstructured near-shore wave model.

Gawehn, M., van Dongeren, A., van Rooijen, A., Storlazzi, C. D., Cheritonand, O. M., and Reniers, A. (2016). Identification and classification of very low frequency waves on a coral reef flat. *Journal of Geophysical Research: Oceans*, 121(10):7560–7574.

Gomis, D., Monserrat, S., and Tintoré, J. (1993). Pressure-forced seiches of large amplitude in inlets of the balearic islands. *Journal of Geophysical Research: Oceans*, 98(C8):14437–14445.

González-Marco, D., Sierra, J. P., de Ybarra, O. F., and Sánchez-Arcilla, A. (2008). Implications of long waves in harbor management: The gijón port case study. *Ocean & Coastal Management*, 51(2):180–201.

Gossard, E. and Munk, W. (1954). On gravity waves in the atmosphere. *Journal of Meteorology*, 11(4):259–269.

Green, A. E. and Naghdi, P. M. (1976). A derivation of equations for wave propagation in water of variable depth. *Journal of Fluid Mechanics*, 78(2):237–246.

Green, G. (1838). On the motion of waves in a variable canal of small depth and width. *Transactions of the Cambridge Philosophical Society*, 6:457.

Greenspan, H. P. (1956). The generation of edge waves by moving pressure distributions. *Journal of Fluid Mechanics*, 1(6):574–592.

Guérin, T., de Bakker, A., and Bertin, X. (2019). On the bound wave phase lag. *Fluids*, 4(3):152.

Guillou, N. and Chapalain, G. (2012). Modeling penetration of tide-influenced waves in le havre harbor. *Journal of Coastal Research*, 28(4):945–955.

Guo, J. (2002). Simple and explicit solution of wave dispersion equation. *Coastal Engineering*, 45(2):71–74.

Guza, R. and Thornton, E. B. (1982). Swash oscillations on a natural beach. *Journal of Geophysical Research: Oceans*, 87(C1):483–491.

général au développement durable, C. (2018). L'activité des ports maritimes français repart en 2017.

Hamm, L. and Peronnard, C. (1997). Wave parameters in the nearshore: A clarification. *Coastal Engineering*, 32(2-3):119–135.

Hashimoto, N. and Kobune, K. (1989). Directional spectrum estimation from a bayesian approach. In *Coastal Engineering 1988*, pages 62–76.

Hashimoto, N., Nagai, T., and Asai, T. (1995). Extension of the maximum entropy principle method for directional wave spectrum estimation. In *Coastal Engineering 1994*, pages 232–246.

Hasselmann, K. (1962). On the non-linear energy transfer in a gravity-wave spectrum part 1. general theory. *Journal of Fluid Mechanics*, 12(4):481–500.

Henderson, S. M. and Bowen, A. (2002). Observations of surf beat forcing and dissipation. *Journal of Geophysical Research: Oceans*, 107(C11).

Henderson, S. M., Elgar, S., and Bowen, A. (2001). Observations of surf beat propagation and energetics. In *Coastal Engineering 2000*, pages 1412–1421.

Henderson, S. M., Guza, R., Elgar, S., Herbers, T., and Bowen, A. (2006). Nonlinear generation and loss of infragravity wave energy. *Journal of Geophysical Research: Oceans*, 111(C12).

Herbers, T., Elgar, S., and Guza, R. (1994). Infragravity-frequency (0.005-0.05 hz) motions on the shelf. part i: forced waves. *Journal of Physical Oceanography*, 24(5):917–927. cited By 83.

Herbers, T., Elgar, S., and Guza, R. (1995a). Generation and propagation of infragravity waves. *Journal of Geophysical Research: Oceans*, 100(C12):24863–24872.

Herbers, T., Elgar, S., Guza, R., and O'Reilly, W. (1995b). Infragravity-frequency (0.005–0.05 hz) motions on the shelf. part ii: Free waves. *Journal of physical oceanography*, 25(6):1063–1079.

Hibiya, T. and Kajiura, K. (1982). Origin of theabiki phenomenon (a kind of seiche) in nagasaki bay. *Journal of the Oceanographical Society of Japan*, 38(3):172–182.

historicair (2006). Mooring of the ship at a quay.

Holman, R. and Bowen, A. (1979). Edge waves on complex beach profiles. *Journal of Geophysical Research: Oceans*, 84(C10):6339–6346.

Holthuijsen, L. H. (2007). *Waves in Oceanic and Coastal Waters*. Cambridge University Press.

Hunt, I. A. (1959). Design of sea-walls and breakwaters. *Transactions of the American Society of Civil Engineers*, 126(4):542–570.

Huntley, D., Guza, R., and Thornton, E. (1981). Field observations of surf beat: 1. progressive edge waves. *Journal of Geophysical Research: Oceans*, 86(C7):6451–6466.

Idier, D. and Pedreros, R. (2005). Modélisation hydrodynamique de la côte basque. partie 1 : marées, courants de marée et surcotes. Technical report, BRGM/RP-53705-FR. (In French).

Inch, K., Davidson, M., Masselink, G., and Russell, P. (2017a). Correcting wave reflection estimates in the coastal zone. *Coastal Engineering*, 119:65–71.

Inch, K., Davidson, M., Masselink, G., and Russell, P. (2017b). Observations of nearshore infragravity wave dynamics under high energy swell and wind-wave conditions. *Continental Shelf Research*, 138:19–31.

Janssen, T., Battjes, J., and Van Dongeren, A. (2003). Long waves induced by short-wave groups over a sloping bottom. *Journal of Geophysical Research: Oceans*, 108(C8).

Kennedy, A. B., Chen, Q., Kirby, J. T., and Dalrymple, R. A. (2000). Boussinesq modeling of wave transformation, breaking, and runup. i: 1d. *Journal of waterway, port, coastal, and ocean engineering*, 126(1):39–47.

Kirby, J. T. (1996). Nonlinear, dispersive long waves in water of variable depth. Technical report, DELAWARE UNIV NEWARK CENTER FOR APPLIED COASTAL RESEARCH.

Kirby, J. T., Wei, G., Chen, Q., Kennedy, A. B., and Dalrymple, R. A. (1998). Funwave 1.0: fully nonlinear boussinesq wave model-documentation and user's manual. *research report NO. CACR-98-06*.

Kolen, B., Slomp, R., and Jonkman, S. (2013). The impacts of storm x ynthia f ebruary 27–28, 2010 in f rance: lessons for flood risk management. *Journal of Flood Risk Management*, 6(3):261–278.

Kuik, A., Van Vledder, G. P., and Holthuijsen, L. (1988). A method for the routine analysis of pitch-and-roll buoy wave data. *Journal of physical oceanography*, 18(7):1020–1034.

Lafaye de Micheaux, P., Drouilhet, R., and Liquet, B. (2013). The r software: fundamentals of programming and statistical analysis.

Lannes, D. and Bonneton, P. (2009). Derivation of asymptotic two-dimensional time-dependent equations for surface water wave propagation. *Physics of fluids*, 21(1):016601.

LCHF (1975). Embouchure de l'adour - protection du chenal de navigation contre l'ensablement - phase iii etude sur modèle réduit - rapport général. Technical report.

Li, N., Yamazaki, Y., Roeber, V., Cheung, K. F., and Chock, G. (2018). Probabilistic mapping of storm-induced coastal inundation for climate change adaptation. *Coastal Engineering*, 133:126–141.

Liberato, M. L., Pinto, J. G., Trigo, I. F., and Trigo, R. M. (2011). Klaus–an exceptional winter storm over northern iberia and southern france. *Weather*, 66(12):330–334.

List, J. H. (1991). Wave groupiness variations in the nearshore. *Coastal Engineering*, 15(5-6):475–496.

littoral Angloy, S. S. (2015). L'histoire méconnue du dragage à l'embouchure de l'adour.

Longuet-Higgins, M. and Stewart, R. (1962). Radiation stress and mass transport in gravity waves, with application to 'surf beats'. *Journal of Fluid Mechanics*, 13(4):481–504.

López, M. and Iglesias, G. (2013). Artificial intelligence for estimating infragravity energy in a harbour. *Ocean Engineering*, 57:56–63.

López, M., Iglesias, G., and Kobayashi, N. (2012). Long period oscillations and tidal level in the port of ferrol. *Applied Ocean Research*, 38:126–134.

Losada, I. J., Liu, P. L., Gonzalez, M., Diaz, G., Gonzalez, J. M., and Woo, S. B. (2005). Harbour short wave agitation and resonance based on modified boussinesq equations. In *Coastal Engineering 2004: (In 4 Volumes)*, pages 1321–1333. World Scientific.

Madsen, P. A., Murray, R., and Sørensen, O. R. (1991). A new form of the boussinesq equations with improved linear dispersion characteristics. *Coastal engineering*, 15(4):371–388.

Marcos, M., Monserrat, S., Medina, R., Orfila, A., and Olabarrieta, M. (2009). External forcing of meteorological tsunamis at the coast of the balearic islands. *Physics and Chemistry of the Earth, Parts A/B/C*, 34(17-18):938–947.

Masselink, G. (1995). Group bound long waves as a source of infragravity energy in the surf zone. *Continental Shelf Research*, 15(13):1525–1547.

Masselink, G., Scott, T., Poate, T., Russell, P., Davidson, M., and Conley, D. (2016). The extreme 2013/2014 winter storms: hydrodynamic forcing and coastal response along the southwest coast of england. *Earth Surface Processes and Landforms*, 41(3):378–391.

Monserrat, S., Ibbetson, A., and Thorpe, A. (1991). Atmospheric gravity waves and the 'rissaga'phenomenon. *Quarterly Journal of the Royal Meteorological Society*, 117(499):553–570.

Monserrat, S., Rabinovich, A., et al. (2006). Meteotsunamis: atmospherically induced destructive ocean waves in the tsunami frequency band. *Natural Hazards and Earth System Science*, 6(6):1035–1051.

Munk, W. H. (1951). Origin and generation of waves. Technical report, SCRIPPS INSTITUTION OF OCEANOGRAPHY LA JOLLA CALIF.

Newman, J. (1990). Numerical solutions of the water-wave dispersion relation. *Applied Ocean Research*, 12(1):14–18.

Nwogu, O. (1993). Alternative form of boussinesq equations for nearshore wave propagation. *Journal of waterway, port, coastal, and ocean engineering*, 119(6):618–638.

Okihiro, M. and Guza, R. (1995). Infragravity energy modulation by tides. *Journal of Geophysical Research: Oceans*, 100(C8):16143–16148.

Okihiro, M. and Guza, R. (1996). Observations of seiche forcing and amplification in three small harbors. *Journal of waterway, port, coastal, and ocean engineering*, 122(5):232–238.

Okihiro, M., Guza, R., and Seymour, R. (1992). Bound infragravity waves. *Journal of Geophysical Research: Oceans*, 97(C7):11453–11469.

Oliveras, K. L., Vasan, V., Deconinck, B., and Henderson, D. (2012). Recovering the water-wave profile from pressure measurements. *SIAM Journal on Applied Mathematics*, 72(3):897–918.

on Trade, U. N. C. and Development (2017). Review of maritime transport.

on Trade, U. N. C. and Development (2018). Review of maritime transport.

Péquignet, A.-C. N., Becker, J. M., and Merrifield, M. A. (2014). Energy transfer between wind waves and low-frequency oscillations on a fringing reef, i pan, g uam. *Journal of Geophysical Research: Oceans*, 119(10):6709–6724.

Peregrine, D. H. (1967). Long waves on a beach. *Journal of fluid mechanics*, 27(4):815–827.

Poelhekke, L., Jäger, W. S., Van Dongeren, A., Plomaritis, T. A., McCall, R., and Ferreira, Ó. (2016). Predicting coastal hazards for sandy coasts with a bayesian network. *Coastal Engineering*, 118:21–34.

Pomeroy, A., Lowe, R., Symonds, G., Van Dongeren, A., and Moore, C. (2012). The dynamics of infragravity wave transformation over a fringing reef. *Journal of Geophysical Research: Oceans*, 117(C11).

Pons, F., Sergent, P., and Lambert, A. (2008). Calcul des seiches à partir du logiciel refonde. *Xèmes Journées Nationales Génie Côtier–Génie*, 155:14–16. (In French).

Proudman, J. (1929). The effects on the sea of changes in atmospheric pressure. *Geophysical Journal International*, 2:197–209.

Rabinovich, A. B. (2009). Seiches and harbor oscillations. *Handbook of coastal and ocean engineering*, pages 193–236.

Rabinovich, A. B., Thomson, R. E., and Stephenson, F. E. (2006). The sumatra tsunami of 26 december 2004 as observed in the north pacific and north atlantic oceans. *Surveys in geophysics*, 27(6):647–677.

Rao, D. B. (1966). Free gravitational oscillations in rotating rectangular basins. *Journal of fluid mechanics*, 25(3):523–555.

Roeber, V. and Bricker, J. D. (2015). Destructive tsunami-like wave generated by surf beat over a coral reef during typhoon haiyan. *Nature Communications*, 6:7854.

Roeber, V. and Cheung, K. F. (2012a). Bosz. *NTHMP (ed.),Proceedings and Results of the 2011 National Tsunami and HazardMitigation (NTHMP) Model Benchmarking Workshop*, pages 361–406.

Roeber, V. and Cheung, K. F. (2012b). Boussinesq-type model for energetic breaking waves in fringing reef environments. *Coastal Engineering*, 70:1–20.

Roeber, V., Cheung, K. F., and Kobayashi, M. H. (2010). Shock-capturing boussinesq-type model for nearshore wave processes. *Coastal Engineering*, 57(4):407–423.

Roelvink, D., Reniers, A., Van Dongeren, A., de Vries, J. v. T., McCall, R., and Lescinski, J. (2009). Modelling storm impacts on beaches, dunes and barrier islands. *Coastal engineering*, 56(11-12):1133–1152.

Ruessink, B. (1998). Bound and free infragravity waves in the nearshore zone under breaking and nonbreaking conditions. *Journal of Geophysical Research: Oceans*, 103(C6):12795–12805.

Ruessink, B. G., Michallet, H., Bonneton, P., Mouazé, D., Lara, J., Silva, P. A., and Wellens, P. (2013). Globex: wave dynamics on a gently sloping laboraty beach. *Proceedings Coastal Dynamics 2013*, pages 1351–1362.

Ruju, A., Lara, J. L., and Losada, I. J. (2012). Radiation stress and low-frequency energy balance within the surf zone: A numerical approach. *Coastal engineering*, 68:44–55.

Région Nouvelle-Aquitaine, Port de Bayonne, C. B. P. B. (2018). Port de bayonne - trafic 2018.

Sand, S. E. (1982). Long waves in directional seas. *Coastal Engineering*, 6(3):195–208.

Schäffer, H. A. (1993). Infragravity waves induced by short-wave groups. *Journal of Fluid Mechanics*, 247:551–588.

Sheremet, A., Guza, R., Elgar, S., and Herbers, T. (2002). Observations of nearshore infragravity waves: Seaward and shoreward propagating components. *Journal of Geophysical Research: Oceans*, 107(C8):10–1.

Shi, F., Kirby, J. T., Dalrymple, R. A., and Chen, Q. (2003). Wave simulations in ponce de leon inlet using boussinesq model. *Journal of waterway, port, coastal, and ocean engineering*, 129(3):124–135.

SHOM (2014). *Références altimétriques maritimes*.

Simarro, G., Orfila, A., and Galan, A. (2013). Linear shoaling in boussinesq-type wave propagation models. *Coastal Engineering*, 80:100–106.

Simon, B. and Manley, D. (2013). *Coastal Tides*. Synthèses - Institut océanographique. Institut océanographique éd.

Sobey, R. J. (2006). Normal mode decomposition for identification of storm tide and tsunami hazard. *Coastal engineering*, 53(2-3):289–301.

Stiassnie, M. and Drimer, N. (2006). Prediction of long forcing waves for harbor agitation studies. *Journal of waterway, port, coastal, and ocean engineering*, 132(3):166–171.

Stockdon, H. F., Holman, R. A., Howd, P. A., and Sallenger Jr, A. H. (2006). Empirical parameterization of setup, swash, and runup. *Coastal engineering*, 53(7):573–588.

Suzuki, T., Altomare, C., Veale, W., Verwaest, T., Trouw, K., Troch, P., and Zijlema, M. (2017). Efficient and robust wave overtopping estimation for impermeable coastal structures in shallow foreshores using swash. *Coastal Engineering*, 122:108–123.

Symonds, G., Huntley, D. A., and Bowen, A. J. (1982). Two-dimensional surf beat: Long wave generation by a time-varying breakpoint. *Journal of Geophysical Research: Oceans*, 87(C1):492–498.

Tappin, D. R., Sibley, A., Horsburgh, K., Daubord, C., Cox, D., and Long, D. (2013). The english channel 'tsunami'of 27 june 2011: a probable meteorological source. *Weather*, 68(6):144–152.

Tavakkol, S. and Lynett, P. (2017). Celeris: A gpu-accelerated open source software with a boussinesq-type wave solver for real-time interactive simulation and visualization. *Computer Physics Communications*, 217:117–127.

team, S. et al. (2007). Swan user manual. *Delft University of Technology. The Netherlands*.

Thomson, R., Rabinovich, A., Fine, I., Sinnott, D., McCarthy, A., Sutherland, N., and Neil, L. (2009). Meteorological tsunamis on the coasts of british columbia and washington. *Physics and Chemistry of the Earth, Parts A/B/C*, 34(17-18):971–988.

Thomson, R. E. and Emery, W. J. (2014). *Data analysis methods in physical oceanography*. Newnes.

Thoresen, C. A. (2003). *Port designer's handbook: recommendations and guidelines*. Thomas Telford.

Thotagamuwage, D. T. and Pattiaratchi, C. B. (2014a). Influence of offshore topography on infragravity period oscillations in two rocks marina, western australia. *Coastal Engineering*, 91:220–230.

Thotagamuwage, D. T. and Pattiaratchi, C. B. (2014b). Observations of infragravity period oscillations in a small marina. *Ocean Engineering*, 88:435–445.

Thotagamuwage, D. T. P. (2014). *Harbour oscillations: Generation and minimisation of their impacts*. PhD thesis, University of Western Australia.

Tissier, M., Bonneton, P., and Ruessink, B. (2017). Infragravity waves and bore merging. In *Proceedings Coastal Dynamics 2017*, pages 451–460.

Tolman, H. L. et al. (2014). User manual and system documentation of wavewatch iii version 4.18. Technical report.

Tsai, C.-H., Huang, M.-C., Young, F.-J., Lin, Y.-C., and Li, H.-W. (2005). On the recovery of surface wave by pressure transfer function. *Ocean Engineering*, 32(10):1247–1259.

Ulbrich, U., Fink, A., Klawa, M., and Pinto, J. G. (2001). Three extreme storms over europe in december 1999. *Weather*, 56(3):70–80.

Uncles, R., Stephens, J., and Harris, C. (2014). Infragravity currents in a small ría: Estuary-amplified coastal edge waves? *Estuarine, Coastal and Shelf Science*, 150:242–251.

Ursell, F. (1952). Edge waves on a sloping beach. *Proceedings of the royal society of London. Series A. Mathematical and Physical Sciences*, 214(1116):79–97.

Van Der Molen, W., Monardez, P., and Van Dongeren, A. (2006). Numerical simulation of long-period waves and ship motions in tomakomai port, japan. *Coastal Engineering Journal*, 48(01):59–79.

Van Dongeren, A., Battjes, J., Janssen, T., Van Noorloos, J., Steenhauer, K., Steenbergen, G., and Reniers, A. (2007). Shoaling and shoreline dissipation of low-frequency waves. *Journal of Geophysical Research: Oceans*, 112(C2).

Van Dongeren, A., De Jong, M., Van der Lem, C., Van Deyzen, A., and Den Bieman, J. (2016). Review of long wave dynamics over reefs and into ports with implication for port operations. *Journal of Marine Science and Engineering*, 4(1):12.

Van Dongeren, A., Lowe, R., Pomeroy, A., Trang, D. M., Roelvink, D., Symonds, G., and Ranasinghe, R. (2013). Numerical modeling of low-frequency wave dynamics over a fringing coral reef. *Coastal Engineering*, 73:178–190.

Van Dongeren, A., Reniers, A., Battjes, J., and Svendsen, I. (2003). Numerical modeling of infragravity wave response during delilah. *Journal of Geophysical Research: Oceans*, 108(C9).

Van Heteren, J. (1983). Estimation of multi-modal directional wave spectra from tri-orthogonal measurements. *Coastal engineering*, 7(3):205–231.

Vilibić, I. (2005). Numerical study of the middle adriatic coastal waters' sensitivity to the various air pressure travelling disturbances. In *Annales Geophysicae*, volume 23, pages 3569–3578. Copernicus GmbH.

Vilibić, I., Domijan, N., Orlić, M., Leder, N., and Pasarić, M. (2004). Resonant coupling of a traveling air pressure disturbance with the east adriatic coastal waters. *Journal of Geophysical Research: Oceans*, 109(C10).

Vilibić, I., Monserrat, S., Rabinovich, A., and Mihanović, H. (2008). Numerical modelling of the destructive meteotsunami of 15 june, 2006 on the coast of the balearic islands. *Pure and Applied geophysics*, 165(11-12):2169–2195.

Waals, O. J., Aalbers, A., and Pinkster, J. (2009). Maximum likelihood method as a means to estimate the directional wave spectrum and the mean wave drift force on a dynamically positioned vessel. In *ASME 2002 21st International Conference on Offshore Mechanics and Arctic Engineering*, pages 605–613. American Society of Mechanical Engineers Digital Collection.

Wang, X., Li, K., Yu, Z., and Wu, J. (1987). Statistical characteristics of seiches in longkou harbour. *Journal of Physical Oceanography*, 17(7):1063–1065.

Wei, G., Kirby, J. T., Grilli, S. T., and Subramanya, R. (1995). A fully nonlinear boussinesq model for surface waves. part 1. highly nonlinear unsteady waves. *Journal of Fluid Mechanics*, 294:71–92.

Welch, P. (1967). The use of fast fourier transform for the estimation of power spectra: a method based on time averaging over short, modified periodograms. *IEEE Transactions on audio and electroacoustics*, 15(2):70–73.

Wilson, B. W. (1972). Seiches. In *Advances in hydroscience*, volume 8, pages 1–94. Elsevier.

Zelt, J. (1991). The run-up of nonbreaking and breaking solitary waves. *Coastal Engineering*, 15(3):205–246.

Zijlema, M., Stelling, G., and Smit, P. (2011). Swash: An operational public domain code for simulating wave fields and rapidly varied flows in coastal waters. *Coastal Engineering*, 58(10):992–1012.